Activity determinants and limiting factors in neutral-pH water oxidation investigated for an electrocatalytic cobalt-phosphate system

A Dissertation

Submitted in Partial Fulfilment of the

Requirements for the Degree of Doctor Rerum Naturalium

(Dr. rer. nat.)

to the Department of Physics

of Freie Universität Berlin

by

Si Liu

Berlin, 2024

Supervisor: Prof. Dr. Holger Dau
Second examiner: Prof. Dr. Peter Strasser

Date of defense: 26. April 2024

Abstract

The massive consumption of fossil fuels and the severe greenhouse gas effect urgently require the development of renewable energy sources. Green hydrogen via water electrolysis powered by renewable energy sources such as solar or wind could drive the upcoming energy transition. While water electrolysis technology is commercially mature, its operation in corrosive electrolytes undoubtedly does not allow for future decentralized energy production by private individuals ("personalized energy"). Moreover, the high kinetic barrier of the water oxidation reaction (also known as oxygen evolution reaction, OER) limits the overall efficiency of water electrolyzer. Therefore, developing OER at neutral pH is crucial but it is typically hampered by low catalytic efficiency. Here, an electrocatalytic cobalt-phosphate system is chosen as a model system to study activity determinants and limiting factors in neutral-pH OER.

Electrochemical experiments were used in combination with various in-situ/operando spectroscopic techniques (e.g. X-ray absorption spectroscopy (XAS), Raman spectroscopy (RM), UV spectroscopy) and total reflection X-ray fluorescence (TXRF) as well as mathematical simulations. As a result, project (a) found out the macroscopic proton transport in the bulk electrolyte dominating the rate limitation of neutral OER and it is facilitated by the diffusion of either phosphate ions (base pathway) or H_3O^+ ions (water pathway). A proof-of-principle experiment shows an achievable current density over 1 A cm^{-2} in neutral-pH OER. Project (b) verified the catalytic current of OER depending exponentially on the Co^{IV} concentration for the volume-active CoCat material, irrespective of electrolyte pH or mass transport limitations. It is the chemical state of the equilibrated material that governs the rate of catalysis, rather than electric potentials or field strengths itself. Project (c) via a novel potassium XAS supports that the important charge-compensated ion flow is not realized by potassium ions but by protons. Project (d) revealed the pronounced local acidification close to the outer surface of CoCat for potential applied beyond the Tafel slope regime. A circular electrolyte flow between anode and cathode is verified and contributed to the buoyancy effect. The non-diffusive flows dominating proton transport may be technically relevant for water electrolyser.

In summary, understanding limiting factors of neutral water oxidation facilitates the knowledge-guided design of efficient, technologically relevant catalysts and water electrolyzers. The new mechanism of OER catalytic rate governed by the chemical state of the equilibrium material may reveal a unifying concept for connecting the heterogeneous, homogeneous and biocatalysis.

Zusammenfassung

Der massive Verbrauch fossiler Brennstoffe und der schwerwiegende Treibhauseffekt erfordern dringend die Entwicklung erneuerbarer Energiequellen. Grüner Wasserstoff durch Wasserelektrolyse, der aus erneuerbaren Energiequellen wie Sonne oder Wind gewonnen wird, könnte die Energiewende vorantreiben. Technologisch betrachtet ist Wasserelektrolyse zwar kommerziell ausgereift, aber ihr Betrieb in korrosiven Elektrolyten lässt eine zukünftige dezentrale Energieerzeugung durch Privatpersonen ("personalisierte Energie") zweifelsohne nicht zu. Darüber hinaus begrenzt die hohe kinetische Barriere der Wasseroxidationsreaktion (auch bekannt als Sauerstoffentwicklungsreaktion, OER) die Gesamteffizienz des Wasserelektrolyseurs. Daher ist die Entwicklung von OER bei neutralem pH-Wert von entscheidender Bedeutung, wird aber in der Regel durch eine geringe katalytische Effizienz behindert. Hier wird ein elektrokatalytisches Kobaltphosphatsystem als Modellsystem gewählt, um die Aktivitätsdeterminanten und begrenzenden Faktoren von OER bei neutralem pH-Wert zu untersuchen.

Elektrochemische Experimente wurden in Kombination mit verschiedenen in-situ/operando spektroskopischen Techniken (z.B. Röntgenabsorptionsspektroskopie (XAS), Raman-Spektroskopie (RM), UV-Spektroskopie) und Totalreflexions-Röntgenfluoreszenz (TXRF) sowie mathematischen Simulationen durchgeführt. Als Ergebnis wurde im Projekt (a) festgestellt, dass der makroskopische Protonentransport im Volumenelektrolyten die geschwindigkeitsbegrenzende neutrale OER dominiert und durch die Diffusion von Phosphationen (Basenweg) oder H_3O^+-Ionen (Wasserweg) erleichtert wird. Ein Proof-of-Principle-Experiment zeigt eine erreichbare Stromdichte von über 1 A cm^{-2} in pH-neutraler OER. In Projekt (b) wurde gezeigt, dass der katalytische Strom von OER exponentiell von der CoIV-Konzentration für das aktive CoCat-Material in der Masse abhängt, unabhängig vom pH-Wert des Elektrolyten oder von Beschränkungen des Massentransports. Es ist der chemische Zustand des Materials im Gleichgewicht, der die katalytische Rate bestimmt, und nicht die elektrischen Potentiale oder Feldstärken selbst. Projekt (c) unter Verwendung eines neuartigen Kalium-XAS beweist, dass der wichtige ladungsausgleichende Ionenfluss nicht durch Kaliumionen, sondern durch Protonen realisiert wird. Projekt (d) zeigte die ausgeprägte lokale Versauerung in der Nähe der äußeren Oberfläche von CoCat bei einem Potenzial, das über den Tafel-Steilbereich hinausgeht. Eine kreisförmige Elektrolytströmung zwischen Anode und Kathode ist nachgewiesen und trägt zum Auftriebseffekt bei. Die nicht-diffusiven Strömungen, die den Protonentransport dominieren, könnten für Wasserelektrolyseure technisch relevant sein.

Zusammenfassend lässt sich sagen, dass das Verständnis der limitierenden Faktoren der neutralen Wasseroxidation die wissensbasierte Entwicklung effizienter, technologisch relevanter Katalysatoren und Wasserelektrolyseure erleichtert. Der neue Mechanismus der OER-Katalysatorrate, der durch den chemischen Zustand des Gleichgewichtsmaterials bestimmt wird, könnte ein vereinheitlichendes Konzept für die Verbindung von heterogener, homogener und Biokatalyse aufzeigen.

Table of Contents

List of Abbreviation

ATP	Adenosine triphosphate
AEM	Adsorbate evolution mechanism
AWE	Alkaline water electrolysis
BP	British Petroleum
BET	Brunauer-Emmetter-Teller theory
BESSY	Berlin Electron Storage Ring Society for Synchrotron Radiation
B_i	Borate buffer
CoCat (CoP_i)	Cobalt oxide catalyst, deposited in KP_i (0.1 M, pH 7)
CoB_i	Cobalt oxide catalyst, deposited in KB_i (0.1 M, pH 9.2)
CV	Cyclic voltammetry
CP	Chronopotentiometry
CA	Chronamperometry
C_{dl}	Electrochemical double-layer capacitance
C_s	Specific capacitance
CO_2RR	Carbon dioxygen reduction reaction
DEMS	Differential electrochemical mass spectroscopy
DFT	Density functional theory
ECSA	Electrochemical active surface area
EXAFS	Extended X-ray absorption fine structure
FE	Faradaic efficiency
FT	Fourier-transform
FEXRAV	Fixed energy X-ray absorption voltammetry
GC	Glassy carbon
HER	Hydrogen evolution reaction
HWHM	Half-width-at-half maximum
IR	Infrared spectroscopy
ITO	Indium tin oxide
ICR	Incoming count rate
IMOC	Intramolecular oxygen coupling
K_D	effective diffusion constant
KMC-3	Hard X-ray beamline for X-ray diffraction and XAS experiments
MeP_i	Methyl phosphate
MCC	Molecular cobaltate cluster
NADPH	Nicotinamide adenine dinucleotide phosphate
NHE	Normal hydrogen electrode
NMR	Nuclear magnetic resonance

NF	Normalization factor
NA	Numercial aperature
[NiFe]-LDH	Nickel-iron layered double hydroxide
LOM	Lattice-oxygen participation mechanism
OER	Oxygen evolution reaction
OCP	Open circuit potential
OCR	Out coming rate
PDF	Pair distribution function
PCET	Proton-coupled electron transfer
PEMWE	Proton exchange membrane water electrolysis
PV	Photovoltaic
PS II	Photosystem II
PS I	Photosystem I
pKa	the negative base 10 logarithm of the acid dissociation constant
RHE	Reversible hydrogen electrode
RRDE	Rotating ring-disc electrode
STH	Solar-to-hydrogen
SOEC	Solid oxide (steam) electrolysis cells
SI-SECM	Surface interrogation scanning electrochemical microscopy
SDD	Silicon drift detectors
TOF	Turnover frequency
TXRF	Total reflection X-ray fluorescence
XAS	X-ray absorption spectroscopy
XANES	X-ray near edge structure
XPS	X-ray photoelectron spectroscopy
WNA	Water nucleophilic attack

1 Introduction

1.1 Broad context

Fossil fuels (i.e., coal, oil, natural gas) have been used for energy supply and in chemical industry for about 260 years.[1] In 2021, the consumption of the three resources reached over 595 EJ accounting for over 80% of the globally consumed energy. Their use has increased steadily over the past two decades, with the exception of 2009 and 2020 due to the global economic crisis and the coronavirus pandemic.[2] Global annual energy consumption is predicted to reach 20 terawatts by 2030, doubling by 2050 and tripling by the end of the century.[3;4] Considering the non-renewable nature of burning fossil fuels, the global community will face energy depletion in the next century. Data published in the 2021 British Petroleum (BP) Statistical Review of World Energy shows that global coal, oil and natural gas could be depleted in 139, 54 and 49 years, respectively, based on trends in the ratio of global coal, oil and natural gas reserve-to-production from 1980 to 2020.[5] Taking into account the accelerated process of industrialization in underdeveloped and developing nations, fossil fuels will undoubtedly remain the main form of energy in the short term to meet the growing demand for energy.[6] Global combustion/oxidation of fossil fuels increases carbon dioxide emissions into the atmosphere and oceans, leading to global warming, extreme weather phenomena, ocean acidification and increased geopolitical instability.[5;7]

Cumulative emissions of carbon dioxide from fossil fuels over the entire 1850-2021 period are about 172 million tons per year, with coal accounting for 46%, oil 35%, and natural gas 15 %.[8] Huge anthropogenic CO_2 emissions are viewed as a major source of the greenhouse gas effect, which is why the Paris Agreement came into force in 2016. The agreement sets a goal of achieving net-zero CO_2 emissions by 2050 in order to keep global average temperatures well below 2 °C or pursue efforts of 1.5 °C above pre-industrial level.[9] In order to realize the provisions of the Paris Agreement, complete or drastic reductions in the use of fossil fuels need to be accompanied by a strong development of clean/renewable energy sources, i.e., wind/solar, hydropower and biomass, among others. According to statistics, the utilization of renewable energy accounts for only about 15% of total global energy consumption.[5] In recent years, countries around the world have developed a variety of policies around renewable energy technologies, carbon pricing policies, carbon dioxide capture and conversion, clean materials development, solar energy utilization, and others.[10;11] Green hydrogen plays an indispensable role in decarbonization processes, for example in industry (e.g., steel manufacture), transport (e.g., shipping or aviation), buildings (e.g., hydrogen heating) and power generation.[12] Demand for pure hydrogen tripled between 1975-2018, leading to more than 70 million tons of hydrogen production in 2018.[12] Currently, 90% of hydrogen is produced by burning fossil fuels (natural gas).[7]

Notably, the electrolysis of water using renewable energy sources such as solar or wind to generate electricity can produce energy without releasing carbon and has emerged as a promising method for producing green hydrogen.[13-15] More than 50 years ago, Fujishima and Honda discovered a titanium dioxide semiconductor that splits water under light illumination,

and their pioneering work inspired (photo)electrochemical water splitting and a combination of photovoltaics and water electrolyzers.[16;17] In practice, water splitting via indirect electricity is currently the most matured technology and is commercially available, but it is 6-25 times more costly than using conventional fossil fuels (e.g., steam-methane reformation, coal gasification).[18;19] As a whole, superior performance to date has mostly been achieved in lab-scale applications, while larger scale applications (>100 W) are more challenging. To date, the most efficient photovoltaic-powered electrolyzers have achieved solar-to-hydrogen (STH) efficiency of up to 30% on a laboratory scale.[20] Noteworthily, a new research on solar hydrogen production shows that an unprecedented large-scale hydrogen production (0.5 kg per day) can be achieved with concentrated sunlight, demonstrating more than 20% STH device (5.5% system), which can power a fuel cell vehicle for about 50 km.[21] In addition, a hydrogen rate of more than 2 kilowatts (>0.8 g min^{-1}) was realized, which represents an improvement of about two orders of magnitude over previous findings.[22] In addition to utilizing renewable energy sources, another way to close the carbon cycle is by electrochemically converting waste carbon dioxide into chemical feedstocks.[11] A report notes that if electricity prices are below 4 cents per kWh and energy conversion efficiency is at least 60 percent, the cost of converting CO_2 into chemicals using green electricity could be comparable to the cost of burning conventional fossil fuels.[11]

Challenges for achieving CO_2 conversion also include capturing CO_2 directly from the air, which currently costs between $94 and $232 per tonne of CO_2 captured due to the lack of mature technologies for capturing CO_2 from the atmosphere.[23] From a practical standpoint, there has never been a better time for academia, government, and industry to join forces to improve the efficiency of catalytic conversion and to understand the determinants of various catalytic reactions, whether hydrogen utilization or CO_2 conversion.

The hydrogen evolution reaction (HER) and carbon dioxygen reduction reaction (CO_2RR) involve multi-electron and multi-proton transfers, similar to the metabolic process involving hydrogenase in microorganisms [24;25] or the dark reaction period in natural photosynthesis that converts CO_2 into glucose.[26-29] Natural photosynthesis has provided great inspiration for energy storage and conversion and has been continually reviewed (Figure 1-1).[4;7;30-35] Natural photosynthesis is divided into light and dark reaction processes, corresponding to photosystem II (PS II) and photosystem I (PS I) systems, respectively.[36] Typically, photosynthesis consists of four stages: (i) light absorption, charge separation and electron transfer; (ii) water oxidation at the center (Mn_4CaO_5) of PSII cluster center; (iii) proton/electron separation for energy storage (generating adenosine triphosphate (ATP) and nicotinamide adenine dinucleotide phosphate (NADPH)); (iv) CO_2 fixation (Calvin cycle).[35] The first two stages of PS II produce oxygen, electrons, and protons, followed by the transfer chains of electron (proton) to PS I. This process is known as the Z-scheme process.[6;32;37] Interestingly, the widespread mimicry of natural photosynthesis occurred during two periods: the oil crisis of the 1970s; and the process of decarbonization initiated by the massive burning of fossil fuels that led to global warming.[38] The complexity of biological photosynthesis has led to many research topics in building artificial photosynthesis, including light capture, charge separation, catalysis, semiconductors, nanoscience, biomimicry, (photo)electrochemistry and photophysics, reaction

mechanisms, and engineering technologies.[32;39-41] It has been noted that the electron and proton equivalents generated by water oxidation (step ii) provide the driving force for carbohydrate production. In addition, the water oxidation center of PS II has been regarded as a natural paradigm for topics involving redox-potential leveling, proton removal, and O-O bond formation. Thus, water oxidation (also known as OER) plays a critical role in storing solar energy, which is the center of my dissertation.

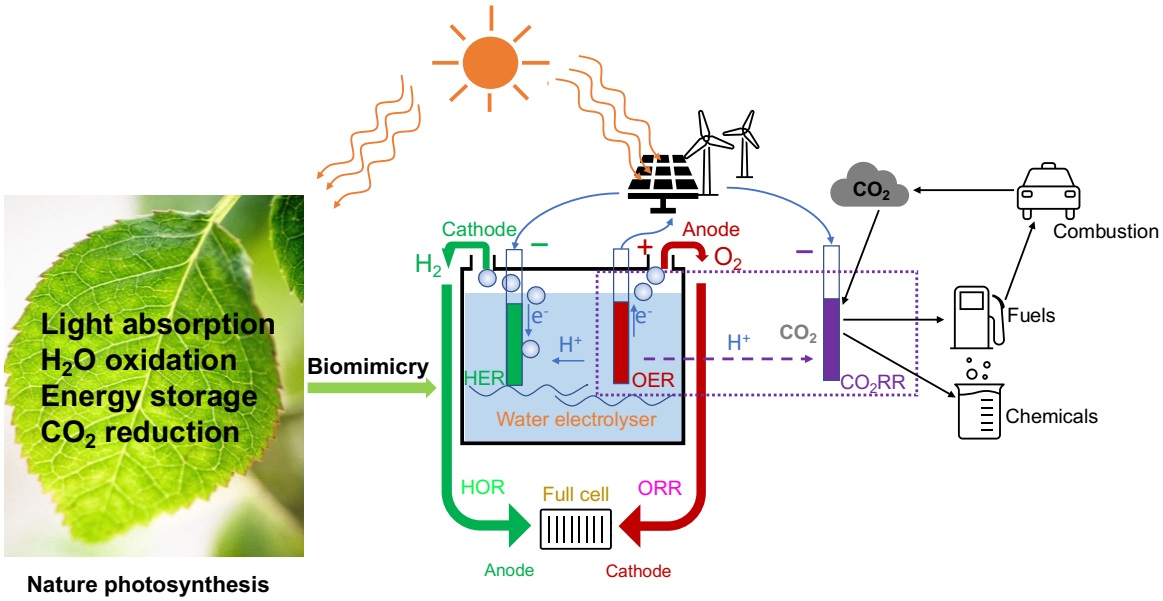

Figure 1-1. A simplified scheme showing experimental techniques of energy storage and conversion inspired by natural photosynthesis. The leftmost picture points out the general steps of natural photosynthesis.[35] The middle cell emphasizes the ideal cycle of a water electrolyzer and a fuel cell. The purple dotted box illustrates the integration of OER and CO_2RR to produce valuable fuel or chemical products and mitigate CO_2 emission. HOR, hydrogen oxidation reaction; ORR, oxygen reduction reaction; CO_2RR, carbon dioxygen reduction reaction.

As a half-reaction of water splitting, OER reduces the overall efficiency of the water electrolyzer because it involves $4e^-/4H^+$ transfer reactions, which have slower kinetics and require higher overpotentials compared to HER.[42] Here, instead of discussing the effect of the electrolyte environment on OER, we summarize the general progress of water electrolysis under different electrolyte conditions. Water electrolysis is a well-established technology, more than two centuries old since its discovery in 1789.[43] Although water splitting was discovered in acidic electrolytes, it has been used commercially in alkaline solutions for over a century.[44] Depending on the type of electrolyte, water electrolyzers are categorized into three systems:[45] alkaline water electrolysis (AWE),[46-48] proton exchange membrane water electrolysis (PEMWE),[43;46;49-51] and solid oxide (steam) electrolysis cells (SOEC). Besides operating in extremely acidic or alkaline media, neutral-pH water electrolysis is another way to produce hydrogen and facilitate the combination with CO_2 reduction reaction.[52-58] However, current densities at neutral pH are still largely lower than those at extreme conditions. Why current

densities at neutral or near-neutral pH are so low? Further discussions of water oxidation in neutral pH media are provided below.

1.2 Water oxidation at neutral pH and evaluation of catalytic performance

Numerous mechanistic studies have been conducted on alkaline or acidic OERs.[59-63] Compared to extreme conditions, water oxidation under neutral pH conditions has been less studied. In order to achieve large-scale water splitting, OER studies at neutral pH will be critical:
(i) In contrast to OER in strong acids or bases, neutral-pH OER facilitates the assembly of catalysts with other semiconducting materials in manufacturing devices (e.g., artificial leaf[32;64]); Furthermore, unlike natural water, where metals or biomolecules are always present, passivating oxide layers (e.g., $Ca(OH)_2$, $Mg(OH)_2$, etc.) are easily formed in alkaline media, which can also lead to denaturation of biomolecules;[65]
(ii) For achieving "personalized energy", where cheap and simple devices substitute the centralized large-scale energy conversion and utilization procedures,[66] its safety aspect is guaranteed at neutral pH and it also reduces the installation costs of the equipment;
(iii) In order to combine OER with CO_2 reduction, neutral pH can reduce the conversion of CO_2 to carbonate and improve the utilization of CO_2 compared with alkaline conditions. In addition, compared with acidic conditions, neutral pH can inhibit the HER side reaction, thus improving the product selectivity of CO_2RR.[67;68]
Since water oxidation is an endothermic process, efficient catalysts usually work under harsh conditions,[69], therefore it is crucial to develop superior catalysts at neutral pH. Ideal catalysts should be characterized by at least four aspects, inter alia, cost-effectiveness, durability (from years to a decade), low overpotential (high current densities), and high turnover frequency (TOF).[53] A simple catalyst synthesis procedure is essential. First-row transition metal compounds involving Co-, Ni-, and Fe-based materials have been extensively studied as efficient electrocatalysts in neutral or alkaline media. Whereas $Ni_vFe_wO_x(OH)_y$ catalysts are widely recognized as the best alkaline OERs, volume-active cobalt oxides (CoCat), pioneered by the Nocera group in 2008, are one of the best-performing electrocatalytic materials currently available at neutral pH conditions.[70;71] Many derived catalysts with other properties have been developed through strategies such as changing components, surface area, morphology,[72] and electronic states.[42;53;73-76] Although the reported catalysts have been tested mainly on a laboratory scale, there is no specific uniform procedure for direct comparison of catalysts prepared in different protocols or laboratories. In order to compare the performance of catalysts in terms of activity, stability and efficiency, the following parameters are usually evaluated:
(1) Overpotential (η): it defines the potential difference between the experimentally measured potential at a specific current density and the theoretically thermodynamic equilibrium potential of the OER at 1.23 V versus reversible hydrogen electrode (RHE). A smaller overpotential means a higher energy conversion efficiency, thus indicating a better performance of the catalysts. Therefore, several common overpotentials are listed here based on electrolyte type and activity value: (a) the "Onset η" is typically found in the field of homogeneous catalysis and is defined as the onset potential at which the catalytic current density just begins. However, the exact starting position at which the initial catalytic reaction

occurs is often poorly defined due to the overlap with the redox peak; (b) the other η is defined at a specific current density such as 1 mA cm^{-2}, and is commonly used as a metric for the OER at a neutral pH; and (c) the overpotential (denoted as η_{10}) at a constant current density of 10 mA cm^{-2} is widely accepted for evaluating the actual performance of electrochemical devices. This value is based on a solar-to-fuel efficiency of 12.3 % under one sun illumination.[77;78] It is worth noting that η_{10} is not measured in terms of the intrinsic activity of the catalyst;[78] (d) importantly, some catalysts (e.g., nickel-based material) can typically reach high current densities (200-400 mA cm^{-2} is often observed in industrial electrolyzers), therefore it is necessary to measure overpotentials at higher current density such as 100 mA cm^{-2} to access the OER performance of a catalyst. It should be noted that the overpotential at a given current density depends on several parameters, including the electrochemical setup device, the type and concentration of the electrolyte, the method of film preparation, the sample size, etc.

(2) Tafel slope and exchange current density: Tafel slope is the slope of a linear regression of a Tafel plot describing the relationship between overpotential (η) and the logarithm of the current density (log(*j*)), and is expressed by the Tafel equation ($\eta = b\log(j) + j_0$, where b represents Tafel slope, j_0 represents the exchange current density). It provides information about the reaction kinetics and therefore the reaction mechanism.[79-82] The exchange-current density (j_0) reflects the intrinsic electrocatalytic activity of the catalyst. Good OER electrocatalysts typically have lower Tafel slopes and larger exchange current densities.[83] It is important to note that the determination of the Tafel slope should be free from mass transfer limitations such as bubble interference.[84-88] Moreover, the Tafel equation adapted from Butler-Volmer model provides insights into the catalytic kinetics involving charge transfer at the metal-electrolyte interface based on a series of assumptions,[89-91] and therefore, understanding the mechanism of OER catalytic rate in terms of the Tafel slope should be mindful of some partially contradictory reports.[40;92]

(3) Catalytic activity: the catalytic performance of catalysts is reflected in the catalytic current normalized by several factors, i.e., the geometric area of the electrode (geometric activity), the mass loading of the catalyst (mass activity), and the effective active area of the catalyst (specific activity). Geometric activity is used to assess the efficiency of solar-to-fuel conversion and does not reflect the intrinsic activity of the catalysts;[78] mass activity is an important indicator, especially for noble-metal catalysts. A high mass activity means that less catalyst is used and therefore more cost-effective; specific activity is proportional to the effective active area, which can be measured by the Brunner-Emmett-Taylor (BET) method [93;94] or by determining the electrochemically active surface area (ECSA). The former is based on the principle of gas (N_2) adsorption and is commonly used for drying samples, assuming that the gas enters the entire surface of the catalyst and is affected by the porosity or morphology of the material.[93;94] The ECSA is proportional to the electrochemical double-layer capacitance (C_{dl}), which can be determined by collecting a series of CVs in a small non-Faradaic region at different scan rates.[95] By plotting half of the difference in anode and cathode current densities versus the scan rates, the fitted slope represents C_{dl} and it is further divided by the specific capacitance (C_s) to get the ECSA value. Cs can usually be found in the literature depending on the electrode

substrate and the electrolyte, but we recommend direct measurement of the capacitance per unit area of a smooth planar electrode substrate under the same electrolyte conditions.[95]

(4) Stability: as one of the crucial parameters for judging the performance of a catalyst, good stability is a prerequisite for practical application, and ideally the catalyst should be able to operate for several years.[96] Catalyst stability is assessed by taking continuous CVs, chronopotentiometry (CP) or chronoamperometry (CA) measurements, respectively, over a long operating period. When comparing CV curves before and after hundreds of cycles, good stability is indicated if the CV curves of the last cycle and the first cycle nearly coincide or if the decrease is less than 10%. Stability measurements at 100-200 mA cm^{-2} and high temperatures (70-100 °C) are typically required for large-scale installations.[45]

(5) Turnover frequency (TOF): it describes the intrinsic activity of OER catalysts by the following equation:[97;98]

$$TOF = \frac{jN_A}{4F\Gamma} \qquad \text{Equation 1-1}$$

j denotes current density at a certain overpotential, N_A represents the Avogadro constant, F is the Faraday constant, Γ stands for the number of active sites. Due to the uncertainty of the exact number of active sites, it is challenging to obtain an accurate TOF value. Typically, there are two methods of calculating TOF. One is to consider the entire mass loading as active sites, which leads to an underestimation of the TOF value because not all meal sites are active sites. The other method is to integrate the redox peak area of the metal element under the cathodic current curve as shown in Equation 1-2:[99]

$$\Gamma = \frac{A}{\nu ne} \qquad \text{Equation 1-2}$$

A denotes the area of integration of the cathodic CV wave (mA V); ν is the scan rate of CV (mV s^{-1}); n is the number of electrons transferred for the redox reaction (a typical value of n is 1, e.g., Co^{2+} to Co^{3+}); e is the elementary charge (e = 1.602 × 10^{-19} C).

(6) Faradaic efficiency (FE): it represents the charge transfer efficiency of transferring charge from an external circuit to oxygen (for OER) and can be quantified as the ratio of actual oxygen evolution to theoretical oxygen evolution. The actual amount of oxygen is often measured by gas chromatography or water-gas displacement, while the theoretical amount of oxygen is calculated by Faraday's law.[100] Moreover, the FE can be used to assess the selectivity of catalysts, such as those catalysts used for CO_2RR. An alternative way to directly quantify FE is to use a rotating disc electrode (RRDE) but it is only applicable to OER.[100;101] The basic principle is that oxygen produced by a glassy carbon (GC) disk is consumed on a Pt ring via the oxygen reduction reaction. The currents recorded from the discs and rings as well as the collection efficiency determined by RRDE can be used to calculate the FE according to Equation 1-3:

$$FE = \frac{I_R n_D}{I_D n_R N_{CL}} \qquad \text{Equation 1-3}$$

Here, the ring and disc currents are denoted as I_R and I_D, respectively; n_R and n_D are the number of electrons transferred on the ring and disc, respectively; N_{CL} represents the collection efficiency of RRDE. Theoretically, the FE should be 100% for an excellent electrocatalyst, but due to the formation of by-products or heat, the FE is often lower than unit.[42;43]

The above parameters reflect the thermodynamic and kinetic behavior of catalysts and are the cornerstone for screening excellent neutral water electrolyzers catalysts.

1.3 Amorphous cobalt-based material

As OER catalysts, noble metal oxides (e.g., IrO_2 and RuO_2) have been widely investigated and have shown excellent performance and are regarded as the benchmark electrocatalysts for OER. However, its high cost and scarcity limit its commercial application.[102] As a result, there is a growing research interest in searching for non-precious transition metal oxides.[42;76;103] In recent years, amorphous catalysts have shown higher catalytic performance and advantages than crystalline materials (Figure 1-2).[42;75;104-108]

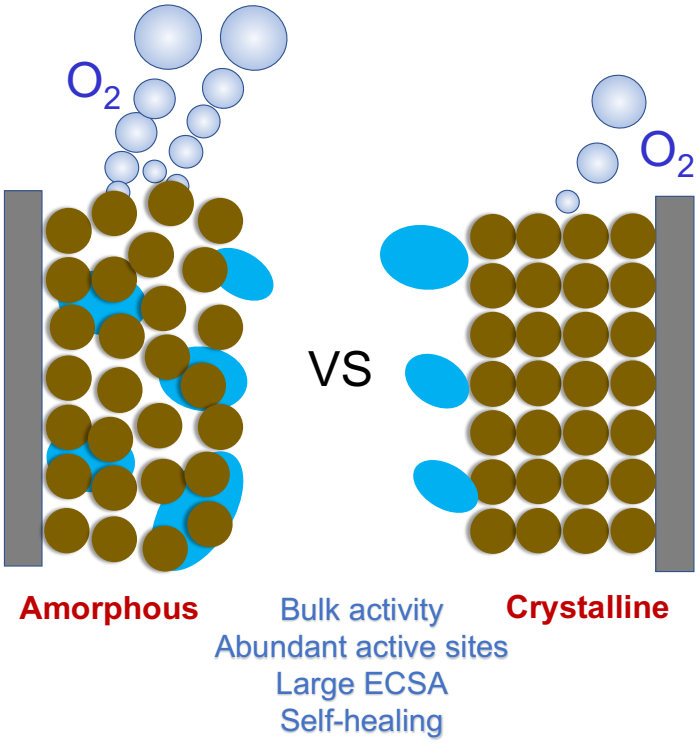

Figure 1-2 Scheme showing amorphous materials having better activity because of the above-mentioned properties. Readapted with permission from ref.[109]. In the case of the CoCat, however, the electrochemically active surface area (ECSA) is not particularly large and corresponds to that of the substrate electrode.[99] The CoCat can be regarded as a hydrated oxide, with thin (mono)layers of water molecules between oxide layer fragments (similar to birnessite), so that there is no ionic double layers within the CoCat material.

As an exemplary model catalyst, the electrodeposited amorphous CoCat catalyst from the pioneering work of Nocera's group,[70] showed the best catalytic performance in neutral OER catalysis, stimulating a strong interest in this material.[65;71;99;110-143] CoCat offers a number of advantages: (i) high catalytic activity at room temperature and neutral pH, (ii) economical and

abundant transitional metal components, (iii) self-healing (repair) properties by reapplying the potential,[71;121;132] (iv) high activity in nature water and salt (sea) water, (v) high manufacturability and broad compatibility with a variety of substrates, and (vi) the ability to be used as a co-catalysts for modifying photoelectrodes to enhance photo- (electro-) chemical activity.[144-146] This is similar to the mechanism involving self-assembly[70] and self-repair[71;132;140] of the PSII active centers ($CaMn_4O_5$ clusters).[147-149] Additional functional and structural comparisons of CoCat with the OER active centers of PS II are given in ref. [66]. It is noteworthy that by slightly modifying the electrodeposition technique or changing the electrolyte, some CoCat-derived catalysts, such as nickel-based[150;151] or manganese-based[152;153] catalysts, have an extremely similar structure to amorphous CoCat.[112;152;154] In the following, previously reported work on CoCat is summarized concerning its preparation, structural and functional relationships, determinants of catalytic activity, and possible catalytic models.

In 2008, CoCat catalysts were electrodeposited on ITO using different cobalt salts (e.g., $CoSO_4$, $Co(NO_3)_2$, or $Co(OTf)_2$ (where OTf = triflate)) dissolved in potassium phosphate buffer (KPi) or similar buffer systems at a catalytic potential (1.29 V vs. NHE) at neutral pH, which was the starting point of the study of neutral CoCat catalyst. Cobalt, phosphate and potassium ions were all incorporated into CoCat with a stoichiometry of approximately 2-3:1:1.[70] Other buffer systems including methyl phosphonate (MePi), borate (Bi) or fluoride were investigated and showed comparable catalytic activity, suggesting that the catalytic activity is electrolyte independent.[111;114] CoCat can be deposited on a variety of semiconductor or conductive substrates such as titanium dioxide,[155-157] silicon,[64] glassy carbon,[111;121;123] nickel foil,[111] etc., which means that it is highly manufacturable and can be used directly to construct photovoltaic electrodes without the need for post-modification. Cobalt metal can also be used to prepare CoCat.[115] Recently, the intrinsic photoelectrochemical effect of CoCat has been reported and its excitation wavelength dependence has been emphasized.[157]

The amount of cobalt deposited can be controlled by varying the deposition time. By selecting the catalytic potential, the prepared CoCat films will be rougher. A quantitative equation for the conversion between deposition amount and film thickness is available in ref. [99;128]. It is worth noting that CoCat can be operated in natural water or even salt water (seawater) with negligible interference from Cl^- or impurities, which means that it has robust properties.[65;111] The presence of KPi or other buffers (e.g., Bi, MePi) promotes the self-repair mechanism. The reason for this is that in the presence of phosphate ions, dissolved Co^{2+} is redeposited when Co^{2+} is oxidized to $Co^{3+,}$ which is analogous to the process of CoCat preparation.[66] In isotope experiments with labeled cobalt (^{57}Co) and phosphate (^{32}P), switching off the electrode potentials, cobalt is released much slower than phosphate, which supports the role of cobalt as the main active center in water oxidation catalysis.[71] The detailed mechanism of self-healing and self-repairing under different potential conditions was discussed in ref. [140].

Structurally, CoCat was first characterized by quasi-X-ray absorption spectroscopy (XAS),[112] and it shows that complete or incomplete Co^{III}–oxo cubanes interconnected by di–$\mu_{2,3}$–O/OH are likely to constitute the central structural unit of CoCat. Subsequently, theoretical

calculations discuss the protonation states of CoCat, including protonated μ_2–O atoms or deprotonated μ_3–O atoms, and suggest existing terminal oxygen atoms for almost all catalysts.[40;112;113;122;158] This facilitates the formation of low-barrier hydrogen bonds and can increase the proton mobility at the catalyst-water interface.[120] Subsequently, by comparing the extended X-ray absorption fine structure (EXAFS) and X-ray absorption near edge structure (XANES) between CoCat and the well-known $LiCoO_2$ reference, it further supports the short-range ordered structure of CoCat and reveals the bulk oxidation state of Co^{3+} at static state.[110] In addition, Nocera group proposed a molecular cobaltate cluster (MCC) model[117] and suggested that CoCat has a similar structural motif to the cobaltate compound CoO(OH) with edge-sharing CoO_6 octahedra that differs from the corner-sharing cubane model.[112] An average Co valency greater than 3 was detected in the catalytic region (1.25 V vs. NHE) by XANES spectroscopy.[117] The MCC model was further supported and extended to a 3D layered double-hydroxide structure by stacking the oligocobaltate lamellae.[118] By X-ray photoelectron spectroscopy (XPS), it was observed that the hydrated layered double-hydroxide structure contains nonstoichiometric electrolyte anions.[118] Direct evidence of Co(IV) species was detected by ex/in situ EPR during catalysis.[116;136] Pair distribution function (PDF) analysis of high energy X-ray scattering indicates that the CoCat structure domain consists of 13–14 cobalt atoms with a disordered component of phosphate.[122] Subsequently, larger cobalt domains with 19 Co atoms were evaluated for CoCat deposited at low potential (1.04 V vs. NHE).[159] Another PDF analysis showed that when electrodeposited with different buffers (CoBi vs. CoPi), intermediate-range structures are distinct, suggesting that CoB_i has multi-layered coherent state domain clusters, while CoP_i has unstacked smaller cluster.[159] Another comparison between CoB_i and CoP_i centered on the charge transport and bulk conductivity properties conducted by various spectroscopies.[133]

Preliminary mechanistic findings of CoCat were deduced from electrodynamic and cyclic voltammetry studies.[113] The results show that catalytic water oxidation involves the pre-equilibrium of one electron, one proton process (PCET), and that phosphate acts as a proton acceptor to facilitate the PCET equilibrium redox process, which precedes the turnover-limiting chemical step of O-O bond formation.[113] However, the critical nature of the rate-determining step in the formation of O-O bonds is not well understood. The O-O bond formation pathways reported in recent years are shown in Figure 1-3, mainly through bulk water nucleophilic attack (BWNA) and intramolecular oxygen coupling (IMOC). Subsequently, the structure, stability, and activity of CoCat in water oxidation reactions were investigated at pH 0–14, revealing the pH dependence of the homogeneous and heterogeneous reactions.[118] The proposed catalytic mechanism for O–O bond formation involves the nucleophilic attack of the Co(IV)=O site by bulk water (BWNA, a path of Figure 1-3A). This was also confirmed by rapid-scan FTIR spectroscopy studies of Co_3O_4 nanoparticles, which identified superoxide species bridging two cobalt ions.[160] Density functional theory (DFT) calculation using the cuboidal Co_4O_4 complex as a structural model [161] suggested that Co(IV) to Co(V) is required for O–O bond formation, also seen more in refs. [128;162-164]. Alternative DFT and molecular dynamics simulation of CoCat suggest that the direct intramolecular oxygen coupling (IMOC) mechanism involves the coupling of a Co(IV)═O oxyl to geminal (i.e., bonded to the same Co

atom) Co–OH (b path of Figure 1-3A) or Co-μO–Co groups (d path of Figure 1-3A) to produce either hydroperoxo or peroxo intermediates prior to the formation of O–O bond.[162;164] However, the coupling of the d-path to the bridging oxygen is discouraged in refs. [131;162;163].

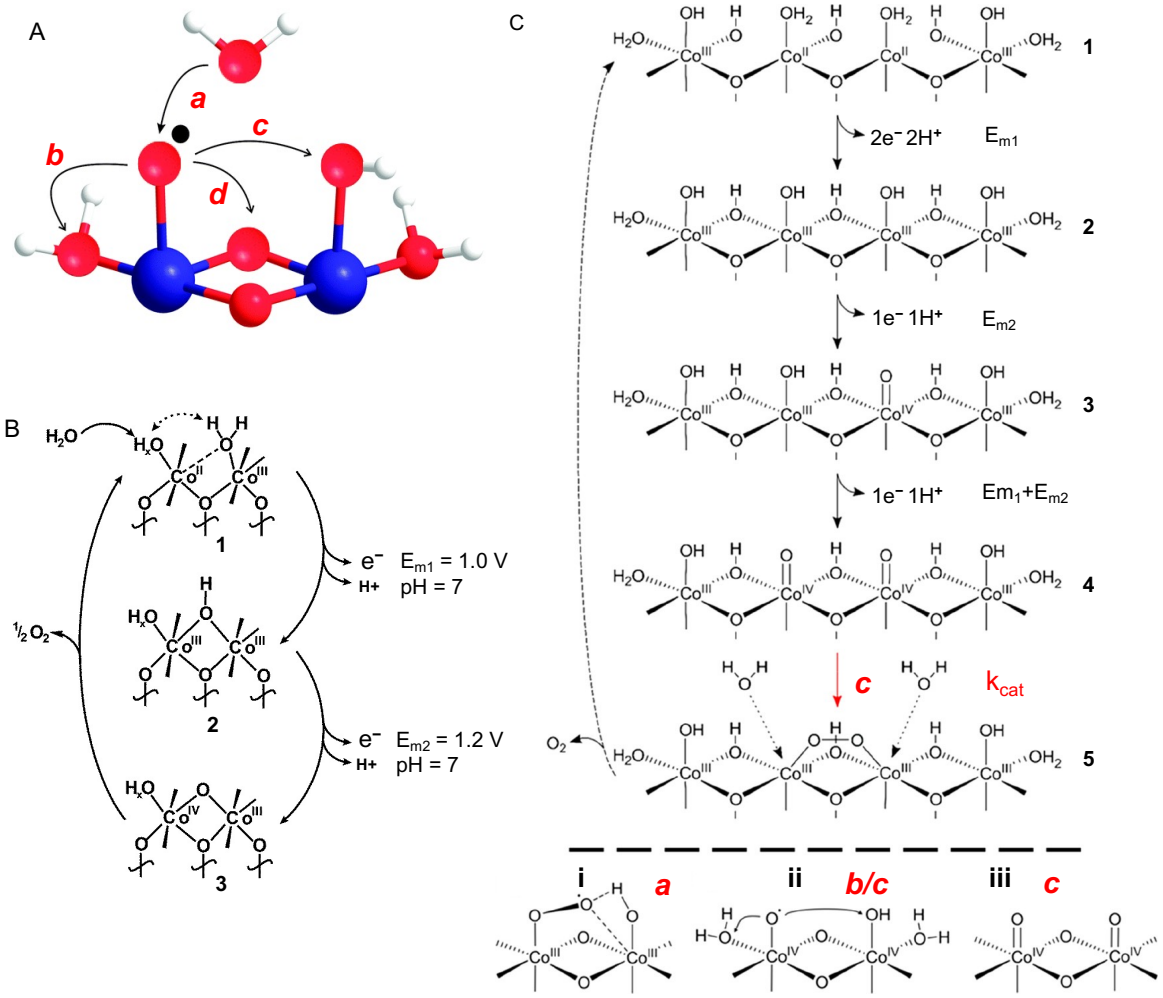

Figure 1-3. Possible pathways for O–O bond formation and the proposed OER models of CoCat. (A) The O–O bond formation pathways via either bulk water nucleophilic attack (BWNA) onto pre-bound oxygen of Co-oxo species (a) or intramolecular oxygen coupling (IMOC), which involves geminal coupling to O atoms bound to the same cobalt atom (b and d) as well as coupling of two adjacent cobalt oxyl radicals (c). Cobalt, blue spheres; oxygen, red spheres; hydrogen, white spheres. For clarity, only a portion of the cobalt coordination is shown. (B) The potential-dependent change of structural motifs for CoCat prior to the oxygen evolution steps. Note that the terminal water/OH ligand or phosphate ligand are not shown for simplicity of presentation. The proposed OER mechanism for CoCat is shown in the upper part of panel C, assuming that catalysis occurs at the periphery of the CoCat fragments. The bottom region of panel C shows representative catalytic intermediate states prior to the rate-determining step, with the red letters (a-c) aligned with panel A. Readapted with permission from refs. [126;134;162].

Another IMOC mechanism reveals the direct coupling between two Co(IV)═O metal oxo groups (c path of Figure 1-3A), as evidenced by computational analysis and experimental studies (e.g., isotopic oxygen labelling experiment coupled with differential electrochemical mass spectrometry (DEMS)) based on CoCat or other cobalt (hydr)oxides.[131;132;134;165] In

addition to the discussion of the direct mechanism of O–O bond formation, other mechanistic factors affecting the turnover of water oxidation reaction have been extensively investigated. Importantly, a methodology focusing on proton transfer or transport within the CoCat film was presented and various Tafel slopes (e.g., F/RT ln 10, F/2RT ln 10 or 0) associated with different rate-controlling factors are elucidated.[124] Furthermore, a simpler model emphasizes proton transport mediated by buffer bases in the electrolyte as the crucial activity limiting factor.[135] Experimentally, in situ XAS tracked the change in the CoCat oxidation states and proposed a catalytic framework model involving the accumulation of oxidation equivalents before O-O bond formation.[126] The proposed changes in structural motif shown in Figure 1-3B include dynamic redox transitions, the most probable O(H)-bridging-type modifications between cobalt ions, and the corresponding changes in proton states.[126] Interestingly, individual cobalt redox transitions involving Co(II/III) and Co(III/IV) were obtained by operando Raman spectroscopy rather than merely obtaining averaged oxidation states by XAS.[139] Surface interrogation scanning electrochemical microscopy (SI-SECM) provides the first direct measurement of the density of surface active sites, enabling the calculation of accurate TOF values.[127] Quantification of OER parameters by Fourier transformed alternating current (FT ac) provides unique mechanistic insights into redox transformations of cobalt oxides and other metal oxides.[129] Additional qualitative and quantitative models related to charge transfer and catalytic activity of CoCat were revealed by CVs measurements under different parameters including KPi buffer concentration, scan rates and film thickness.[128] Furthermore, another model shows a close relationship between film conductivity, cobalt cluster size, redox properties, and catalytic performance.[138] H/D isotopic labeling studies and the oxidation states measurements as well as time-resolved UV-vis spectroscopy indicate that the rate-determining step is independent of proton or electron transfer and support the c path involving the pairing of terminal oxygen atoms of two neighboring cobalt species shown in Figure 1-3A. Moreover, the important role of Co(IV) oxidation states accumulation in the turnover-limiting O–O bond formation was verified (Figure 1-3C).[134]

Whereas phosphate function has been emphasized,[71;99;111-113;117;118;122;123;128;158;166;167] there is no direct evidence for phosphate coordination environment in CoCat. ^{31}P NMR analysis indicates that most phosphate ions in the intercalation of cobalt hydroxide sheets are not bonded to the cobalt ions but have pseudo-contact interactions with the interlayer.[168] The Co K-edge XAS and P K-edge XAS consistently show that phosphate species are bound to the edges of CoO_2 fragments.[130] With arsenate substituting phosphorus, the first arsenate binding motif in an amorphous catalyst is acquired by EXAFS at the As K-edge, and the results of the study indicate that the rate-determining steps is independent of the anion type.[169] Subsequently, by the stimulated Raman spectroscopy, the presence of orthophosphate species and the corresponding network in CoCat clusters is hypothesized.[137] The presence of different redox-inert anions (Cl^-, OAc^-, Pi) and cations (K, Li, Ca) apparently had no significant effect on CoCat activity.[123] The effect of anion type is reflected in the difference in Co-oxide cluster size, long-range ordering, and redox charge accumulation, electrodeposition rates, and catalytic properties.[123] The decrease in the catalytic current is due to an increase in the cluster size, which implies that the active sites may locate at the periphery of clusters likely linked to the

terminal oxygen ligands of the cobalt domain.[123] XAS at the Ca K edge shows that CoCat prepared from Ca salts has a small portion of $CaCo_3O_4$ cubes, similar to the Mn complex of PS II, otherwise other monovalent cations are present in hydrated form and are located unspecifically between the Co-oxide layers.[123] Infrared spectroscopy (IR) suggests that phosphates may be incorporated into CoCat clusters.[170] Atomic force microscopy combined with synchrotron-based X-ray grazing incidence diffraction analysis showed that the high porosity of CoCat films originated from the aggregation of nanoparticles.[170] The thickness-independent TOF per cobalt ion under low overpotential conditions suggests the volume activity of CoCat.[99] Based on CoCat, the distinction between OERs occurring at the surface or in the bulk is revealed, providing a complete picture for the study of heterogeneous water oxidation.[105]

Despite the numerous research reports on the catalytic properties, structural modeling, and reaction mechanisms of CoCat, there is still a lack of knowledge guiding the determinants of catalytic activity from the macroscopic to microscopic scales, which is the focus of this dissertation.

1.4 Potential determinants of OER behavior

In the last two decades, OER catalysts have sprung up, elucidating a large number of activity determinants through experimental methods and theoretical calculations, which have facilitated the knowledge-oriented design of novel catalyst materials.[74;171;172] Two strategies are commonly used to increase the activity of catalysts, i.e., increasing the intrinsic activity and/or increasing the number of active sites.[42] The former approach described in the literature includes heteroatom doping,[75;173;174] controlling the atomic coordination environment[175-177] and the electronic structure (charge, spin, orbitals etc.),[42;176;178-183], engineering modifications including regulating phase components,[184;185] defect,[186-190], crystal facets[191], and creation of heterogeneous nanointerfaces,[73;192;193] among others; the latter increases the number of active sites through morphological or structural engineering, which alters the surface area and exposes more active sites,[194] electrode structure (e.g., growth of catalysts on three-dimensional substrates) [43;195], size, particle distribution, and porosity modulation can also increase the number of active sites.[95;196;197] Generally, those factors interplay with each other to achieve optimal performance. Several activity determinants of neutral water oxidation related to the four topics of this dissertation are discussed below.

1.4.1 Role of the electrolyte

For water oxidation reactions operating at neutral pH, the choice of electrolyte is of great importance,[54;198] and it has been extensively studied due to its role in OER performance, reaction mechanism and stability.[54;99;111;118;123;135;138;199-203] The need for a neutral pH has been discussed in section 1.2 and is usually represented by protonatable ion pairs (e.g., phosphate species). Parameters such as buffer concentration, pH, and electrolyte composition (identity of cations, anions) have already been discussed.[54;99;111;118;123;135;138;142;143;199-203] Another noticeable phenomenon of OER under neutral pH conditions is the formation of a pH gradient due to a limited (de)protonation process of buffer species, which leads to the need for higher

water oxidation overpotentials or catalyst corrosion.[54;111] Quantification of local pH was reviewed.[204-207] Due to the lack of high concentration of hydroxide, the deprotonation process is crucial for accelerating OER kinetics at neutral pH,[200;208-210] which is dependent on factors such as buffer capacity, current density, and the design of electrochemical cell.[135;198;200] The availability and mobility of electrolyte ions (anions and cations) at the electrodes were also emphasized for converting catalysts from laboratory to industry.[211] Therefore, efficient proton transfer or transport and maximizing the mass transfer flux of buffer species are necessary to prevent proton accumulation and increase the reaction rate of OER. In addition, aqueous inert salts are commonly used to enhance the ionic conductivity of electrolytes. Therefore, my thesis discusses the role of various salt concentrations (including buffered electrolytes) and redox-inert salts in determining catalytic neutral water oxidation activity.

Buffers (e.g., KPi) can function as proton acceptors, facilitating proton transfer.[66;99;113;121;124;134;208;212] Insights into the subject of proton transfer or transport have been unveiled, involving three different hypotheses, all using CoCat as an example.[99;124;135] (i) Assuming that proton transfer and transport limitation (proton-coupled electron hopping) occurs within CoCat films, Tafel slopes coexist over a wide range of potentials as a function of KPi concentrations and other physical parameters, and the reaction kinetics and mechanism are revealed (Figure 1-4A);[124] (ii) Among nine different buffered electrolytes, the catalytic activity at high potentials (1.35 V vs. NHE) under stirring conditions was not related to the classical pH dependence but was determined by the pKa of the buffered base. The proposed reason is the proton transfer limitations occuring at the catalyst-bulk electrolyte interface (Figure 1-4B);[99] (iii) We propose that it is the macroscopic diffusion of buffer base in the electrolyte that mediates proton transport. Thus, (macroscopic) acidification near the electrode surface was predicated and the increased Tafel slope under moderate current density conditions was explained by a simple mathematical model. Therefore, the rate limitation of neutral OER is investigated in Chapter 2, and in particular, three possible proton transport limitations are distinguished.

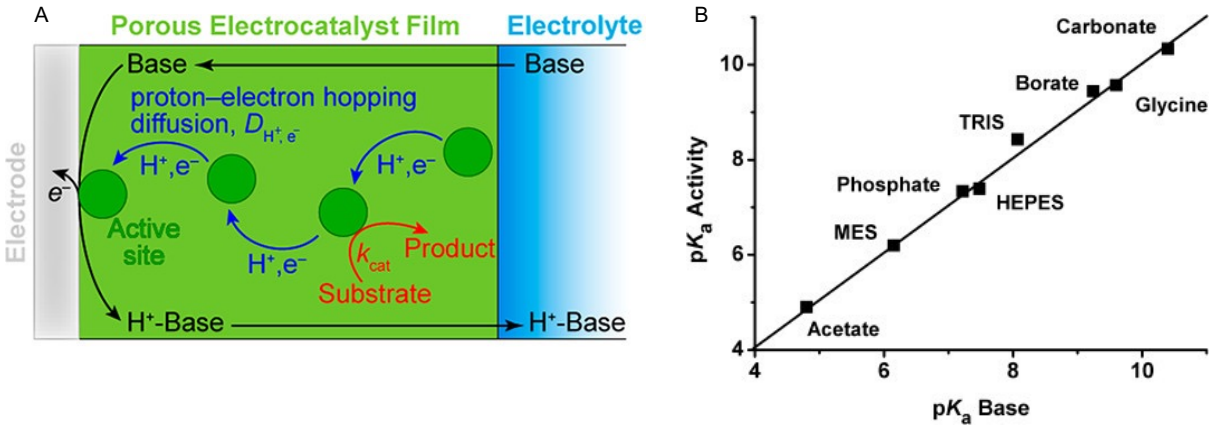

Figure 1-4. Possible controlling factors for neutral OER catalytic activities on CoCat. (A) The proton-coupled electron hopping within internal CoCat film is the rate-controlling factor.[124] (B) The availability of buffer base at the catalyst-electrolyte interface controls the OER rate.[99] Reproduced with permission from refs. [99;124]. Copyright American Chemical Society (2013) and Wiley-VCH GmbH (2014).

1.4.2 Accumulation of high-valence oxidation states

Transitional metal oxides based on the elements Co, Mn, Fe, and Ni have been reported to accumulate oxidized equivalents in a charge-neutral form, which is mediated by charge compensation from proton release or other ionic fluxes.[126;134;139;213-221] Accumulation of oxidizing equivalences prior to the OER rate-determining steps seems to affect the catalytic activity.[222-224] It is not unprecedented for charge-neutral accumulation to produce higher oxidation states, as is often seen in batteries[225-228] and photosystem II[40;229-231]. A recent review concludes that the effect of the oxidation state on catalyst performance is achieved by modulating the spin state, work function, active site, and energy band structure.[218] In biological photosynthesis (PSII), the water oxidation complex (Mn_4CaO_5) promotes the optimal redox-potential leveling through the thermodynamic coupling of metal oxidation, the corresponding deprotonation events and changes in oxo bridging between metal ions, which leads to the accumulation of multiple Mn oxidizing equivalents in a low free energy pathway and induces the generation of reactive intermediates for the formation of O–O bonds.[40;229;232] The stable accumulation of oxidizing equivalents, known as "molecular picture", prior to the multi-electron O–O bond formation facilitates OER kinetics, as is the case for the Mn_4CaO_5 complex in PSII or molecular transitional-metal complexes.[40] Therefore, is it possible that molecular-scale mechanisms in natural photosynthesis can be applied to artificial systems such as (photo)electrochemical catalysis and serve as a knowledge-guided approach for the development of efficient catalysts?

Functional studies of oxide species began in the 1950s, initiated by Conway,[233] in which oxygen was continuously produced after the potential was turned off, implying that oxide species were reduced to produce oxygen, as was the case of CoCat[126] and Ni(Fe)OOH[216]. Similar redox dynamics between biocatalysts and inorganic Mn oxides are discussed, suggesting that Mn oxidation coupled with structural changes involving bridging oxygen between two Mn ions is used to accumulate oxidizing equivalents prior to the onset of water oxidation,[213] which is the same case as the amorphous CoCat catalyst[113;118;126] as well as catalysts undergoing post-modification at the surface layer.[105;234-236] It has also been pointed out that the common determinants of the catalytic activity of redox reactions include not only the accumulation of oxidizing equivalents, but also the rate of redox transformations and the specific active-site structures.[213] Furthermore, spectroelectrochemical studies performed on a series of NiFeOx catalysts showed that catalytic activity is controlled by the equilibrium between accumulated species and reactive intermediates and that the increase in oxidative species correlates with an acceleration of the OER kinetics, leading to a reaction order of approximately four (Figure 1-5A).[216] Based on iridium oxide catalysts, Nong et al. found that the accumulation of oxidation states rather than electron transfer plays a key role in determining the rate of OER catalysis. Accordingly, an increase in electrode potential raises the amount of oxidized charge stored on the surface, while the accumulation of oxidized equivalents further reduces the free energy of activation for the rate-determining step, which involves the formation of an O-O bond through the chemical reaction of water with adsorbed oxygen (Figure 1-5B).[217] Similar to the study of Nong et al., a series of metal oxide photoanodes (WO_3,

TiO_2, $BiVO_4$, α-Fe_2O_3) showed a rate law between current and the concentration of holes on the surface(Figure 1-5D).[232;237-240] Spectroelectrochemical analyses of nickel oxides doped with different elements showed that the change in the density of the oxide species clearly reflects the change in the redox potential of the nickel center, which in turn affects the OER kinetics (Figure 1-5C).[221] Cooperation or interactions between active species on heterogeneous catalysts (e.g., IrOx, CoCat [126]) directly contribute to the rate of OER, which does not exist for isolated metal centers in molecular catalysts.[224;241] Therefore, the role of accumulated oxide species in the kinetics of water oxidation, whether metal oxides or semiconductors or electrocatalysis or photocatalysis, is crucial and independent of the type of catalyst and catalytic reaction.

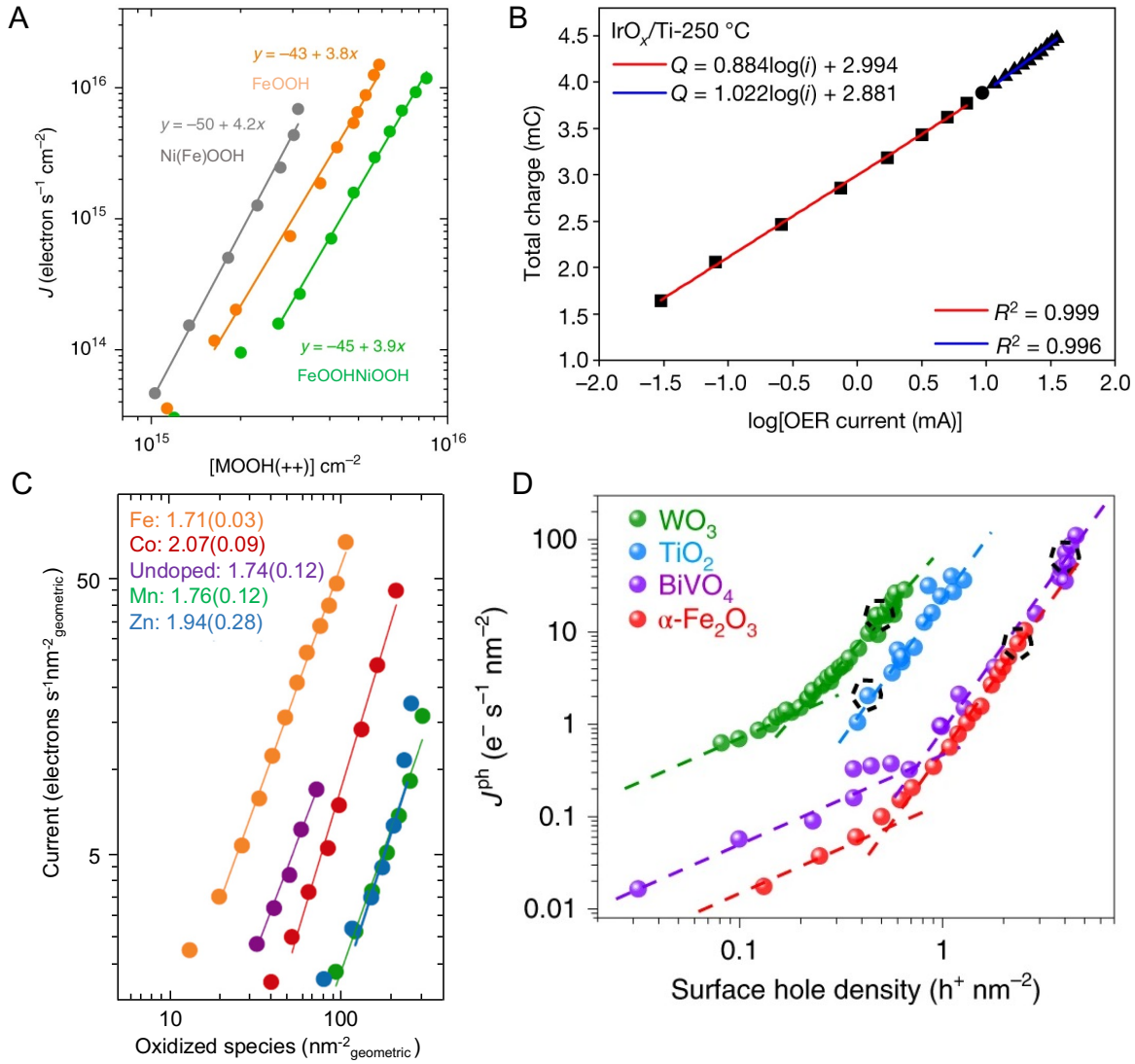

Figure 1-5. Rate law plots of OER current density (or OER kinetics) versus the concentration of oxidative species or hole densities or photogenerated charge carriers. (A) The log-log plot of the current density versus the concentration of oxidation states. MOOH(++) represents the concentration of high oxidation states. (B) A linear relationship between stored charge and the logarithmic current density. The stored charge is obtained by integrating the current trace of the cathodic pulses. (C) A unified slope of 2 for the log-log plot for nickel oxides doping with different elements. (D) The log-log plot of water oxidation current density versus surface hole density shows the biphasic behavior of the transition from

first-order to approximately third-order reactions. Reproduced with permission from refs.[216;217;221;232]. Copyright Spring Nature (2019, 2020), Nature Protfolio (2020), American Chemical Society (2022).

In order to track redox processes and the density of oxidative species, a variety of advanced techniques are available, including electrochemical measurements,[217] XAS,[126;213] Raman spectroscopy,[139;242] spectroelectrochemistry,[203;216;220] XPS,[243;244] and others (Figure 1-6). Among these techniques, in situ XAS and atmospheric pressure XPS can obtain direct oxidation states due to their high bulk or surface sensitivity. In situ Raman spectroscopy can identify individual redox transitions by combining XAS results.[139] As a simple method, pulsed electrochemical voltammetry with potential jumps can gain information on oxidatively stored charges by integrating the cathodic current trace.[217] In addition, time-resolved spectroelectrochemistry can provide an experimental method for detecting the kinetics of redox transitions or OER catalytic reactions, for which UV-vis spectroscopy is employed to extract the concentrations of oxide species by tracking changes in optical absorption at fixed wavelengths.[126;216;220;221;232]

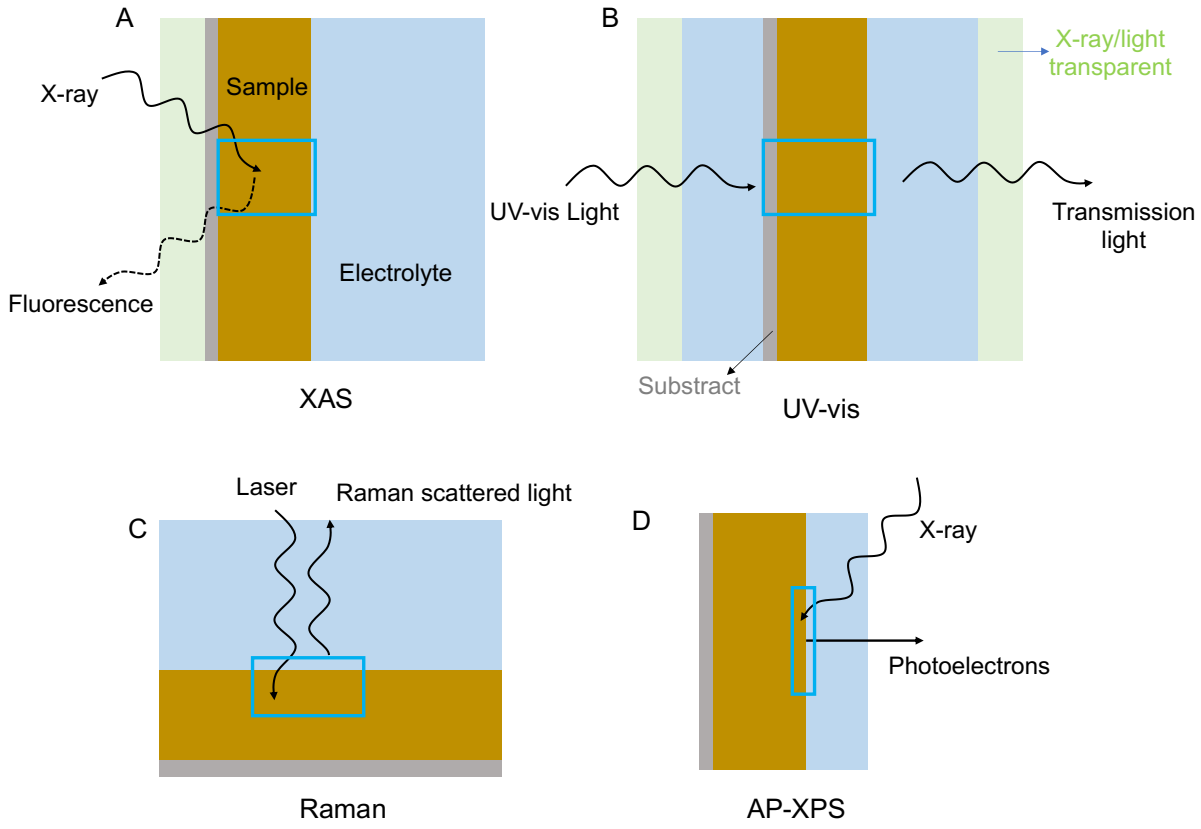

Figure 1-6. Representative operando techniques for extracting oxidation state information. (A) X-ray absorption spectroscopy (XAS) in fluorescence mode. (B) UV-vis spectrum in transmission mode used in photoelectrochemistry. (C) Operando Raman spectroscopy is combined with XAS to extract information on individual redox transitions. (D) Ambient pressure X-ray photoelectron spectroscopy (AP-XPS) directly monitoring surface oxidation states. Note that the detection direction of this technique is not exclusive. The areas within the blue boxes illustrate the range of detection for each technique. Readapted from ref.[245]. Copyright Wiley-VCH GmbH (2023).

In brief, the heterogeneous metal oxides described above revealed that the stored charge (concentration of oxidized species) can determine the kinetics of water oxidation in the aspect of the molecular domain, and that the potential bias exclusively controls the formation of oxidizing equivalents, which contrasts with the classical picture of electrochemical water oxidation. Conventionally, it assumes that catalytic reaction occurs at a single metal site on the surface of the electrode, or at adjacent metal sites, and involves a four-step process of concerted proton and electron transfer.[40;118;172;246-249] According to DFT studies, the formation of *OH, *O, and *OOH intermediates prior to the release of oxygen from the active site is often considered to be the thermodynamic barrier associated with the "potential-limitation" step, which takes the free energy of all the elementary reaction steps downhill.[40;246;247] In contrast to the classical mechanisms for heterogeneous catalysts,[246;247] the mechanistic concepts often discussed in protein-bound Mn_4CaO_5 complexes or molecular homogeneous catalysts,[40;213;229] are better suited to describing the behavior of these amorphous metal oxide catalysts.[126;213] The advent of quantitative and time-resolved spectroscopy (e.g., in situ XAS) as well as DFT calculations have allowed us to get insights into whether electrochemical reactions are determined by chemical interactions or electrochemical potentials.[221-223] For water oxidation, the corresponding chemical effects of heterogeneous (photo)electrocatalysts, i.e., the accumulated charge density or hole populations, are mostly found in alkaline or acidic electrolytes. [216;217;220;221;232] Accordingly, in Chapter 3, we will investigate the relationship between oxidation states and catalytic rate for neutral water oxidation reaction by various in situ methods based on the CoCat model catalyst, thus further verifying the universality of chemical effects in electrochemistry.

1.4.3 Role of redox-inert cations and anions

Aimed at adjusting the OER catalytic performance, we often focus on transitional metal elements of catalysts (e.g., Fe, Mn, Ni, Co) because of their enriched redox chemistry.[99;126;250-252] The role of redox-inert ions in catalysts or electrolytes has been studied under alkaline (more) or neutral pH (less) condition.[123;201;202;253-267] The role of redox-inactive ions in maintaining charge neutrality during redox transition of metal atoms or water oxidation is not fully understood.

Here, we review the reported effects of redox-inert cations or anions on OER, although some have not yet been experimentally verified.[99;126;250-252] Specific studies on the redox-inactive cations or anions of CoCat are described in Section 1.3 and will not be repeated here.[111;123;143;169;268] The charge compensation effect of potassium ions is demonstrated in iridium oxide [265] and $NiFeO_x$ oxide,[269] both of which exhibit a layered structure and operate under alkaline conditions. The corresponding content is described in Chapter 4 and will not be discussed here. Here the other properties or functions of redox-inert ions are emphasized. Notably, the redox-inactive metal ion Ca^{2+} in the PSII CaMn complex is of crucial importance, and its exact role has been suggested as a potential binding site for water activation, contributing to S-state cycling or influencing the redox properties of the OER cluster.[261;262;270;271] Interestingly, in the synthesis of model complexes including redox-active metal ions in different oxidation states, the redox properties of the OER catalysts are closely

correlated with the Lewis acidity of the redox-inactive metal.[262] Potassium ions have a strong influence on the local microenvironment near the active site, the structure of the water and the local electric field, which can control the PCET process and the oxidation reaction of the water.[259;272;273] In addition, adding hydrated metal cations (e.g., Ca^{2+}, K^{+}) to the framework of synthesized catalysts (e.g., MnO_x) promotes water adsorption at the catalyst-electrolyte interface or in the vicinity of the active site, which facilitates the involvement of lattice oxygen and thus enhances OER activity.[274-276] Similarly, a phase conversion between $Ni(OH)_2$ and NiOOH occurs with the intercalation of the electrolyte cations, implying that the cations play a role in tuning the structure of the NiOOH active phase and thus modulating the catalytic performance.[277-280] Among the different types of redox inert ions (K^{+},Ca^{2+},Sr^{2+}, Mg^{2+}), Ca^{2+} cation has the best catalytic activity for MnO_x[261] and it can influence the valence of manganese to further improve the stability of manganese oxide catalysts.[254;267] The increase in OER activity with increasing cation size was carefully studied in Ni(Fe)OOH catalysts.[253;256;281] However, recent works reveal that the effect of alkali metal cations on the OER activity of Ni(Fe)OOH catalyst can be attributed to pH differences of the electrolyte that induce the shift of the redox peak of Ni and further affect the OER activity.[266] Highly valent cations have an inverse effect on activity, which may be due to the electric field shielding effect that reduces the concentration of reactants.[256;260;281] In addition, most of the findings have focused on the interactions between electrolyte cations and OER intermediates that modify the energy barrier of reaction, which are commonly found on NiOOH catalysts operated in alkaline solutions without or with iron impurities as well as perovskite oxides.[253;281-284]

In addition to the redox-inert cations, the OER catalytic activity depends significantly on the type of anions, e.g., nickel-iron layered double hydroxide ([NiFe]-LDH).[253;281-283] This suggests that anions with strong Lewis basicity and higher valence exhibit better activity due to their stronger proton-accepting and electron-donating ability.[263] Earlier studies have shown that among the various interlayer anions in carbonate-free solutions, PO_4^{3-} has a larger pKa value and therefore exhibits the greatest activity.[263] A linear relationship was established between the reducing ability of intercalated anions of [NiFe]-LDH and OER activity as well as the electron density of metal host.[264] Noteworthily, the binding motif of the proton acceptor (e.g., phosphate groups) is crucial for the catalytic performance.[285] A CoO-core catalyst was reported to be more active than CoCat when cobalt catalysts were prepared in acetate buffer due to the presence of acetate, chloride and sodium ions in the catalysts, and the role of anionic ligands in stabilizing the highly oxidized intermediates likely explains this.[286]

In Section 1.4.2, the importance of accumulating oxidative species in various metal oxides or hydroxides is emphasized, and the involvement of proton transfer is confirmed.[126;134] However, there is no direct experimental evidence for the flux of redox-inert cation release or anion uptake to compensate for a charge, which leads us Chapter 4.

1.4.4 Bulk electrolyte transport flow and bubble effect

Neutral water oxidation provides a safe and ecological method for producing renewable fuels. An important factor in neutral pH water oxidation on a laboratory or industrial scale is the mass transfer of protons and hydroxides.[54;124;135;142;207] This transport limitation is more severe in

larger-scale installations with higher current densities (> 50 mA cm^{-2}).[287;288] In pursuit of efficient application of water oxidation in the engineering field, we should not only focus on the intrinsic properties of catalysts, electrocatalytic activity and catalyst stability, but it is crucial to understand the macroscopic transport of buffer species and the engineering issues of large-scale OER. We discuss here potential macro- or micro-factors, including natural convection, bubble effects, and engineering aspects of electrolyzer system configurations, and then summarize the corresponding strategies that have been reported for high-current water splitting systems.

The model of proton transport limitations is detailed in Section 1.4.1. In ref. [135], proton transport is assisted by diffusion of protonated and unprotonated buffer bases into the bulk electrolytes while assuming that the proton activity of the inner catalyst film is equivalent to that of the near-surface electrolyte. The current density depends on the concentration of buffer molecules, the effective diffusion constant (K_D), and the proportion of unprotonated buffer molecules. Thus, a first-order model of proton transport during neutral water oxidation is proposed and a linear spatial concentration profile of (de)protonated buffer species between anode and cathode is derived (Figure 1-7A).[135] The spatial-resolved distribution of buffer species concentration or pH changes in a two-electrode water splitting cell was monitored by fluorescence pH sensor foils.[207] Direct experimental results and model simulations suggest that buffer solutions can mitigate local pH by natural electrolyte convection, which is attributed to the buoyancy effect resulting from changes in electrolyte density due to ion depletion and accumulation.[207] Acidic and alkaline regions were observed at the top and bottom of the cell, respectively.[207] Depending on current density, electrolyte, and cell configuration, the acidic and alkaline regions extend into the bulk electrolyte and even the original pH value in the middle of the cell changes with electrolysis time.[207] In the absence of a buffer solution, a clockwise convection is formed, with the acidic region rising and the basic region falling (Figure 1-7B).[207] This study emphasizes the role of convection induced by buoyancy effects in bulk electrolyte mass transport, which suppresses local pH, and also illustrates the complicated nature of bulk electrolytes.

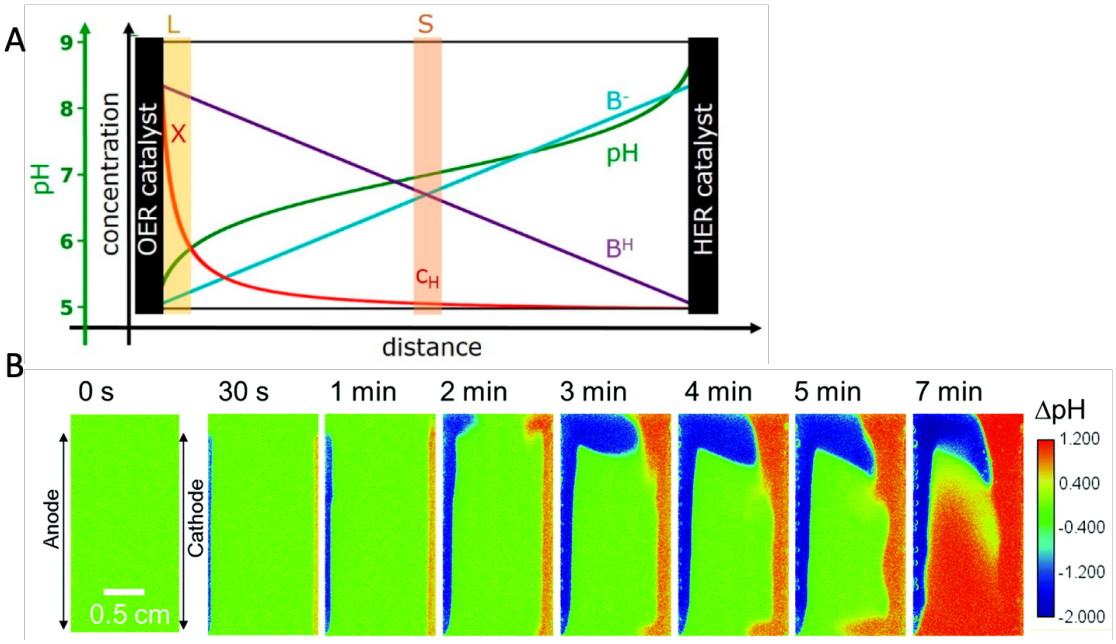

Figure 1-7. (A) Schematic representation of pH and concentration distribution of buffer species in a simple parallel two-electrode electrochemical cell at constant diffusive flux. X, proton activity; B^-, deprotonated buffer base; B^H, protonated buffer base. Reproduced with permission from ref.[135]. Copyright MDPI (2019). (B) Experimentally measured temporal evolution of pH distribution in a water electrolyzer with 0.5 M K_2SO_4 solution at a current density of 1 mA cm^{-2}. Reproduced with permission from ref.[207]. Copyright Royal Society of Chemistry (2020).

In addition to the neglected convection caused by electrolytes (buoyancy effect), other factors including bubble-induced convection can have a great impact on the electrolyte flow scheme and affect the cell efficiency, which is mainly verified by mathematical modeling and simulation.[289-291] Various potential losses with and without electrolyte flow (passive and active systems) under different electrolyte conditions and electrochemical cell device sizes were evaluated, and solution transport losses (e.g., diffusion, migration, and convection), Ohmic resistance losses, and Nernst potential losses due to pH gradients, as well as electrodialysis or concentration overpotentials, were derived in different electrolytes at different operating currents.[289;290] Thus, the limiting factors that play a dominant role vary under different conditions of controllable variables. Notably, bubble-induced convection exhibits a dual role in the presence or absence of membrane cells, with gas cross-losses dominating in membrane-free devices, while electrodialysis of buffer species reduces the current density and thus the cell efficiency.[290] In short, bubble formation appears to affect the various components of the overpotential, i.e., an increase in the activation overpotential by decreasing the active area or active sites, an increase in the Ohmic overpotential by blocking the ion transfer pathway, and a decrease in the concentration overpotential by decreasing the degree of supersaturation of the electrolyte and absorption of the dissolved gas products.[292] These overpotential losses are particularly prominent in neutral electrolyte devices.[288;293] Therefore, an optimization strategy must be identified to minimize overpotential losses.[38] It was found that the bubble effect affects the catalytic efficiency, leading to energy loss and catalyst decomposition.[77;289;292;294-296] In terms of passive approaches, several strategies have

been elucidated to mitigate the bubble effect, including modifying the electrode structure at the macro- and micro-levels,[211;297-300] surface wettability,[301;302] electrolyte properties (e.g., adding extra additives).[42] For active methods, external energy were used, i.e., forced electrolyte convection,[42] ultrasonic fields,[303-305] magnetic forces,[306;307] photothermal effects.[308] The former method of removing bubbles is more suitable for small current ranges. The field-assisted method is usually applicable to high current conditions. Both methods have benefits and drawbacks and need to be optimized.[309] The cell configuration also affects bubble management.[38;211;310] Attractively, for alkaline water splitting, a capillary-fed cell with bubble-free operation at electrodes was developed with a water-splitting performance superior to that of a commercial electrolyser.[310] Since larger cells lead to longer transport pathways and large amounts of bubble evolution, mass transport limitation of reactants or electrolytes, heat effects, and losses associated with bubbles should be minimized.[38;211]

In conclusion, for practical water-splitting electrolysers, aspects such as mass transfer of electrolyte, natural convection caused by bubbles and/or changes in electrolyte density, and reasonable cell configurations must be fully considered and optimized to achieve high cell efficiencies.

1.5 Hard X-ray absorption spectroscopy

In order to rationally improve the efficiency of catalytic water oxidation reactions, it is important to elucidate the reactive sites and nature of the catalysts.[311;312] The numerous topics of catalytic research can be generally categorized into the following aspects: the effect of elemental doping on metal redox equilibrium, material structure transformation, metal redox transition, and O_2 evolution kinetics， detecting the reaction intermediates in the catalytic process, dynamic reconstruction, and the response of the catalytic performance to the external environment (e.g., pH value, electrolyte concentration), and so forth.[126;134;142;214;219;313-316] The electrochemical response is investigated by operando, cryogenic, and time-resolved X-ray absorption spectroscopy (XAS). XAS is element-specific, does not require long-range order materials,[317;318], and has relatively low interference with water[319]. Requirements for samples are relatively low, as there are no size/magnetic/labeled isotope requirements. In principle, XAS is applicable to all metal centers or inorganic co-factors and substrates. The available elemental XAS spectra depend on the beamline configuration. Currently, the bending-magnet beamline KMC-3 at the BESSY II synchrotron (Helmholtz Center Berlin) can access to the energy range of about 2–15 keV, and a phosphorus K-edge XAS spectrum recently was obtained.[143]

The absorption of X-rays by specific elements is similar to the process of obtaining UV-vis spectra and is described by the Beer-Lambert law. The absorption coefficient (μ) can be obtained either in transmission mode, where the intensity of the incident photon before (I_0) and after (I_t) its interaction with absorbing atoms in the sample is recorded (Equation 1-4), or in fluorescence mode, where the fluorescence detector is usually a 13 element silicon drift detector (SDD), oriented at 90° to the incident X-ray beam, and the absorption coefficient ($\mu \sim I_f/I_0$) is proportional to the fluorescence intensity (I_f).[318;320;321] It should be noted that the latter method is no longer applicable for thicker catalysts or samples containing a large number

of absorbing atoms due to self-absorption. X-ray absorption occurs when the energy of incident X-ray (I_0) equals or exceeds the binding energy of an electron in one of the core levels of an atom. In the process, the occupied higher energy level electrons fall into the core holes of the inner shell and release the excess energy, resulting in X-ray fluorescence or secondary excitation and the emission of Auger electrons.[322]

$$I_t = I_0 e^{-\mu t} \qquad \text{Equation 1-4}$$

Here t is the sample thickness. Note that for a homogeneous sample of the same element, there is an empirical formula (Equation 1-5) for calculating the absorption coefficient, which is related to the sample density (ρ), the atomic number (Z), the relative atomic mass (A), and the incident X-ray energy (E).[320]

$$\mu(E) \sim \frac{\rho Z^4}{AE^3} \qquad \text{Equation 1-5}$$

1.5.1 XANES and EXAFS

As an example, the Co K-edge XAS spectrum (Figure 1-8C) is divided into three regions:

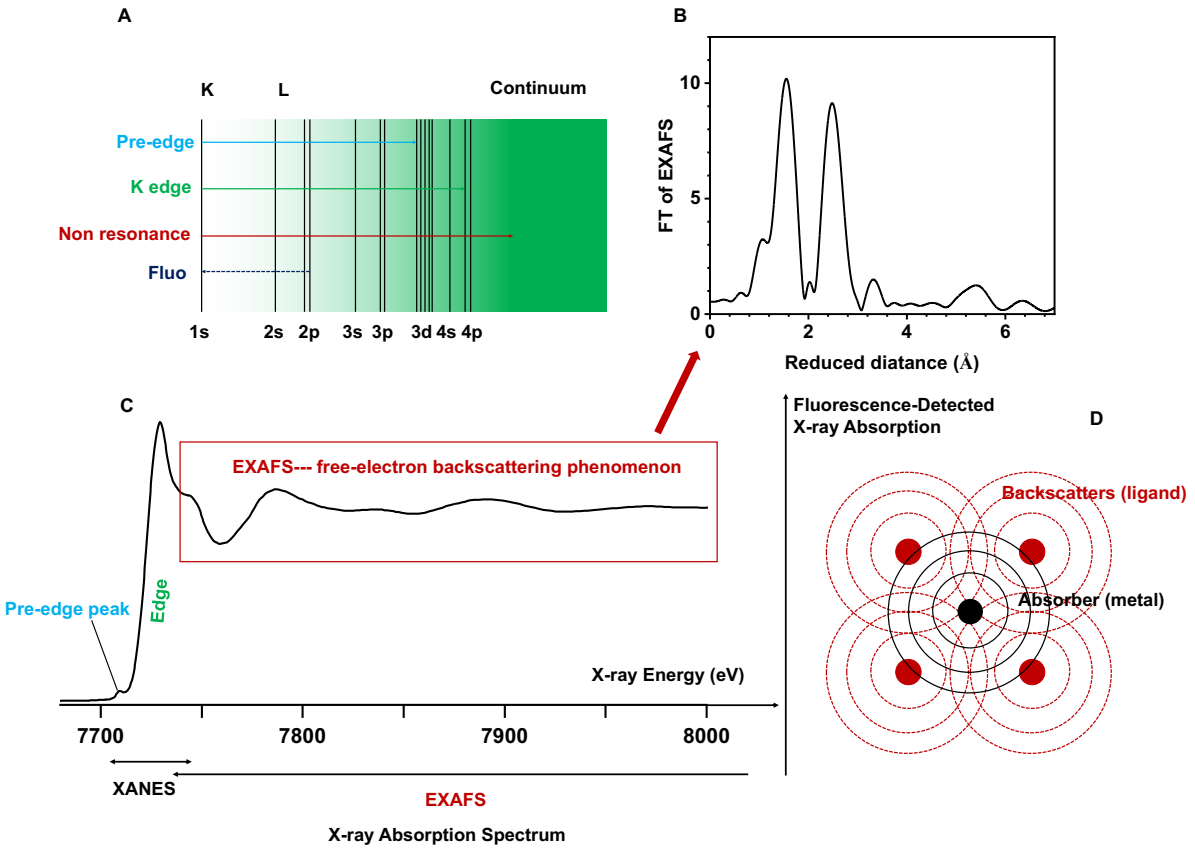

Figure 1-8. Schematic representation of an X-ray absorption spectrum, exemplified by XAS at the Co K-edge, including the XANES (pre-edge and the main absorption edge) and EXAFS regions (C). (A) the process of X-ray absorption and core-electron excitation. Note that panels A and C use the same color code. (B)The Fourier transforms of the EXAFS spectra extracted from panel C. (D) The formation of EXAFS by the interference of photoelectron waves scattered from neighboring atoms.[323] The

outgoing and scattered photoelectron waves are shown in black and red, respectively. Reproduced with permission from ref.[323]. Copyright Springer Nature (2019).

(a) pre-edge, (b) the Co absorption edge, and (c) EXAFS region. The first two regions constitute the XANES, which provides information about the symmetry of the metal-ligand environment (pre-edge), the electronic structure, the oxidation state, and the first-sphere ligands of the absorbing atoms (Metal K-edge).[324] EXAFS extends to the energy region above the absorption edge of about thousand eV, allowing the extraction of important (but limited) information on the coordination numbers (N, ±10%), reduced distances (R, ±0.01 Å) between absorbing and scattering atoms that ideally in the first three coordination shells, and (dis)order via the Debye-Waller factor (σ^2).[318;322;325]

(a) The appearance of a pre-edge peak at the Co K-edge is due to a transition from 1s state to partially occupied 3d states, which is usually interpreted as an increase in the mixing of the p-d orbitals due to the shorter distances of the metal-oxygen upon Co being oxidized.[123;326] Essentially, the dipole selection rule ($\Delta l = \pm 1$) of octahedral symmetry mainly prohibits such a transition. (Figure 1-8A) (b) The Co absorption edge involves dipole transitions from 1s to unoccupied 4p continuum states (Figure 1-8A). The white line is at the top of the edge and has a sharp maximum.[318] The shift of the edge position to higher energies is frequently attributed to an increase in the oxidation state of the absorbing metal atom, but the nature and local structure of the metal-ligand may also be relevant.[318;327] There are two plausible explanations for the relationship between edge position shifts and oxidation state changes[328], which are related to the shielding effect of the core electrons and the semi-empirical Natoli's rule.[318;329;330] The determination of oxidation state is based on calibration curves for several well-known reference materials, the accuracy of which depends on the definition of the edge position. Representative methods for determining the edge position include the energy at the normalized intensity of 0.5, the inflection point, and the area under the edge rise, etc.[316;318;320] In short, the shape and intensity of XANES is determined by the combination of the density of unoccupied localized and delocalized states and selection rules.[322] (c) EXAFS is the phenomenon of backscattering of free electrons by neighbouring atoms as the photoelectron transitions to the continuum state, which leads to oscillations due to constructive and deconstructive interferences (Figure 1-8D).[318;320;322] To extract the structural parameters, the EXAFS oscillations are isolated from the edge spectrum and further converted from energy space (E) to photoelectron wavenumber space (k) and then Fourier transformed to (reduced) real space (R).[322] The extracted oscillations can be described by the sum of the contributions of the n_{shell} shells, according to Equation 1-6:[325;331]

$$\chi(k) = S_0^2 \sum_i^{n_{shell}} \cdot A(R_i, k)_i \cdot N_i \cdot e^{-2\sigma_i^2 \cdot k^2} \sin(2k \cdot R_i + \emptyset_i) \qquad \text{Equation 1-6}$$

Here, each coordination shell is consisted of N_i atoms of a specific atom that is at a distance R_i from the absorbing atom. The Debye-Waller factor (σ^2) describes the variations of each shell over the defined R_i, with the sum of oscillations dampened by an amplitude reduction factor (S_0^2). For each shell, the scattering amplitude ($A(R_i, k)_i$) and phase correction (ϕ_i) were obtained by ab-initio calculations based on the atomic coordination generated from the known model

structure by the FEFF program. The extracted EXAFS oscillations are weighted by k^3 and simulated by a least-squares fit in k-space.[112;252] The fitting error is evaluated by Fourier-filtered R_f, which is defined as the relative deviations of the experimental from the simulated spectrum respective to the overall magnitude of the experimental spectrum.[112;252] For the R_f, a reasonable fit is usually less than 25 %.[112] It is worth noting that the indicated reduced distance R is about 0.03 Å smaller than the actual distances between the absorbing and backscattering atoms (Figure 1-8B).[316] The interatomic distance has been reported to be accurate to 0.01 Å for shorter distances such as metal-oxygen.[328] The fitting error of the coordination number (N) is about 5-10 % due to the correlation with the Debye-Waller factor (σ^2).[332] The value of Debye-Waller factor σ^2 is affected by two factors, including thermal and static disorder.[322] The increase in σ^2 suggests more disorder in the identified shells. In conclusion, XANES and EXAFS provide important electronic and geometric structural information and are widely used in OER.

1.5.2 XAS Application in OER

Representative applications for OER include freeze-quench XAS experiments (also known as quasi-in-situ XAS experiments and operando (= in situ) XAS experiments. In the former method, data are collected at low temperatures (e.g., 20 K), the target sample is rapidly frozen in liquid nitrogen to maintain its original state when a potential is applied, and the sample is then disconnected from the electrode. The results show that the freeze-quench method gives similar results to the operando measurements, but its EXAFS quality is higher because the Debye-Waller parameters (σ) are less affected at low temperatures.[126] In addition, in situ XAS combined with electrochemistry can be run at room temperature, providing time-resolved insights into the formation of reaction intermediates, electronic and structural changes, and information about the mechanism of the OER reaction.[318;333] Extended applications of the operando XAS include changing electrochemical protocols or upgrading the XAS setup configuration.

Conventional operando XAS can be combined with electrochemistry via the chronoamperometry (CA) technique. With the stepwise change of electrode potentials, a series of full absorption spectra at various potentials can be collected at (quasi) equilibrium, providing information on oxidation states, coordination environments, phases, and bond lengths. Acquisition time is typically a few minutes per spectrum.[333] The often-used CV technique combined with conventional operando XAS is limited in its temporal resolution because the complete XAS spectrum usually takes at least few minutes, depending obviously on the beamline configuration, sample concentration, or the requirements for spectral quality. Currently, fast XAS scans can measure full spectra on time scales of tens to hundreds of milliseconds, e.g., quick EXAFS,[334-336] energy-dispersive XAS[337;338], but only at dedicated beamlines.

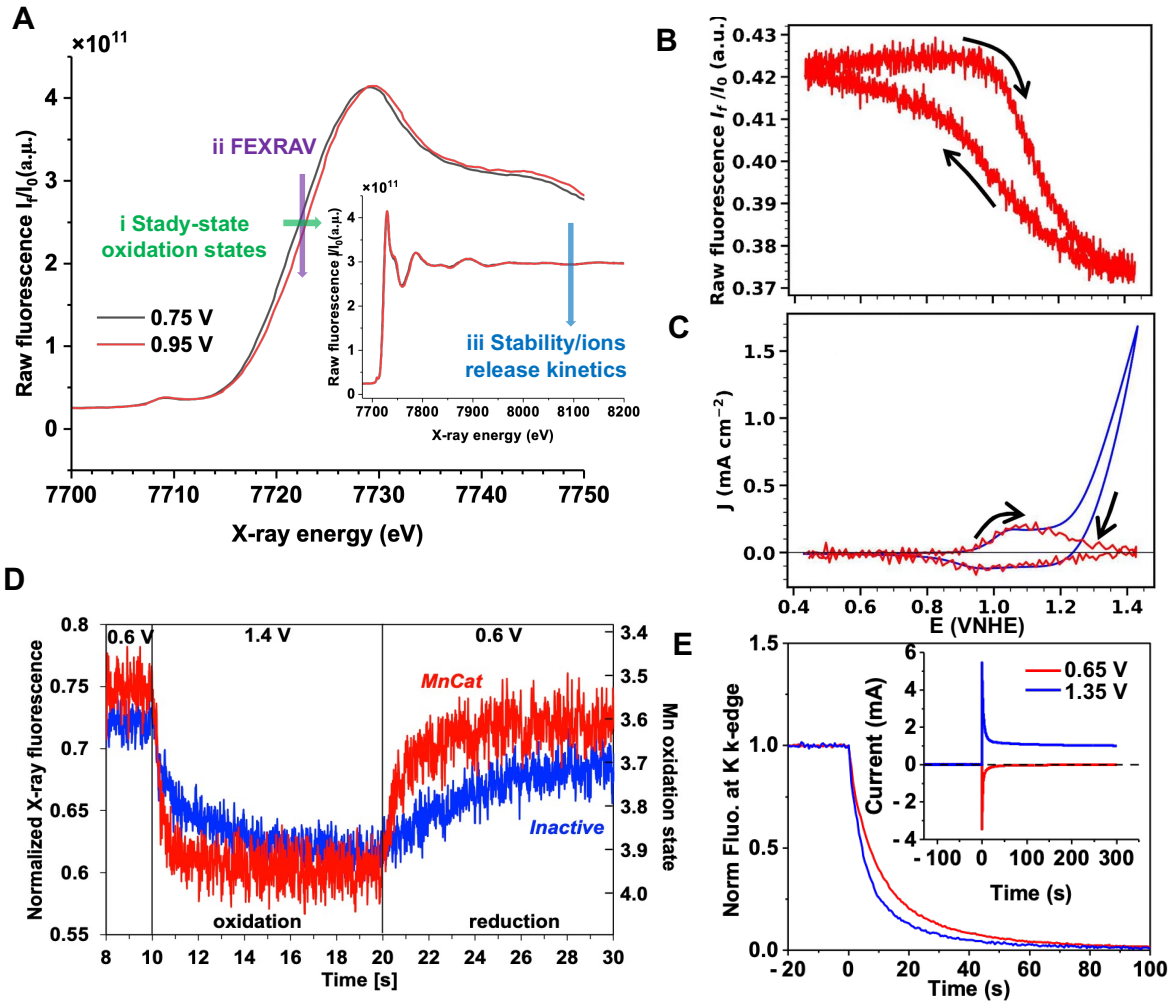

Figure 1-9. Application of XAS in OER research. (A) Insights from the XANES and full XAS spectrum (inset). Method i shows the increase in oxidation states associated with an increase in the edge position of the XAS spectrum (green arrow from left to right) and can be used to get absolute oxidation states in the combination with oxidation states calibration curve from well-known compounds; method ii reflects the intensity change of X-ray fluorescence at fixed X-ray excitation energy (violet arrow up to down) and can apply for kinetics analysis, i.e., distinguishing redox and catalytic currents (panel B, C) or obtaining time constants of redox transition at metal sites (panel D); method iii allows for determining the stability of the catalyst and the kinetics of ions release (panel E) by recording changes in absorption coefficients at energy far above the edge absorption energy (blue arrow up to down). (B) Raw fluorescence recorded at a fixed incident energy during CV. (C) The first derivative of time traces of the fluorescence signal in (B) overlapped with CV. Reproduced from ref.[315]. (D) Time-resolved XAS spectrum at the Mn K-edge used to extract time constant of redox process by recording the fluorescence changes at a fixed incident energy during potential pulses, reproduced from ref.[213]. (E) Fluorescence changes recorded at the potassium K-edge (4 keV) at various potentials, reproduced from ref.[143].

Fixed energy X-ray absorption voltammetry (FEXRAV)[339] has recently attracted a great deal of attention because it can be used in conventional bending-magnetic beamline and double-crystal monochromators (e.g., the KMC-3) to record the X-ray absorption coefficients or X-ray fluorescence at fixed X-ray incident energy in conjunction with electrochemical protocols (e.g., CVs or potential jumps).[140;213;214;252;315;340] At constant X-ray energy, by

comparing the first-order derivatives of X-ray fluorescence and CVs (Figure 1-9 B and C), we can discern current from redox state changes in metals and catalytic process or other processes, a methodology used in Chapter 2 of this dissertation.[315] In addition, the continuous recording of fluorescence transients with (sub)millisecond time resolution by using potential pulses enables the accessibility of redox transition kinetics (Figure 1-9D).[140;143;315;333] Furthermore, by fixing the incident X-ray energy beyond the absorption edge energy (e.g., ~500 eV), we can monitor catalysts' stability and the exchange kinetics of ions (Figure 1-9E).[143;315] To sum up, the FEXRAV experimental method exhibits a wide range of applications in OER, such as: distinguishing redox currents from catalytic currents or other charge processes, determining rate constants for redox transitions, determining the stability of catalysts, identifying redox transition processes of specific element in multi-element catalysts, and tracking the reversibility of redox processes.[315;333]

1.6 UV-vis spectroscopy

In addition to the bulk-sensitive and element-specific XAS technique commonly used to track oxidation states,[117;126;134;214;315;316;318;322] UV-vis spectroscopy can also monitor redox transitions by recording changes in optical properties.[126;134;203;221;341-343] In contrast to XAS, UV-spectroscopy is widely used in most laboratories and barely causes damage to the sample.[344;345] Therefore, UV-visible spectroscopy is an optimal choice for making preliminary measurements before using a synchrotron light source for XAS measurement.

UV-vis spectra are typically measured in transmission mode (Figure 1-10A) for solutions or catalysts grown on transparent substrates such as conductive FTO or ITO glass. However, for non-transparent metal substrates or solids, the transmission mode would have to be replaced by the reflectance mode (Figure 1-10B). For the reflectance mode, the thickness of the sample and the type of substrate are not crucial.[343;346]

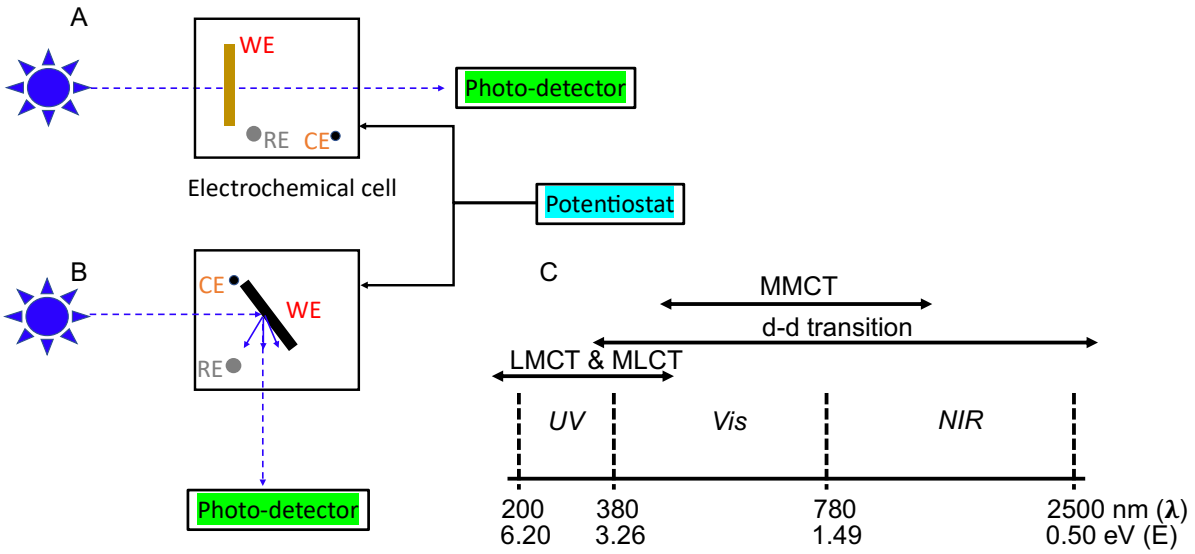

Figure 1-10. Simplified scheme for in situ UV-visible spectroscopy measurements in transmission mode (A) and reflectance mode (B). Note that the electronics that may involve, such as monochromators, slits, light guides, and gratings, are not shown. (C) Different types of major electronic transitions may occur

in the ultraviolet (UV), visible (Vis), and near-infrared (NIR) regions. Adapted with permission.[343;347] Copyright Wiley-VCH GmbH (2008, 2019).

The theory of UV-vis absorption spectroscopy is similar to that of XAS and follows the Beer-Lambert rule in transmission mode. The difference lies in the excitation sources (UV-vis light vs. X-ray, respectively) and the different electronic transitions involved (outer-shell electrons vs. electron excited at K-edge from 1s to 4 p orbitals).[344;348] The UV-visible spectrum has an excitation energy ~ 10^3 times lower than that of XAS, which excites the outer electrons, leading to a d-d transition or charge transfer transition (Figure 1-10C).[344;348] According to the Laporte selection rule, the d-d transition in octahedral complexes has a very weak absorption because it is typically symmetry-forbidden ($\Delta l = 0$).[349] The violation of the classical selection rule may be due to the mixing of the p-d orbitals between the metal and the ligand. Meanwhile, charge transfer usually leads to very strong and broad absorption bands, which are usually due to electron transfer between donor and acceptor (Figure 1-10C), i.e., ligand-to-metal charge transfer transitions (LMCTs) or metal-to-ligand charge transfer transitions (MLCTs) and metal-to-metal charge transfers (MMCT).[126;347] The range of molar absorption coefficients for d-d transition and charge transfer is about 10^{-1}–10^6 $Lmol^{-1}cm^{-1}$.[350;351] The calculated molar extinction coefficients in the thousands of CoCat[126] may indicate a relevance to the charge transfer process.

Since the application of in situ UV-visible absorption spectroscopy to electrocatalysis in the 1960s,[346;352], changes in the oxidation state of metal ions and their kinetics have been tracked based on changes in absorption or reflection signals.[126;134;203;221;341-343] Changes in optical properties are closely related to the electrochromic effect of materials such as Mn-, Ni-, and Co-based materials. Common approaches for in situ UV-visible absorption experiments include obtaining steady-state spectra at individual potentials or collecting time traces of light absorption at specific wavelengths as a function of given potentials for kinetic experiments. In our previous studies of CoCat, absorption spectra at steady state were recorded at various potential steps (Figure 1-11A).[126] The relationship between the absorbance extracted at a fixed wavelength and the applied potential is consistent with that between the oxidation state of the metal and the potential shown in the XAS measurements. This suggests that the oxidation state of the central metal ion can be tracked by UV-visible absorption spectroscopy (Figure 1-11B), which was also applied for manganese catalysts.[126;341] Subsequently, time-resolved in situ UV-vis absorption spectroscopy was applied to CoCat with a resolution of 10 ms (Figure 1-11C).[134] Recording the absorption at fixed excitation wavelengths during the potential-jump experiment yields unaffected time constants of the cobalt redox transition for the H/D isotopic experiment, indicating no kinetic isotope effect (KIE).[134] A similar study of catalyst redox states and reaction dynamics based on nickel-iron oxyhydroxide was also carried out by recording the optical absorption signal or reflected light signal (Figure 1-11D) during cyclic voltammetry.[203;343] Recently, spectroelectrochemistry has investigated the doping effects of nickel oxides by using in situ UV-visible spectroscopy.[221] As a result, the density of oxidized species can be extracted from the changes in the optical signal (Figure 1-5C).[221]

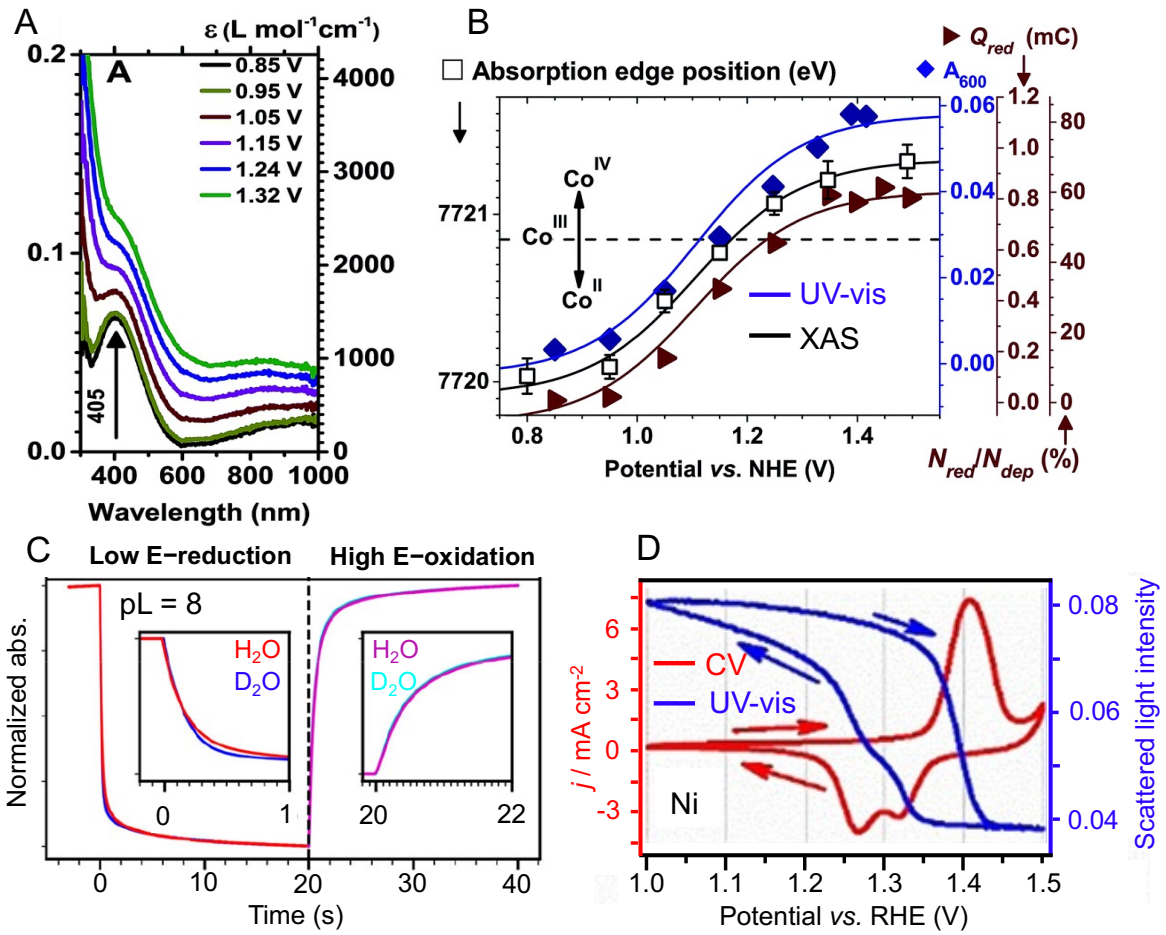

Figure 1-11. In situ UV-vis spectroelectrochemistry: (A) Optical absorption spectra of a CoCat film electrodeposited on transparent electrodes and collected at the indicated potentials (pH 7). (B) Oxidative charging of CoCat at pH 7 followed by freeze-quench XAS (squares), optical absorption spectroscopy (diamonds) and electrochemical coulometry (triangles). The optical absorption at 600 nm (A600; diamonds) derived from panel A provides a qualitative measure of the cobalt oxidation state as its trace is congruent with the other two traces. (C) Time-resolved in situ visible absorption spectroscopy during stepwise changes between reducing and oxidizing potential, for CoCat in 0.1 M KPi H_2O electrolyte or D_2O electrolyte with pL 8. The potential jumps were repeated 30 times, and the recorded absorption signals were averaged. (D) Current densities (red) and scattered-light intensities (for tracking of oxidation state changes; blue) during cyclic voltammetry (10 mV s^{-1}) based on Ni-only catalysts. Adapted with permission.[126;134;343] Copyright Royal Society of Chemistry (2015), Wiley-VCH GmbH (2019), American Chemical Society (2019).

It should also be noted that scattered light from bubbles at high catalytic potentials may cause potential errors when recording light absorption. Therefore, the electrochemical system should be properly agitated and/or the equipment should be placed under dark conditions.[343]

1.7 Raman spectroscopy

1.7.1 Theory and application of Raman spectroscopy

XAS and UV-vis spectroscopy predominate their bulk-sensitive properties. However, direct information concerning reaction intermediates or structural change at the catalyst-electrolyte

interface during electrocatalysis may be compromised. As a surface-sensitive technique, Raman spectroscopy coupled with electrochemistry can detect the redox states and structure of catalysts, and adsorbed intermediates on a catalyst surface.[344;345] Raman spectroscopy originates from Raman scattering, a form of inelastic photon scattering phenomenon that was discovered in 1928 for liquids and crystals.[353] It is produced after the interaction between laser light and molecular that induces changes in molecular polarizability.[344;354] In general, the monochromatic laser light illuminates the sample, and the molecule on the ground state is excited into a virtual state. This is followed by potentially three decaying processes (Figure 1-12), which are: (i) Rayleigh or elastic scattering, where the energy of incident and scattered photons are equal; (ii) Stokes scattering where the scattered photons are red-shifted; (iii) Anti-Stokes scattering, where excess energy is released during relaxation. This results in a blue shift of the scattered photons since their initial location was in an excited vibrational state.[354-356] However, according to the Boltzmann statistics, the probability of initial molecules resting at excited states is much lower than that of molecules located at fundamental vibrational energy states.[354-356] The scattering intensity ratio of anti-Stokes and Stokes is given by Equation 1-7:

$$\frac{I_{AS}}{I_S} \propto e^{\frac{-\hbar\omega}{k_B T}} \qquad \text{Equation 1-7}$$

where I_{AS} is the anti-Stokes Raman scattering intensity, Is is the Stokes Raman scattering intensity, k_B is the Boltzmann constant, T is the temperature associated with the scattering species, $\hbar$ is the reduced Planck constant; and ω is the angular frequency. Raman spectrometers are operated by recording inelastically scattered Raman signals, which are typically acquired in confocal mode, i.e., using an objective lens to focus a laser on a sample followed by co-linear reflection, where the dominant Rayleigh scattering is filtered out by notch- or edge- filter (scheme of Raman spectrometer see Figure 5-1 and Figure 5-6).[355;357]

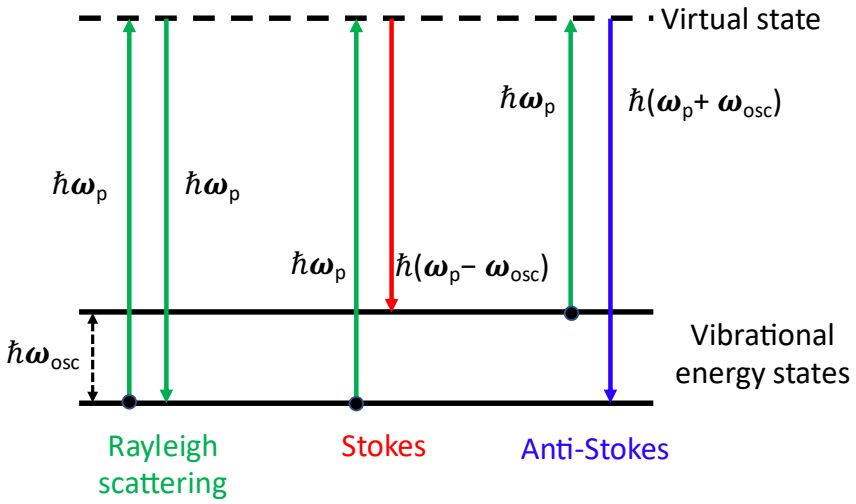

Figure 1-12. Energy scheme of vibrational transition states: (green) elastic (Rayleigh) scattering; (red) Stokes Raman scattering; (blue) anti-Stokes Raman scattering. Here, $\hbar$ is reduced Planck's constant; ω is angular frequency; the subscripts of p and osc denote the incident photon and the lattice or molecule vibration. Adapted with permission.[354;355] Copyright Springer Nature (2019), Wiley-VCH GmbH (2023).

The Raman active rule obeying the change in polarizability of the molecule is different from the IR absorption spectroscopy, where the entire dipole moment has to change during the vibration.[355] Consequently, different information is obtained from Raman and IR absorption spectroscopy. Compared to IR, Raman spectroscopy has several advantages: (a) weak Raman band of water in contrast to strong water absorption under infrared light, thus Raman spectroscopy is more suitable for operando measurement combined with an electrochemical setup;[354;355;358] (b) abundant information of bond vibrations (e.g. M-OH, M-OH_2, and M = O) in the low wavenumber regime are offered;[359] (c) recording gas-phases such as CO_2, O_2, H_2 without interference for Raman spectroscopy but not applied for IR;[355;356;360] (d) the weak Raman scatters of transparent glass or quartz material has benefits for constructing operando electrochemical cell;[356] (e) Raman spectroscopy at high temperatures is accessible, particularly with high-frequency excitation but not for IR due to strong sample emission.[355;356] Moreover, compared to in situ XAS, some potential advantages of operando Raman spectroscopy should not be overlooked: 1) faster acquisition time of each spectrum in the order of seconds in contrast to several minutes for individual XAS spectrum collection for non-dedicated beamline, which facilitates the real-time tracking of catalytic activity of catalysts that changes occur over minutes; 2) all the chemical information is revealed from one spectrum with a broad range (such as 100–4000 cm^{-1}), [355;356;361] while XAS merely focuses on one specific element; 3) Raman measurement is cost-effective and more laboratory-accessible.[355;362]

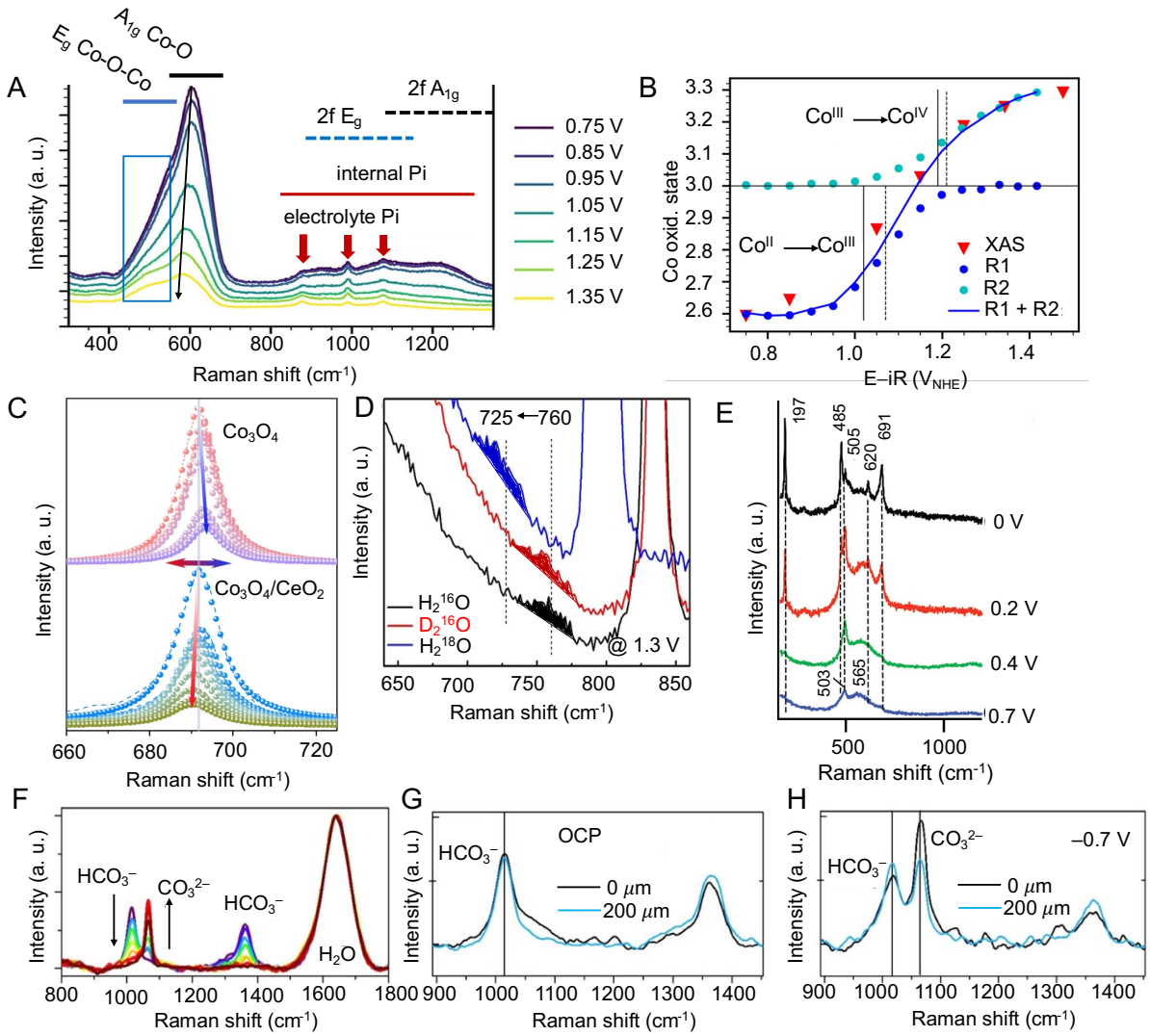

Figure 1-13. Potential applications of Raman spectroscopy in tracking oxidation states (A–C), reaction intermediates (D), phase transformation (E), and local pH (F–H). (A) Raman spectra of a Co-oxide catalyst material at various potentials (vs. NHE).[139] The thinner black arrow highlights a redshift of the main redox peak with increasing potentials; the blue rectangle, a gradually appearing shoulder. Band assignments are indicated following the study by Pasquini et al.[139]; Pi refers to phosphate ions in the electrolyte ($H_2PO_4^-$ and HPO_4^{2-}) and as an internal constituent of the catalyst material. (B) Co oxidation state changes deduced from the operando Raman data (of A) and X-ray absorption data.[139] (C) Raman bands for the Co_3O_4 and Co_3O_4 with CeO_2 show the different directions of peak shift.[363] (D) Raman bands assigned to Mn(IV) = O intermediate based on ^{18}O-labeled aqueous electrolyte. The large, out-of-scale Raman peaks result from permanganate ions formed in a side reaction.[303] (E) In situ Raman spectra of Co surface in 0.1M KOH as a dependence of various electrode potentials. The spectra were acquired over linear sweep voltammetry scans at 2 mV s^{-1}.[364] (F-H) Local-pH analysis by operando Raman spectroscopy;[57] (F) Calibration spectra for $KHCO_3$ solution at various pH values; spectra of the Cu-foam CO_2RR catalyst (G) without applied potential (OCP) and (H) at catalytic potential (−0.7 V vs. RHE) detected at the catalyst surface (0 μm) and 200 μm away. Adapted with permission. [57;139;303;363;364] Copyrights AIP Publishing (2020), Wiley-VCH GmbH (2018, 2021), Nature Portfolio (2021), American Chemical Society (2011).

Therefore, operando Raman spectroscopy can be a powerful technique in electrocatalysis, i.e., for monitoring potential dependence of chemical states, active intermediates at the electrolyte-catalyst interface, the structure or phase evolution of catalysts, and spatially resolved detection of electrolyte ion concentrations and local pH.[206;356-358] The redox transition of redox-active electrode materials and the formation of active intermediates are closely relevant to the OER catalytic mechanism.[206] (i) By employing operando Raman spectroscopy, two individual cobalt oxidation-state transitions ($Co^{II/III}$, $Co^{III/IV}$) of CoCat are distinguished (Figure 1-13 A and B) by combing with previous XAS results[126] that merely show average Co oxidation states.[139] (ii) In addition, operando Raman spectroscopy detected the potential-dependent formation of high-valent Co^{IV} active species for CeO_2-modified Co_3O_4 catalyst, resulting in improved OER activities (Figure 1-13C).[365] The monitored changes of redox states typically reflect in either (i) the decay(rise) of vibrational Raman peaks or (ii) continuous Raman peak shifts as a dependence on electrode potentials. As a result, the shape change of the Raman spectrum can be deconvoluted into a superposition of 2, 3, or more spectra assignable to 2, 3, or more (redox) states of the material.[206] Moreover, the possible identification of reaction intermediates such as in Mn-, and Co-based catalysts is revealed through operando Raman spectroscopy.[364;366-368] Accordingly, the potential-dependent Raman band located at 760 cm^{-1} assignable to Mn^{IV}=O species is resolved coupled with isotope labelling of water (Figure 1-13D).[367] Likewise, the different levels of Raman peak shifts are observed when operating CoCat in deuterated water ($D_2{}^{16}O$ isotope) and ^{18}O water ($^1H_2{}^{18}O$) electrolyte.[139] Consequently, the isotopic H/D substitution suggests the involvement of both terminal and bridging oxygen atoms in the (de)protonation process. However, spectra obtained in ^{18}O versus ^{16}O electrolytes show no major differences, most likely implying that the bridging oxygen of CoCat does not participate in O–O information or merely in indirect form.[139] Furthermore, with cobalt oxides deposited on Au substrate and operated in KOH, operando Raman spectroscopy monitored the redshift of the Raman peak from 609 cm^{-1} to 579 cm^{-1} coupled with the disappearance of Co_3O_4 spinel signature, indicating new phase formation of CoO(OH) that promoting more Co^{IV} species involved (Figure 1-13E).[362] A similar phase change was also deduced in Ni-based catalysts in the absence or presence of Fe by utilizing operando Raman spectroscopy, suggesting that the active species $NiOO^-$ is involved in the mediation of OER activity and that it is related to the electrolyte pH.[355] Furthermore, using operando spectroscopy, the potential-dependent vibration band of Co_3O_4 at 931 cm^{-1} is attributed to the μ-OO peroxide (Co–OO–Co) species, suggesting that the structural change in Co_3O_4 is associated with the presence of tetrahedral Co^{2+} ions.[369] Interestingly, anodic-deposited cobalt oxyhydroxide grown on Au substrate revealed a broad band around 1075 cm^{-1} assigned to Co–O–O–Co superoxide at catalytic potential.[368] Importantly, beyond detecting material-relevant transformation, spatially resolved operando Raman spectroscopy is able to monitor electrolyte ion concentration and local pH at electrode-electrolyte interface with micrometer resolution (ca. 1-2 μm). In our earlier work on electrodeposited Cu foam, the interfacial pH at different locations from the Cu electrode surface was achieved by monitoring the magnitude changes in specific peak bands of pH-determining electrolyte ions (HCO_3^- and CO_3^{2-}) after reaching equilibrium (Figure 1-13 F-H).[57] The pH values were calculated by

establishing calibration curves of the corresponding electrolyte involving the comparison of the peak intensities of the two specific vibrational bands. Consequently, distinct local alkalization of more than 10 at the interface was observed.[57] Subsequently, we monitored pronounced electrolyte acidification close to the outer CoCat surface (ca. 20 μm) when operating CoCat at neutral pH, which implies the limitations of macroscopic proton transport, resulting in the low OER catalytic current.[142] Therefore, in Chapter 5, we make use of the spatially resolved feature of operando Raman spectroscopy to detect the local and bulk pH variations in relation to proton transport by diffusing anions or cations.

1.7.2 SERM and challenges of Raman spectroscopy

Operando Raman spectroscopy provides insight into the catalytic mechanism at the molecular level during electrocatalytic reactions. However, a challenge for Raman spectroscopy is the low probability of inelastic scattering processes. Therefore, high concentrations of analytes or reaction intermediates are usually required to improve the sensitivity of Raman measurements.[355;370] In addition, the depth of detection and spatial resolution (approximately $\lambda/2$, λ denotes the wavelength of the laser excitation light) is still comparably low due to the limitations of visible light diffraction. [355] This limitation can be surpassed by creating a point source of less than half the wavelength ($\lambda/2$).[362] Importantly, several Raman-based techniques, such as surface-enhanced Raman spectroscopy (SERS),[371-373] tip-enhanced Raman spectroscopy (TERS)[374-377], and shell-isolated nanoparticle-enhanced Raman scattering (SHINERS)[378-380], have been developed to enhance the Raman signal of target molecules. Since surface enhancement effects typically occur on metals such as Au, Ag, and Cu, the latter two technologies have the potential to eliminate limitations associated with specific material requirements.[206;355;359] Here, we will delve into the SERM principle, which is widely discussed in the literature. The discovery of SERS in the 1970s dramatically improved the detection sensitivity of Raman scattering signals.[206;381;382] For molecular species that are firmly or loosely bound (adsorbed) to the surface of the SERS substrate—typically rough metallic surfaces or nanoparticles of gold, silver, or copper, their plasmonic properties can facilitate the SERS effect—the Raman signal can be enhanced by at least a factor of 10^6-10^7.[206;383] As a result, high-quality Raman spectra can be obtained even if there are only a few molecules of interest on the SERS surface. For substances that are not directly bound but are still close to the metallic SERS surface (within about 3 nm), [206;372;373;383] the enhancement factor is relatively low but still significant. Therefore, when electrocatalytic thin films are deposited or grown on SERS-active substrates, the surface enhancement effect can increase the signal intensity, thus enabling in situ surface-enhanced Raman spectroscopy.[206;215;364;368]

The SERS enhancement effect is commonly explained by two main theories: the electromagnetic (EM) theory and the chemical (CE) theory.[359;384;385] The EM enhancement is considered to be the predominant contributor, enhancing the Raman signal by about 5-10 orders of magnitude.[375;385] According to the EM mechanism, surface plasmon resonance is triggered when exposed to laser light, leading to an elevated electromagnetic field on the surface (local field enhancement). This in turn amplifies the light-matter interaction, leading to an enhancement of Raman scattered light (irradiation enhancement).[354] The chemical

enhancement mechanism typically arises from the transfer of charge between the metal surface and the analyte or absorbed molecules. Compared to the electromagnetic enhancement, the chemical enhancement is still smaller (up to 10^3).[386-388] It has been noted that the charge transfer mechanism is limited to specific molecules, whereas the electromagnetic (EM) mechanism applies to all analytes. Thus, the EM theory leads to a generalized enhancement of the Raman band rather than a selective enhancement. In most cases, the enhanced SERS signal is produced by the synergistic effect of the two theories.[354;384;389;390] When analyzing operando SERS spectra, Raman peak intensities were found to be strongly dependent on the electrode potential or even the history of previously applied potentials, thus complicating potential-dependent spectral analysis.[206;391-393] For a reasonable quantitative analysis, it is recommended that the Raman signal intensity is normalized to the background amplitude since the local surface plasmon resonance determines both the Raman intensity and the broad, featureless background amplitude.[206;391]

Challenges in operando Raman spectroscopy also include sample damage[139;367;394] and fluorescence interference.[355;358] The laser heating effect is the most severe and easily underestimated source of artifacts in operando Raman experiments.[206] The laser can heat up the catalyst and even modify the sample, for example, converting amorphous CoO_x material into a crystalline phase Co_3O_4, resulting in the emergence of sharp Raman peaks.[206;394] Several methods have been implemented for avoiding laser damage,[206;355;356] including optimizing the laser wavelength/power/ exposure time, constantly moving or rotating either sample or laser beam, and the use of a line focus (available only in some commercial instruments) to focus the laser on a line-shaped area of 1 mm×100 mm, thereby reducing the laser power per unit area without significant loss of signal intensity.[206] Defocusing the Raman beam reduces the signal intensity more than the illumination intensity, so defocusing is not an effective approach.[206] In addition, selecting materials with high thermal conductivity (eg., metallic Pt electrodes) could mitigate the heating effect.[139] Care should be taken when selecting lasers not to trigger absorption and photochemical reactions.[355] Moreover, Raman scattering intensity can be maximized by selecting appropriate optics (primarily microscope objectives) to direct the excitation laser radiation and collect the scattered radiation in a confocal mode (see Figure 5-6).[206;358] Typically, the theoretical maximum Raman signal intensity can be obtained using a water immersion microscope objective with a large numerical aperture (N.A.).[206] Water immersion objective reduces the mismatch of refractive index in the light path and minimizes light loss.[356] The objective lens can be used in any electrolyte solution by covering it with a Teflon protective film that has a similar refractive index to water (n = 1.33).[355] However, using an immersion objective may shorten the distance between the objective and the working electrode. Bubbles formed during gas reactions may be trapped in this gap, thus attenuating the Raman signal.[354] Furthermore, the larger the numerical aperture of the objective lens used, the more tightly the laser can be focused onto a spot (a few hundred nanometers in diameter), while also greatly increasing the collection of scattered signals.[206;362] Fluorescence leading to a broad Raman background affects Raman intensity analysis and can be caused by the support material, the catalyst material itself, electrolyte impurities, certain components of the reaction mixture, or even emerging species.[355;356] Elimination or reduction of the fluorescence

background can be achieved by tuning the excitation wavelength using a near-infrared or ultraviolet laser. Another method is the employment of shifted excitation Raman difference spectroscopy (SERDS),[363;395;396] which uses two slightly shifted excitation wavelengths to acquire two consecutive Raman spectra at the same position. The excitation wavelengths are shifted by only a few nanometers. The resulting Raman signal is relatively shifted, while the fluorescence remains essentially unchanged. By subtracting these two shifted Raman spectra, the fluorescence disappears and only the Raman signal remains.[355;395]

In summary, this section compares Raman spectroscopy with XAS and infrared spectroscopy and further describes the differences between conventional Raman spectroscopy and surface-enhanced Raman spectroscopy. We highlight the various powerful roles of operando Raman spectroscopy in monitoring potential-dependent chemical states, structural or phase transitions, the evolution of reaction intermediates, protonation states, and local pH, especially at electrolyte-electrode surfaces. In addition, some potential challenges are pointed out.

1.8 Scope and organization of this thesis

The goal of this dissertation is to investigate the activity determinants and limiting factors in neutral-pH water oxidation based on an electrocatalytic cobalt-phosphate system. The focus of the studies includes: 1) the role of electrolyte phosphate species in assisting proton transfer and their influence on catalytic activity, 2) deciphering the role of oxidation state accumulation in determining the catalytic rate of OER, 3) judging whether redox inert ions (potassium ions and phosphate ions) are involved in the redox transition or catalytic process acting as charge compensating role, and 4) quantifying the local pH and electrolyte pH profile by operando Raman spectroscopy. The results reported here likely are generally valid for a broader class of volume-active OER catalyst materials and for the amorphized near-surface regions of microcrystalline materials as well as other technically relevant electrolysis cells.

The studied contents are divided into four chapters, organized as follows:

Chapter 2 (Macroscopic proton transport) proposed three possible rate-limiting processes related to proton transport and concluded the role of macroscopic diffusion of phosphate species in mediating proton transport. Extensive Tafel plots (*j*-V curves) at various KPi concentrations in the neutral CoCat-KPi system are analyzed. The potential-dependent structure and oxidation states of CoCat are studied by operando XAS at different concentrations of KPi electrolyte. The role of the phosphate buffer in mitigating local pH is further confirmed by FEXRAV at a fixed X-ray incident energy. Quantitative analysis of internal phosphate amount and mathematic simulations of *j*-V curves provide additional evidence. A proof-of-principle experiment shows that current densities exceeding 1 A cm^{-2} can be achieved in neutral-pH OER.

Chapter 3 (Oxidation states versus catalytic rate) discusses the relationship among the catalytic rate of OER, the accumulated redox states, and the electrode potential for CoCat operated in KPi electrolyte systems with either varying KPi concentrations or pH values. The studies are achieved by operando X-ray absorption spectroscopy (XAS), electrochemistry experiments with potential jumps, and in situ UV-vis absorption spectroscopy.

Chapter 4 (Role of the potassium ion) scrutinizes the binding motif of redox-inert potassium ions from the internal CoCat and verifies that potassium ions do not play a charge-compensating role in the redox transition of cobalt. The structure of potassium was investigated by analyzing the EXAFS of potassium at the K-edge. The exchange kinetics of K^+ as a function of electric potential were investigated by a novel operando XAS experiment with fixing incident X-ray energy at high energy. Elemental analysis of potassium and phosphorus provided complementary results.

Chapter 5 (Local pH and electrolyte pH profiles) quantifies the local pH and electrolyte pH profiles (and the corresponding phosphate species amount profiles) based on the CoCat-KPi system by using different Raman spectroscopic configurations. In addition, a broad distribution of electrolyte pH near the same anode or cathode is detected by the spatially resolved Raman spectroscopy in a stagnant electrolyser, and a complicated diffusion of proton-transporting molecules between the anode and cathode is revealed.

2 Deciphering the proton transport limitation of electrocatalytic water oxidation at neutral pH for an amorphous cobalt-phosphate catalyst system

Abstract Neutral-pH OER reduces operational risks and enables direct coupling to electrochemical CO_2 reduction, but typically is hampered by low current densities. In this chapter, the rate limitations from proton transport in neutral-pH OER are clarified. Using cobalt-based catalyst films and phosphate ions as essential electrolyte bases, current-potential curves (*j*-V) are recorded and simulated. Operando X-ray spectroscopy shows the potential-dependent structural changes independent of the electrolyte phosphate concentration. Operando Raman spectroscopy uncovers electrolyte acidification at a micrometer distance from the catalyst surface, limiting the Tafel slope regime to low current densities (presented in Chapter 5). The electrolyte proton transport is facilitated by diffusion of either phosphate ions (base pathway) or H_3O^+ ions (water pathway). The water pathway is not associated with an absolute current limit but is energetically inefficient due to the Tafel-slope increase by 60 mV dec^{-1} shown by an uncomplicated mathematical model. The base pathway is a specific requirement in neutral-pH OER and can support high current densities, but only with accelerated buffer-base diffusion. Catalyst internal phosphate diffusion or other internal transport mechanisms do not limit the current densities. A proof-of-principle experiment shows that current densities exceeding 1 A cm^{-2} can also be achieved in neutral-pH OER.

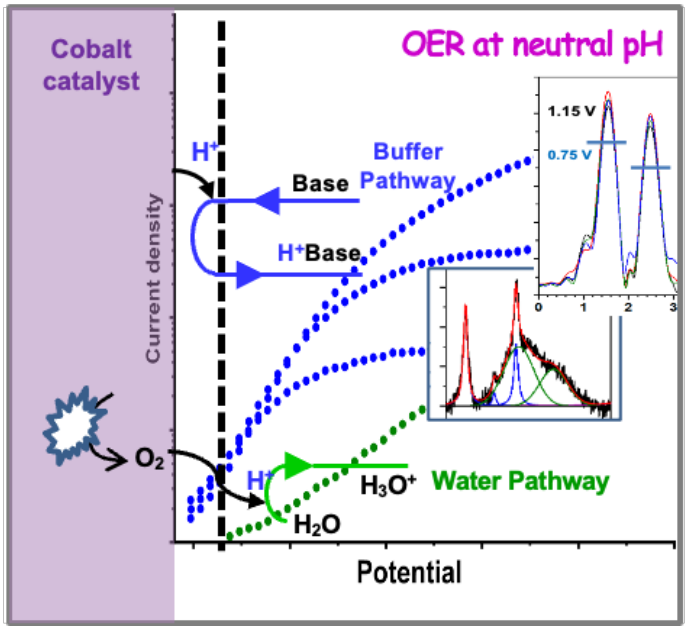

A portion of this chapter reproduced from:
S. Liu, I. Zaharieva, L. D'Amario, S. Mebs, P. Kubella, F. Yang, P. Beyer, M. Haumann, H. Dau*. Electrocatalytic Water Oxidation at Neutral pH–Deciphering the Rate Constraints for an Amorphous Cobalt-Phosphate Catalyst System. *Advanced Energy Materials* **2022**, 12, 2202914. https://doi.org/10.1002/aenm.202202914

Author Contributions:

S. Liu performed all the experiments and data evaluation of this chapter unless otherwise noted.
P. Kubella conducted the high current density experiment shown in Figure 2-32.
F. Yang supported SEM measurement.
I. Zaharieva wrote mathematical simulation software.
I. Zaharieva, L. D'Amario, S. Mebs, P. Beyer, M. Haumann supported synchrotron measurements and provided valuable discussion.
H. Dau draw the schemes, deduced equations, and supervised research.

2.1 Introduction and motivation

Neutral pH OERs are essential for sustainable fuel production, but their current densities are typically low. Thereby, clarifying the catalytic rate limitations in neutral-pH OER is crucial. Here, we chose an amorphous CoCat material combined with a potassium dihydrogen phosphate (KPi) electrolyte as a model system to explore the factors that limit the flow of electrocatalytic currents in OER at neutral pH. A series of studies have investigated the structure and function of CoCat catalysts in detail.[65;70;71;112;113;116;118;119;121-124;126;128;134;158;159;168;170] However, the critical role of KPi or alternative protonatable ions[99] in the neutral pH system has been almost exclusively scrutinized.[67;123;397-399] Although the structural and functional importance of phosphate or other "buffer ions" in electrocatalysis is generally accepted,[65;71;99;110-143] we consider the experimental characterization and understanding of the technological decisive current-density−electric-potential relations (in the following denoted as 'current-voltage' or '*j*-V' relations) to be insufficient, which motivates our present investigation.

Possible rate-limiting processes in neutral-pH OER were proposed (Figure 2-1) based on previous CoCat studies.[99;124;135] (i) Costentin and coworkers modelled *j*-V curves for CoCat-OER and further electrokinetic data in a series of inspiring investigations.[124;128;400] In ref.[124] they suggest film-internal diffusion of the buffer molecules ($HPO_4^{2-}/H_2PO_4^-$) between the external electrolyte-exposed surface of the catalyst film and the catalyst-film–substrate electrode interface, with phosphate ions serving as proton shuttle within the CoCat catalyst (option a. in Figure 2-1).[124] According to this proposal, also the CoCat-internal diffusion of phosphate ions could be a rate-determining process. (ii) In an early study addressing the role of electrolyte bases in near-neutral-pH water oxidation, we found that for nine different protonatable ions employed as a pH-buffering system, the catalytic current density at comparably high electrode potentials (1.35 V vs. NHE) does not follow a classical “thermodynamic” pH dependence.[99] It is rather determined by the electrolyte pH and the pKa-value of the buffering groups such that the availability of a (deprotonated) proton-accepting base determines the current density.[99] To rationalize this finding, we proposed that the current-limiting process in OER is the transfer of protons from the catalyst material to unprotonated buffer molecules as it takes place at the catalyst-electrolyte interface. (option *b*. in Figure 2-1). (iii) Recently, we have developed an analytical model, which quantitatively explains the presence of proton transfer limitation by macroscopic diffusion of the buffer base in the bulk electrolyte, and thus, outside of the catalyst film (option *c.* in Figure 2-1).[135] This model predicts that at high catalytic potential, the maximum current density is

determined by the protonation state of the buffer base, its concentration, and an effective diffusion constant describing the diffusion of the buffer ions within the bulk electrolyte.

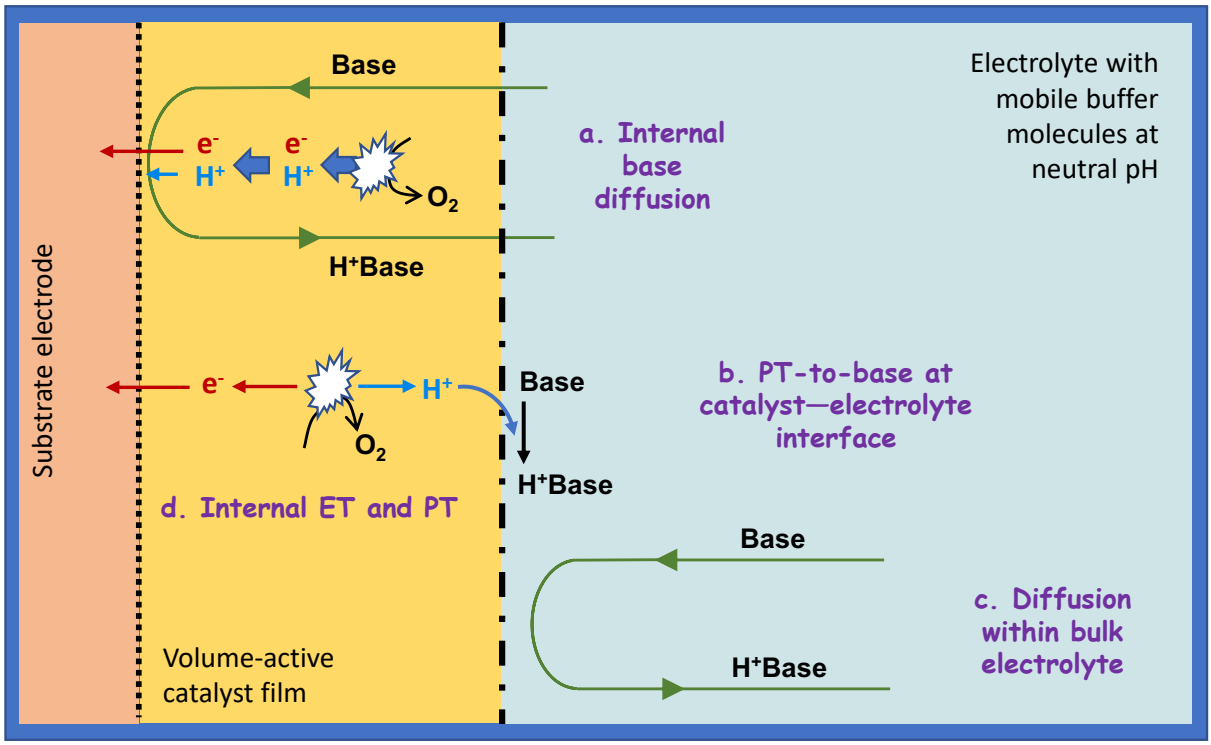

Figure 2-1. Possible rate-limiting processes in neutral-pH OER. Reproduced with permission from ref.[142]. Copyright Wiley-VCH (2022).

In this chapter, three different scenarios for the rate-limiting process in proton transport mediated by mobile phosphate ions can be distinguished (see Figure 2-1): (a) internal diffusion within the catalyst, (b) proton transfer at the outer catalyst surface, and (c) macroscopic diffusion and thereby proton transfer within the bulk electrolyte. In the present study, we succeed in distinguishing between these options, thereby, identifying the dominant rate-determining processes. Experimentally, we focus on the low current density regime because it is relevant for artificial photosynthesis applications. Furthermore, we provide a proof-of-principle experiment with high-current OER at near-neutral pH. We examine catalyst films deposited on a transparent conducting oxide, complemented by experiments with CoCat films deposited on nickel foam electrodes and a discussion of the high-current regime relevant to industrial electrolyzer systems. Consequently, we consider the determining factors potentially may be generally valid for a neutral water oxidation system.[67;123;397-399]

2.2 Results and discussion

2.2.1 Phosphate dependence of j-V curves

To investigate the role of phosphate ions in the bulk electrolytes at neutral pH (7.0) for water oxidation catalyzed by CoCat, complete *j*-V curves were collected at various potassium phosphate (KPi) concentrations ranging from 1.6 mM to 250 mM, in four sets of experiments (Figure 2-2):

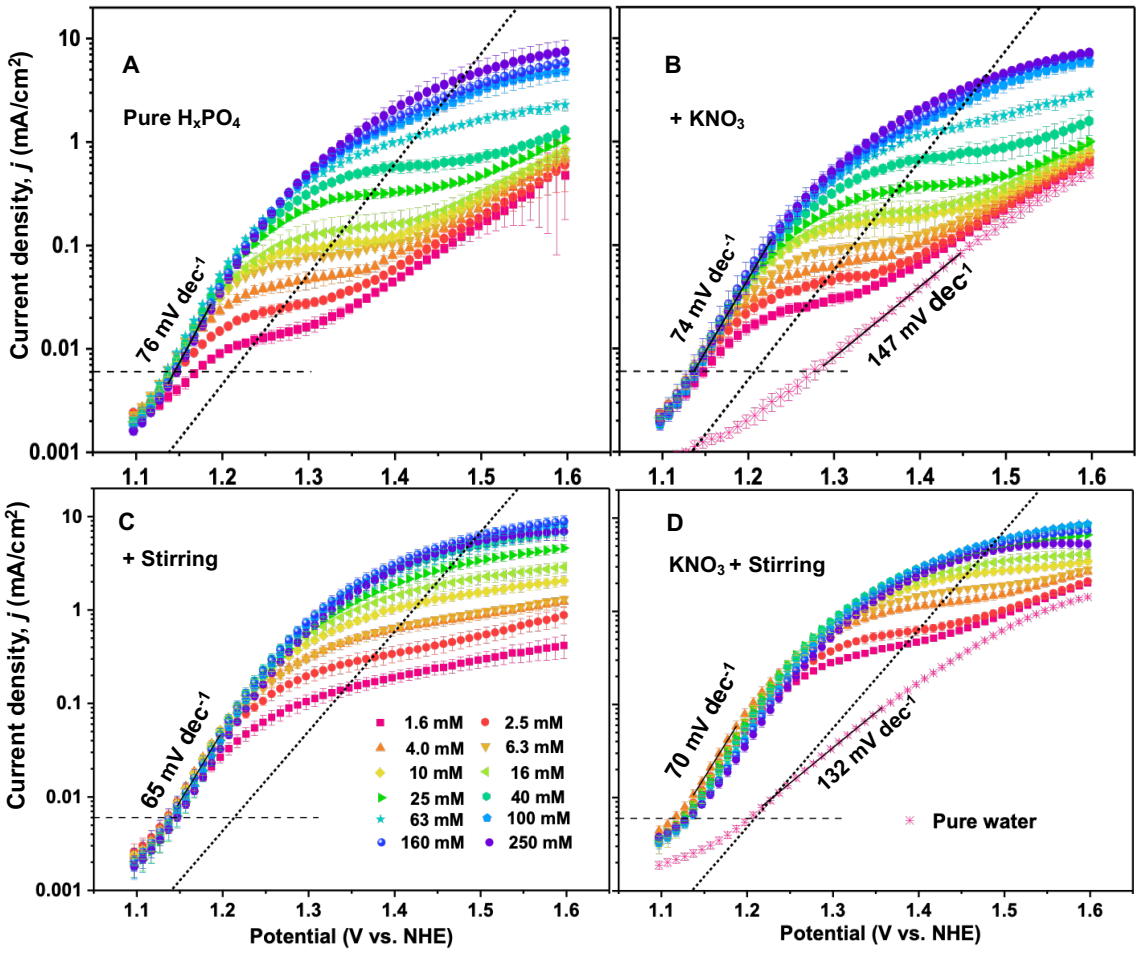

Figure 2-2. Phosphate concentration dependence of *j*-V curves investigated at pH 7. The current density (j) was recorded at various electrode potentials (V in Volt vs. NHE), for static operation of the electrochemical cell (no stirring) or with enhanced convection (stirred, 500 rpm), without or with 500 mM KNO_3 as a supporting electrolyte component. For collection of *j*-V curves, the potential was increased stepwise (from lowest to highest values) and the current density was determined after an equilibration period of 1 min at the respective potential. For each *j*-V curve, a fresh CoCat film had been prepared, with a deposition charge of 10 mC cm^{-2}, corresponding to ca. 100 nmol of Co ions per cm^2. All experiments were repeated at least three times; vertical error bars indicate standard deviations (σ) calculated according to Equation 2-1. The dotted lines mark the approximate inflection points of the *j*-V curves (same line in A, B, C, and D), which were determined as shown in Figure 2-4 and herein are discussed as 'plateau levels'. In B and D, approximate Tafel slopes are indicated (rough graphical estimates, excluding the current-density regime below the dashed-line level of 7 µA cm^{-2} in the estimation). We note that at high phosphate concentrations, control experiments revealed a partial CoCat film loss (Figures 2-10 to 2-15, see also Figures 2-14 to 2-15 for SEM images), which explains the decrease in current density at high potentials as observed in some experiments. Reproduced with permission from ref.[142]. Copyright Wiley-VCH (2022).

$$\sigma = \sqrt{\frac{1}{N-1}\sum_{i=1}^{N}(x_i - \bar{x})^2} \qquad \text{Equation 2-1}$$

Here N is the number of samples measured in each condition, x_i is current density of a single sample, $\bar{x}$ is the average current density.

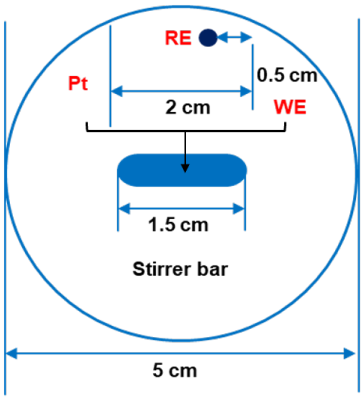

Figure 2-3. Top view scheme of the electrochemical cell arrangement with magnetic bar for experiments with stirred electrolyte in Figure 2-2. For experiments in pure H_xPO_4 or with the addition of KNO_3, no stirring was used. The area of working and counter electrodes is 10×10 mm^2 and 20×20 mm^2, respectively. The distance between Pt-grid and ITO working electrode (WE) was 20 mm. The distance between reference electrode (RE) and working electrode (WE) was 5 mm. Note that the black arrow shows that the three electrodes were located in the center of the beaker during the experiment, as was the position of the stirring bar.

Variation of KPi concentration without additional salts in unstirred electrolyte solution (Figure 2-2A);

Variation of KPi concentration in high-salt (500 mM KNO_3) and unstirred electrolyte solution (Figure 2-2B);
Variation of KPi concentration without additional salts in stirred electrolyte solution (Figure 2-2C);
Variation of KPi concentration in high-salt (500 mM KNO_3) and stirred electrolyte solution (Figure 2-2D);
In sets B and D, *j*-V curves were also collected in the pure water without KPi but with the addition of a high-salt electrolyte (500 mM KNO_3), without or with stirring (initial pH adjusted close to 7). The same electrochemical cell configuration in Figure 2-3 was used for the four sets of *j*-V curve collection to ensure identical diffusion characteristics in A and B (unstirred) as well as C and D (stirred with 500 rpm;). Analysis of Figure 2-2 by visual inspection and summarizing informative values in respective graphics (Figures 2-5 to 2-7) reveals:
(i) Common Tafel-slope characteristics at all KPi concentrations. At low potentials (around 1.15 V vs. NHE) an overlapping and approximately exponential increase of the current density (linear increase of log *j*) is observed in all curves, suggesting similar Tafel slopes (close to 70 mV dec^{-1}, Figure 2-2B). Consequently, at low overpotentials, the current density is independent of the KPi buffer concentration (Figure 2-5A), as also reported in ref. [113]. Assuming that the observed Tafel slope and exchange current density reflect a specific reaction mechanism, this observation implies that the OER reaction mechanism is unaffected by the KPi concentration. Although the Tafel slope itself is not significantly affected by the KPi

concentration, the extension of the linear regime (of log *j*) increases strongly with increasing KPi concentration, from clearly less than one decade increase in current density (for pure H_xPO_4 without stirring, Figure 2-2A) to clearly more than one decade, which relates to the KPi-dependence of the plateau level in the *j*-V curves.

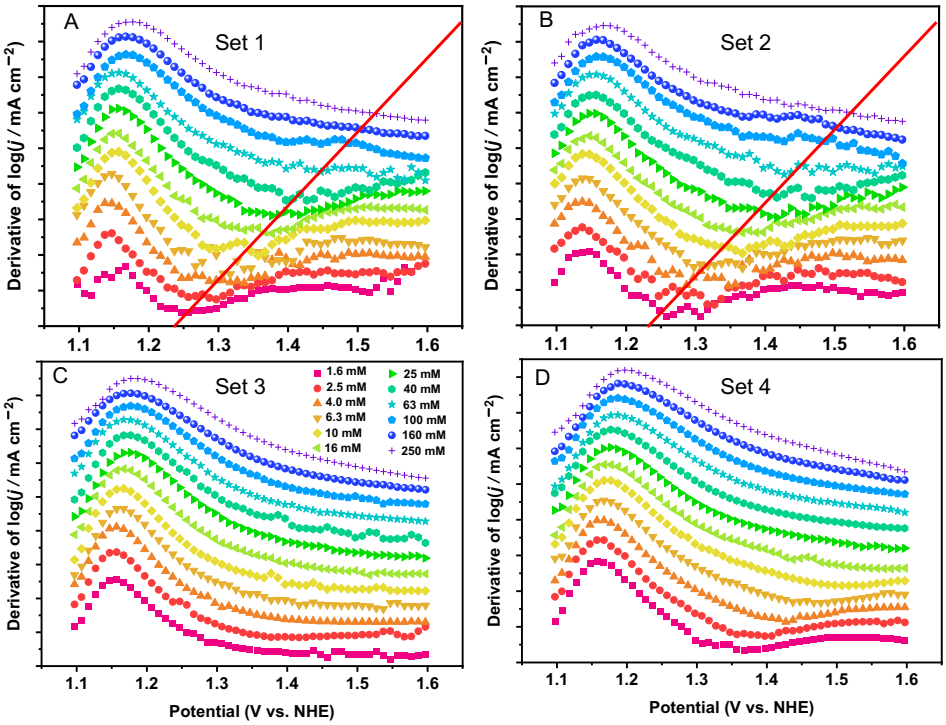

Figure 2-4. The first derivative of the logarithm of the current as a function of the applied potential (data of Figure 2-2) and their role in rough quantification of plateau levels of the *j*-V curves for data shown in Figure 2-2B. Noticeably, at high KPi concentrations and high current conditions (e.g., panels C and D) none or only a minor indication of a local minimum is visible. The red line shown in panels A and B has identical slopes and offsets. They were positioned manually such that they cross the estimated minima visible in the curves for low phosphate concentrations and used for obtaining the data points shown in Figure 2-5B. To obtain the plateau level in Figure 2-5B, we determined the points where the red line shown above in panels A and B (and shown for A, B, C, and D in Figure 2-2, always the same line with identical slope and offset) cross the *j*-V curves. These crossing points were considered to provide an approximate measure of the plateau-level current. We emphasize that the used procedure to estimate a plateau-level current exclusively serves to provide a qualitative overview of phenomenology.

(ii) Strongly increased Tafel slope without KPi. For the *j*-V curve collected in "pure water" (without KPi buffer, but with 500 mM KNO_3), a strikingly different behavior is observed: an increase in current density with a Tafel slope that is approximately two times larger than in KPi buffer and extends over a large potential range (Figure 2-2 B and D). This behavior is also reproduced in the simulations presented further below for proton transport by H_3O^+ ions (see also in ref.[124]).

(iii) Plateau level determined by KPi concentration. With increasing the applied potential beyond the Tafel slope region, a plateau level of the current density is reached at 1.25 V to 1.4 V, which is well visible (in Figures 2-2A and 2B) as an inflection point of the *j*-V curves for KPi concentrations ranging from 1.6 mM to 40 mM. A quantitative analysis of current

densities at the inflection points for various KPi concentrations is shown in Figure 2-5B. A roughly first-order dependence of the plateau-level current density and KPi concentration was revealed for all four sets of electrolyte systems, in line with a current limitation determined by the availability of unprotonated buffer ions (HPO_4^{2-}) needed for accepting the 'product protons' from water oxidation.[99] Compared to unstirred electrolyte conditions, the plateau current at low current density is clearly enhanced for the stirred electrolyte conditions (about 12-fold or 18-fold increase in low-salt or high-salt electrolyte, respectively. This finding suggests a current limitation by macroscopic KPi diffusion.

Table 2-1. Summary of all Tafel slopes determined from Figure 2-2. The unit of Tafel slope is mV dec^{-1}. SD represents standard deviation from at least three individual measurements.

	Pure H_XPO_4		+ KNO_3		+ Stirring		KNO_3+Stirring	
KPi conc. (mM)	Tafel slope	SD	Tafel slope	SD	Tafel slope	SD	Tafel slope	SD
1.6	126	6.7	97	2.8	72	8.9	74	0.1
2.5	98	4.1	90	5.9	71	3.0	71	0.6
4.0	83	3.5	81	2.8	66	0.9	69	0.4
6.3	74	0.6	76	1.2	65	0.7	67	0.3
10	71	1.0	72	1.6	63	0.6	65	1.3
16	68	0.8	72	0.8	61	0.5	67	1.0
25	66	0.5	68	1.2	61	2.1	67	0.2
40	65	0.5	68	0.8	61	0.5	68	0.3
63	65	0.9	66	0.7	62	1.6	69	0.5
100	66	0.8	66	1.4	64	2.1	70	0.8
160	65	2.5	67	2.2	66	2.9	72	0.8
250	66	0.5	68	1.8	68	0.5	75	0.5

(iv) Influence of ionic strength. In Figure 2-2A, variation of the KPi concentration did not only change the availability of proton-accepting buffer molecules but at the same time altered the total ion concentration. To investigate whether changes in ionic strength affect the *j*-V curves, the ionic strength was kept at a high level irrespective of the KPi concentration by adding 500 mM KNO_3 to the buffer (Figure 2-2B). We observe qualitatively the same *j*-V behavior with and without KNO_3 complementation, but at very low KPi concentrations the plateau level is moderately enhanced with KNO_3 in unstirred electrolytes (by a factor of about 2.0, 1.8, or 1.4 at 1.6 mM, 2.5 mM, or 4 mM KPi, Figure 2-2 A and B). In stirred electrolyte, a comparison of the low-salt to the high-salt *j*-V curves reveals a more pronounced high-salt enhancement than observed in unstirred electrolytes (at low KPi concentrations), approaching a factor of three. This salt enhancement effect is particularly evident at low current densities and is likely *not* explained by the effect of ‘normal' Ohmic resistance, as also confirmed by the simulations

discussed further below. Furthermore, the KNO_3-enhancement effect that contributes to the diffusion of KPi between the anode and cathode was investigated by replacing the large platinum grid with a fine platinum wire and by studying other system geometries (Figure 2-6). The same plateau current was observed with the addition of high salt and was independent of the geometry of the electrode. Similar results were obtained for the pure KPi electrolyte. This demonstrates, apparently, that the macroscopic diffusion of KPi species from the catalyst electrode to the platinum electrode is not strongly influenced by the KNO_3. However, we do not exclude the influence of the large cell capacity (50 mL). We conclude that for a low KPi concentration also the added salt (500 mm KNO_3) plays a role in enhancing the current density. Therefore, an ionic strength effect on either KPi diffusion or protonation states in the Helmholtz layer at the catalyst–electrolyte interface represents a more likely explanation.

*(v) Biphasic j-*V *curves relating to H_2O acting as proton acceptor.* For low and intermediate KPi concentrations at high overpotentials, the *j*-V curves approach asymptotically the *j*-V curve obtained for operation of the catalyst film in the KNO_3-containing, but KPi-free electrolyte, as clearly visible in Figures 2-2B and 2D. Assuming that the plateau level can be explained by the exhausted proton accepting capacity of the KPi buffer close to the catalyst surface (Figure 2-18), water obviously serves as an additional proton acceptor at high overpotentials. Therefore, the current density at 1.6 V for low KPi concentrations approaches the current for the KPi-free electrolyte (Figure 2-5C). Furthermore, with stirring, the *j*-V curves in the absence of any KPi result in an enhanced current density, demonstrating proton transport limitation most likely comes from the diffusion of H_3O^+ from the anode to the cathode rather than the process of water accepting protons (Figure 2-7), as also supported by *j*-V curve simulation.

(vi) Ohmic limitation at high current densities. At high current densities, increasing KPi concentrations no longer leads to a proportional increase of the current density, but rather to plateau levels (Figures 2-2, 2-5B and 2-5C), which largely result from Ohmic limitations. The linear current-voltage relation visible at the highest KPi concentration in Figure 2-8 reveals an Ohmic resistance close to 35 Ohm for all four data sets (dotted lines in Figure 2-8). This Ohmic resistance is not a catalyst-intrinsic property but derives from the sum of the electrolyte resistance and the Ohmic resistance of the ITO substrate of the working electrode, the latter being the dominating contribution at high salt concentrations, as also supported by Ohmic resistance calculation from thicker CoCat film (Figure 2-9) as well as Ni foam as substrate (Figure 2-29). (We note that at the highest KPi concentrations with stirred electrolyte, the current densities decrease for increasingly positive potentials exceeding about 1.5 V, which is explainable by catalyst film degradation, see Figure 2-10 to 2-12).

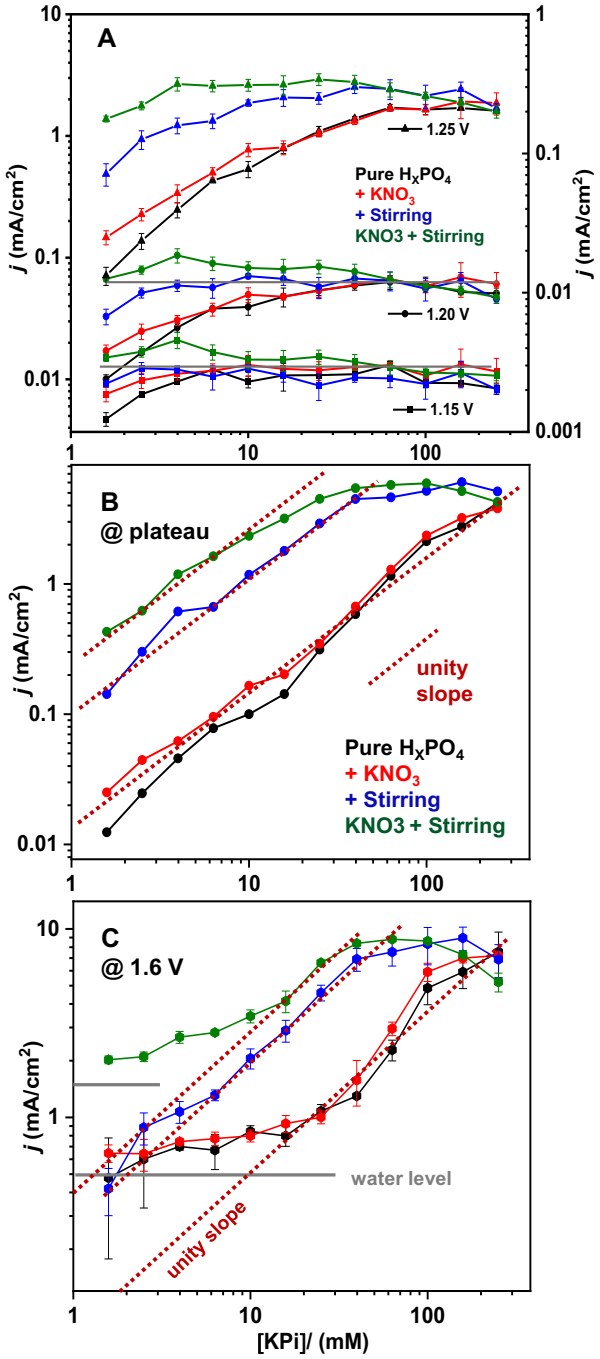

Figure 2-5. Current density of CoCat as a function of phosphate buffer (KPi) concentration at selected potential regions. The symbols represent data of Figure 2-2, A in black, B in red, C in blue, and D, green. Panel A shows the characteristic current corresponding to the indicated low potential in Figure 2-2. To avoid overlapping of data points, current densities at 1.25 V are shown on the right y-axis. Parallel grey lines of panel A mark equal current densities. Panel B indicates the characteristic current at the plateau of Figure 2-2 (dotted line). In panel C, each point represents the current density at 1.6 V. The slope of the red dotted line is unity which corresponds to a first-order (linear) relation between current density and KPi concentration. In panel C, the two grey lines mark current densities at 1.6 V vs. NHE determined for 'pure water' in the absence of KPi molecules (but with 500 mM KNO_3; see Figures 2-2 B and D). Reproduced with permission from ref.[142]. Copyright Wiley-VCH (2022).

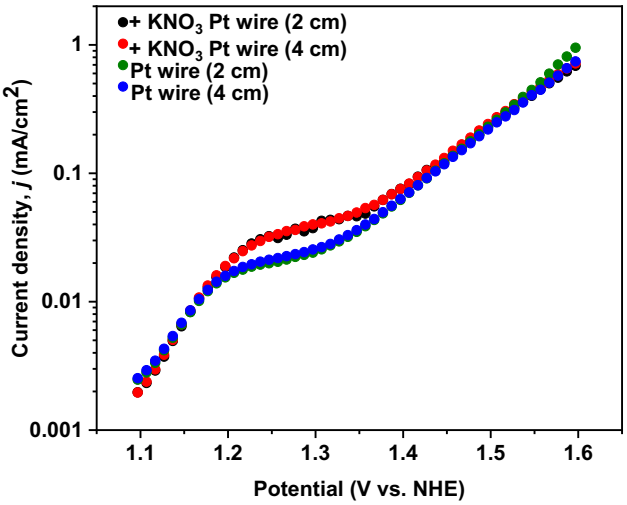

Figure 2-6. *j*-V curves of CoCat by varying the distance between CoCat and the Pt counter electrode with or without the addition of KNO_3 salt. CoCat (10 mC cm^{-2}) deposited on ITO was operated at 2.5 mM KPi (pH 7). A platinum wire (unwound) was used instead of a platinum grid for the measurement of the *j*-V curves.

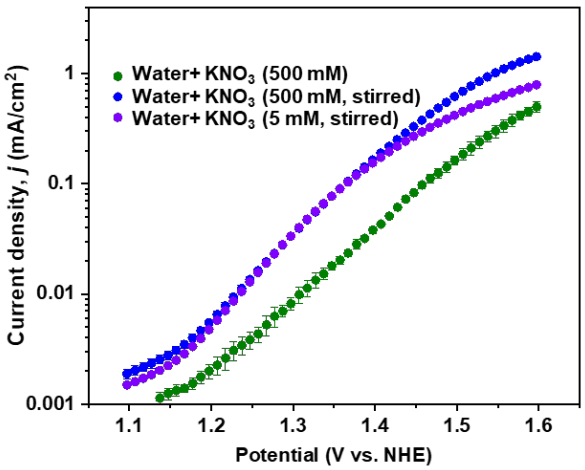

Figure 2-7. *j*-V curves collected in the stirred or non-stirred electrolyte with varying the KNO_3 concentration, when CoCat (10 mC cm^{-2}) was operated in KPi-free buffer. More details seen Figure 2-6.

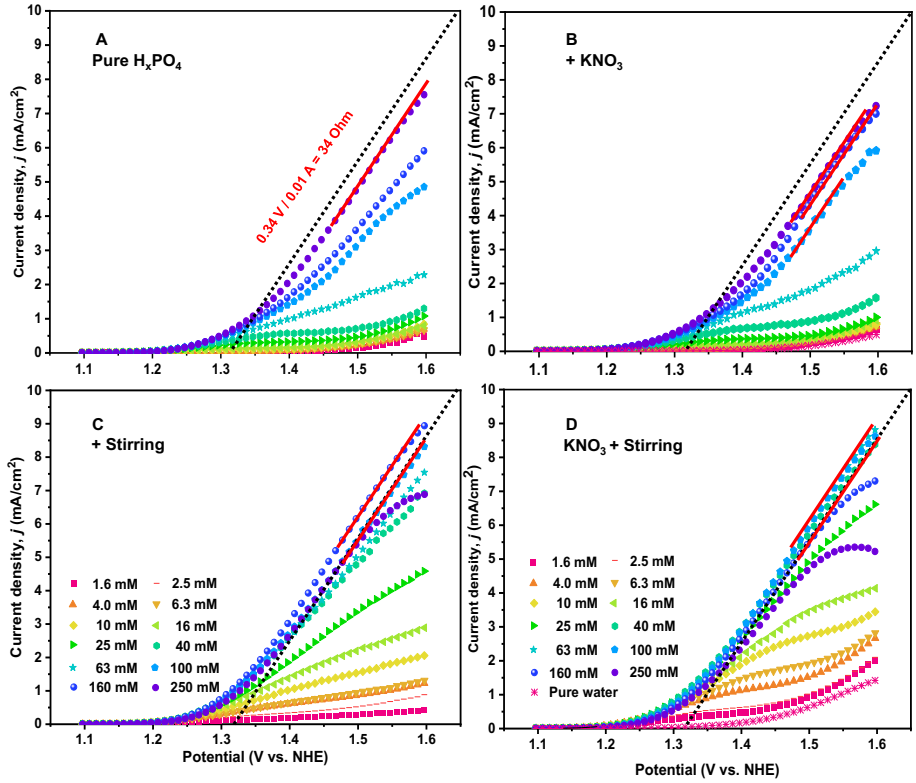

Figure 2-8. Current density (*j*) versus electric potential (V) corresponding to the data in Figure 2-2, but here using a linear scale. The same slope (black dotted lines) is used to estimate the Ohmic resistance for high KPi concentration data, which is approximately 34 Ohm. The red solid lines are parallel to the black dotted lines.

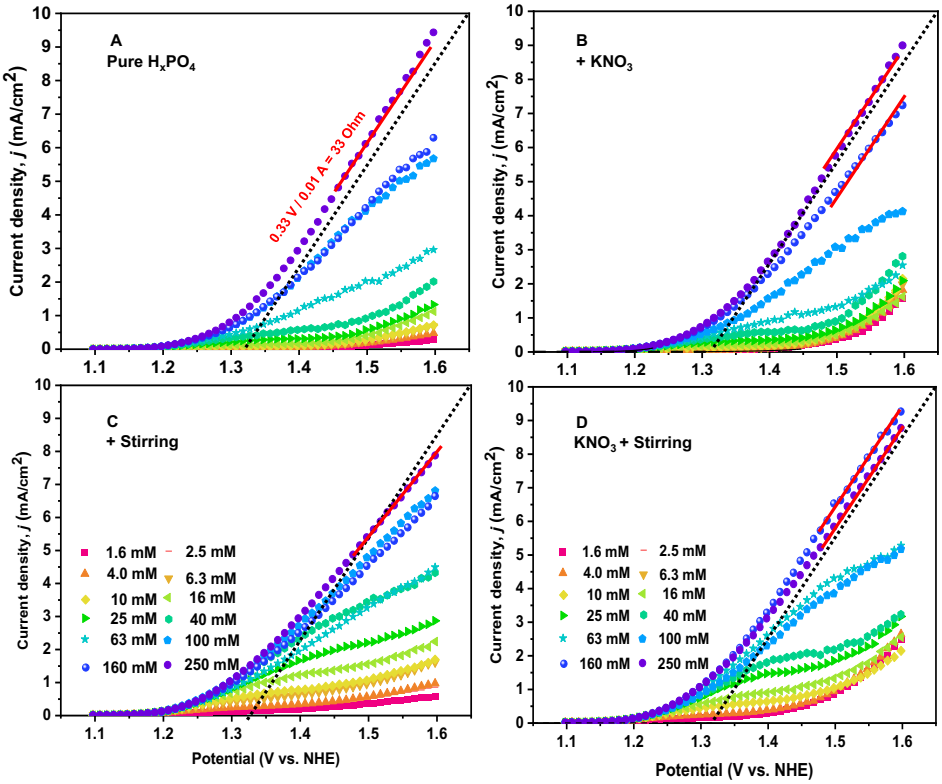

Figure 2-9. Current density (*j*) versus electric potential (V) in the linear scale for the four KPi system by using thicker film 50 mC cm^{-2}. Same dotted line is used to estimate the Ohmic resistance for high KPi concentration data at high potential region, here is around 33 Ohm. The red lines parallel to the dotted line or having slightly deviation show almost same ohmic resistance.

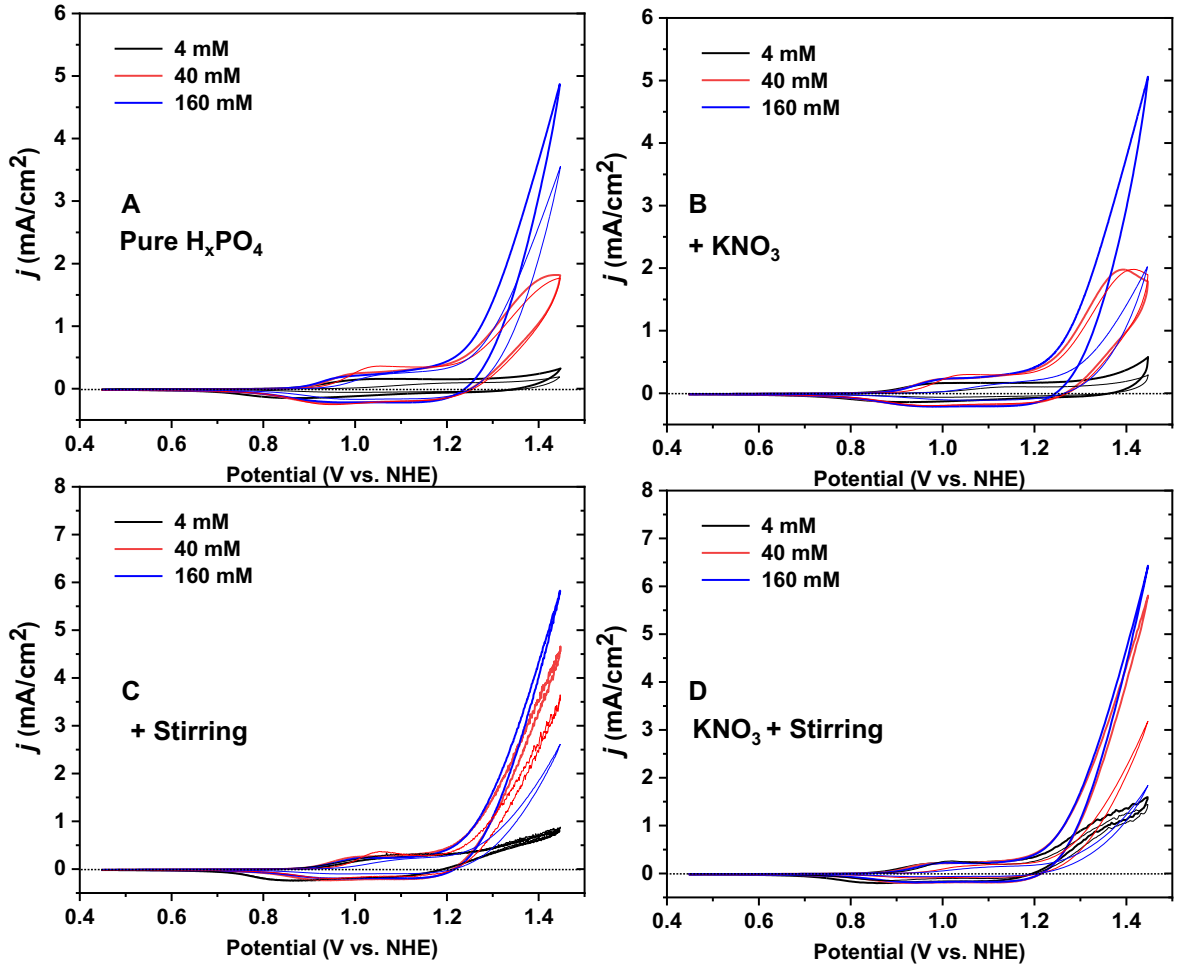

Figure 2-10. Cyclic voltammograms (CVs) measured before (thick lines) and after (thin lines) collection of *j*-V curves for 10 mC cm^{-2} CoCat film operated at indicated KPi concentrations at pH 7 (black:4 mM, red:40 mM, blue:160 mM). Panels A-D show CVs for KPi solutions with or without additional KNO_3 or stirring under otherwise similar conditions as for the data in Figure 2-2. The scan rate was 20 mV s^{-1}. Average currents of the last two CVs are shown, all CVs were corrected for iR drop during the measurements.

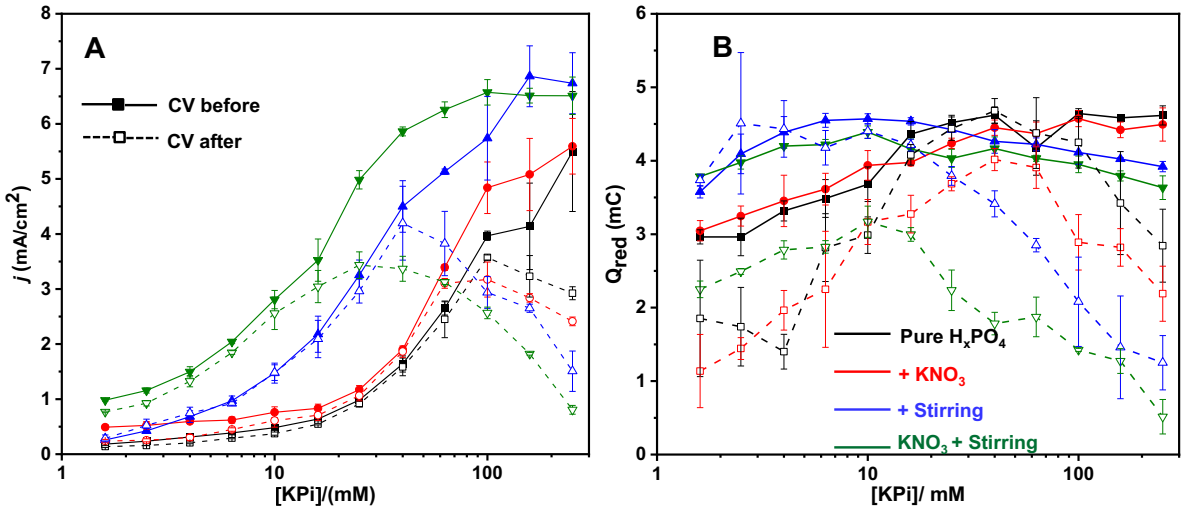

Figure 2-11. (Panel A) Maximum current density (at 1.45 V vs. NHE, pH 7) and calculated charge from CVs of measured before (solid lines) and after (broken lines) collection of *j*-V curves. CVs were measured in the indicated buffer system by using 10 mC cm^{-2} deposited CoCat film at 20 mV s^{-1}. (Panel B) Charges were estimated from the integration of the reductive area of CV curves from three independent experiments. We note that the maximal current density at 1.45 V detected in CVs before and after the *j*-V curve collection often shows a large decrease, which overestimates catalyst degradation during operation seriously. The reason is the sudden potential jump from high potential to low potential *after* completion of the *j*-V data collection, which affects catalyst integrity seriously, as shown in Figure 2-12.

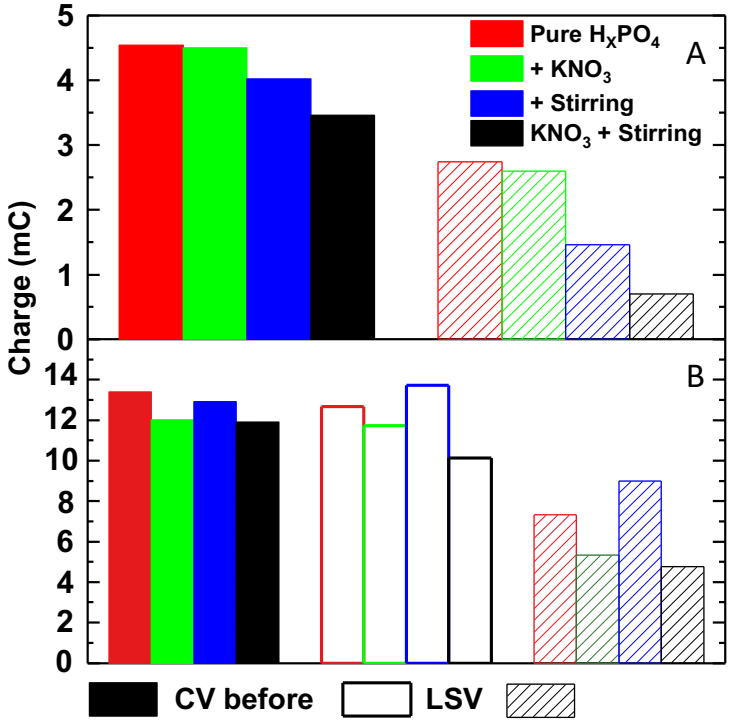

Figure 2-12. Charge estimated from the integration of the reductive area of CV or linear sweep voltammetry (LSV) traces measured in 160 mM KPi in the four different buffer systems. The charges correspond to the amount of redox-active cobalt ions. Panel A shows the integrated charge solely from CVs before and after *j*-V curves collection without LSV. 'CV after' without LSV in panel A shows data

from CVs collected after the ending of the last potential step in the *j*-V curve, meaning after a sudden potential jump from 1.6 V to 0.45 V vs. NHE prior to the start of the last three CVs scans. In panel A, a pronounced loss of charge is visible when comparing CV before and CV after results, which we consider as overestimated. When determining the redox area immediately after the last potential step by using a slow LSV scan (20 mV s^{-1}), in panel B such a pronounced charge loss was not observable, but the integrated charges from CV before and LSV are similar, which means that the large potential jump may cause film dissolution. The calculated charges represent the averaged values from the last two CVs. For panel A 10 mC cm^{-2} films and for panel B, 50 mC cm^{-2} film were used, which accounts for the charge differences in the "CV before" data.

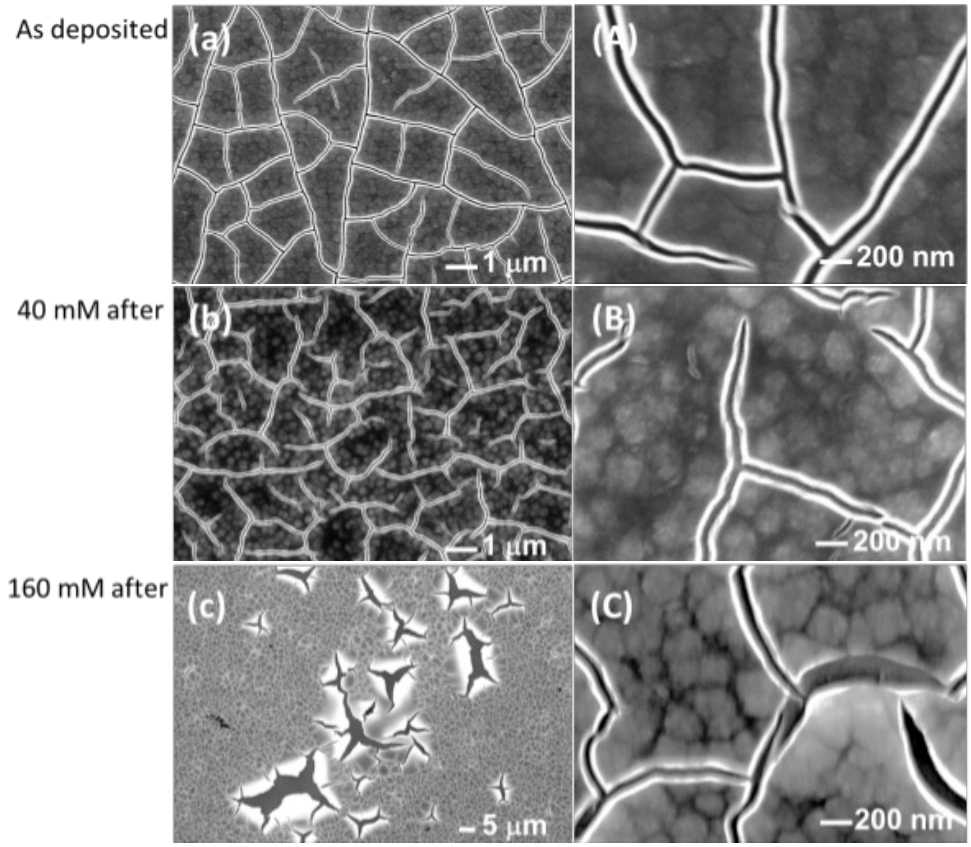

Figure 2-13. SEM comparison of 50 mC cm^{-2} CoCat film as-deposited (a) and after OER operation at 40 mM (b) or 160 mM (c) KPi at pH 7 without adding KNO_3 and without stirring. The corresponding high-resolution pictures are shown on the right side. The cracks resulting from drying of the hydrated CoCat film upon vacuum exposure; the glowing edges of the cracks relate to charge build-up resulting from insufficient electrical conductivity. For operation at 160 mM, fractions of the CoCat film become detached from the electrode, as clearly visible in panel (c). Otherwise, major morphological differences are not detected when comparing the as-deposited electrode film (a) and the film after electrochemical operation (b-c).

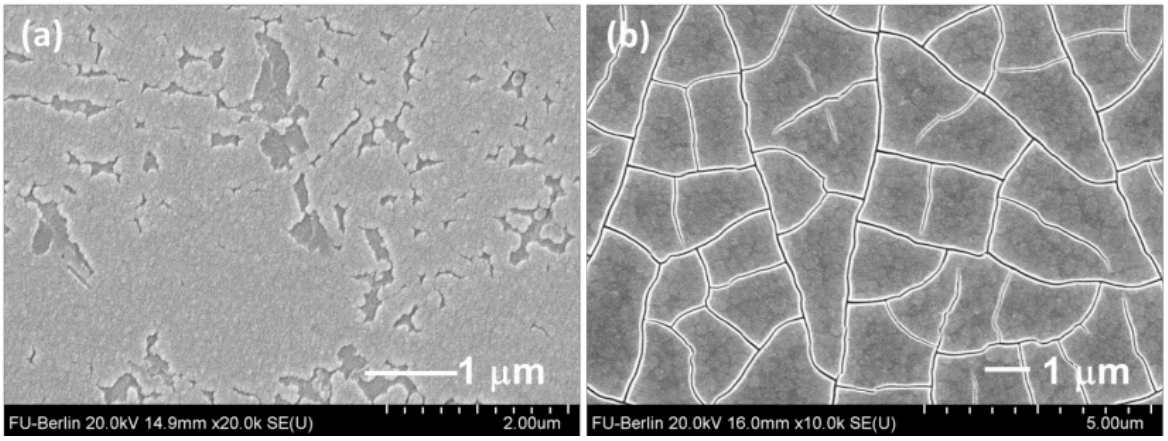

Figure 2-14. SEM of 10 mC cm^{-2} CoCat film (a) or 50 mC cm^{-2} CoCat film (b) deposited on ITO substrate at 1.05 V vs. NHE. The left sample was sputtered with gold coating before SEM characterization due to a lower conductivity for the low contents of CoCat. Note: two types of ITO substrates were used, the left is ITO coated on 1.1 mm thickness soda lime float glass, and the right is ITO on coverslip glass with 0.13–0.16 mm thickness. There are no indications that a potassium phosphate overlayer is formed. A denser electrode surface is observed for thicker CoCat film.

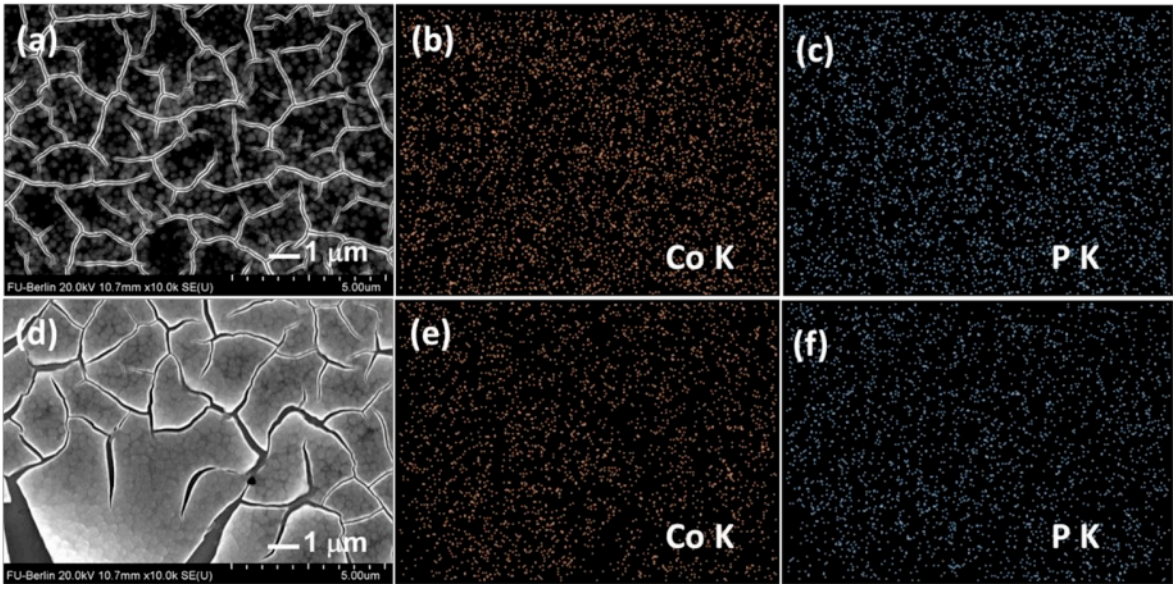

Figure 2-15. SEM image and elemental mapping of 50 mC cm^{-2} CoCat film after operation at 40 mM (a, b, c) or 160 mM (d, e, f) KPi without adding KNO_3 and without stirring. Potassium (K) determination is unreliable due to the interference of indium within the ITO glass. For operation at 160 mM, fractions of the CoCat film become detached from the electrode, as clearly visible in panel (d). Otherwise, major differences are not detected when comparing the as-deposited electrode film and the film after electrochemical operation.

2.2.2 Proton acceptor depletion revealed by FEXAV

In Figure 2-5B, we observed a first-order dependence of the plateau current density on KPi concentration between 1.25 V and 1.4 V (vs. NHE), suggesting that proton transport limitations arise from the availability of buffer base.[99] At higher potentials, assuming that the proton acceptor of the KPi buffer is depleted near the catalyst surface, water becomes effective as an

additional proton acceptor. Here, we verified the depletion of the KPi buffer base by combining CV with operando XAS experiments. By fixing the X-ray excitation energy, called fixed energy X-ray absorption voltammetry (FEXAV), it is possible to follow the dynamic redox process during the CV.[315;340] Figure 2-16 illustrates the rationale of the experimental approach. Typically, the absorbing metal atoms are oxidized progressively with increasing potential, resulting in a shift of the XANES edge to higher X-ray energies. At a fixed incident X-ray energy, oxidizing processes correspond to a decrease in fluorescence intensity, while reducing processes correspond to an increase in fluorescence intensity. To a good approximation, the changes in the X-ray fluorescence intensity are proportional to the extent of oxidation (intensity decrease) or reduction (intensity increase) of the Co ions.[315] By calculating the first-order time derivative of the X-ray fluorescence recorded during a CV, we can extract information about the oxidation state dynamics and distinguish redox currents from catalytic currents or other processes. Here, the FEXAV experiment was performed at a fixed X-ray excitation energy (7722 eV) with five consecutive CV acquisitions at a scan rate of 10 mVs^{-1}. The same broad potential regime as the *j*-V curve (Figure 2-2) was chosen (Figure 2-17).

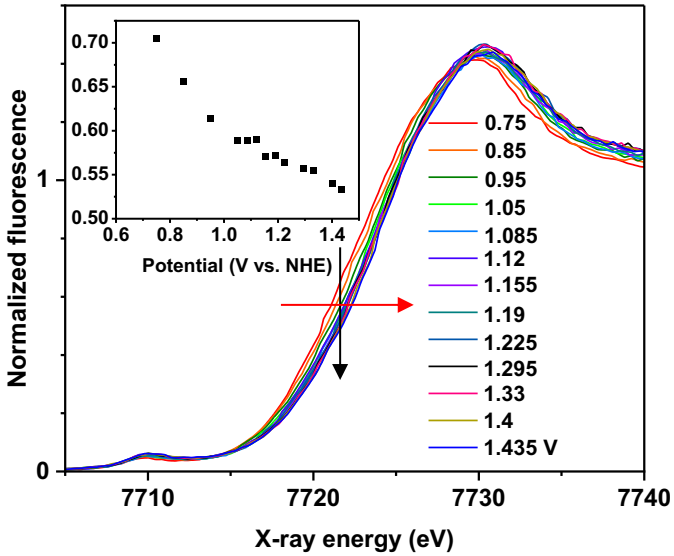

Figure 2-16. Schematic diagram of the FEXRV experiment. The main panel shows the XANES spectra of CoCat in KPi solution (pH 9, 0.1 M) at different electrode potentials. Inset: at a fixed X-ray excitation energy of 7722 eV, X-ray fluorescence decreases with increasing potential (black arrows) while the edge shifts (red arrow) toward higher X-ray energies. The decrease in the X-ray fluorescence for excitation at 7722 eV is proportional, to a good approximation, to the changes in the Co oxidation state.[315]

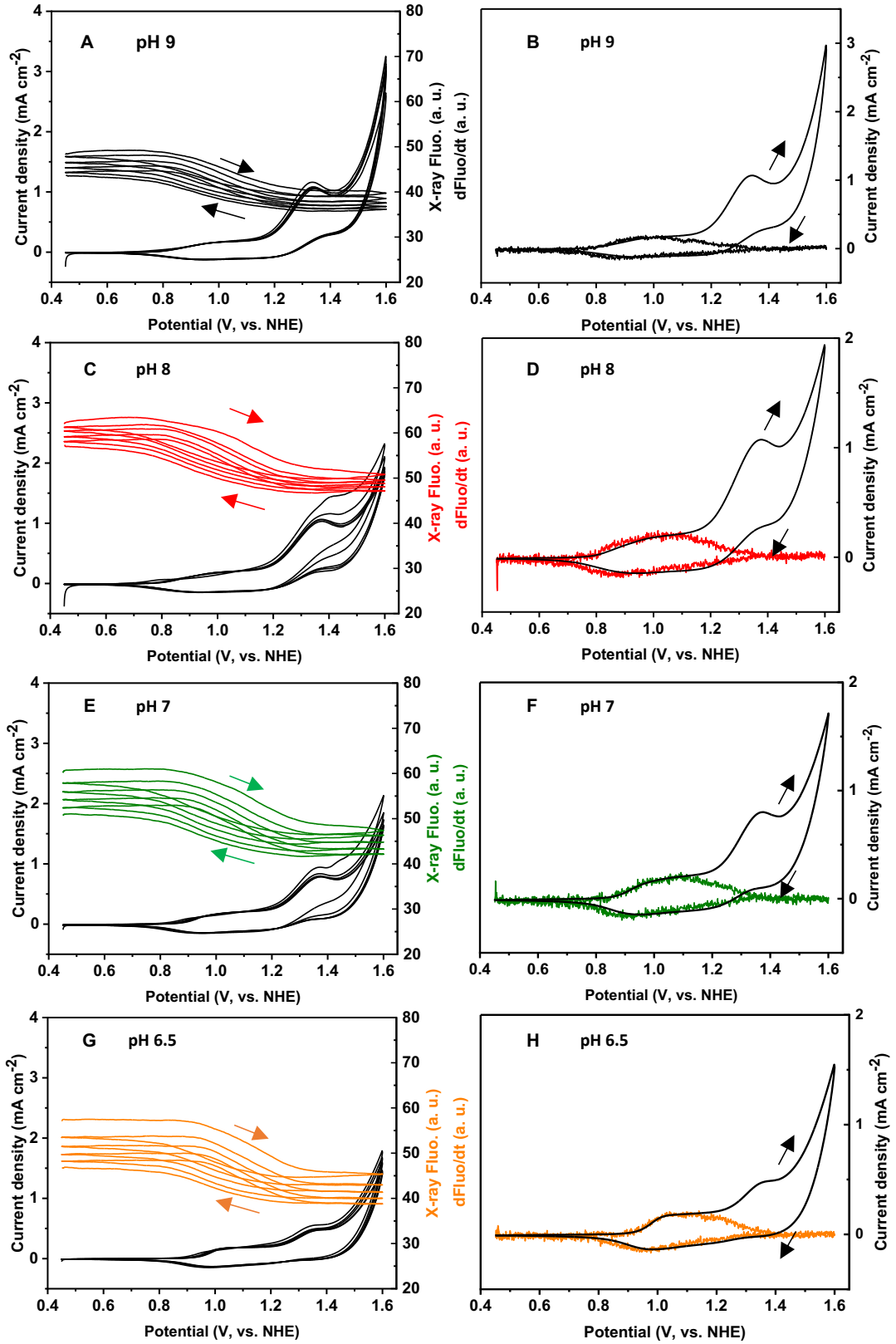

Figure 2-17. X-ray fluorescence at Co K-edge measured at fixed 7722 eV excitation energy (left column) and the corresponding derivative of fluorescence (vs. time) (right column) during cyclic voltammograms (CVs) at various pH of KPi. CoCat catalyst deposited on the graphene sheet, five CVs continuously measured at 25 mM KPi with the addition of 500 mM KNO_3. CVs at a scan rate of 10 mV s^{-1} (black) and the X-ray fluorescence intensity (colored) were in real-time recorded. The arrow

signs the scan direction. Data was shown after smoothing using a moving average method in a 51 data points window with a time resolution of 10 ms. The right column shows the average of the last four cycles. For the sake of clarity, the dFluo axis was scaled to distinguish redox current and catalytic current. The applied potential was corrected for the iR drop.

Impressively, when CoCat was operated in 25 mM KPi buffer at different pHs (Figure 2-17), all CVs showed two broad peaks, while only the first broad peak was attributed to cobalt redox transition processes involving $Co^{II} \rightarrow Co^{III}/Co^{III} \rightarrow Co^{IV}$.[126] The evidence comes from the low-potential region, where the CV curve overlaps completely with the derivative fluorescence trace. This is further confirmed by the disappearance of the second peak of CV measured at a KPi buffer concentration of 100 mM (Figure 2-18). The region where the second broad peak occurs (1.2 to 1.4 V vs. NHE) almost coincides with the plateau region of the *j*-V curve in Figure 2-2, which further suggests a lack of proton receptors. In addition, neither the absolute fluorescence (left column) nor the time trajectory of the derivative fluorescence (right column) changes significantly during the second peak potential interval, suggesting that it is not related to the cobalt redox transition process. Although increasing pH suggests an increase of buffer base concentration, a second peak is still observed(Figure 2-17), suggesting that the buffering capacity is inefficient and a higher concentration of proton acceptors is required to mitigate local proton accumulation.

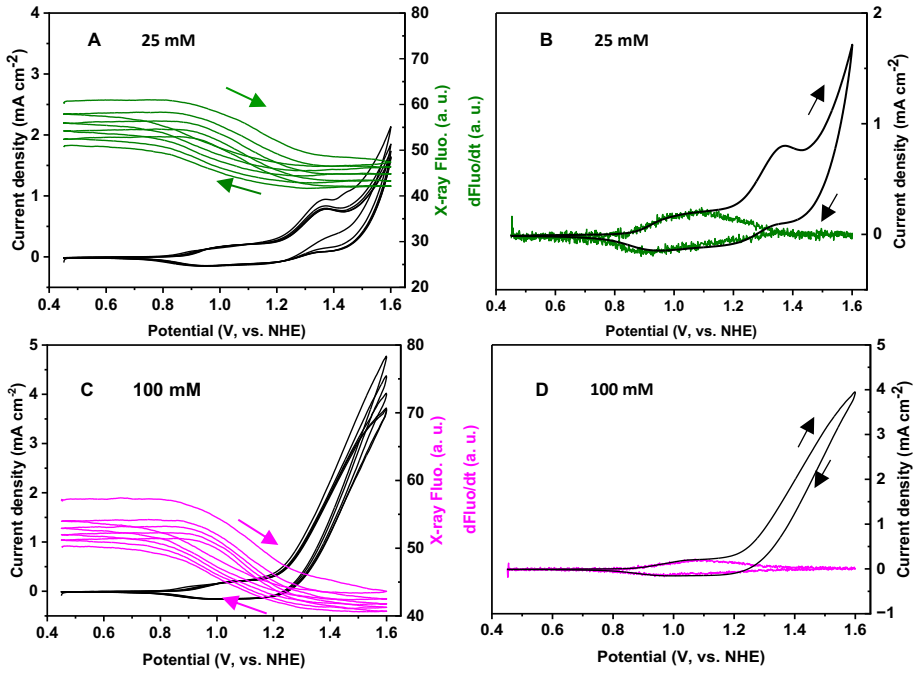

Figure 2-18. X-ray fluorescence (left column) and the first-order derivative of fluorescence (right column) at Co K-edge (left column) were recorded at a fixed excitation energy (7722 eV) in cyclic voltammograms (CVs). KNO_3 electrolyte salts (500 mM) are added to 25 mM and 100 mM KPi (pH 7). The 25 mM data is from Figure 2-17. See Figure 2-17 for more details.

In conclusion, as a complementary technique, FEXAV enabled us to further verify the ability of KPi buffers to act as proton acceptors for proton transport and to alleviate local acidification.

2.2.3 Structure analysis by operando X-ray absorption spectroscopy

Phosphate and potassium ions are components of CoCat deposited in 100 mM KPi with a Co:K:P stoichiometry of about 2-3:1:1.[70] Specifically, the phosphate ions are often assumed to be functionally relevant, that is, an integral part of the catalyst material.[71] It indeed has been shown that phosphate ions can affect the atomic structure of the catalyst significantly.[122;123;130;168;170] With our present *j*-V curves measured at various phosphate concentrations (Figure 2-2), it is plausible that structural changes result from operation in low-phosphate or phosphate-free electrolyte (via phosphate depletion); we thus explored this possibility by employing operando X-ray absorption spectroscopy (XAS) at the Co K-edge to analyse the X-ray edge region and the extended X-ray absorption fine-structure (EXAFS) spectrum.

CoCat films (20 mC cm^{-2}) deposited on glassy carbon substrate (0.1 mm thick) were operated at four selected KPi conditions at pH 7 with low, medium, or high phosphate buffer concentrations (1.6 mM, 25 mM, or 100 mM) or without KPi; KNO_3 salt was added to maintain an approximately constant ionic strength of 0.5-0.8 M in all experiments. After equilibration at 0.75 V, 1.15 V, or 1.33 V (vs. NHE, pH 7; see details in experimental section 2.4.3), EXAFS spectra were collected at the respective electric potentials. The electrode potentials were selected such that the complete range of accessible oxidation states of the CoCat material is covered, with the most reduced $Co^{II}Co^{III}$ state at 0.75 V, the all-Co^{III} state at 1.15 V, and a highly oxidized $Co^{III,\,IV}$ state at 1.33 V.[126] The resulting spectra are shown in Figure 2-19 and Figure 2-20. Edge spectra and complete EXAFS spectra were recorded at room temperature within only 5 min at a low-flux bending-magnet beamline (ca. 10^{10} photons per s at the Co K-edge) with an extended irradiated sample area (about 5 mm^2). Under these experimental conditions, the X-ray dose per area is especially low, which prevents sample modifications from X-ray irradiation (radiation damage), as also verified in ref.[315] for the same CoCat electrode films. Further details are provided in the experimental section.

Analysis of the X-ray edge spectra resulted in estimates of the Co oxidation states (Table 2-2), which ranged from the mixed-valent $Co^{II}_{0.4}Co^{III}_{0.6}$ state (at 0.75 V) via the all-Co^{III} state (at 1.15 V) to the mixed valent $Co^{III}_{0.85}Co^{IV}_{0.15}$ state (at 1.33 V), in good agreement with previous results.[126;134] These oxidation state estimates are, within the limits of accuracy, independent of the KPi concentration.

In the Fourier-transformed EXAFS spectra, the two main peaks correspond to the oxygen ligands in the first Co coordination sphere (Co–O bonds of ~1.9 Å), and the Co ions in the second coordination sphere of the X-ray absorbing Co atom (Co–Co distance of ~2.8 Å), respectively. The amplitudes of these two peaks reflect the abundance of the respective Co-O and Co-Co motifs in the catalyst film.

Based on analysis of the EXAFS data in Figure 2-19, we conclude:

(i) Taking the noise level into account, comparing the amplitudes of Co-O and Co-Co at different phosphate concentrations, there exists a negligible distinction between spectra collected at the same potential. Therefore, we conclude that structural changes are invalid for CoCat operated in various KPi concentrations.

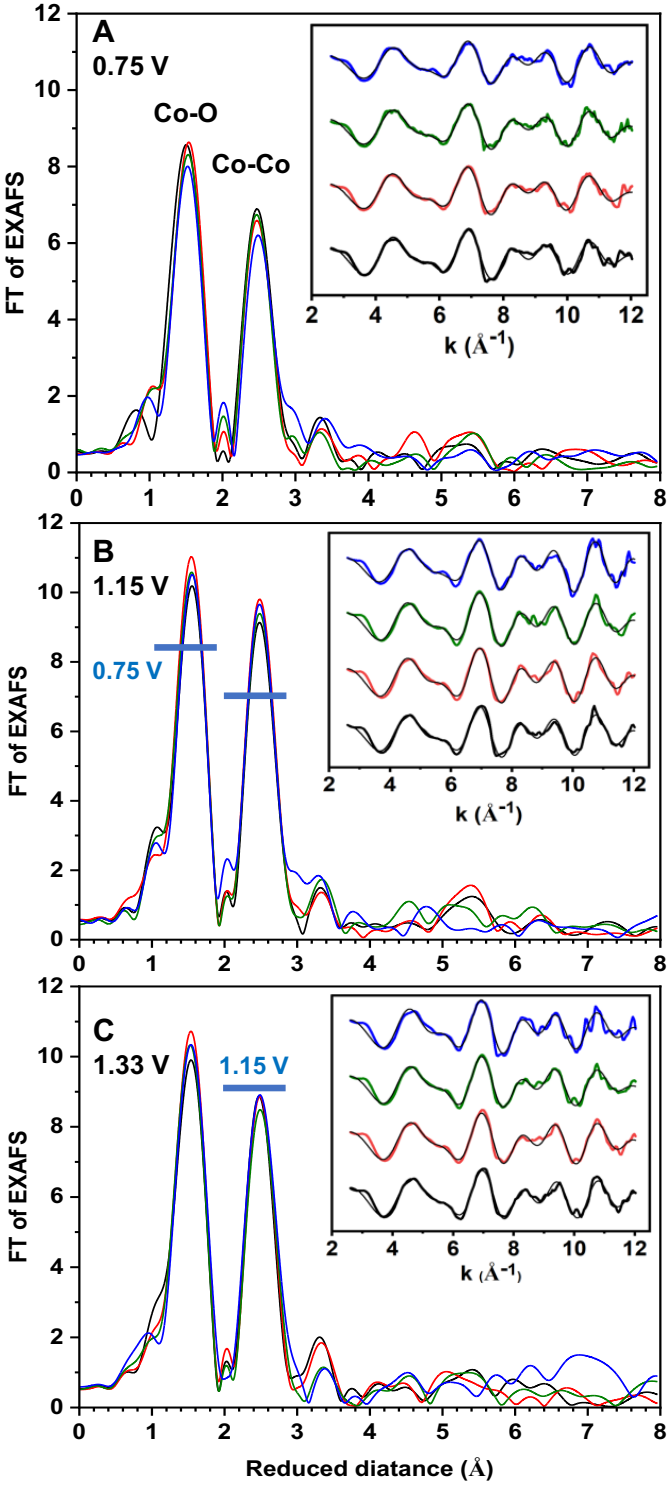

Figure 2-19. In situ EXAFS spectra at the Co K-edge at different phosphate buffer concentrations during electrochemical operation at 0.75 V (A), 1.15 V (B), or 1.33 V (C) (vs. NHE, pH 7). Fourier-transforms (FTs) of experimental k^3-weighted EXAFS spectra are shown for phosphate buffer (KPi) concentrations of zero (blue), 1.6 mM (green), 25 mM (red), or 100 mM (black). The insets show the k^3-weighted EXAFS data on a wavevector scale (colored lines) as well as the respective least-square simulations (thin black lines). Further details on the EXAFS experiment and data analysis are provided in the experimental section. Reproduced with permission from ref.[142]. Copyright Wiley-VCH (2022).

(ii) The potential dependence of the peak amplitudes is highlighted by horizontal bars in Figure 2-19 and is fully consistent with our previous results.[126] There are no inconsistencies with the previously observed structural changes during the redox transition of cobalt at the herein-selected potentials. Accordingly, the atomic structure and the oxidation state as well as structural changes, which are likely functionally relevant,[126;134] remain unaffected by operation at different phosphate concentrations.

The above conclusions were summarized from visual inspection of EXAFS spectra in Figure 2-19, further quantitative analysis was approached by simulating the k^3-weighted EXAFS spectra (insets of Figure 2-19, Tables 2-3 and 2-4) using two coordination shells (Co-O or Co-Co), leading to three free parameters, i.e., coordination number (N), atomic-pair distance (R), and Debye-Waller parameters (σ). Especially via alternative fixing σ (Table 2-4), the effect of shell coordination number and Debye-Waller parameter on the peak amplitude can be deconvoluted.

The EXAFS simulations reveal that at all phosphate concentrations, the transition from 0.75 V to 1.15 V is associated with (i) a shortening of the mean Co-O bond lengths from 1.90 Å to 1.87 Å, as expected as a result of cobalt oxidation process, (ii) a rise of the first-sphere mean Co-coordination number from 5 to 6, and (iii) increased di-μ-oxo bridging between Co ions. The transition from 1.15 V to 1.33 V is associated with a further shortening of the Co-O bond lengths, in line with Co^{IV} formation, and subtle differences in either the amount or the distance spread of the 2.8 Å EXAFS interactions. A more detailed discussion of the potential-dependent structural changes and their likely mechanistic relevance has been provided elsewhere, based on XAS results for CoCat operation in 100 mM phosphate electrolyte.[126;134] Directly, the same potential-dependent changes in atomic structure are detected at all investigated electrolyte phosphate concentrations. Concerning the mechanistic role of phosphate ions, we thus conclude that redox dynamics of the CoCat material are independent of the electrolyte phosphate concentration during CoCat operation.

Table 2-2. Cobalt K-edge positions and oxidation states (oxid. state) of CoCat films (20 mC cm^{-2}) operated at various KPi concentrations and electrode potentials. Edge positions were determined from the edge spectra by the integral method.[316] The experimental error of the edge positions is around 0.1 eV; the oxidation states were estimated based on a calibration curve obtained for simple cobalt oxides (see ref. [126]).

	0.75 V_{NHE}		1.15 V_{NHE}		1.33 V_{NHE}	
KPi concentration (mM)	Edge position (eV)	Oxid state	Edge position (eV)	Oxid. state	Edge position (eV)	Oxid. state
0	7719.92	2.60	7720.78	2.97	7721.12	3.12
1.6	7719.91	2.60	7720.80	2.98	7721.11	3.12
25	7719.91	2.60	7720.85	3.00	7721.16	3.14
100	7719.93	2.61	7720.77	2.97	7721.18	3.15

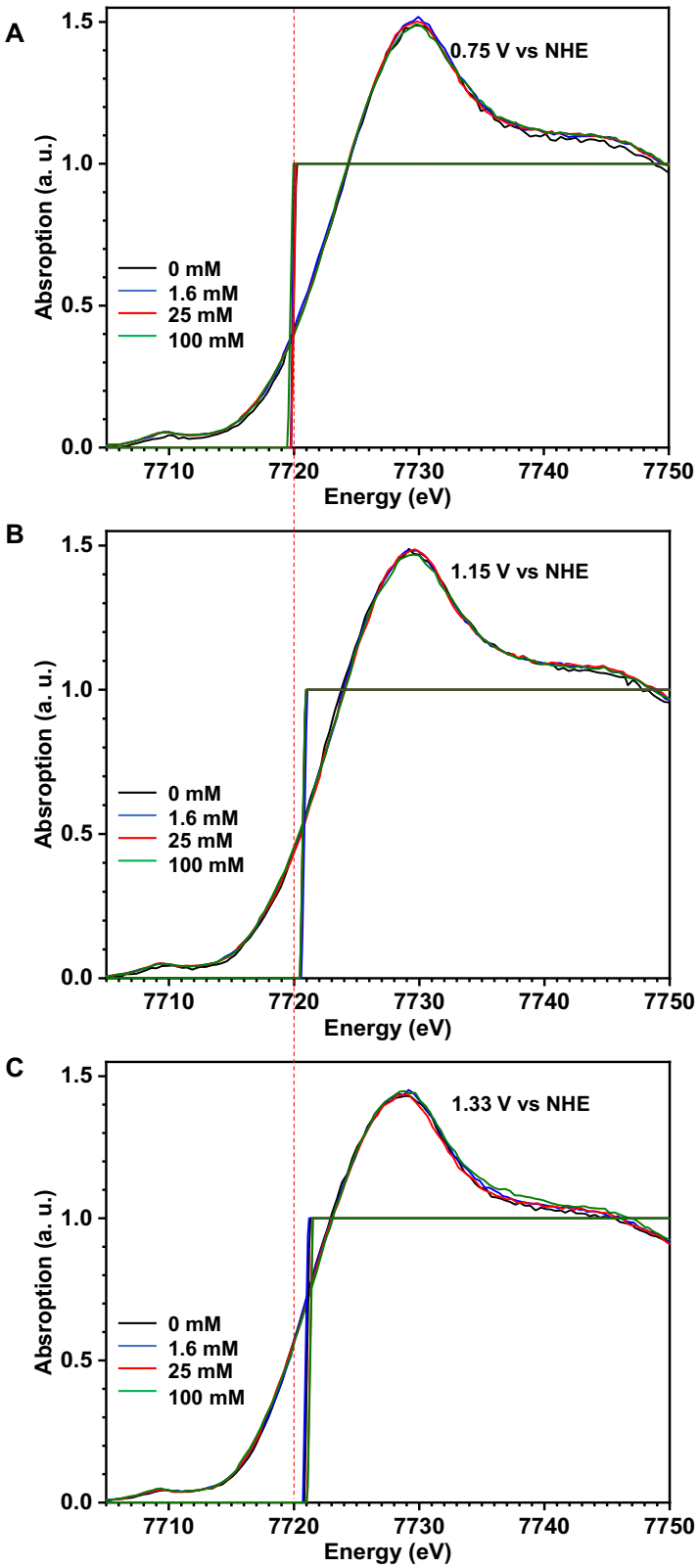

Figure 2-20. Operando Cobalt K-edge X-ray absorption spectra of the CoCat film (20 mC cm^{-2}) at various KPi concentration for (A) 0.75 V, (B) 1.15 V and (C) 1.35 V vs. NHE. The red dashed line located at 7720 eV serves as an eye-guide for identification of potential-dependent edge shifts.

Table 2-3. EXAFS simulation parameters for the CoCat spectra in Figure 2-19. The data range used in the simulations was 20–570 eV (2.3–12.2 $Å^{-1}$). The amplitude reduction factor, S_0^2 was 0.78, as used previously,[123] E_0 was refined to ~ 7710 eV.

KPi concentration (mM)	Potential (V vs. NHE)	Co-O N	Co-O R (Å)	Co-O σ (Å)	Co-Co N	Co-Co R (Å)	Co-Co σ (Å)	R_f (%)
100	0.75	5.5(6)	1.89(1)	0.069(7)	4.5(9)	2.81(1)	0.079(9)	12.6
25		5.0(5)	1.90(1)	0.058(8)	4.0(9)	2.82(1)	0.077(9)	7.9
1.6		5.0(5)	1.90(1)	0.062(8)	3.3(7)	2.82(1)	0.066(0)	8.6
0		4.4(5)	1.89(1)	0.055(9)	2.8(7)	2.82(1)	0.061(12)	11.9
100	1.15	5.8(5)	1.88(1)	0.061(7)	4.5(7)	2.81(1)	0.065(7)	15.2
25		6.1(5)	1.88(1)	0.059(6)	5.0(7)	2.81(1)	0.066(6)	12.4
1.6		6.0(5)	1.88(1)	0.060(6)	5.1(8)	2.81(1)	0.069(6)	13.6
0		5.3(5)	1.89(1)	0.050(7)	2.9(5)	2.81(1)	0.030(17)	11.0
100	1.33	6.4(6)	1.87(1)	0.071(6)	4.1(7)	2.80(1)	0.062(8)	14.6
25		6.0(5)	1.88(1)	0.059(6)	4.3(7)	2.81(1)	0.065(8)	12.8
1.6		5.9(5)	1.87(1)	0.060(6)	5.6(9)	2.82(1)	0.079(7)	11.5
0		6.4(5)	1.88(1)	0.067(6)	5.9(9)	2.81(1)	0.078(6)	16.9

Table 2-4. Alternative simulation of the Co K-edge EXAFS data shown in Figure 2-19. The simulations (fits) differ from that of Table 2-3 by employment of fixed Debye-Waller parameters (σ), which are marked by an asterisk*. The other fit parameters were determined with the same simulation approach as described in Table 2-3.

KPi concentration (mM)	Potential (V vs. NHE)	Co-O N	Co-O R (Å)	Co-O σ (Å)	Co-Co N	Co-Co R (Å)	Co-Co σ (Å)	R_f (%)
100	0.75	5.0(5)	1.89(1)	0.061*	3.4(4)	2.82(1)	0.066*	16.5
25		5.1(5)	1.90(1)	0.061*	3.2(4)	2.82(1)	0.066*	10.7
1.6		4.9(5)	1.90(1)	0.061*	3.2(4)	2.82(1)	0.066*	9.1
0		4.6(5)	1.90(1)	0.061*	3.1(4)	2.82(1)	0.066*	12.3
100	1.15	5.8(5)	1.89(1)	0.061*	4.6(4)	2.81(1)	0.066*	13.8
25		6.3(5)	1.88(1)	0.061*	4.9(4)	2.81(1)	0.066*	11.3
1.6		6.1(4)	1.88(1)	0.061*	4.7(4)	2.81(1)	0.066*	12.7
0		5.9(5)	1.89(1)	0.061*	4.9(4)	2.82(1)	0.066*	16.4
100	1.33	5.7(4)	1.87(1)	0.061*	4.4(4)	2.80(1)	0.066*	14.8
25		6.1(4)	1.88(1)	0.061*	4.4(4)	2.81(1)	0.066*	11.6
1.6		5.9(4)	1.88(1)	0.061*	4.2(4)	2.82(1)	0.066*	13.4
0		5.9(5)	1.89(1)	0.061*	4.6(4)	2.81(1)	0.066*	18.9

2.2.4 Internal phosphate amount

In Figures 2-2 and 2-5B, the first-order electrolyte KPi concentration dependence of the plateau-level current density in the *j*-V curves has been verified. Assuming that proton transfer is facilitated by the diffusion of phosphate ions within the catalyst film as proposed by Bediako et al. is valid,[124] it is expected that the absolute P amount within catalyst film is proportional to the concentration of electrolyte phosphate ions. Accordingly, we investigated the correlation between the amount of phosphate within the catalyst and the concentration of electrolyte phosphate (0, 1.6, 25, 100 mM) for the catalyst operated in sub-catalytic (1.0 V vs. NHE) and catalytic (1.3 V vs. NHE) potentials.

The 'Malachite green' method was applied for phosphorus quantification with a commercially available malachite green phosphate assay kit. The kit comprises three components (reagent A, reagent B and 1 mM phosphate standard). The stock working reagent was prepared by mixing reagent A and reagent B (100:1, v/v) followed by adding to the sample or P standard solutions at a 1:4 v/v ratio. The assay mixtures were incubated for 30 min followed by UV-vis absorption measurement based on the formation of chemical complex between phosphorus and the malachite green phosphate assay kit at 620 nm (90000 $M^{-1}cm^{-1}$).[401] The calibration curve was constructed by using a serial of P standards (Figure 2-22), accordingly, the absolute phosphorous amounts of internal-CoCat samples (Figure 2-21) can be determined by comparing the absorption at 620 nm with the calibration curve.

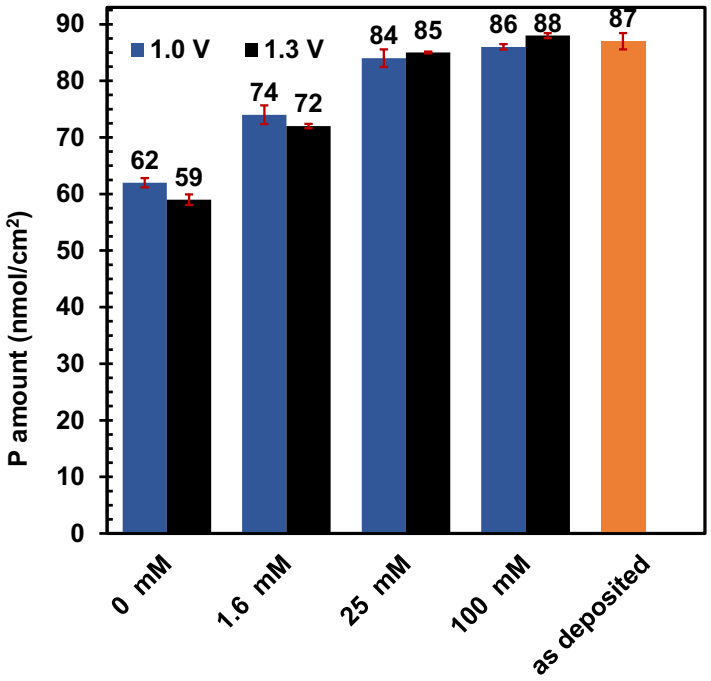

Figure 2-21. Quantification of phosphate amounts within CoCat films at selected KPi concentrations and electrode potentials. The blue and black bars show values from films operated at 1.0 V and 1.3 V vs. NHE, respectively. The phosphate amount in the as-deposited film (deposited in 100 mM KPi) without further electrochemical operation is shown as an orange bar. Reproduced with permission from ref.[142]. Copyright Wiley-VCH (2022).

From Figure 2-21, crucial information is summarized in the following.

(i) As a whole, the internal-phosphate amount has minor dependence on the KPi electrolyte concentration; With an around 62 times increment of electrolyte phosphate concentration, the absolute P amount only increased by less than 1.2-fold; (ii) Potential alteration has negligible influence on inner phosphate amount, implying slow exchange between the inner-catalyst phosphate and bulk phosphate electrolyte.

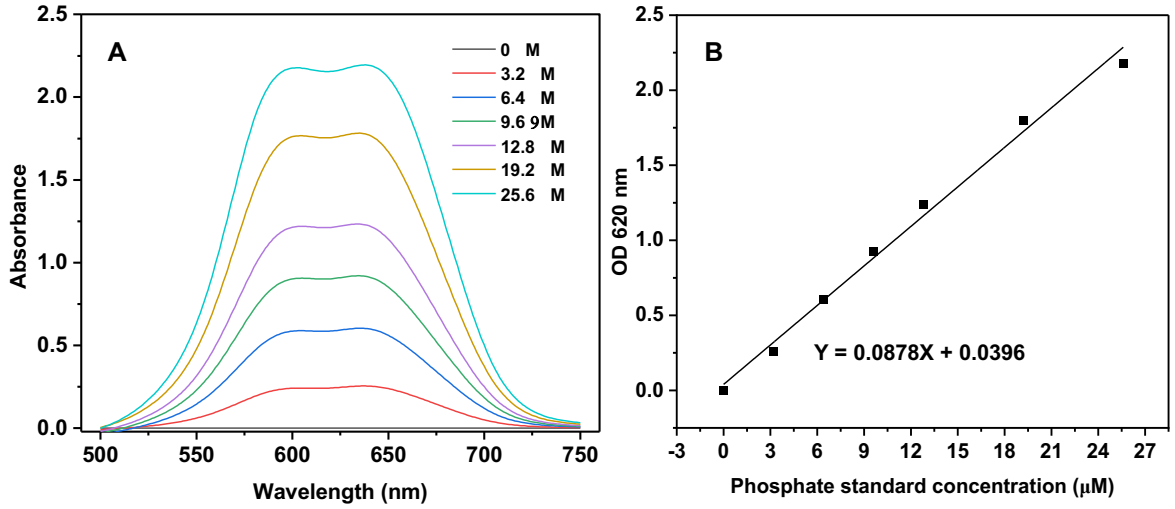

Figure 2-22. (A) UV-vis absorption spectra at various phosphate standard concentrations. (B) Absorption at 620 nm was plotted versus the phosphate concentration. Data points are the mean values of duplicate measurements after incubation of the "malachite green" assay mixture for 30 minutes at room temperature.

The result of Figure 2-21, not only argues against effective exchange of phosphate ions between electrolyte and catalyst material, but also rules out the possibility that the first-order phosphate concentration dependence of current density can be explained by correspondingly increased catalyst-internal phosphate concentrations.

2.2.5 Simulation of j-V curves

The four sets of *j*-V curves in Figure 2-2 were simulated by a model, which describes the influence of macroscopic proton transport in the bulk electrolyte on the current density and is schematically shown in Figure 2-23.

The simulations are based on our earlier description of the effect of buffer molecule-mediated proton transport on catalytic activity,[135] in which we assumed that the proton activity (effective proton concentration) of the inner catalyst film (a_H^{cat}) during steady-state operation of the catalyst operation is equal to that in the boundary layer between catalyst and electrolyte (a_H^{BL}). The total catalytic current at neutral pH is equivalent to the total proton current (J_{BH}) because in an equilibrated, continuously operated electrochemical system, the electron current should be equal to the proton current.

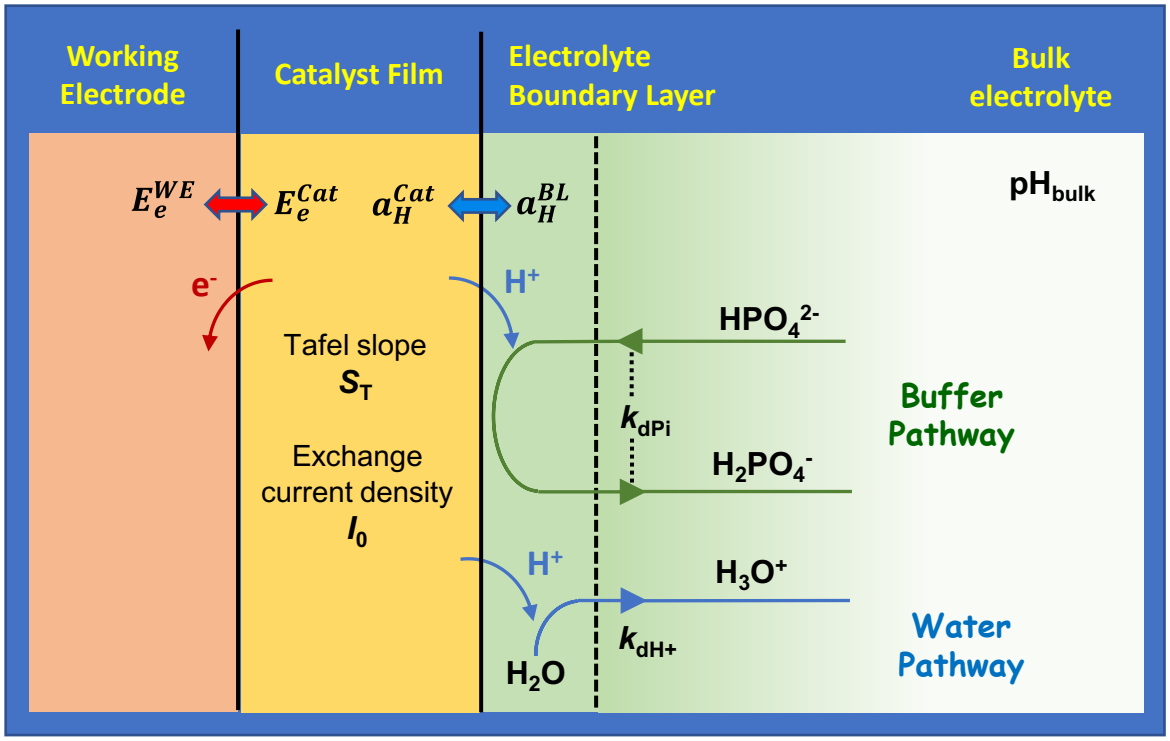

Figure 2-23. Modeling *j*-V curves by considering rate-limiting electrolyte proton transport via both, the buffer-base pathway and the water pathway. It is assumed that in the interior of the catalyst film, electron and proton transfer is fast (not rate-limiting); consequently, electric potential and proton activity do not vary within the catalyst material. Moreover, rapid equilibration of the proton activity between the boundary layer (a_H^{cat}) and the catalyst interior (a_H^{BL}) is assumed so that $a_H^{cat} = a_H^{BL}$. The protons produced during OER are accepted either by a buffer base molecule (HPO_4^{2-}) or a water molecule, where the proton transfer between catalyst film and accepting molecule is not a rate-limiting factor. The parameters S_T and I_0 represent Tafel slope and exchange current density, which describe the catalytic properties of the catalyst material. The diffusion of HPO_4^{2-} and $H_2PO_4^-$ are described by the diffusion constant k_{dPi}; proton diffusion is described by k_{dH+}. These are effective diffusion constants with values that depend on the geometry of the electrochemical cell as well as diffusion accelerating factors (mechanical stirring, possibly further convective flows). All simulations were performed for the experimental pH value ($pH_{bulk} = 7$). Reproduced with permission from ref.[142]. Copyright Wiley-VCH (2022).

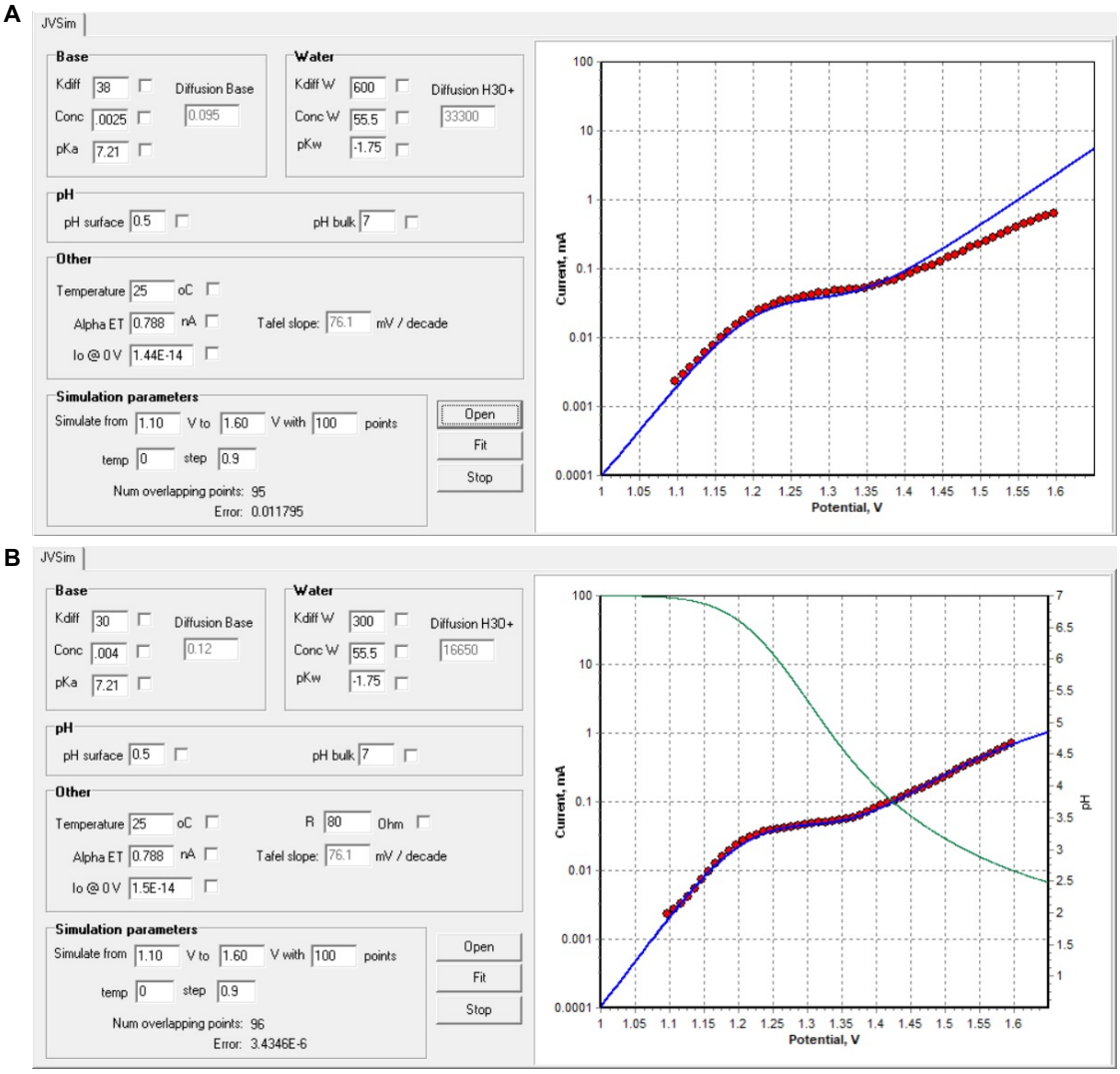

Figure 2-24. Visualization of the software interface for the *j*-V curve simulations with or without R-factor. It consists of five sub-windows. The "simulation parameters" and "pH" windows are fixed. The 'other' window is used to determine the Tafel slope. The "base" and "water windows" consists of the concentrations of KPi or water, and the effective diffusion constants as well as pKa for buffer base and pKw for water. Note that it is constant for the water concentration, pKa and pKw. Panel B adds R term for Ohmic resistance compensation.

The total proton current is obtained by the addition of the buffer base current (J_{base}, protons carried by protonated base molecules) and the 'water current' (J_{water}, protons carried by protonated water molecules, that is, H_3O^+). The following equations are applied in the model:[135]

$$J_{base} = k_{dPi} \cdot C_{Pi} \left[{a_H}/{(K_B + a_H)} - {C_H}/{(K_B + C_H)} \right] \quad \text{Equation 2-2}$$

$$J_{water} = k_{dH^+} \cdot C_W \cdot \left[{a_H}/{(K_W + a_H)} - {C_H}/{(K_W + C_H)} \right] \quad \text{Equation 2-3}$$

$$J_{water} \approx k_{dH^+} \cdot C_W \cdot \left[{(a_H - C_H)}/{K_W} \right] \quad \text{Equation 2-4}$$

$$J_{water} \approx k_{dH^+} \cdot (a_H - C_H) \quad \text{Equation 2-5}$$

Here k_{dPi} is the effective diffusion constant for the phosphate buffer molecule; C_{Pi} is the KPi buffer concentration; a_H is the proton activity within the catalyst and at the catalyst/electrolyte boundary under steady-state conditions; K_B is the acid-base dissociation constant of KPi buffer (pK_B value of 7.21); C_H is the proton concentration in the bulk solution.[135] Equation 2-3 is an adapted version of Equation 2-2[135], written for water instead of buffer molecules. k_{dH+} is the effective diffusion constant for protonated water (for H_3O^+), C_W is the concentration of water (55.5 M) and K_w is the dissociation constant for H_3O^+ ($pK_W = -1.75$).[402;403] The numerical value of K_W is debatable, but mostly a value is assumed that equals C_W. Equation 2-4 is obtained from Equation 2-3, because a_H is much smaller than K_W; Equation 2-5 is obtained from Equation 2-4 because K_W equals C_W. Essentially in the simplified simulation, each set of j-V curves (twelve KPi concentrations) was simulated with fixed k_{dpi} and k_{dH+} but adapted KPi concentrations. A custom-built software was used to fit the four sets of j-V curves (see GUI in Figure 2-24).

For the numerical simulation, a large set of a_H values were generated ranging from 10^{-7} M (pH 7 in the bulk) to $10^{-0.5}$ M (hypothetical extreme pH of 0.5 at the catalyst surface) with those values spaced by a constant factor (equidistant on a logarithmic scale) and 100 points per decade. Using $J_{BH} = J_{base} + J_{water}$ (Equation 2-2 and Equation 2-5), we calculated a set of J_{BH} values corresponding to each value of a_H. Then, for each a_H and J_{BH} couple, the required potential V, (required to 'drive' the current J_{BH}) was calculated, according to Equation 2-6:[135]

$$V = \frac{1}{\alpha} \cdot (k_B T/e) \ln \frac{J_{BH}}{J_0} + (k_B T/e)\, ln\, a_H + R \cdot J_{BH} \quad \text{Equation 2-6}$$

The above equation is based on our earlier quantitative analysis model on proton transport effect[135] plus an additional term on Ohmic resistance factor. The parameter α depends on electrocatalytic properties of the material (catalytic mechanisms and other properties) and is related to the Tafel slope. For example, at 25°C, α equal to 1 corresponds to a Tafel slope of 60 mV per decade, while α equal to 0.5 corresponds to 120 mV dec^{-1}.[404;405] J_0 is the exchange current density and R is the Ohmic resistance (e, elementary charge; k_B, Boltzmann constant; the units of a_H are dropped).

In Figure 2-25, three simulation approaches were employed to simulate the four sets of experimental j-V curves:

(1st) The first simulations involve a minimal set of variable parameters for panels A to D. For each panel, all the twelve j-V curves at the twelve phosphate concentrations were simulated with identical values for I_0, k_{dPi}, and k_{dH+}. The value for k_{dH+} was obtained by fitting the water data that were collected with pure water and adding 500 mM KNO_3 with or without stirring (Figure 2-2 B and D), using a variable k_{dH+} as a fit parameter. To determine the value of k_{dpi}, simulations were performed by varying its value in steps of five, for instance, for determining k_{dpi} for pure H_xPO_4, we tried 20, 25, 30, 35, 45, and the best-fit value was selected according to the lowest error value as reported by the fit program (Figure 2-24) The exchange current density I_0 was fixed to a suitable value that accounted best for all j-V curves (1.44×10^{-14} A cm^{-2}, in all three simulation approaches). Only the value of α was a variable parameter leading to all

the values close to 0.79 (± 0.01), which corresponds to Tafel slopes of 76±1 mV dec^{-1}. For current densities below about 200 µA cm^{-2}, the experimental and simulated curves agree reasonably well. Therefore, we conclude that in the low current regime the rate-limiting effect of the buffer and the water pathway of electrolyte proton transport is well predicted by the model of Figure 2-23. At higher current densities, however a further rate-limitation comes into play, which is the Ohmic resistance (see 2.2.1-*vi*).

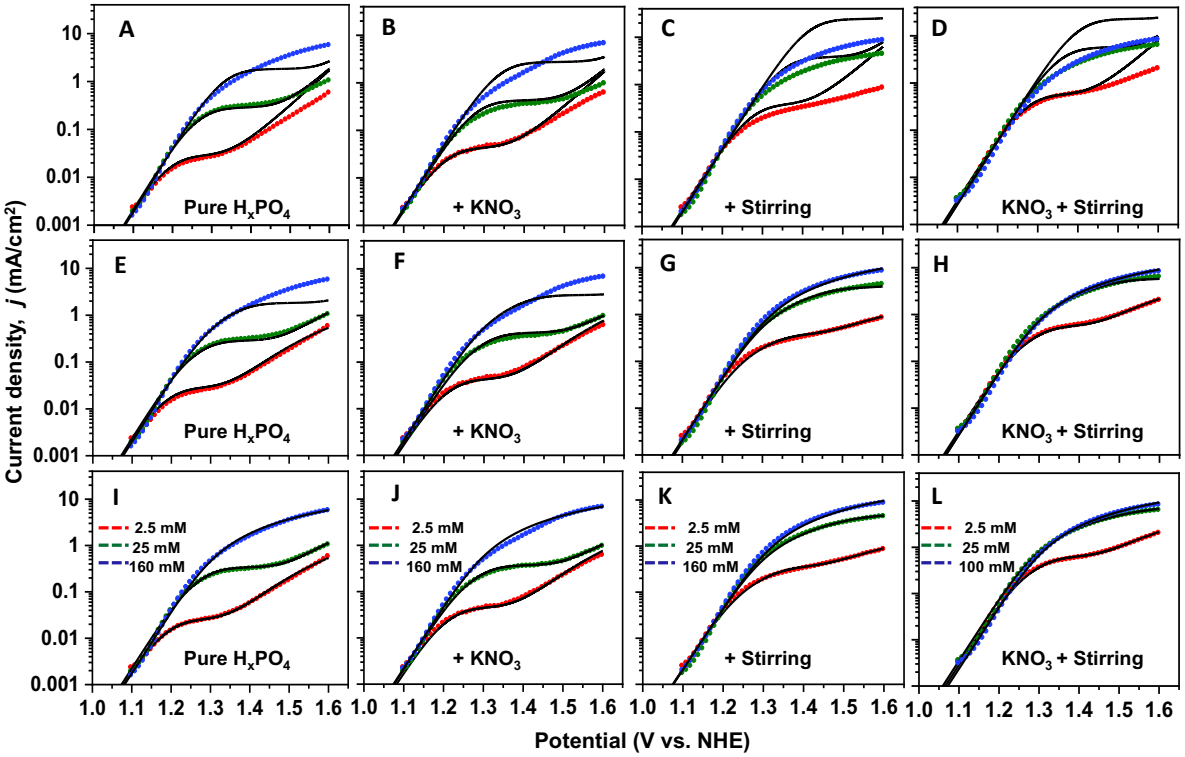

Figure 2-25. Experimental and simulated current densities versus electric potential for the four sets of experimental *j*-V curves of Figure 2-2. We selected for presentation *j*-V curves for low (2.5 mM), intermediate (25 mM) and high (160 mM) potassium phosphate concentration; the complete sets of simulated curves are shown in Figures 2-26 to 2-28 (simulation parameters listed in Tables 2-5 to 2-7). The experimental data is indicated by colored points, the simulated curves are shown as black lines. The left column of panel (A, E, I) relates to the experimental data of Figure 2-2A (pure H_xPO_4); the column with panels B, F, and J relate to Figure 2-2B (+ KNO_3); C, G, and K relate to Figure 2-2C (+ Stirring); D, H, and L relate to Figure 2-2D (+ KNO_3 + Stirring). The first, second, and third row of panels relates to the 1st, 2nd, and 3rd simulation approaches described in the following. Reproduced with permission from ref.[142]. Copyright Wiley-VCH (2022).

Table 2-5. Simulation parameters of *j*-V data for the 1st simulation approach. The simulation approach and meaning of the listed simulation parameters are described further above in the section 'Simulation of *j*-V curves' ('Alpha ET' corresponds to α in Equation 2-6; the Tafel slope is calculated from Alpha ET and was not a simulation parameter). The units of I_0, k_{dpi}, k_{dH+}, and S_T are A cm^{-2}, mA cm^{-1} mol^{-1}, and mV dec^{-1}, respectively.

Data sets	k_{dpi}	k_{dH+}	Alpha ET	I_0	S_T
Pure H_XPO_4	30	300	0.785±0.005	1.44E−14	76
+ KNO_3	45	300	0.785±0.005	1.44E−14	76
+ Stirring	400	5000	0.785±0.005	1.44E−14	76
KNO_3 + Stirring	600	5000	0.785±0.005	1.44E−14	76

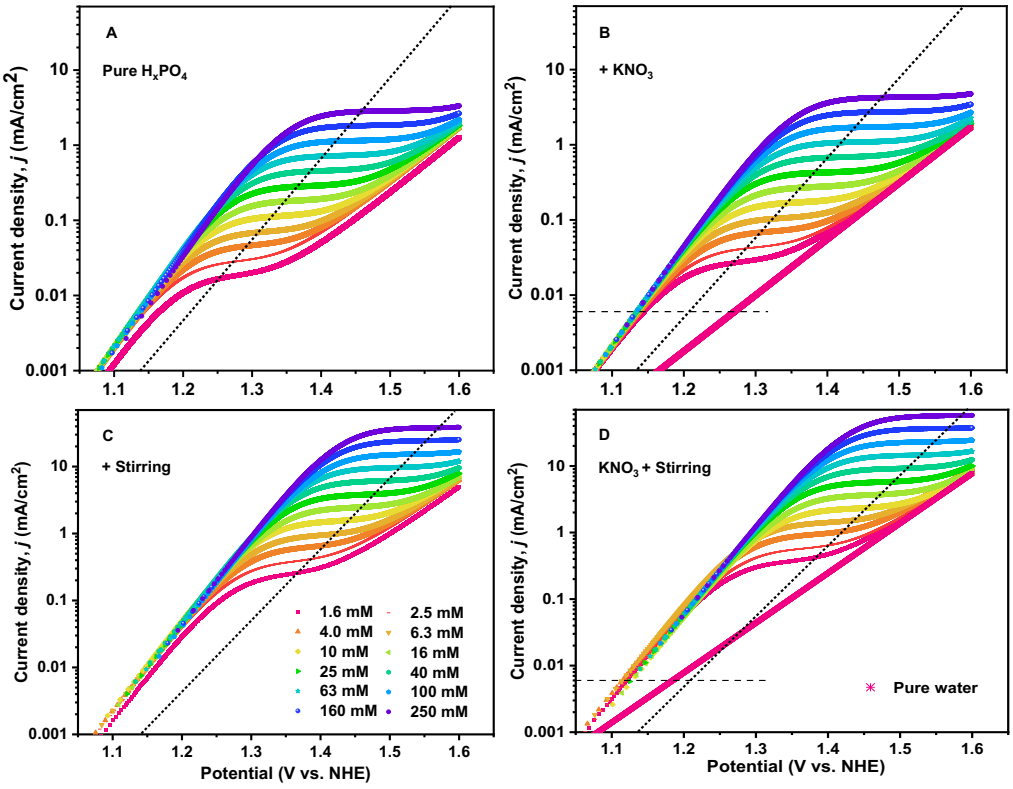

Figure 2-26. Simulated *j*-V curves corresponding to the four experimental data sets from the simplest model (1st). The simulation parameters are shown in Table 2-5.

(2nd) The 2nd simulation approach differs from the 1st one by introducing an Ohmic resistance term, where the resistance value (R) was adapted for each *j*-V curve individually. Excellent agreement is obtained for most *j*-V curves (panels E-H in Figure 2-25). At high current densities (reached at high KPi concentrations), however, the experimental current densities exceeded the simulated curves significantly (see Figure 2-25 E and F), revealing an 'enhancement' effect in the experimental *j*-V curves.

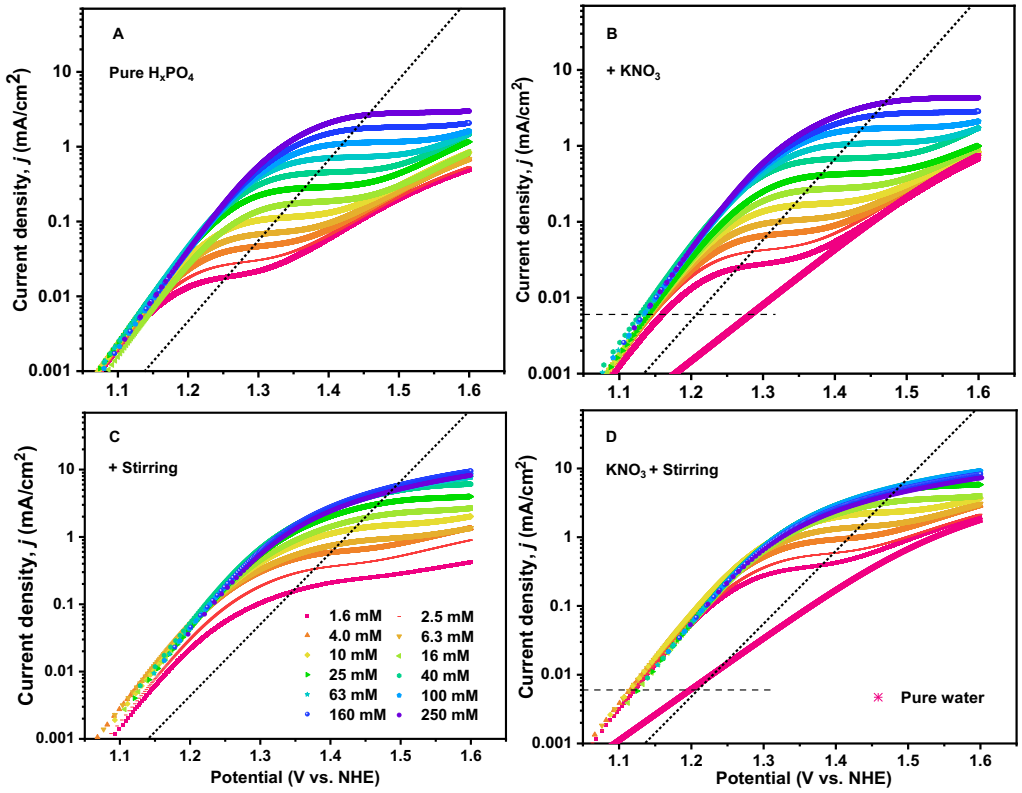

Figure 2-27. Simulated *j*-V curves for adding variable R at different KPi concentrations (2nd). The fitting details are shown in Table 2-6. For panels A and B (static conditions) and panels C and D (stirring conditions), the same effective diffusion coefficients as the 1st simulation approach for KPi and water were used in the simulations (see Table 2-5).

Table 2-6. Simulation parameters of *j*-V data for the 2nd simulation approach. The simulation approach and meaning of the listed simulation parameters are described further above in the section 'Simulation of *j*-V curves' ('Alpha ET' corresponds to α in Equation 2-6). The unit of *R* is Ohm.

KPi conc. (mM)	Pure H_XPO_4		+ KNO_3		+ Stirring		KNO_3 + Stirring	
	R	Alpha ET	*R*	Alpha ET	*R*	Alpha ET	*R*	Alpha ET
1.6	155	0.79	54	0.78	386	0.782	39.6	0.795
2.5	136	0.79	52	0.785	131	0.785	38.3	0.795
4	87.2	0.79	52.9	0.783	83.7	0.793	25.5	0.798
6.3	87.6	0.79	51.4	0.785	93.5	0.786	25	0.798
10	58.8	0.79	48.9	0.785	51.3	0.79	19.9	0.798
16	43.4	0.783	39.7	0.785	41.2	0.789	24	0.792
25	32.4	0.79	39.2	0.785	25.8	0.788	18.7	0.792
40	15.5	0.79	11.1	0.791	20.5	0.791	20.1	0.792
63	20	0.79	15	0.788	23.6	0.788	21.9	0.792
100	20	0.787	15	0.788	23.2	0.788	23.7	0.792
160	20	0.787	20	0.788	21.7	0.788	27.7	0.792
250	15	0.787	17.4	0.788	26.3	0.786	32.8	0.785
Pure water			47.6	0.782			39.6	0.788

(3rd) To provide an approximate description of the enhanced diffusion at high current density, the 3rd simulation approach involved variation of k_{dPi} for individual *j*-V curves (Figure 2-25, panels I-L). Here parameter correlations hamper the determination of *R* and k_{dPi} values severely, especially in the experiments with stirred solutions. We conclude that accelerated diffusion at high current densities is in line with the experimental *j*-V data. Importantly, further investigations in Chapter 5 (section 5.2.3.4) confirm the herein-suggested accelerated diffusion from convective flow investigated by operando Raman spectroscopy. A possible explanation may come from the buoyancy effect, as also reported in ref. [207], for which it contributed to the density difference of the hydrated phosphate ions.

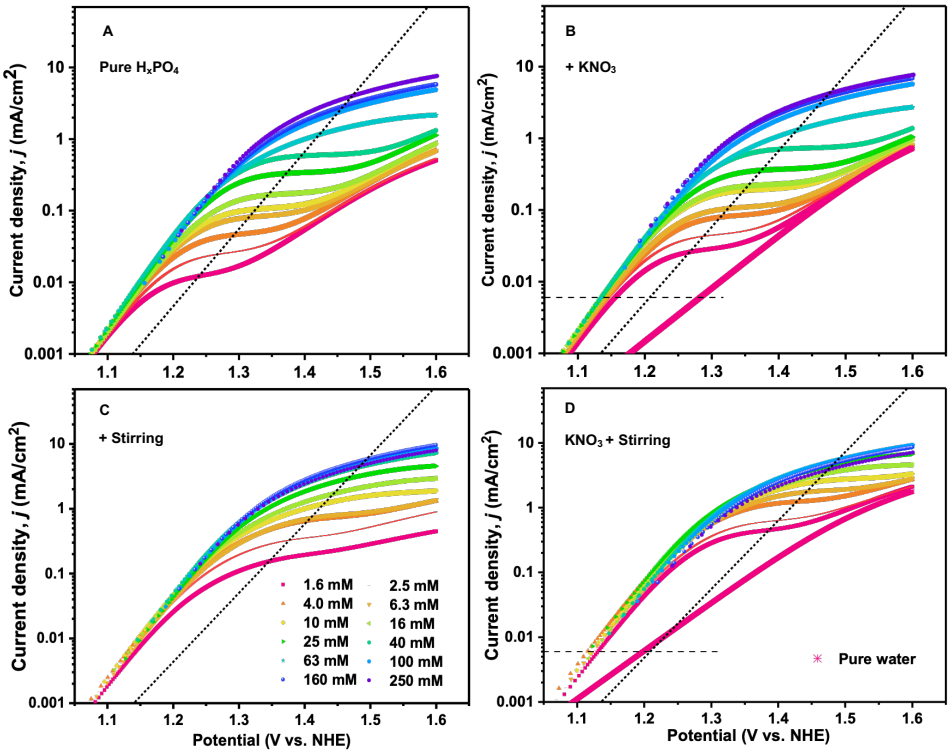

Figure 2-28. Simulated *j*-V curves for variable R and variable k_{dpi} at different KPi concentrations (Figure 2-25 I-L). The fitting details are shown in Table 2-7. For panels A and B (static conditions) and panels C and D (stirring conditions), the same effective diffusion coefficient for water as 1st (2nd) approach was used in the simulations.

Table 2-7. Simulation parameters of *j*-V data for the 3rd simulation approach. The simulation approach and meaning of the listed simulation parameters are described further above in the section 'Simulation of *j*-V curves'. The units of *R* and k_{dpi} are Ohm and mA cm mol^{-1}, respectively.

KPi conc.	Pure H_XPO_4		+ KNO_3		+ Stirring		KNO_3 + Stirring	
(mM)	*R*	k_{dpi}	*R*	k_{dpi}	*R*	k_{dpi}	*R*	k_{dpi}
1.6	141	20.1	54.5	46.3	356	325	33.1	726
2.5	124	26.7	56.2	47.6	139	378	37.1	664
4	82.5	30.4	54.4	53.9	85.9	476	29.8	803
6.3	82.3	35.5	51.6	46.8	79.6	350	29.6	788
10	51.3	28.4	43.9	51	76.9	474	29	742
16	47.9	28.2	39.6	37	58	497	28	750
25	31.1	35.7	38.6	39	33.8	497	26.5	769
40	26.5	39.4	23	48	26.4	642	22.3	779
63	82.4	92.6	75.7	131	27.8	888	23.4	927
100	44.6	276	39	445	25.6	862	23.7	1010
160	38.8	402	33.6	657	22.7	1020	25.5	1240
250	29.2	596	30.2	691	28.8	1600	32.2	1430

With our comparably simple modeling, the experimental *j*-V curves were successively simulated, implying that in our neutral pH system, the crucial proton transport process was mediated by the macroscopic diffusion of buffer ions and water molecules (plus expected Ohmic resistance effects). There is no need to build a more complex model to incorporate various current limiting factors, for instance, internal-catalyst proton or phosphate ions diffusion.[124;128;400] The simulations do not provide any indications that the potentially rate-limiting processes *a*, *b*, and *d* in Figure 2-1 are relevant limiting factors in the here investigated *j*-V curves of CoCat water oxidation at neutral pH. However, we cannot rule out the possibility that additional restrictions in the internal transport of electrons and protons may also play a role in significantly thicker catalyst films.

According to the simplified model, now not only the proton transfer mediated by buffer base pathway and water pathway was verified, but the different characteristics of those two pathways can be clarified. In Figure 2-2 B and D, at high potential (e.g., 1.6 V vs. NHE), in comparison of the current density at high KPi concentration and the pure water, a roughly one order of magnitude difference (15-times in Figure 2-2 B and 6-times in 2-2D or 2-5C) was observed, which was not in line with the expected several orders of magnitude of current improvement for the observed difference in Tafel slope for KPi and pure water condition. We thus further deduced the below equations and found out the distinctly different roles between the buffer base path and the water pathway. The former generates a maximal current density, therefore, leading to a saturated *j*-V curve (Equation 2-7), which is related to the depletion of the unprotonated phosphate base at the anode. In terms of the water pathway, a similar saturation behavior is neither observed nor predicted. Instead, the proton transport limitation results in a strongly increased Tafel slope for the water pathway (See Equation 2-8 to Equation 2-14), which predicts an increase of the catalyst-intrinsic Tafel slope by about 60 mV dec^{-1}.

Equation 2-7 was deduced from Equation 2-2 when considering a_H is clearly greater than K_B, which describes the base pathway of electrolyte proton transport. It predicts an absolute maximum of the current density:

$$J_{base,max} = k_{dPi} \cdot C_{Pi} \left[{K_B}/{(K_B + C_H)} \right] \quad \text{Equation 2-7}$$

In clear contrast, no absolute current limit is predicted for the water pathway, but a pronounced increase of the experimental Tafel slope, as shown in the following.

Equation 2-8 describes the water pathway of electrolyte proton transport. Significant current densities correspond to a situation where a_H is clearly greater than c_H. Accordingly, the adapted Equation 2-8 from Equation 2-5 implies that for the water pathway, as opposed to the base pathway, no absolute current limit is predicted.

$$J_{water} = k_{dH^+} \cdot a_H \quad \text{Equation 2-8}$$

The transformation of Equation 2-8 yields:

$$a_H = \frac{J_{water}}{k_{dH^+}} \quad \text{Equation 2-9}$$

Insertion of the expression for *a*Equation 2-6

$$V = \frac{1}{\alpha} \cdot \frac{k_B T}{e} \ln \frac{J}{J_0} + \frac{k_B T}{e} \, ln \, \frac{J}{k_{dH^+}} \quad \text{Equation 2-10}$$

We emphasize that Equation 2-9 and Equation 2-10 to Equation 2-12 apply to large current densities supported solely by the water pathway of proton transport. In the following, J equals J_{water} and corresponds to J_{BH} in Equation 2-6. Transformation of Equation 2-10 results in:

$$V = \tfrac{1}{\alpha} \cdot \tfrac{k_B T}{e} \ln J + \tfrac{k_B T}{e} \ln J - \tfrac{1}{\alpha} \cdot \tfrac{k_B T}{e} \ln J_0 - \tfrac{k_B T}{e} \ln k_{dH^+} \quad \text{Equation 2-11}$$

$$V = \left(\frac{1}{\alpha} + 1 \right) \cdot \frac{k_B T}{e} \ln J - \left(\frac{1}{\alpha} \cdot \frac{k_B T}{e} \ln J_0 + \frac{k_B T}{e} \ln k_{dH^+} \right) \quad \text{Equation 2-12}$$

Comparison of Equation 2-6 and Equation 2-12 indicates that the intrinsic Tafel slope of the catalyst (in the absence of any transport limitations) increases significantly for sizeable currents supported by the water pathway of electrolyte proton transport and low (or no) current supported by the base pathway. The experimentally detectable Tafel slope (S, in mV per decade) is predicted to increase from

$$S_{intrinsic} = \left(\frac{1}{\alpha} \right) \cdot \frac{k_B T}{e} \cdot \ln 10 \; / \; dec \quad \text{Equation 2-13}$$

$$\text{to } S_{water} = \left(\tfrac{1}{\alpha} + 1 \right) \cdot \tfrac{k_B T}{e} \cdot \ln 10 \; / \; dec \quad \text{Equation 2-14}$$

The Tafel slope is predicted to increase by about 60 mV dec^{-1} ($\frac{k_B T}{e} \cdot \ln 10$ equals 60 mV at 25°C) for dominance of the water pathway, but without any *j*-V curve saturation behavior relating directly to the water pathway of electrolyte proton transport.

In summary, the simple model confirmed that in a neutral pH system, the pivotal proton transport is mediated by the buffer base pathway and water molecules (plus expected Ohmic resistance effects) but features different characteristics. The buffer base pathway results in a saturation-type behavior of the *j*-V curves with an absolute maximal current density, in contrast to the water pathway predicting a strongly increased intrinsic Tafel slope by 60 mV dec^{-1}. The Tafel-slope increase applies to near-neutral OER for sizeable currents supported by the water pathway of electrolyte proton transport and low (or no) current supported by the base pathway. Consequently, the water pathway can outcompete the base pathway at high potentials, but at the price of high energetic losses due to exceedingly high overpotential requirement.

2.2.6 High current densities are achievable

In 2-2, the current densities for the amorphous Cobalt phosphate system with ITO as substrate electrode never exceed 10 mA cm^{-2}. As shown above, current limitations result from both, limited availability of proton-transporting buffer bases as well as the Ohmic resistance of the electrolyte and of the ITO substrate electrode. To reach higher current densities, we replaced the ITO substrate with a Ni foam of negligible Ohmic resistance and increased the amount of deposited CoCat material by a factor of 30 on the metallic foam with roughly 30-fold increased electrochemical surface area (when compared to a planar substrate electrode). Thereby current densities beyond 10 mA cm^{-2} were reached (Figures 2-29 and 2-30).

The experimental *j*-V curves for CoCat film deposited on Ni foam were simulated by using identical k_{dpi} values in the 3rd simulation approach (Table 2-7), resulting in reasonably good simulations (Figure 2-30). This finding shows that neither the increased surface area of the Ni foam nor the increased amount of catalytically active catalyst material modifies the current limitations assignable to macroscopic proton transport by buffer molecules. We observe the same current-limiting mechanisms as identified in the current regime below 10 mA cm^{-2}.

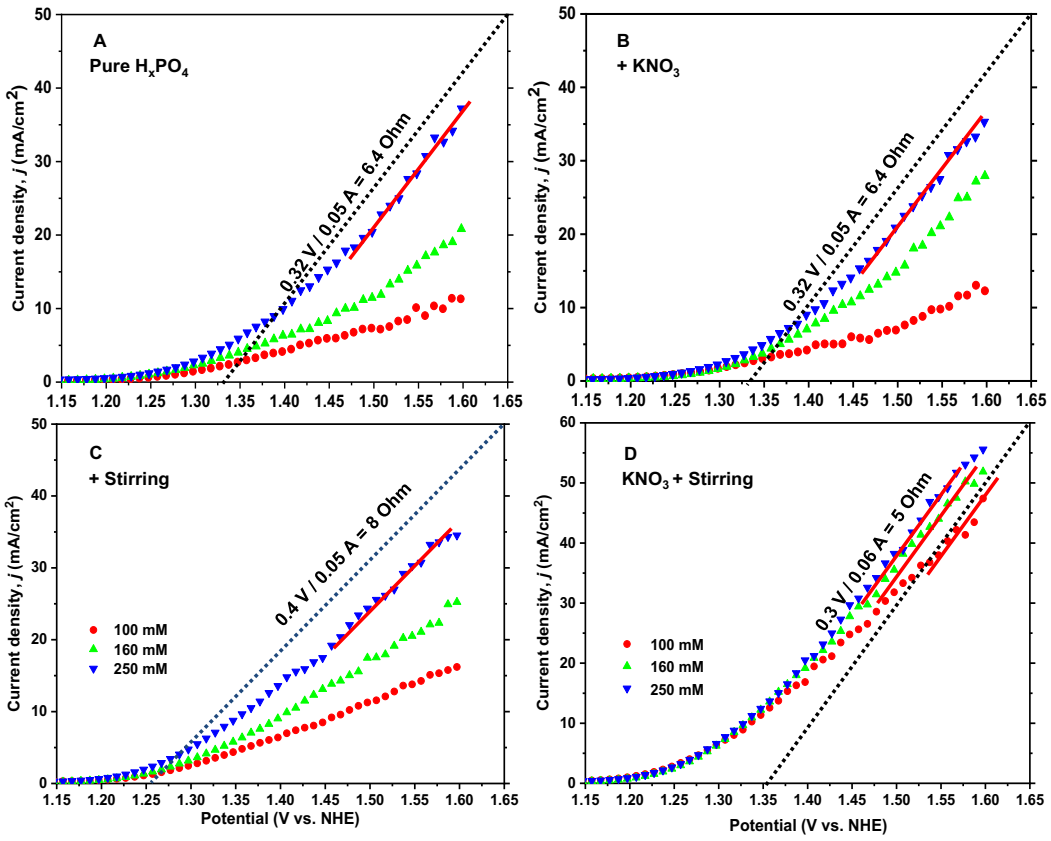

Figure 2-29. Current density (j) on a linear scale versus electrode potential (V) for 300 mC CoCat film deposited on Ni foam operated at various KPi concentrations. The straight lines describe Ohmic resistances (see more details in Figure 2-8). Note that the intercept of the dotted lines in panels C and D is different.

Table 2-8. Simulation parameters of j-V data with variable R and I_0 for the 300 mC CoCat deposited on Ni foam. A fixed k_{dpi} value from Table 2-7 was used and an Alpha ET of 0.769 corresponds to a Tafel slope of 78 mV dec^{-1} and was fixed in the simulation. The units of R, k_{dpi} and I_0 are Ohm, mA cm mol^{-1} and $\times 10^{-13}$ A cm^{-2}, respectively.

KPi conc. (mM)	Pure H_XPO_4			+ KNO_3			+ Stirring			KNO_3 + Stirring		
	R	k_{dpi}	I_0	R	k_{dpi}	I_0	R	k_{dpi}	I_0	R	k_{dpi}	I_0
100	21.3	276	3.66	20.2	445	4.23	15.5	862	4.53	4.44	1010	7.95
160	12.5	402	4.23	8.5	657	2.02	9.5	1020	4.20	4.01	1240	6.92
250	6.52	596	3.41	6.34	691	3.83	7.9	1600	6.96	4.52	1430	7.84

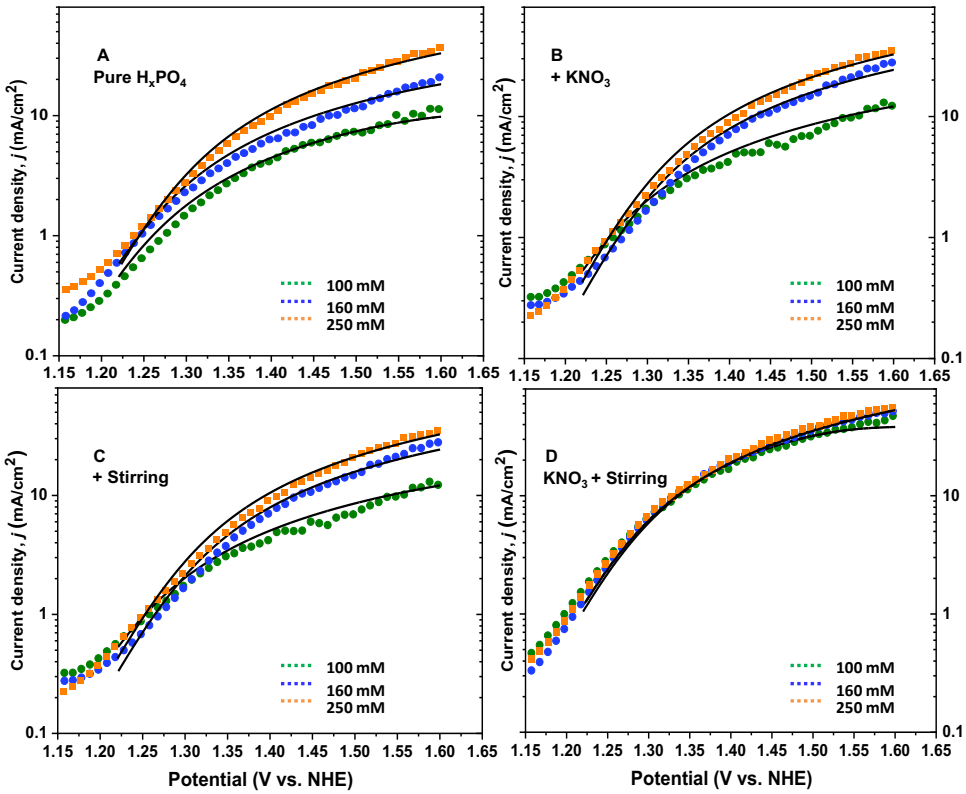

Figure 2-30. Experimental and simulated current densities on a logarithmic scale versus electric potential at indicated KPi concentrations for 300 mC CoCat deposited on Ni foam. The fitting range is from 1.22 V to 1.6 V by using a fixed k_{dpi} value from Table 2-7. Fitted values for R and I_0 are listed in Table 2-8. Simulations are shown as black lines.

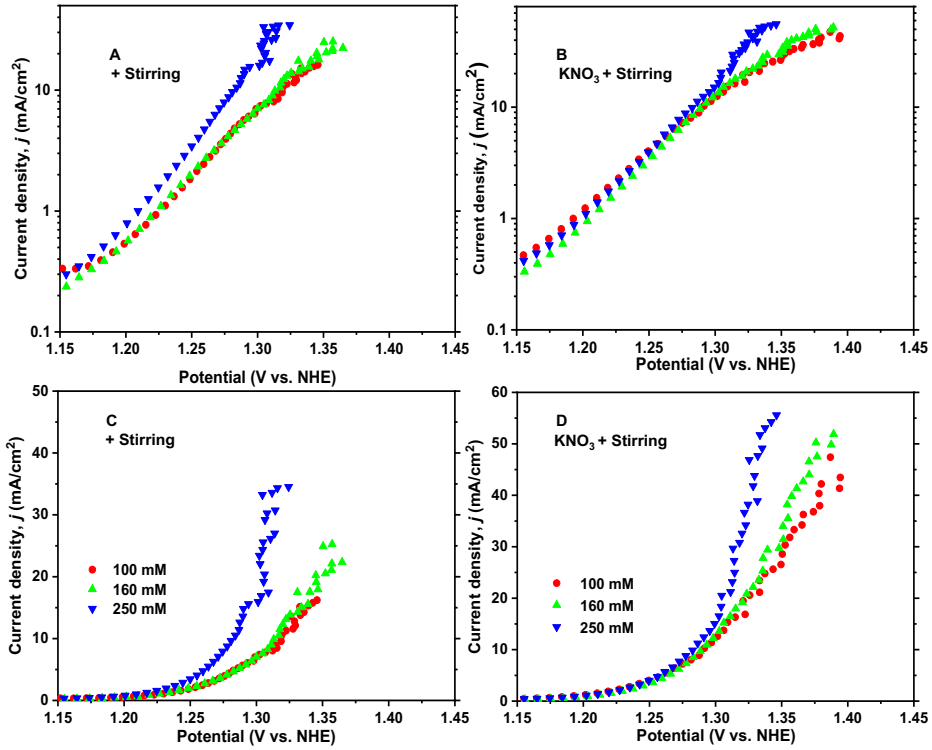

Figure 2-31. Corrected current-densities (*j*) on a logarithmic scale (A, B) or a linear scale (C, D) versus electric potential (V) for 300 mC CoCat film deposited on Ni foam operated at the indicated KPi

concentrations under the stirring condition. The indicated potential axis was derived after correction of the raw potentials according to the expression ($V_{corrected} = V_{app} - iR$). The R value stems from the simulated Ohmic resistance in Table 2-8.

As a proof-of-principle experiment, a three-electrode rapid-flow system was employed to achieve OER current densities well above 1 A cm^{-1} (Figure 2-32). The CoCat was cathodically electro-deposited at 250 mA for 60 s on the Ni-foam in 150 mL de-ionized water with 80 mM methylphosphonic acid and 10 mM $Co^{II}(NO_3)_2 \cdot 6H_2O$ (pH 8.5, adjusted with KOH). The amount of electrodeposited Co ions was estimated after integration of the negative current wave yielding 450 mC; following ref. [99], this corresponds a $Co^{2+/3+}$ deposition charge of about 1500 mC. Thus, the total amount of Co ions was roughly 150 times greater than in the experiments of Figure 2-2. The amount per foam surface area (ECSA) was about 55 mC cm^{-2}, likely corresponding to an increase in CoCat film thickness by a factor of 5-6. It is observed that the here current density reached about 500 mA cm^{-2} at 1.4 V (vs. NHE, pH 7 of the flowing electrolyte with 1 M KPi), which is approximately 250 times greater than the maximal current in the data sets of Figure 2-2B, a similar 'recipe' had been applied in ref.[65]. We note that despite high current densities at five times the catalyst layer thickness (when compared to the catalyst films of Figure 2-2), there is no obvious evidence of incipient catalyst-internal charge transport limitation.

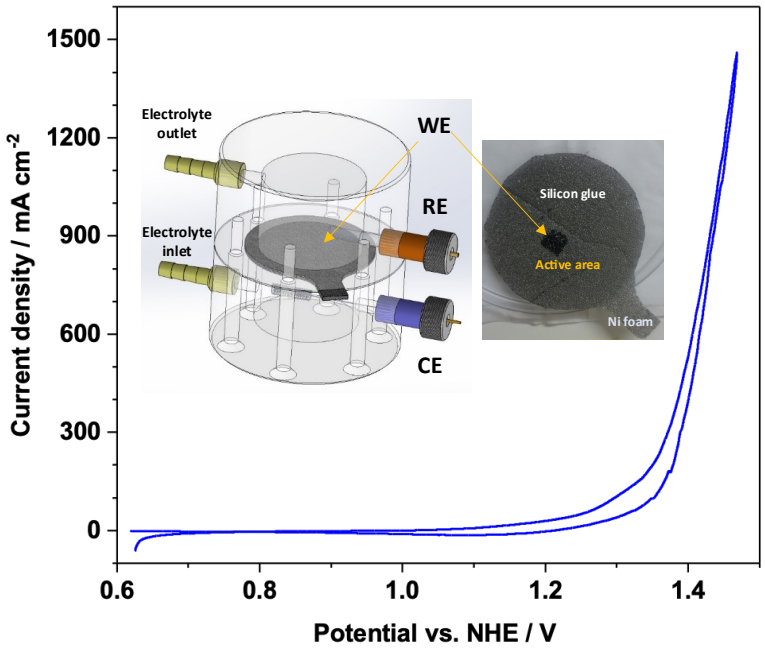

Figure 2-32. Large density achieved for neutral-pH OER in an electrochemical flow cell. A cyclic voltammetry (CV) sweep was performed with a scan rate of 10 mV s^{-1} in 1 M phosphate buffer (KPi) at pH 7.0 (no iR compensation applied). The electrolyte streaming rate in the flow cell was 100 mL min^{-1}. The left inset shows a scheme of the used laboratory-build flow cell with its three-electrode arrangement; the right inset shows a photo of a representative working electrode. In the shown flow cell, the reference electrode (RE) is mounted such that the working electrode (WE) is located between the reference electrode (RE) and counter electrode (CE), thereby ensuring that RE relates to the WE potential without significant *iR*-drop effects. The working electrode (WE) was a

cobalt-oxyhydroxide catalyst (CoCat) film deposited on Ni-foam support (macroscopic geometric area of the catalyst electrode of 0.56 cm^2). The electrochemically active surface (ECSA) of the Ni foam was ca. 27 larger than the ECSA of a planar Ni foil. The black area visible in the right inset corresponds to the active area of the catalyst electrode; the grey material is Ni foam fully masked with silicon glue. A coiled platinum counter electrode (CE, ca. 1.5 cm to WE) and an $Ag/AgCl/NaCl_{3M}$ reference electrode (at ca. 0.5 cm to WE) were used.

As a result, we present a proof-of-principle experiment that does not represent a technical electrolyzer system due to the use of a three-electrode cell with optimized reference electrode positioning. Nonetheless, this experiment demonstrates that by consistently removing the limitations identified here, technically relevant current densities at reasonable overpotential are achievable also in neutral-pH OER.

2.3 Summary

Using volume-active cobalt-based oxyhydroxide films (CoCat) as a model system, electrolyte proton transport was identified as the main rate-limiting factor in the electrochemical water oxidation (OER) process at neutral pH by varying the electrolyte buffer conditions. Comprehensive sets of *j*-V curves are analyzed combined with operando X-ray absorption spectroscopy, elemental analysis and mathematic simulation. We conclude:

(1) *Unaffected structure and function of catalyst at various electrolyte concentrations of KPi.* The variation of oxidation state and structure as a function of electrode potential follows the previous ref.[126]. Similar Tafel slopes essentially verified that the mechanism of neutral water oxidation is independent of the electrolyte phosphate concentration.

(2) *Origin of plateau-level current.* Of the four options for proton transport limitation (Figure 2-1), merely the macroscopic electrolyte proton transport by the $H_2PO_4^-/HPO_4^{2-}$ shuttle explains the first-order phosphate requirement of the maximal (plateau-level) current density (Figures 2-2 and 2-5B). It suggests that macroscopic proton transfer limitation results in the plateau level current in the middle potential regime.

(3) *Electrolyte proton transport* via *base and water pathway.* Two pathways for proton transport between anode and cathode are identified: (i) the $H_2PO_4^-/HPO_4^{2-}$ shuttle and (ii) the water pathway with proton-loading of H_2O molecules followed by H_3O^+ diffusion (see Figure 2-23). The water pathway is technologically irrelevant in OER at neutral pH because it requires extremely high overpotentials. The base pathway causing saturated current is essential for efficient water oxidation at neutral pH or in the near-neutral pH regime, thus optimizing the diffusion of proton-transporting buffer molecules is crucial.

(4) *Ionic conductivity influence.* Aside from a technically irrelevant synergism observed at very low ionic strength, increased electrical conductivity does not enhance the electrolyte proton transport and leads to unaffected catalytic activity (Figures 2-5 A and B).

(5) *Ohmic resistance and enhanced buffer-base diffusion.* Mathematical simulations show that the Ohmic resistance, mainly from the substrate, hinders the enhancement of the catalytic current at high potential (Figure 2-25), whereas additional effects of the bubble effect or the buoyancy effect may affect the macroscopic proton transport of the bulk

electrolyte (see Chapter 5, Section 5.2.3.4 for details).

(6) *Technical electrolysis guidelines*. For efficient neutral water oxidation, high-current operation in the Tafel-slope regime is feasible if not only Ohmic resistance effects but also catalyst-external proton transport limitations are minimized. The limiting factors already come into play in the current region of 5–20 mA cm^{-2}. Yet, a proof-of-principle experiment indicated that current densities exceeding 1 A cm^{-2} can be reached in neutral pH OER for (Figure 2-32):
   (i) high loading of the volume-active catalyst material,
   (ii) avoidance of Ohmic limitations,
   (iii) and accelerated diffusion of proton-transporting buffer molecules.

   Only the third point is a specific requirement for high-current electrocatalysis at neutral pH because of the inefficiency of proton transport via the water pathway in the neutral pH regime. In neutral-pH OER, catalyst-specific performance characteristics (Tafel slopes, exchange current densities) remain relevant overpotential determinants unless reaching the current region of limiting proton transport capacity.

2.4 Experimental details

2.4.1 CoCat electrode film preparation

For a parallel deposition of CoCat, the 10-channel potentiostat system (Gamry) was employed. For each channel, the three-electrode cell consists of ITO (1 cm^2) working electrode, platinum-grid (20 × 20 mm^2) counter electrode, and Ag/AgCl (saturated) reference electrode. CoCat film was deposited in 0.1 M KPi buffer with a cobalt concentration ($Co^{II}(OH_2)_6(NO_3)_2$) of 0.5 mM. The potassium phosphate buffer (KPi) was prepared by mixing ~ 40% 0.1 M KH_2PO_4 and ~ 60% 0.1 M K_2HPO_4. The pH of the KPi was adjusted to 7.0 by adding KH_2PO_4 or K_2HPO_4. A single-compartment static cell was employed to mitigate large pH gradient.[111] Anodic deposition protocol was used for CoCat deposition by applying a constant potential at 1.05 V vs. NHE and the film thickness was controlled by the accumulated charge on the working electrode via chronocoulometry.[134] Note that i*R* drop was not applied because of low current densities (around 5 μA). The deposited film amounts involved in our experiments were 10, 20, 50 or 300 mC cm^{-2}. ITO glass (VisionTek Systems Ltd., 12 to 15 Ohms/square) or glassy carbon (Hochtemperatur-Werkstoffe GmbH) serves as a substrate. All solutions were prepared from purified, deionized water (Milli-Q, >18 MΩ·cm).

Ni foam electrode preparation: commercial Ni foam (JYS Corporation, China, 0.4 g/cm^3, 50 ppi, 1.5 mm thickness) was cut into appropriate electrode sizes (10 mm × 25 mm) followed by cleaning procedures, i.e., sequentially sonicating for 15 min in acetone, ethanol, distilled water, and 5 M hydrochloric acid, after three-time washing with deionized water, dried in an oven at 70 °C for 80 min. For approaching a similar geometric condition with ITO (i.e., a single-faced electrode), one side of Ni foam was covered by a normal glass sheet, and the effective geometrical size of the reverse side of Ni foam was reduced to 10 mm × 10 mm. The remaining area was compressed with fulling epoxy glue and Kapton tape attachment. The Ni foam-based CoCat deposition (300 mC cm^{-2}) was performed using the same procedure as

CoCat deposition on ITO substrates, except that stirring was performed at 600 rpm during deposition process.

2.4.2 Extended Tafel plots and CVs analysis

For the extended *j*-V plots, different KPi concentrations were prepared by appropriate dilution of 0.5 M KPi buffer, and the pH was adjusted to 7.0 by adding KH_2PO_4 or K_2HPO_4 that has the same concentration as the prepared buffer solution. For conditions including additional salt, 500 mM KNO_3 was added to the KPi buffer solution to increase the ionic conductivity. For the measurement of a series of *j*-V curves, the SP-300 potentiostat (BioLogic) was employed with moderate iR compensation near 50%, ensuring stable potentiostat operation over an extended potential and current range. Due to imprecision in the determination of the Ohmic resistance, the precise level of iR compensation may vary between different experiments. Three consecutive cyclic voltammetry scans (CVs) were measured before and after the chronoamperometry steps (CAs), with a scan range from 0.45 V to 1.45 V vs. NHE at a scan rate of 20 mV s^{-1}. For the potential-step experiments, the potential started from 1.1 V vs. NHE, after stabilization for 5 min at the lowest potential and increasing the potential in increments of 10 mV until reaching 1.6 V vs. NHE with each potential step being applied for 1 min. The static current densities were determined by averaging the last 400 data points of each potential step. For the FEXRV experiments, KNO_3 (500 mM) was added to the electrochemical system and compensated for the iR compensation (0.7 V vs. Ag/AgCl, 85% iR compensation, software mode, 10 kHz), and the system was not stirred during the measurements. The FEXRV protocol was initiated with CA at 0.8 V vs. NHE, followed by five CVs (10 mV s^{-1}). The CV scan ranges from 0.45 V to 1.61 V vs. NHE.

2.4.3 X-ray absorption spectroscopy

Operando X-ray absorption spectroscopy (XAS) was measured at the BESSY-II synchrotron (Helmholtz-Center Berlin) at beamline KMC-3 with a laboratory-built Teflon cell. Electrochemistry was operated by using a SP-200 BioLogic potentiostat with 85% i*R* compensation. For a complete EXAFS spectrum collection, samples were exposed to the X-ray beam for ~5 mins at each potential. The incident X-ray beam passing through the glassy carbon substrate (0.1 mm thickness) probed the CoCat film in contact with the electrolyte at room temperature. An energy-resolving 13-element silicon-drift detector (SDD) was used to record the X-ray fluorescence at the Co K-edge. For the energy calibration of operando experiment, XAS spectrum of cobalt foil was frequently measured, and its inflection point at 7709 eV was chosen as energy reference for calibrating the monochromator energy axis.[112] A further fine energy calibration was performed by aligning the center position of the derivative of pre-edge spectrum, where the corresponding X-ray energy position is independent of the change of the Co oxidation state.[316] The corresponding edge positions (edge energies) were determined by the integral method described in ref.[316]. The edge position is converted into oxidation state via a calibration curve obtained from the known oxidation state of cobalt compounds.[126;316] Fourier-transformation (FT) of the EXAFS oscillations included a cosine window function extending over 10% at both k-range ends (2.3-12.2 $Å^{-1}$). k^3-weighted EXAFS spectra and phase

functions calculated with FEFF10[406;407] were used for simulations. All simulations were conducted by using in-house software, facilitating least-square fits for the determination of structural parameters. For further technical details see refs[126;316]. For extended CVs, X-ray fluorescence was simultaneously tracked at fixed X-ray energy of 7722 eV during CVs. The fluorescence signal was normalized by the initial incoming X-ray beam intensity (I_0) followed by a smoothing average of 51 pts. The derivative of the time trace of fluorescence was calculated followed by averaging the last four cycles of CV.

2.4.4 Phosphate quantification by the malachite green method

The malachite green method supports a highly sensitive P concentration detection ranging from 0.02 to 40 μM. The rationale is the formation of a green complex featuring a high molar absorption coefficient (90,000 $M^{-1}cm^{-1}$)[401] after a complexation reaction between malachite green, molybdate, and free orthophosphate under acidic conditions. P quantification with the malachite green phosphate assay kit MAK307 from Sigma-Aldrich (reagent A, reagent B, and 1 mM phosphate standard) was achieved via spectrophotometric determination of the amount of the formed chemical complex at 620 nm. A calibration curve was derived from a series of P standard solutions (200 μL of working solution was mixed with 800 μL of P standard in a semi-micro UV cuvette (Brand) to produce P standard concentrations of 0, 3.2, 6.4, 9.6, 12.8, 19.2, or 25.6 μM, see Figure 2-22. The provided phosphate standard was first diluted into 0, 4, 8, 12, 16, 24, 32 μM with 0.1 M H_2SO_4. The assay mixtures were incubated for 30 min before measuring the absorbance spectra (Figure 2-22). The absorbance at 620 nm was extracted from a full UV-vis absorption spectrum from 500 nm to 750 nm. We note that the disposable cuvette was favorable to avoid potential phosphate contamination from cleaning detergent. The blank absorption was less than 0.1 and has been corrected.

Sample preparation for the malachite green method: CoCat (20 mC cm^{-2}) film was deposited on ITO substrate. The prepared films were operated at the potential of 1.0 V or 1.3 V vs. NHE for 10 min in the selected concentrations (0, 1.6, 25, 100 mM) of KPi buffer with potassium nitrate (KNO_3, 500 mM) added to increase conductivity. Afterward, the operated film was quickly removed from the electrolyte and rinsed with Milli-Q water, followed by the digestion of the sample film. We note that water rinsing or immersion in reagent water represents a reproducible procedure to remove excess electrolyte ions.[250;408] The film was dissolved in 3 mL sulfuric acid (0.1 M), 800 μL of the sample solution was added to 200 μL stock working solution, and spectra were collected after 30 min (SPECORD PLUS 50 UV/Vis spectrometer). All measurements were repeated three times and two independent samples were assayed for each experimental condition. The absolute P amounts in the various CoCat films were determined from the corresponding absorption at 620 nm in the calibration curve (Figure 2-22).

3 Redox chemistry determines the rate of water-oxidation electrocatalysis as revealed by investigation of an amorphous cobalt-based material

Abstract The electrocatalytic oxygen evolution reaction (OER) is of prime importance in the sustainable production of hydrogen and other chemicals. The OER rate generally depends strongly on the electrode potential, typically with an exponential dependence in the so-called Tafel slope regime. However, the underlying mechanisms are insufficiently understood and may differ strongly from classical paradigms. Here electrochemical experimentation is combined with X-ray absorption and visible-light spectroscopy in operando experiments for investigation of a volume-active OER catalyst material of the cobalt oxyhydroxide type. Atomic structure and mean metal oxidation state of the catalyst material are found to equilibrate with the electrochemical potential that is determined by the applied electric potential and electrolyte proton activity. Rather than electric potentials or field strengths itself, it is the chemical state of the equilibrated material that governs the rate of catalysis. Non-Nernstian redox transitions of the catalyst material and the steepness of the potential dependence of catalytic currents are explainable by energetically interacting high-valent metal sites. The herein presented conclusions may apply to a broader class of electrocatalytic materials and could support the development of catalysts with an improved energetic efficiency that results from superior steepness of the exponential potential dependence of the rate of catalysis.

The above generic conclusions are derived from two key findings: (a) The catalytic current and thus the rate of catalysis depends strictly exponentially on the Co^{4+} concentration in the redox-active catalyst material, irrespective of electrolyte pH or mass transport limitations. (b) The equilibration proceeds by formation of Co^{4+} ions in a redox transition during which the Co^{4+} concentration does not follow a classical Nernstian behavior but depends linearly on the electrochemical potential. This is explained by comparably strong interactions between Co^{4+} metal ions with a total positive interaction energy that is proportional to the Co^{4+} concentration, thereby positioning the catalyst material between solutions of redox-active molecules with Nernstian behavior, on the one hand, and redox-inactive solid-state materials with potential-dependent Fermi energy, on the other hand. Based on the above experimental results, it is proposed: (1) The mean cobalt oxidation state depends linearly on the electrochemical potential due to a total positive interaction energy that increases linearly with increasing Co^{4+} concentration. (2) The same interaction energy causes an increase of the oxidizing power at the OER active site. Consequently, the free energy difference towards the transition-state decreases linearly with increasing overpotential, thereby explaining the exponential relation between Co^{4+} concentration and catalytic current.

3.1 Introduction and motivation

Water oxidation reactions play an important role in realizing two closed cycles, the carbon cycle and the renewable fuel cycle, which has spurred scientists to develop water oxidation catalysts, including molecular and heterogeneous catalysts.[17;40;218;409;410] Regardless of the type of catalysts, understanding and elucidating the catalytic reaction mechanisms and intrinsic descriptors of catalytic rate are critical for knowledge-guided catalyst design.[411] Amorphous CoCat catalyst, pioneered by the Nocera group in 2008, has evoked a great deal of inspiration because of its ability to unify solid-state and molecular catalysis, and the CoCat catalyst has become an important model for the study of neutral OER mechanisms.[70;113;125;126;412] In recent years, activity determinants at the macroscopic and atomic levels and even at the nanoscale have been derived by means of electrochemistry, advanced operando spectroscopic methods (e.g., XAS, Raman),[126;139;272;322] scanning electrochemical cell microscopy (SECM)[345;413] and theoretical calculation[171;414]. Conventionally, the catalytic mechanisms of heterogeneous crystalline material are related to their surface, i.e., "surface only", involving the binding strength of water oxidation intermediates to surface metal sites.[40;246;415-417] In contrast, the OER activity on amorphous CoCat is volume-active, which involves the accumulation of Co^{IV} species.[99;126] The presence of Co^{IV} has also been verified by ex/in-situ EPR and bulk-sensitive XAS experiments.[116;126;136] The proposed Co(IV)—oxo or Co(III)—oxyl radicals at the domain edge site play a crucial role in the formation of O—O bond.[126;131;164] Specifically, the generation of two-terminal Co-oxo intermediates either by direct intramolecular oxygen coupling (IMOC) or the water nucleophilic attack (WNA) is generally accepted.[131;134;141;162;418] Experimentally, the mechanistic derivation still leaves some unanswered questions as to how high-valent redox-active metal ions affect the formation of O-O bonds and their role in determining the OER catalytic rate.

It is well-known that the formation of high-valent metal ions is closely related to the redox chemistry of metal center, and the important role of high-valent metal ions on the catalytic rate of water-splitting reactions has been emphasized.[219;419-422] Impressively, several representative studies based on noble metal and transition-metal oxide catalysts have shown that metallic redox or oxygen chemistry plays a role in electrocatalytic water oxidation in neutral or alkaline electrolytes.[126;134;216;217;221;232;237-240] (i) In our earlier work[126] based on CoCat solid-state material, we elucidated a possible OER mechanism from the aspect of molecular chemistry, which involves the dynamic equilibrium of two specific redox transition processes and structural rearrangement under different potential and pH conditions. We observed non-classical Nernstian behavior for redox transitions and accumulation of oxidized equivalences prior to water oxidation. Furthermore, in the ref.[134], we explored the effect of proton-coupled electron transfer (PCET) by H/D isotopic substitution on the redox chemistry and the formation of O—O bond. In both H_2O and D_2O solution, the exponential dependence between current activity and the average Co oxidation state and their overlap suggest that this is independent of the state of the proton. (ii) Spectroelectrochemical techniques based on nickel (iron) hydroxide catalysts also revealed the above exponential relationship when OER occurs under alkaline conditions.[216] (iii) Similarly, the linear behavior between the logarithmic

current and the oxidative storage charge of iridium-based catalysts was elucidated.[217] It has been proposed that charge accumulation contributes to lowering the activation energy and thus increasing the reaction rate.

Although catalytic rate determinants have been frequently described,[74;134;142;423] the influence of redox chemistry and oxygen chemistry on reaction rates at neutral pH is still not fully understood, especially for amorphous CoCat materials. (1) On the one side, our preliminary results lack a more extensive study to consolidate the hypothesis of an exponential relationship between current density and charge accumulation in the cobalt oxidation state. The question of whether the accumulated charge is affected by other factors (e.g., buffer concentration, electrolyte pH) and whether it further affects the exponential behavior has not yet been addressed. Meanwhile, the reaction order of the $NiFeO_x$-based catalysts was referred to pH-dependent when operating the catalyst from alkaline to neutral solution,[216] which gave rise to our current study of the pH series. (2) On the other side, the source of charge accumulation reported in ref.[217] is different from our findings, whether it is from cobalt oxidation or ligand oxidation or other processes.

Based on these issues, this chapter investigates the role of oxidation state accumulation in determining the rate of electrocatalytic water oxidation in the CoCat-KPi system by combing electrochemistry with operando X-ray absorption structure spectroscopy (XAS) and in situ UV-vis absorption spectroscopy under varying concentrations of KPi or varying pHs of the electrolyte, as well as under a wide range of selected electrode potential conditions.

3.2 Results and discussion

3.2.1 Direct correlation between current and oxidation states

In ref.[134] (H/D experiments with isotopic substitution), the accumulated Co oxidation states were monitored by quasi-in situ XAS. Here, oxidation states are extracted by collecting XAS spectra in real-time during the period of potential applied by operando X-ray absorption spectroscopy.[315;424] A series of electrode potentials were applied in small step increments (35 mV, potential jumps see Figure 3-1A). After 1 minute equilibrium, the collection of individual XAS spectrum was initiated. CoCat films (20 mC cm^{-2}) were deposited on graphene sheet substrates or glassy carbons as working electrodes, and freshly prepared film was used in each experiment. In order to revisit this "surprising" exponential behavior, thereby the current is not directly determined by the applied potential but by the accumulation of oxidation states, we further expanded the electrolyte system to different pH and KPi buffer concentrations.

3.2.1.1 Oxidation states at different pH of KPi buffer (100 mM)

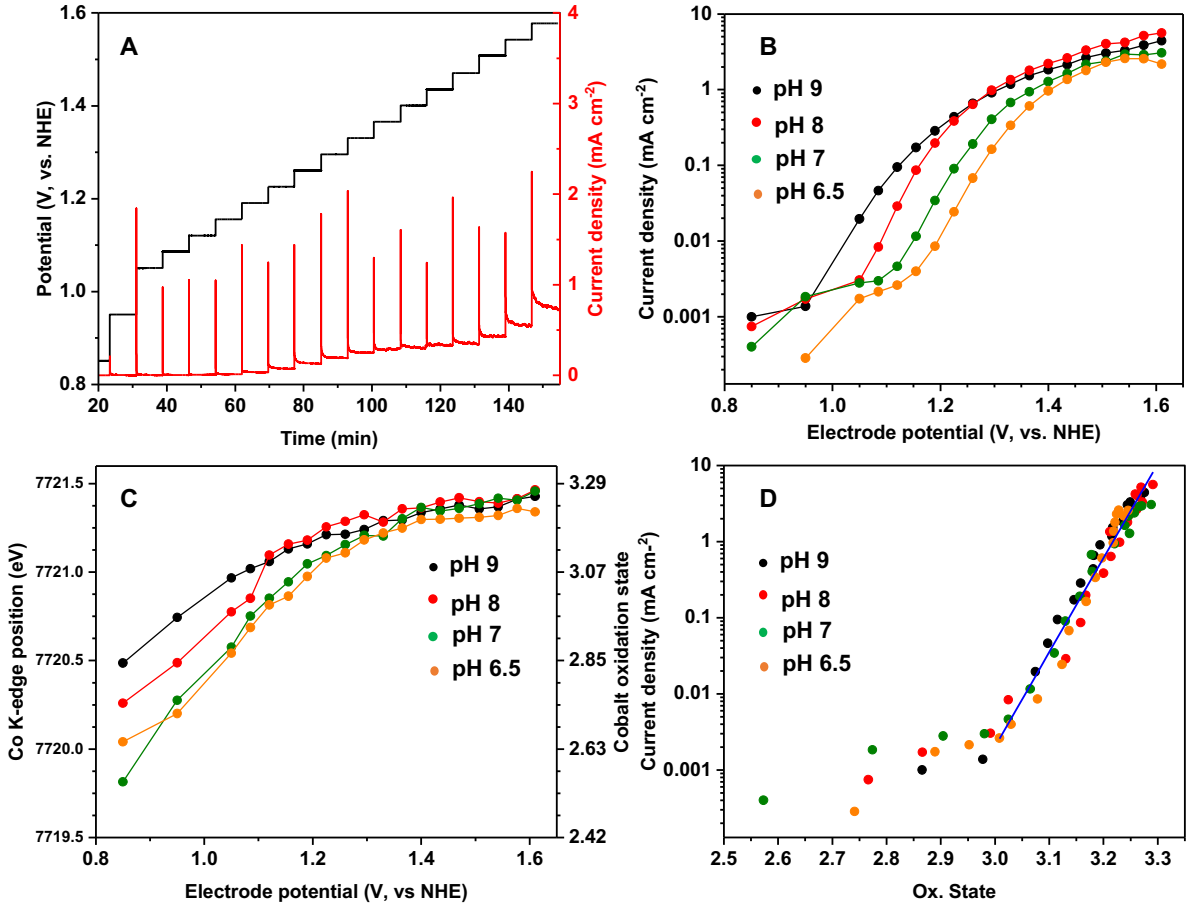

Figure 3-1. Operando X-ray absorption measurements at the Co K-edge of a CoCat sample (20 mC cm^{-2}) run in stirred solutions (~300 rpm) of KPi (0.1 M) at different pH values, to which the electrolyte salt KNO_3 (500 mM) was added to enhance ionic conductivity. (A) Potential jumping protocols for the XAS experiment. (B) Current as a function of electrode potential. (C) Co oxidation states at different electrode potentials. The oxidation states (right y axis in panel C) are determined from the calibration curve in Figure 3-2. (D) Steady-state current (panel B) is plotted against the Co oxidation states (panel C). The blue line indicates a concatenated linear fit at different pH values, showing a slope of about 12 (12.4±0.3) between the logarithmic current and the oxidation states. Note that the current density (B, D) axis is displayed on a logarithmic scale. The potential axis is not corrected for iR drop.

The effect of protons on the catalytic activity was derived from H/D isotope substitution experiments at pH 7.[134] Here, the selected pH values of KPi ranged from 6.5 to 9 to maintain sufficient buffering capacity (pKa of KPi = 7.2). Under extreme acidic or alkaline conditions, catalyst stability and intrinsic properties (e.g., structural or phase transitions) can affect and complicate the understanding of the mechanism.[199;200] Addition of KNO_3 electrolyte salt (500 mM) and agitation of the electrochemical cell at approximately 300 rpm improves ionic conductivity and reduces mass transfer limitations. In Figure 3-1, the relation among static current density, oxidation state at static state and electrode potential is displayed at a wide range of potentials from 0.85 V to 1.61 V vs. NHE at various pH values. Current densities were averaged for each CA step between 420 and 425 s divided by the geometric area (~1.33 cm^2),

while XANES spectra were collected after 1 min equilibration. Figure 3-1B shows the Tafel plots at different pH values. It is noteworthy that in the Tafel regime, a cathodic shift of about 160 mV in potential occurs at the same current density (e.g., 30 μA cm^{-2}) when the CoCat film is operated from a low pH (pH 6.5) to a higher pH (pH 9), which is almost consistent with the theoretical Nernst slope (59 mV pH^{-1} × (9–6.5) ~148 mV). As the potential increases, the current density increases sequentially until it reaches a plateau level where the current depends on the protonation state of the buffer base (as verified in Chapter 2). Therefore, the higher the pH, the higher the plateau current level. At high potentials, the current at pH 9 is slightly less than that at pH 8. This may be due to insufficient diffusion of the buffer, which limits the response to the electrodes and thus affects the overall current in the circuit.

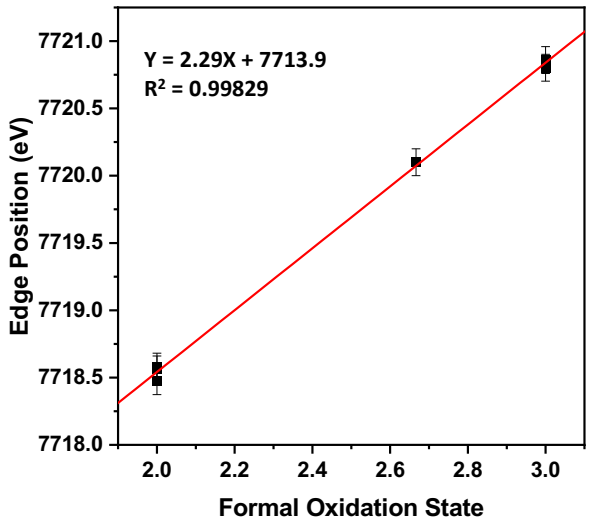

Figure 3-2. Calibration curve for converting XANES edge positions to Co oxidation state. The edge positions were determined by the integral method.[316] The calibration curve obtained from Co-based reference compounds with known oxidation states, i.e., $(Co^{II}(OH2)_6(NO_3)_2)$ solution, $(Co^{II}(OH2)_6(NO_3)_2)$ powder, $Co^{II}_3(PO_4)_2$ powder, $Co^{II,III}_3O_4$ powder, $Co^{III}OOH$ powder, $LiCo^{III}O_2$ powder. Readapted from ref. [126].

In Figure 3-1C, the oxidation state of cobalt at different potentials was quantified from the edge position of the XANES based on the calibration curves of the well-known cobalt compounds in Figure 3-2. As the anodic potential or pH increases, the edge position of XANES moves to higher energies, suggesting that the Co redox transition is pH or potential-dependent (Figures 3-3 and 3-4). Significant changes in the oxidation state were observed at all pH values at low potentials ranging from 0.85 V to~1.25 V. In contrast, at high potentials, the small shift of the edge position (and thus the oxidation state) around 7721.5 eV reveals the limitations of oxidation state accumulation and the independence of oxidation state changes from potential. The initially apparent oxidation state increases at all pH values and then saturates with a gradual increase in the anodic potential, which is similar to the behavior of the extended *j*-V curves (Figure 3-1B). The calculated lowest oxidation state was around 2.6 ± 0.1 at 0.85 V (pH 7), rising to 3.3 ± 0.1 at 1.61 V at pH 9, which is consistent with our earlier findings over a limited potential range.[126] Here, the extension of the potential range leads to a negligible change in

the oxidation state at high potentials for all the pH values, with an absolute edge position about 7721.5 eV, indicating that the oxidation state in the catalytic region is independent of the electrolyte pH. Differentially, under low-potential conditions (Figure 3-1C), the change in oxidation state from pH 7 to pH 9 showed an almost equal edge shift at a fixed low potential, suggesting that the variation of oxidation state depends on both pH and potential changes. The pH dependence of the redox transition confirms the charge compensation effect of proton removal. At 0.85 V, complete equilibrium may not be reached at pH 6.5, resulting in a higher oxidation state. Importantly, with the joint plot of current density and oxidation state (Figure 3-1D), all curves overlap each other, and a linear behavior between log(j) and oxidation state is displayed when oxidation states exceed about 3.00 ± 0.05 (formation of Co^{IV}). The results show that the exponential growth of current exclusively depends on the involvement of Co^{IV} species and it is not directly dependent on applied potential. The overlap at different pH values of KPi suggests that catalytic current is independent of electrolyte proton activity, supporting the earlier H/D experiments.[134]

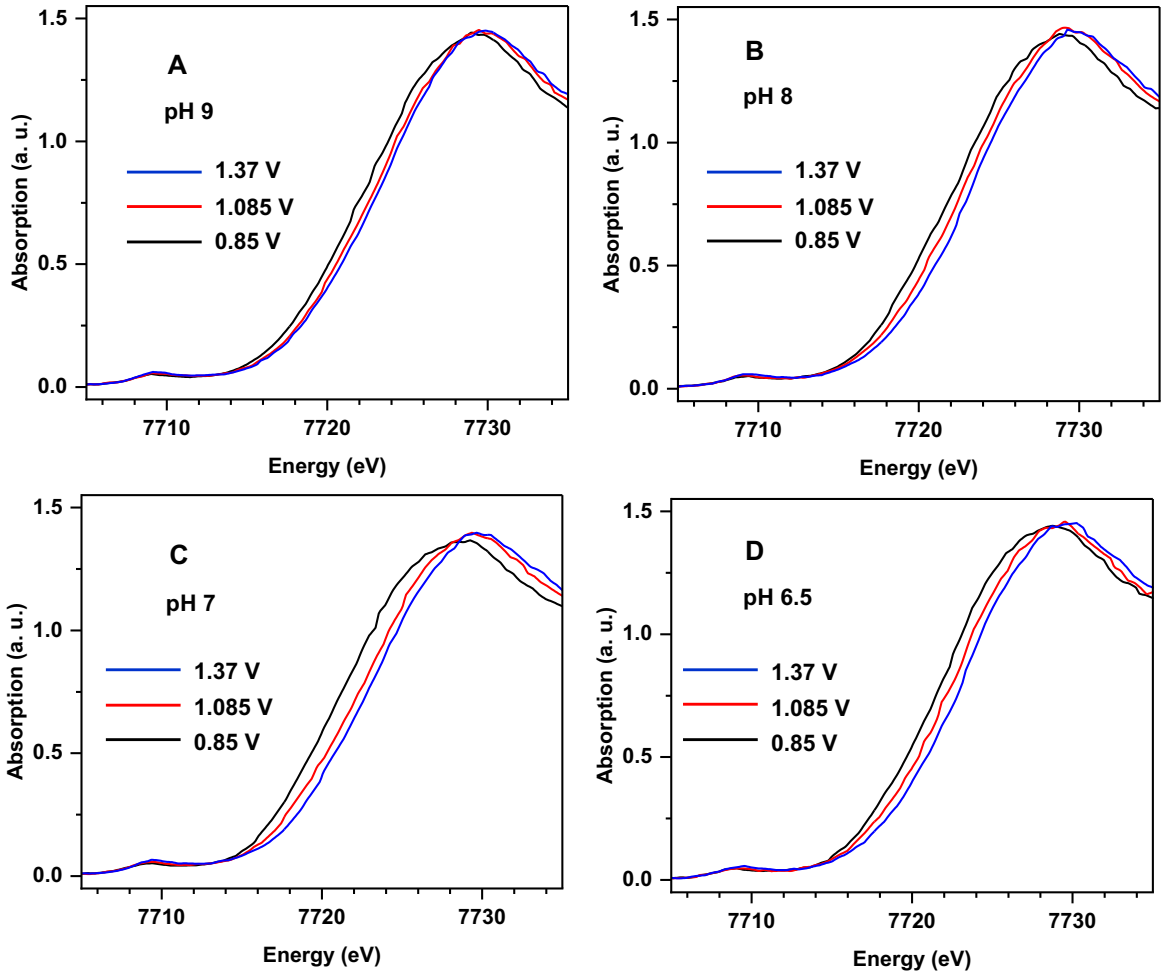

Figure 3-3. X-ray near edge spectra (XANES) of CoCat (20 mC cm^{-2}) at the cobalt K-edge with CoCat operated at different pH values. The CoCat edge spectra are all shifted to higher energies with increasing potential, suggesting that the increase in oxidation state is driven by the increase in electrode potential.

It is noteworthy that the exponential behavior between catalytic current and oxidation state is reflected in the log *j* versus oxidation state plot (Figure 3-1D), which can also be presented in the form of a power law (Figure 7-1A), similar to Figure 1-5D. The log-log plots of current density and extracted Co^{4+} concentration appear to exhibit a biphasic behavior, and here we propose the exponential behavior is the intrinsic relation between the catalytic rate and the chemical states because the accuracy and selection of the specific point for determining Co^{IV} concentration are critical factors. Further explanation of the exponential behavior is discussed in Section 3.2.1.4 and Section 3.3.

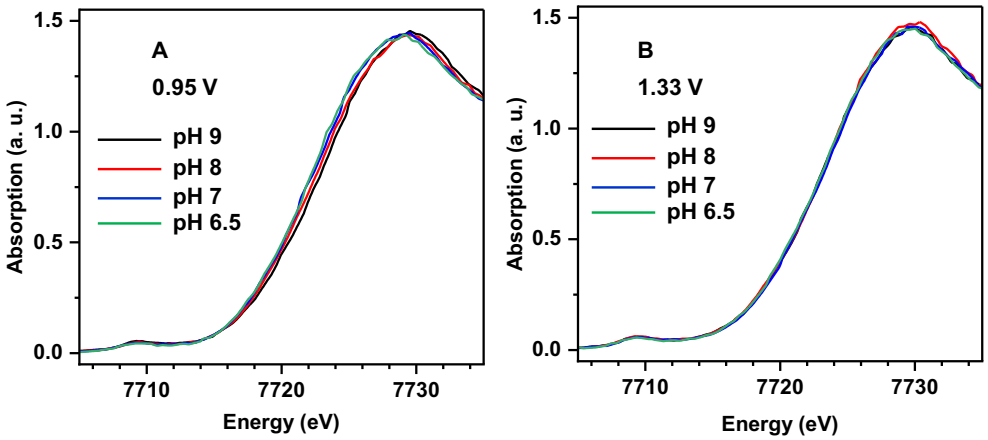

Figure 3-4. Comparison of XANES spectra at the cobalt K-edge at the indicated pH values at 0.95 V (A) and 1.33 V (B) (vs. NHE). More details are described in the experimental methods.

3.2.1.2 Oxidation states at different concentrations of KPi buffer

The effect of mass transport was also investigated by operating CoCat at various KPi concentrations in neutral KPi solutions. The experimental details are similar to the pH series, unless otherwise noted. The KPi concentrations selected cover two orders of magnitude (0, 1.6, 25, 100 mM). The total ionic intensity of electrolyte was maintained at a high level of about 500 mM by adding KNO_3 salt to the solution (KNO_3 concentrations of 500 mM for 0 mM and 1.6 mM KPi, 450 mM for 25 mM KPi and 300 mM for 100 mM KPi, respectively). The electrochemical cell was not stirred. The redox chemistry of Co at different KPi concentrations was investigated by determining the oxidation state via XANES. As with the collection of pH series, Tafel plots, oxidation states at different potentials, and plots of logarithmic current versus oxidation state were summarized in Figure 3-5, respectively. The current-potential curves at different KPi concentrations are in agreement with our previous study[142], showing consistent Tafel slopes of about 70 mV dec^{-1} at low potentials and the plateau levels in the intermediate potential region (Figure 3-5A). At high KPi concentrations (e.g., 100 mM, 25 mM), as the potential increases, the edge position, which corresponds to the oxidation state, progressively moves towards higher energy levels. This shift plateaus and stabilizes at approximately 7721.5 ± 0.1 eV. Similarly, the potential independence of oxidation state changes is observed in the high-potential regime (Figure 3-5B). However, with an insufficient buffering capacity of KPi (e.g., 0 mM), the raw fluorescence signal decreases dramatically

(Figures 3-8 and 3-9). At higher potentials, the fluorescence is seriously attenuated due to severe film detachment. Therefore, in the following analysis, we truncated the data points from film detachment to extract the intrinsic relationship between oxidation state and catalytic rate.

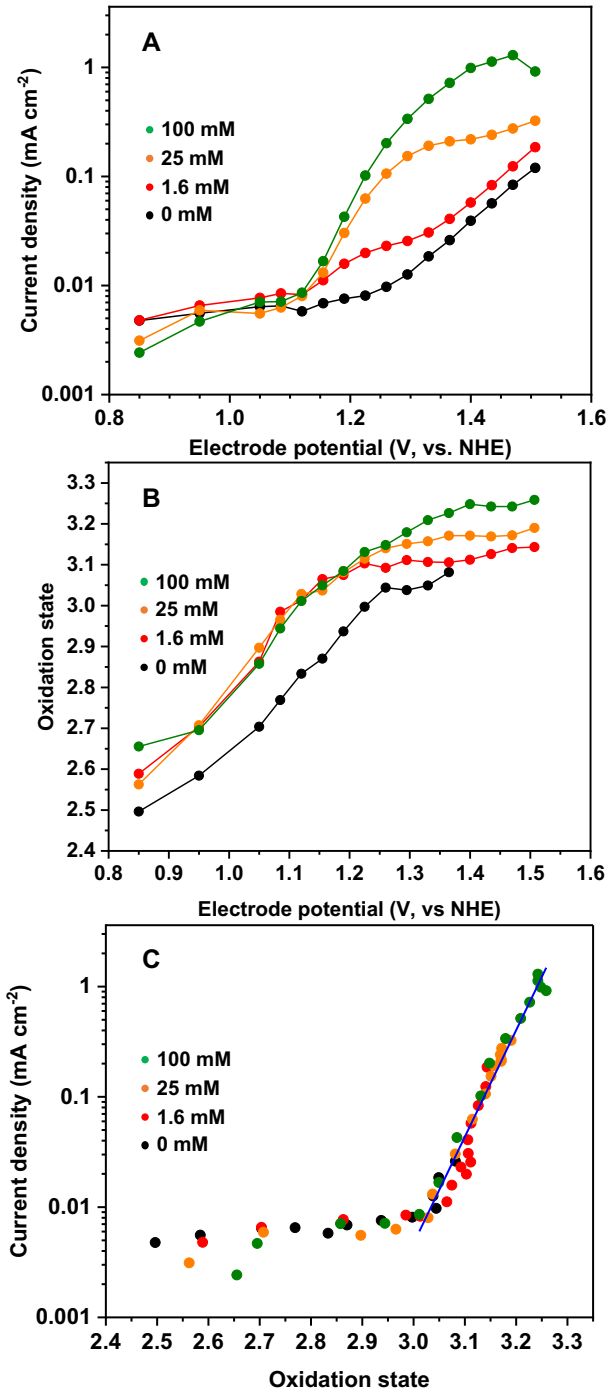

Figure 3-5. XAS measurements at the Co K-edge of CoCat samples (20 mC cm^{-2}) operated in different concentrations of KPi solution (pH 7) to which KNO_3 was added to keep the total ionic strength around 500 mM. (A) Current density as a function of electrode potential. (B) Cobalt oxidation states at various potentials for different concentrations of KPi. (C) Current density as a function of Co oxidation state. The blue line represents a concatenated linear fit showing a slope between the logarithm of the current and the oxidation state of about 10 (9.7±0.3). Note that the current densities (A, C) are shown on a

logarithmic scale. The potential axis has been corrected for iR drop. The oxidation state is calibrated by the calibration curve in Figure 3-2.

The oxidation state increased from 2.5±0.1 to 3.0±0.1 when applying low (0.85 V) to moderate (1.1 V) potentials, which is associated with the first redox process ($Co^{II} \rightarrow Co^{III}$). In the catalytic region, the change of oxidation states as a function of the applied potential tends to be saturated for all the KPi concentrations. The saturation level of the oxidation state appears to be influenced by the KPi concentration, which is consistent with the finding in the Chapter 2. The increased KPi concentration offers a greater number of effective proton acceptors, which facilitates the buildup of higher oxidation states. Consequently, this enhancement in proton management leads to an increased rate of catalysis.

Regardless of the magnitude of the apparent oxidation state, the OER catalytic current (referring to catalytic rate) exhibits an exponential relationship with the accumulated redox states (Figure 3-5C). The subtle variation in the slopes observed between the pH and concentration series (K_{pH} ~ 12 vs. $K_{Conc.}$ ~10) (Figures 3-1D and 3-5C) could be attributed to the precise selection of the initial fitting point, i.e., this difference may be linked to the accurate determination of the Co^{3+} position. The specific point of reference may lead to inconsistent interpretations of the relationship between current density and oxidation state, specifically, whether this relationship follows an exponential pattern (Figures 3-1D and 3-5C) or adheres to a power law (Figure 7-1 and Figure 1-5D). By examining the log-log plot of current density against Co^{IV} concentration (Figure 7-1), a power law relationship between the catalytic current and the oxidation state is clearly discernible. In this context, we propose that the exponential behavior is more closely aligned with the characteristics of CoCat materials, with an extensive discussion provided in Section 3.2.1.4 and Section 3.3 Importantly, our XAS measurements have established a direct correlation between current density and the oxidation states. This finding deviates from the classical mechanism of water oxidation, where current is primarily governed by the electrode potential applied.

3.2.1.3 Stability of CoCat monitored by XAS

To confirm that determination of oxidation states is not affected by film instability, it is important to compare the non-normalized X-ray fluorescence at different voltages at fixed high X-ray excitation energies (e.g. 8000 eV) and apply it to the pH (Figure 3-6 and Figure 3-7) and concentration series (Figure 3-8 and Figure 3-9) measurements. For the pH series (100 mM KPi), the fluorescence was stable at various potential conditions from pH 7 to pH 9. Due to monochromator crashes, outliers may appear when remeasuring new samples at the corresponding potential and are thus not comparable. At pH 6.5, there is an initial decrease in fluorescence, followed by an increase, and eventually, the fluorescence stabilizes, which could be indicative of a redeposition process. In the concentration series (Figure 3-8), the fluorescence spectra across various KPi concentrations (1.6, 25, and 100 mM) exhibit good alignment at different potentials, with the exception of the condition lacking KPi buffer. This observation implies that the films remain effectively stabilized under these tested conditions. Thus, the oxidation states at different potentials can be extracted without being affected by film instability or radiation damage[315].

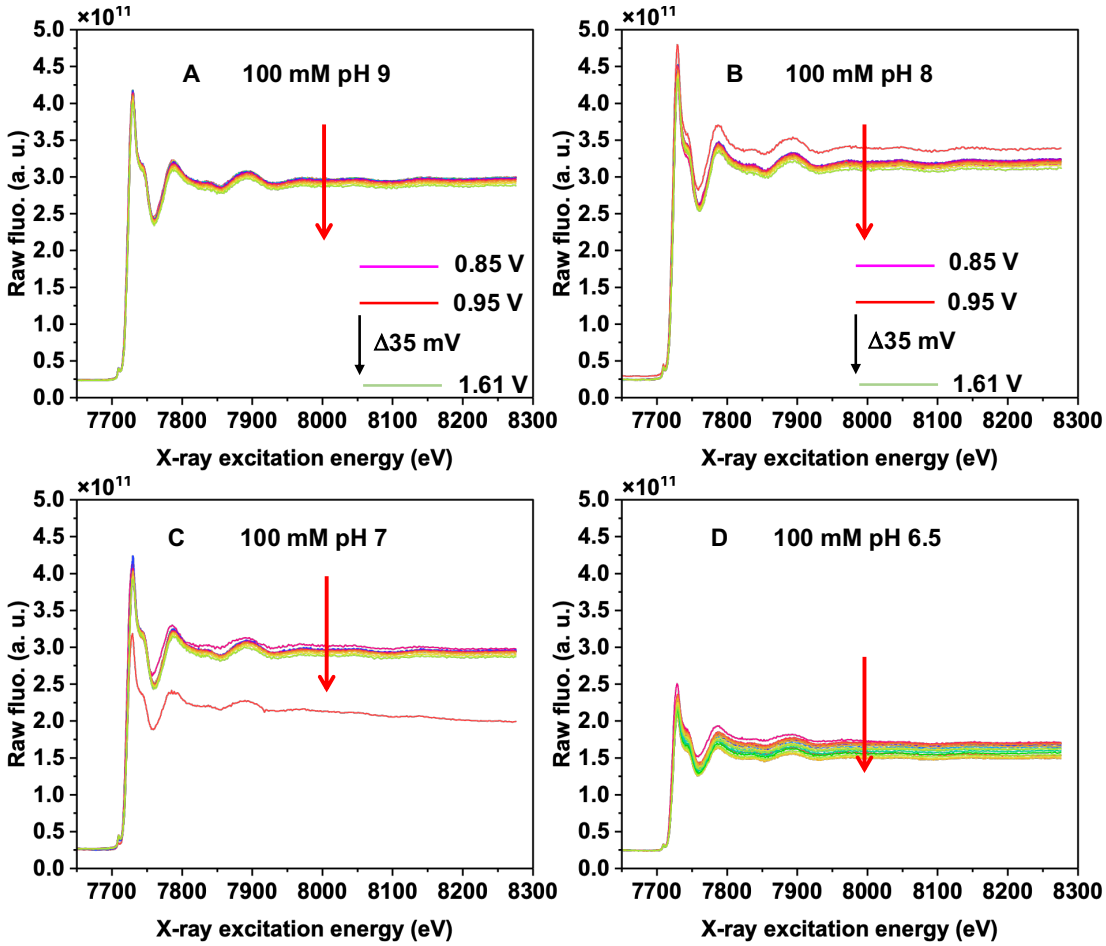

Figure 3-6. Raw XAS spectra at different potential steps (vs. NHE, no iR drop correction) while operating CoCat in KPi buffer (100 mM) at the indicated pH values. The raw fluorescence signal is divided by the incoming X-ray intensity (I_0) and corrected for dead time. The spectra shown are consistent with Figure 3-1. The red arrow at 8000 eV is used to extract the raw fluorescence at various potentials (see Figure 3-7). Figure 3-7 explains the deviation lines.

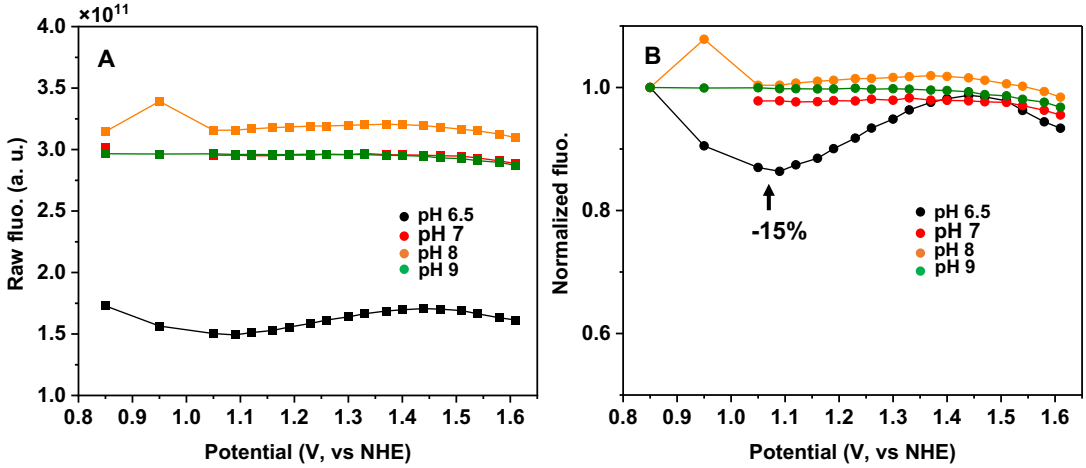

Figure 3-7. Comparison of raw XAS fluorescence (A) and normalized fluorescence (B) of CoCat films run in KPi buffers of different pH at 8000 eV. The fluorescence normalization was based on fluorescence at 0.85 V. Missing or deviating points at 0.95 V (pH 8 or pH 7) are related to the use of a different XAS sample and is unrelated to catalyst degradation due to the monochromator crashed. At

pH 6.5, a clear trend towards dissolution of the CoCat film is visible, but at a level, we found as being still irrelevant for analysis of the normalized spectra.

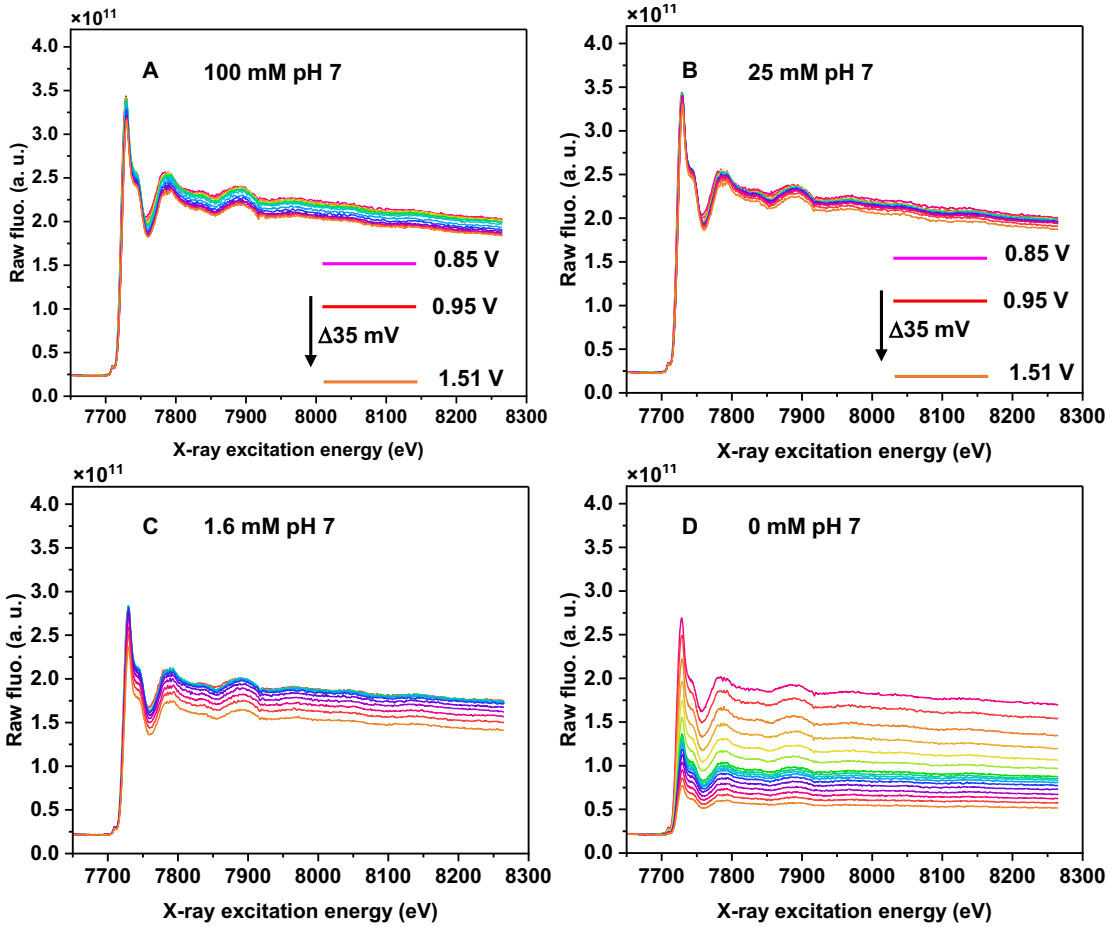

Figure 3-8. Raw XAS spectra of CoCat at various electrode potentials (vs. NHE, 85% iR drop correction) at the indicated KPi concentrations (pH 7). The fluorescence signal was divided by the incoming X-ray intensity (I0) and corrected for detector dead time, without approaching the otherwise standard normalization to the post-edge signal level. The spectrum corresponds to Figure 3-5. At a KPi concentration of 0 mM, the fluorescence gradually decreased until it reached half of the initial fluorescence, and the position corresponding to the stabilization of fluorescence was used as the upper limit for extracting the oxidation state. We note that partial sample dissolution does not necessarily prevent informative analysis of the normalized XAS spectra. Only for the 0 mM KPi experiment, we needed to exclude the four spectra collected at the highest potentials from subsequent analysis. For these four spectra, the normalized spectra were modified by a contribution likely stemming from dissolved Co^{2+} ions so that the here required accuracy in the Co oxidation determination could not be reached. More description is shown in the caption of Figure 3-7 or Figure 3-9.

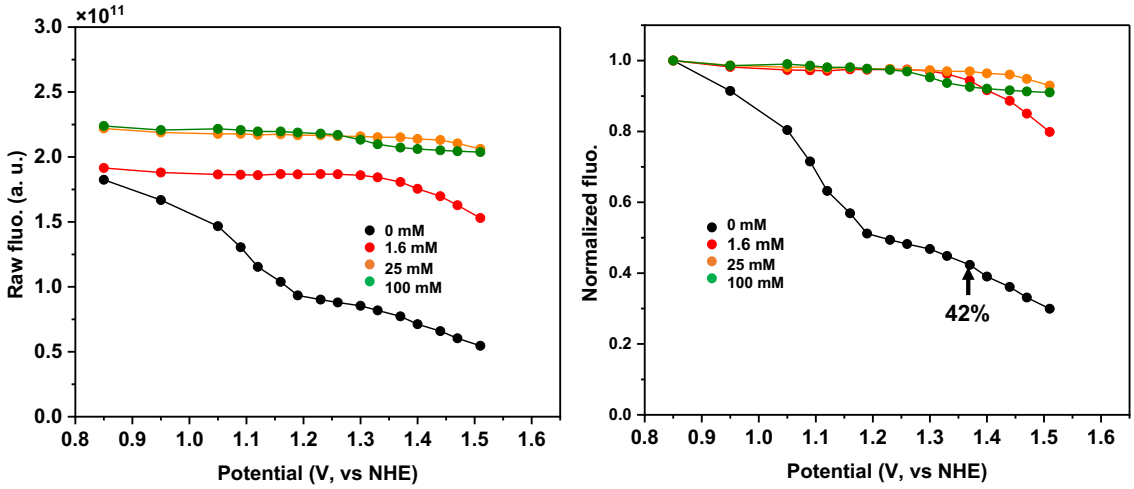

Figure 3-9. Raw XAS fluorescence (left) and normalized fluorescence (right) at 8000 eV at different potentials in different concentrations of KPi buffer. For 0 mM KPi, the arrow represents the upper limit of oxidation state extracted, where about 60 % of the fluorescence lost. The displayed results correspond to Figure 3-5 and Figure 3-8.

3.2.1.4 Insights from XAS for tracking oxidation states

The important high-valent Co^{IV} as an active component or intermediate in the OER mechanism of cobalt-based catalysts has been widely reported.[116;119;126;160;164;368;422] The formation of O-O bonds is usually associated with the formation of Co^{IV}=O species at the edge site. According to this hypothesis, the observed exponential behavior occurs only at Co^{IV} generation potential higher than ca. 1.15 V, which validates the key role of Co^{IV} in the OER process. In a previous report of Risch et al,[126] redox processes involving Co^{II}→Co^{III} and Co^{III}→Co^{IV} at pH 7 and 100 mM KPi could not be described by the classical Nernst equation but had to take into account the additional factor of interaction energy that increase with an increasing number of oxidized Co ions. In order to explain the exponential relationship between current density and oxidation state, also here we propose the concept of interaction energy between cobalt oxide ions. Assuming that the interaction model of ref. [126] also applies to the extended structure of CoCat, the requirement to oxidize Co ions increases as the interaction energy increases, implying that not every Co^{IV} ion has the same redox potential, and thus the redox potential of Co^{IV} ions depends on the interaction between neighboring Co ions. This may tentatively explain why the current density is exponentially related to the oxidation state of Co.

In kinetics, for transition state theory, the probability of reaching the transition state is exponentially related to the activation energy.[425] In view of this, the exponential relationship presented in the XAS experimental results seems to be related to the activation energy for the formation of the active site in the transition state theory. Strong interactions between high-valent Co species can generate high potential energies, leading to lower activation energies and further lowering the overpotential. Thus, it is the local chemical reaction that controls the rate of reaction, independent of the electric field. The electric field may play a direct role in the accumulation concentration of oxidation state prior to the formation of active sites (e.g., Co^{IV}=O).[126] It fits to the XAS result that the dynamics of the redox state

concentration are more pronounced in the low potential region and less pronounced in the catalytic region (Figures 3-1C and 3-5C).

We therefore conclude that the current density is directly independent of the applied potential but is related to the accumulated oxidation state. Typically, heterogeneous catalysts (e.g., perovskite) have "pure surface-activity" properties, including adsorbate evolution mechanism (AEM) and lattice oxygen participation mechanism (LOM), where an electric field plays a role in the electrocatalytic OER.[102;103;426] The different scenarios for CoCat may be due to the large involvement of the catalyst in the accumulation of oxide species, as indicated by the relatively large change in oxidation state (~ 0.65 oxidation state).[99;126] Hypothetically, our experimental results emphasize that it is not the electric field or the applied electric potential itself but the intrinsic chemical states of the catalyst material that determine the catalytic rate. This conclusion may relate to the properties of two commonly discussed catalytic OER pathways, namely intramolecular oxygen coupling (IMOC) and nucleophilic water attack (WNA). According to ref.[141], the IMOC is not influenced by the electrode potential, in contrast to the WNA pathway, which exhibits a significant dependency on the electric field, as evidenced by its substantial dipole moment and polarization characteristics.[427-429] Based on this rationale, the rate-determining step for CoCat O-O bond formation is presumed to involve the coupling of two Co-oxyl groups via the IMOC mechanism.[131;132;134;162;164;165]

3.2.2 Oxidatively stored charge quantification

The operando XAS studies were followed by simple electrochemical experiments to quantify the oxidatively stored charge by oxidation at equilibrium, primarily using a "jump potential" protocol to jump from a high potential to a constant cathodic potential (Figure 3-10). By integrating the reductive current, the oxidatively stored charge at high potentials can be obtained.

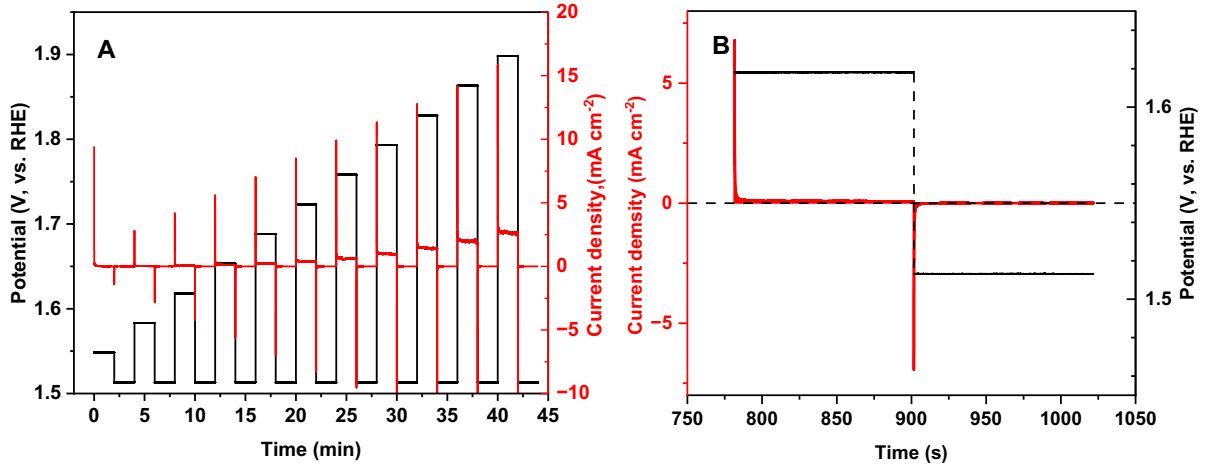

Figure 3-10. Graphical representation of the potential jump scheme (A) and quantitative estimation of the oxidatively stored charges (B). (A) Current density is recorded by the chronoamperometry technique at different potentials. The corresponding high potential was raised from 1.548 V to 1.898 V (vs. RHE) in steps of 35 mV while constantly jumping back to 1.513 V (vs. RHE). Each potential step applied for 2 minutes to reach equilibrium. Electrode potentials are corrected for iR drop. (B) As an example, the CoCat film was held at 1.618 V for 2 minutes and then dropped to 1.513 V for 2 minutes. Integration

of the complete reduction current trajectory is used to quantify the charge stored during the oxidation process Black lines are the applied potentials; red lines are current densities.

In order to exclude the associated sub-catalytic process ($Co^{II} \rightarrow Co^{III}$), the cathodic potential at 1.1 V vs. NHE at pH 7 (1.513 V vs. RHE) was chosen to merely focus on the oxidation process of Co^{III} to Co^{IV} (oxidation state at 1.1 V vs. NHE, pH 7 is about 3.0 ± 0.1). Experiments were performed at different pH or KPi concentrations. The same range of electrode potentials (vs. RHE) is used for pH series measurements. This experiment was inspired by a number of studies that attributed the catalytic current to ligand oxidation.[217;220;430] X-ray absorption spectroscopy and computational analysis reveal the involvement of holes of the surface oxide group in the catalytic OER.[220;430] Negatively charged oxygen ligands promote the formation of reactive oxygen species such as peroxides or superoxides by interacting with vicinal or geminal OH ligands from lattice oxygen.[431] In addition, it has shown that the introduction of oxygen vacancies can adjust the electronic structure and further improve the catalytic activity.[415] Thus, the electrochemical potential jumps experiment may be valuable in determining the amount of oxidatively stored charge by integrating cathodic reduction. The information on average oxidation state from XAS measurements based on CoCat films (20 mC cm^{-2}, ~200 nmol cm^{-2}) is similar to the oxidation equivalents stored in the form of Co oxidation state changes. Quantitative comparisons between changes in oxidation charge and absolute changes in cobalt oxidation state can facilitate the determination of whether the source of the catalytic current is metal oxidation or ligand oxidation (or some other process).

As shown in Figure 3-11 (column 1–3), with this potential jump protocol, we can obtain the Tafel plot (1) and the relationship between the oxidatively stored charge and the electrode potential (2) or the logarithm (current density) (3). Rows A-D sequentially represent pure KPi buffer (A), addition of additional electrolyte salt (KNO_3) (B), stirred cell without KNO_3 (C), and electrochemical cell with stirring and addition of KNO_3 (D). Tafel plots for different pH values overlap in the low potential region because the applied voltage on the RHE scale is independent of pH. As pH increases, the higher the pH, the higher the current density at higher voltage ranges due to the presence of more unprotonated buffer bases.[142] In column 2, the maximum absolute charge stored in the given potential region is about 5 mC, which represents 25% of the CoCat film involved in oxidative charge storage (5 mC divided by 20 mC). More interestingly, compared to Figure 3-1 and Figure 3-5, this ratio corresponds well to the change in Co oxidation state during the redox transition from Co^{III} to Co^{IV}, where the Co oxidation state changes from 3.0 ± 0.1 to 3.28 ± 0.1, i.e., about 28% of the Co atoms are involved in the second redox transition. As a result, the oxidatively stored charge data (column 2) agrees quantitatively with the extent of Co oxidations state changes detected in XAS experiments, thereby excluding the quantitative oxidation of bound water species. In addition, the consistency of the oxidatively stored charge and the change in the oxidation state of the metal are independent of the sample thickness. In our previous study,[126] very thin films (~14 nmol cm^{-2})[99] showed an oxidized storage charge of 0.8 mC, and about 60% of the Co atoms were oxidized during the redox process from Co^{II} to Co^{IV}. According to the reference [126], we can estimate that about 38% of all Co atoms involved in redox processes involve Co^{III} to Co^{IV} (0.25/0.65). Thus, for thin films (~14 nmol cm^{-2}), we can calculate that about 0.3 mC of the

oxidized charge belongs to the Co^{III} to Co^{IV} process. A 14-fold increase in film thickness (14 nmol cm^{-2} to 200 nmol cm^{-2}) corresponds to oxidatively stored charges of 4.3 mC on the thicker film. Our experimental results show that there is a storage charge of about 5 mC on the ~200 nmol CoCat film, which is almost identical to that generated during Co oxidation and confirms the volume-active property of CoCat films.

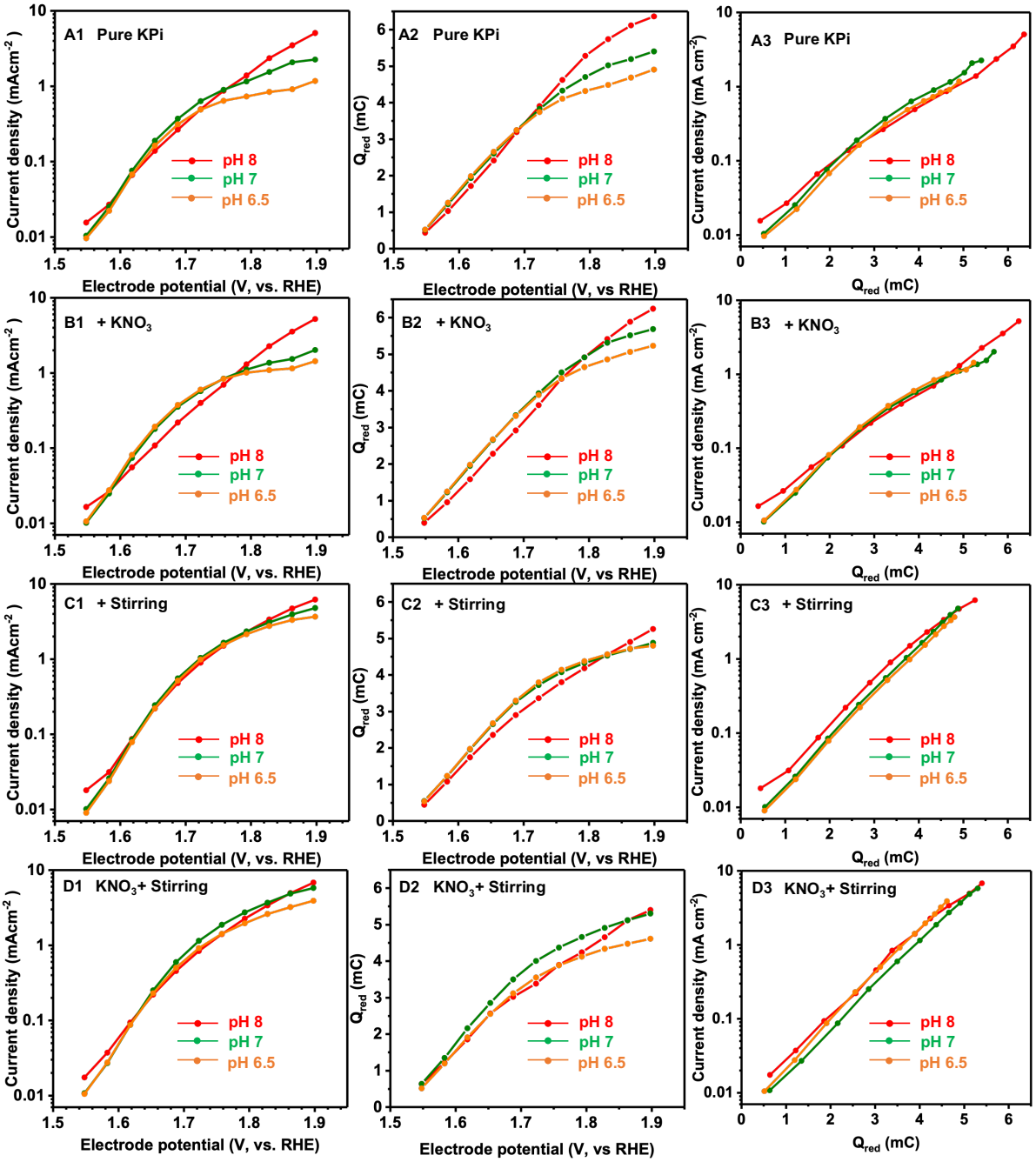

Figure 3-11. Comparison of the relationship between current density, oxidatively stored charge, and applied electrode potential at different pH values of KPi (0.1 M). The amount of CoCat deposited was 20 mC cm^{-2}. The electrochemical cell of the KPi system was varied under four conditions, i.e., A: pure KPi buffer as electrolyte; B: KPi buffer + KNO_3 (500 mM); C: pure KPi with stirring (400 rpm); D: KPi buffer stirred with adding KNO_3 (500 mM). The numbers in each column represent the type of graph:**1**: *j*–V plots (Tafel plots); **2**: oxidatively stored charge as a function of potential; **3**: current density

(logarithmic scale) in **1** as a function of oxidative charge in **2**. The potential axis has been corrected for iR drop.

Quantitative analysis showed that the amount of oxidatively stored charge obtained from the integrated cathodic current is not from the oxidative charge of ligand oxidation but from the redox transition process of cobalt ions. Importantly, in column 3, we observe a similar linear relationship between log(current density) and oxidatively stored charge, and it is independent of pH over the entire current range (Figure 3-11, panels C3 and D3). In panels A3 and B3, curvature seems to appear at high potentials, which limits the extensive nature of the linear trend. A further explanation is given below.

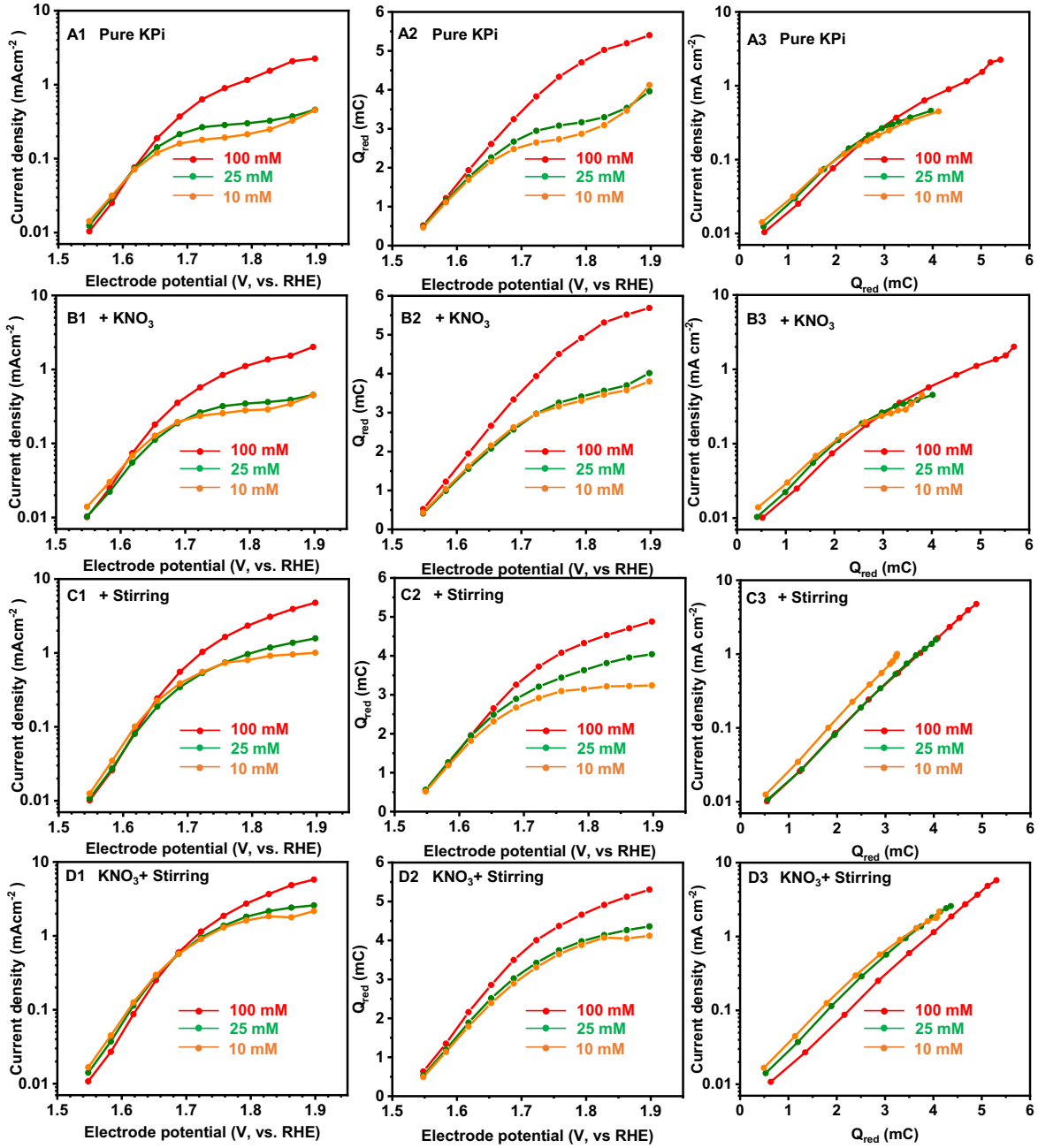

Figure 3-12. Comparison of the relationship between current density, oxidatively stored charge, and applied electrode potential at different KPi concentrations using the potential jumps method. See Figure 3-11 for more description.

Similarly, the exponential relationship in the neutral KPi system was further confirmed with changes in KPi concentration (10, 20, and 100 mM, Figure 3-12). At lower KPi buffer concentrations (e.g., 10 mM of pure KPi), the amount of buffer base may be insufficient, and the oxidatively stored charge is reduced compared to that stored under higher KPi conditions. However, a linear relationship between log(*j*) and the oxidatively stored charge is still clearly observed over the entire potential range (1.513–1.898 V vs. RHE, Panel C3 and D3). The same curvature as in the pH series is also observed in panels A3 and B3 of Figure 3-12, both cases in the absence of stirring. This may result from limitations caused by macroscopic electrolyte diffusion or bubble accumulation, which reduces the accessibility of the active site and limits the efficiency of charge passage through the circuit, leading to a reduction in oxidatively stored charge under high potential conditions. Likewise, the exponential law similar to the results of XAS measurement can also be displayed in the form of a power law (Figure 7-2) contributing to the same reason as the discussion at the end of Section 3.2.1.2.

The stability of the film was confirmed by integrating the CV cathode waves that were collected before and after the potential jumps (Table 3-1). The similar charge amount obtained from the CV_{bf}, accounting for about 35-40 % of the deposited charge (20 mC cm^{-2}), suggesting reproducibly prepared CoCat film.

In summary, the pH or concentration series of experiments here served to support the exponential relationship between redox chemistry and catalytic activity. The quantitively consistent redox-charge from integration approach with the Co oxidation states change from XAS excludes the oxidation of bound water species and confirmed the catalytic activity is uniquely related to the average cobalt oxidation state.

Table 3-1 Charge is estimated from the integration of the reductive area of CV measured at different pH or KPi concentrations in the four different buffer systems. The charge corresponds to the amount of redox-active cobalt ions. CV_{bf} and CV_{af} represent the charge integrated from the CVs collected before and after the potential jumping collection. The calculated charges represent the average of the last two CVs. Δ % represents the percent change in charge calculated from the CVs before and after a series of potential jumps.

	Pure KPi Q_{dep} (mC)		Δ %	+ KNO_3 Q_{dep} (mC)		Δ %	+ Stirring Q_{dep} (mC)		Δ %	+KNO_3+ Stirring Q_{dep} (mC)		Δ %
	CV_{bf}	CV_{af}		CV_{bf}	CV_{af}		CV_{bf}	CV_{af}		CV_{bf}	CV_{af}	
pH 8.0, 100 mM	8.4	8.5	1%	8.3	6.8	18%	8.1	7.5	7%	8.1	6.4	21%
pH 7.0, 100 mM	7.6	7.3	4%	7.7	7.0	10%	7.7	6.3	18%	8.1	6.1	25%
pH 6.5, 100 mM	7.6	7.6	0%	7.8	7.3	6%	7.6	7.2	7%	7.6	5.9	22%
pH 7.0, 10 mM	6.8	6.6	3%	6.9	6.3	9%	7.2	8.1	13%	7.5	5.2	31%
pH 7.0, 25 mM	7.3	7.5	2%	6.6	6.5	2%	7.8	8.4	8%	7.9	6.8	14%

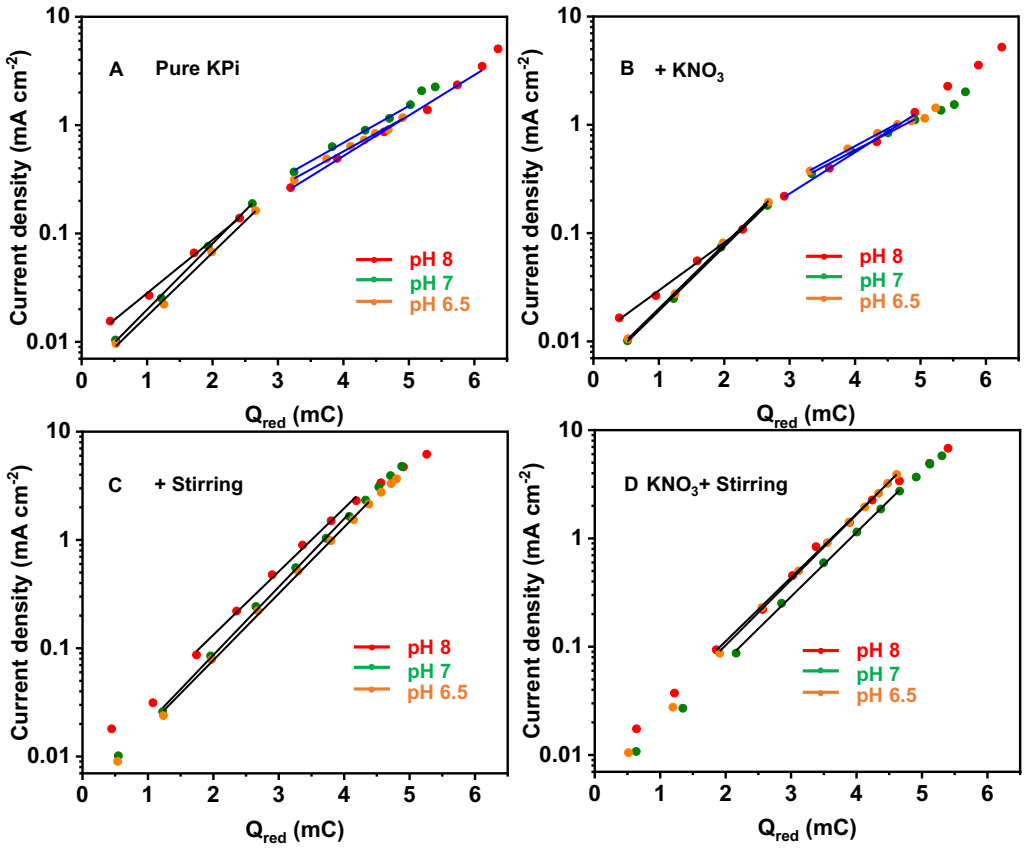

Figure 3-13. Linear regression of CoCat current density versus oxidatively stored charge for different pH values corresponding to the 3rd column of Figure 3-11. Panels A and B show curvature and are individually fitted. The black and blue lines are fitted lines. As the electrochemical cell is stirred, the linear range (black) extends across the entire potential regime (Panels C and D). The fitting results are shown in Table 3-2.

Table 3-2. Fit results of Figure 3-13. K and Y_0 represent the slope and intercept of the linear regression fit. The fits in the high current region of panels A and B are shown in blue.

	pH 6.5		pH 7.0		pH 8.0		pH 6.5		pH 7.0		pH 8.0	
	Slope (K)	Intercept (Y_0)	K	Y_0	K	Y_0	K	Y_0	K	Y_0	K	Y_0
Pure KPi	0.58	2.34	0.61	2.31	0.49	2.04	0.33	1.57	0.34	1.52	0.37	1.78
+ KNO_3	0.59	2.30	0.59	2.31	0.44	1.97	0.32	1.49	0.31	1.49	0.38	1.78
+ Stirring	0.61	2.34	0.63	2.32	0.58	2.05	/	/	/	/	/	/
+KNO_3+ Stirring	0.60	2.19	0.59	2.32	0.58	2.12	/	/	/	/	/	/

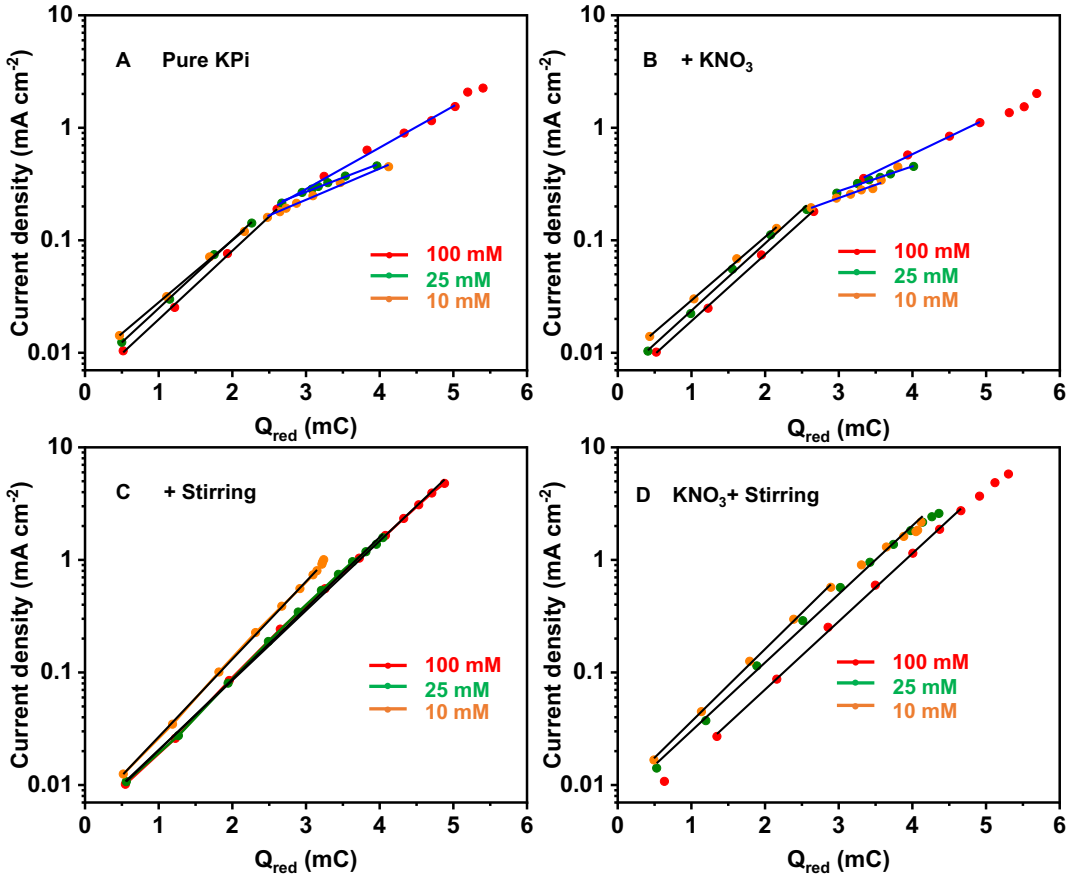

Figure 3-14. Linear regression fit of current density-oxidative charge plot for CoCat operated at different KPi concentrations corresponding to the 3rd column of Figure 3-12. See Figure 3-13 for further details.

Table 3-3. Fit results of Figure 3-14. K and Y_0 represent the slope and intercept. More details see Table 3-2.

	10 mM		25 mM		100 mM		10 mM		25 mM		100 mM	
	Slope (K)	Intercept (Y_0)	K	Y_0	K	Y_0	K	Y_0	K	Y_0	K	Y_0
Pure KPi	0.55	2.10	0.61	2.21	0.61	2.31	0.28	1.47	0.25	1.32	0.37	1.65
+ KNO_3	0.56	2.10	0.60	2.22	0.59	2.31	0.23	1.33	0.22	1.22	0.31	1.49
+ Stirring	0.69	2.26	0.63	2.32	0.62	2.31	/	/	/	/	/	/
+KNO_3+ Stirring	0.64	2.08	0.61	2.13	0.60	2.36	/	/	/	/	/	/

In order to quantify the relationship between catalytic rate (current density) and oxidatively stored charge, we approached linear regression fit. (Figures 3-13 and 3-14, Tables 3-2 and 3-3). In a comparison of the fitting results of steady (A-B) or stirred systems (C-D) under pH or KPi

concentration series, curvature transitions is solely observed in the steady-state system, limiting the extension of the linear regime. The fitting slopes for the pH and KPi concentration series in the high-current region (~0.3) are about half of those in the low-current region (~0.6). We assumed that it contributed to the mass transport of the buffer base or the accumulation of bubbles on the CoCat surface that limits the oxidized charge going through the electric circuit, which is also consistent with our earlier studies.[142] When agitating the cells, the linear trend extends significantly because mechanical agitation attenuates local acidification and bubble accumulation. It is clear that under all KPi conditions (pH and concentration series, Figures 3-13 and 3-14), the fits in the stirred system are similar, with slopes of about 0.6 dec mC^{-1}. Because the amount of Co ions in the electrodeposited CoCat film is 20 mC, we obtain a slope of around 20 × 0.6 = 12 decades per stored charge unit of the log10(j)–Q_{red} plot, in excellent agreement with the results of the XAS on Co oxidation state changes of Figure 3-1D. The value of 12 means that the catalytic current increases by 1.2 decades (×16) per increase of the oxidation state by 0.1 units. In summary, the oxidatively stored charge in the catalytic region is quantified and exhibits a similar principle to the XAS results, i.e., an exponential relationship between current activity and oxidatively charge. The catalytic current is exclusively determined by the redox chemistry of the metal ions rather than the oxidation of bound water species.

3.2.3 Oxidation states changes tracked by optical absorption via in situ UV-vis spectroscopy

XAS allows for direct monitoring of absolute changes in the oxidation state on CoCat,[126;134;158] but the beam time allocation of the synchrotron light source is limited for most working groups. UV-vis absorption spectroscopy (UV-vis) is the most widely used equipment in laboratories for monitoring the electronic transition of molecules or substances as they interact with UV-visible light. Therefore, it is often used as a preliminary analytical technique.[126;152;203;343;345;346;432;433] One advantage of UV-visible spectroscopy over XAS is that there is less radiation damage. Therefore, we collected optical absorption spectra here to follow the oxidation state of cobalt. The spectra were collected after equilibrating the system for 2 min in KPi solution (0.1 M) at different potentials and pH values. Thin CoCat (10 mC cm^{-2}, ~70 nm thickness) was used for optical spectrum acquisition.

Regarding the application of UV-visible spectroscopy to CoCat, Risch et al. in 2015 found that changes in light absorption in the near-UV and visible ranges correlate closely with trends in oxidation state changes measured by XAS at different potentials.[126] Subsequently, Pasquini et al. 2019 used time-resolved in situ visible absorption spectroscopy to perform a kinetic experiment to track the Co redox transition process at a fixed optical wavelength.[134] Therefore, UV-visible absorption spectroscopy is an important technique for monitoring electrochemical redox transitions, which may relate to the electrochromic effect of CoCat,[434;435] also revealed from other transition metal oxides or hydroxides.[213;252;436-439]

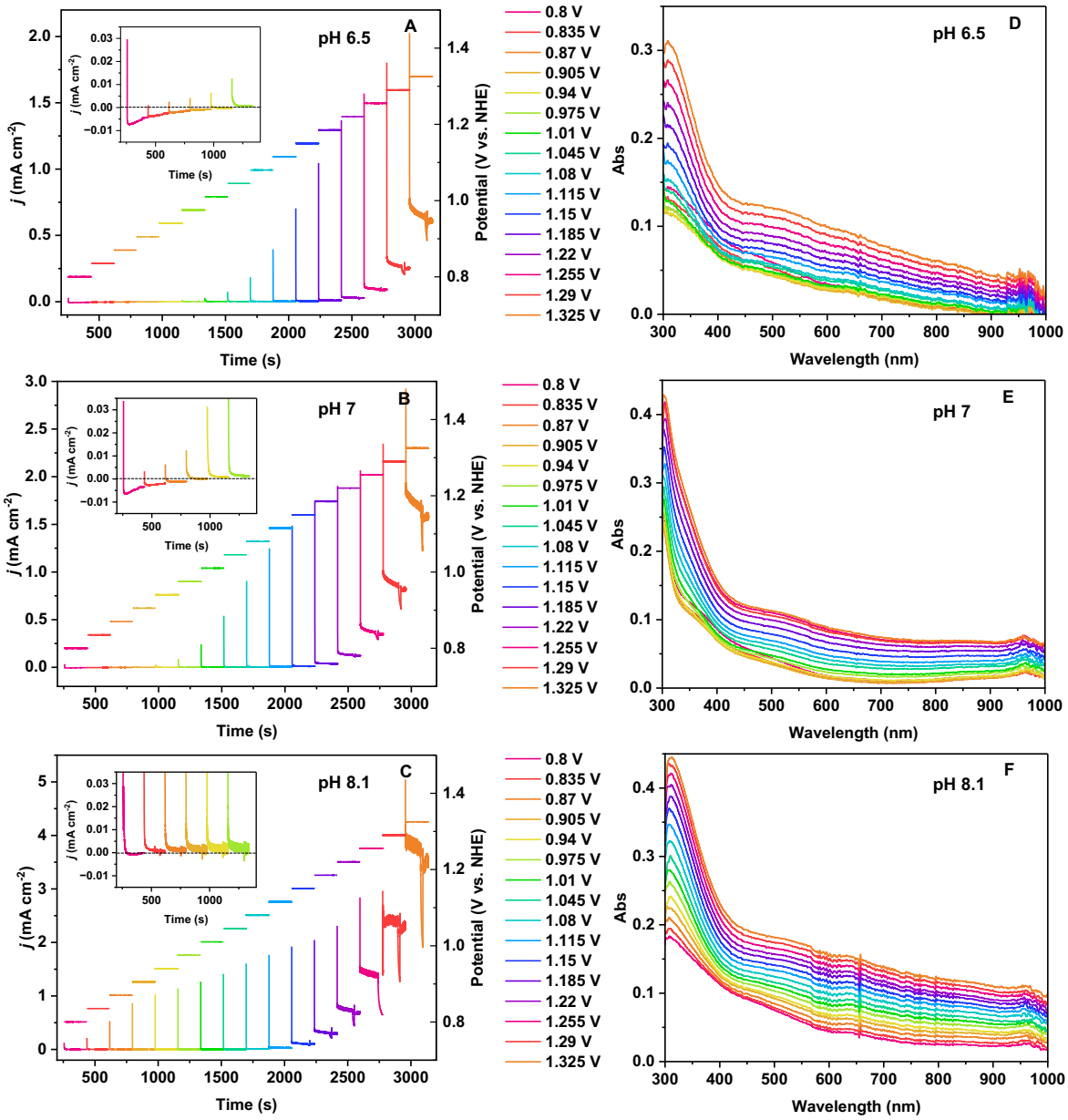

Figure 3-15. Electrochemical protocol for in situ UV-vis absorption spectroscopy measurements (A–C) and optical absorption spectra (D–F) of CoCat at different electrode potentials for CoCat operated in KPi solutions (0.1 M) at different pH values. Insets of A-C zoom in current density traces from 0.8 V to 0.975 V. CoCat films were deposited on ITO (10 mC cm^{-2}, ~ 70 nm thickness). The applied potential is 0.8 V to 1.325 V vs. NHE. In panels A-C, the sharp peaks at the end of current traces resulted from the switch off the stirrer for spectrum collection. Note that the electrochemical system is constantly agitated at 500 rpm and is only left unstirred when collecting spectra. We also note that difference of absolute absorbance at different pH values may due to subtle changes of the position of the working electrode. The displayed absorbance curves were smoothed using commercially available software (OriginPro 2020b). The adjacent averaging method is used here with a window size of 5 points. The figure shown here is from individual measurement.

Steady-state light absorption spectra (Figure 3-15 D-F) were measured using a constant potential staircase protocol (Figure 3-15 A-C) under different pH conditions. Negative current

densities ranging from 0.8 V to 0.94 V were observed at pH 6.5. As pH rises to 7, the onset potential of the positive current shifts to 0.905 V toward the cathode. At pH 8.1, negative currents only appear at the lowest applied potential (0.8 V). The negative current originates from the incomplete reduction process after initial 3 CVs (1.3 V-0.45 V vs. NHE). The onset potential of the forward current is pH-dependent resulting from the pH-dependent Nernst potential shift. Interestingly, the absorption spectra at all pH values appear to follow a similar trend of *j*-V curves (Figure 3-15 D-F). In the negative current regime, the absorption spectra overlap with those in the positive current regime and decrease with increasing potential. The lowest absorption occurs before the current density becomes positive, which applies to all pH conditions, i.e., pH 6.5 (0.94 V), pH 7 (0.905 V), pH 8.1 (0.8 V). All spectra were taken between 300 nm and 1000 nm. There is a peak near 310 nm, followed by a sharp drop in absorption up to about 420 nm. The peak below 340 nm may be interfered with the absorption of the glass cuvette in the UV region. Subsequently, a broad peak centered at 500 nm appears. At ~656 nm, it is attributed to the hydrogen Balmer characteristic line (Dα) in the deuterium lamp emission spectrum. Following this, the absorption gradually diminishes until the region of 950-1000 nm. In this high wavelength region, the absorption features are very faint, and the peak at about 970 nm is probably from a water vibrational transition, which can be attributed to the combination of 2V1 (H–O–H symmetric stretching mode) and V3 (H–O–H asymmetric stretching mode).[440]

Since the absolute absorption intensity of CoCat films varies at different potentials and pH, the absorption at 0.94 V was used as a baseline and was successively subtracted from the spectra at all pH conditions to obtain the absorption difference spectra (ΔAbs) (Figure 3-16). At a specified potential, if the ΔAbs value is larger than zero, an oxidation process occurs. There are two distinct features of ΔAbs at ~400 nm and ~560 nm, with the peak of the former corresponding to a local minimum that appears to redshift with increasing potential (400 nm to 430 nm). At high potentials, the broad peak at ~560 nm becomes more prominent.

Furthermore, the ΔAbs curves were normalized (0-1) to compare the differences in ΔAbs at different potentials. It is clear that in the region between ~560 nm and 900 nm, the shapes of absorption differences at different potentials overlap, suggesting that the change in the shape of ΔAbs is independent of the potential. This suggests that changes in the magnitude of ΔAbs in this region can be used to extract information about redox chemistry at different potentials.[126] Therefore, in Figure 3-17, we chose ΔAbs at 600 nm to explain the relationship between current activity and absorption difference ΔAbs. In the lower wavelength region (300 ~ 400 nm), there also seems to be an overlap, but it may be affected by glass absorption. In Figure 3-17D, the normalized ΔAbs at 0.975 V have a slight deviation, but the shape is similar to the other deviations, so we attribute the incomplete overlap to noise. As a whole, the normalized spectra at different potentials overlap between 500 nm and 900 nm. In order to correspond to previous studies,[126] we chose the absorption difference at 600 nm to study the potential-induced absorption at different pH values of KPi solutions.

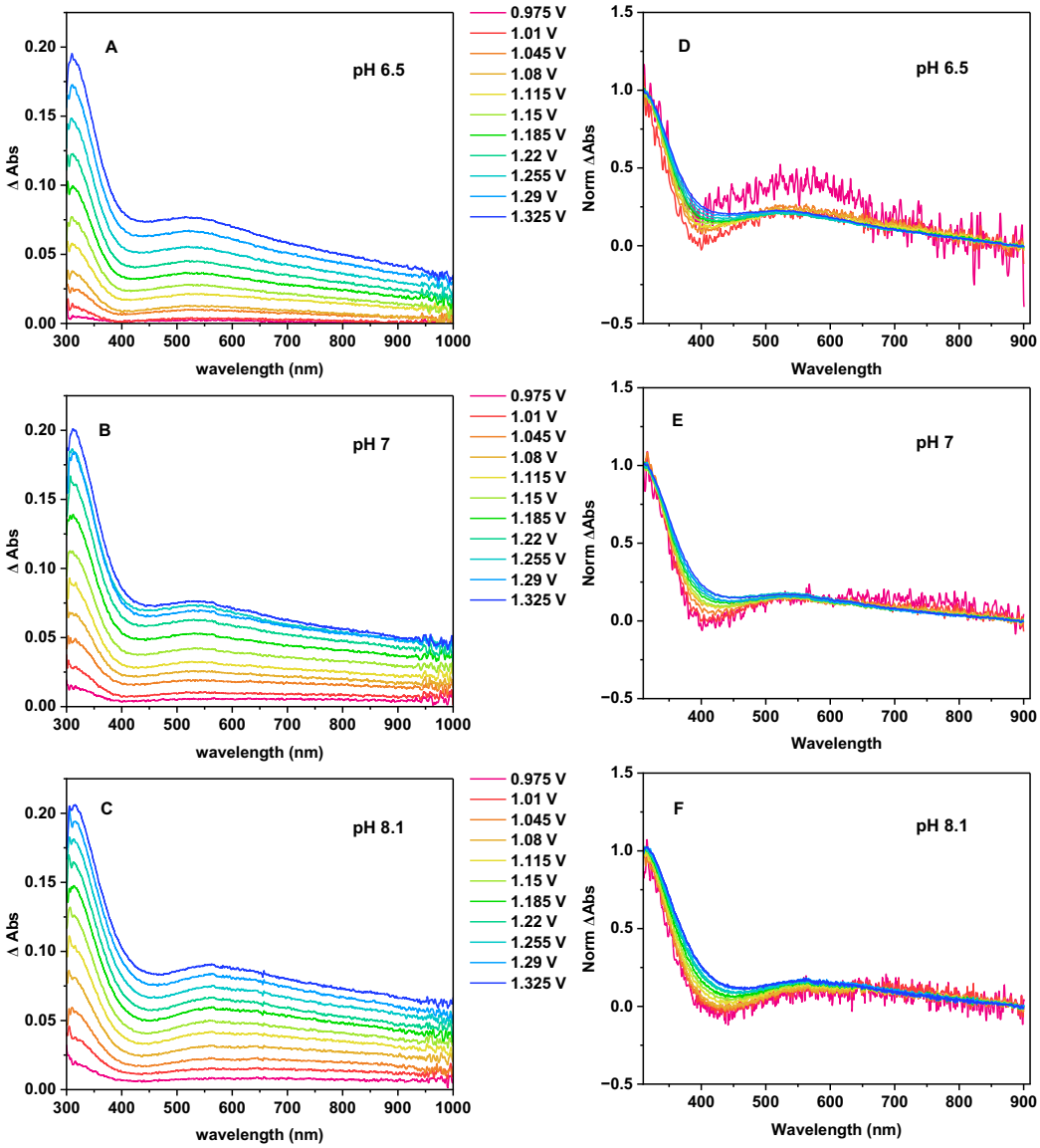

Figure 3-16. Absorption difference (ΔAbs) (A-C) and normalized absorption difference (D-F) at different potentials for CoCat operating in KPi buffer (0.1 M) at different pH values. ΔAbs at the indicated potentials (colour code) are the Abs values at the corresponding potential minus the Abs value at 0.94 V (baseline), respectively. ΔAbs at potentials above 0.94 V are displayed. The ΔAbs were normalized by setting ΔAbs at 900 nm to 0 and ΔAbs at 310 nm to 1. The displayed absorbance curves were smoothed using commercially available software (OriginPro 2020b). Adjacent averaging was used here with a window size of 5 points. The graph displayed figure from single measurement. The data corresponds to Figure 3-15.

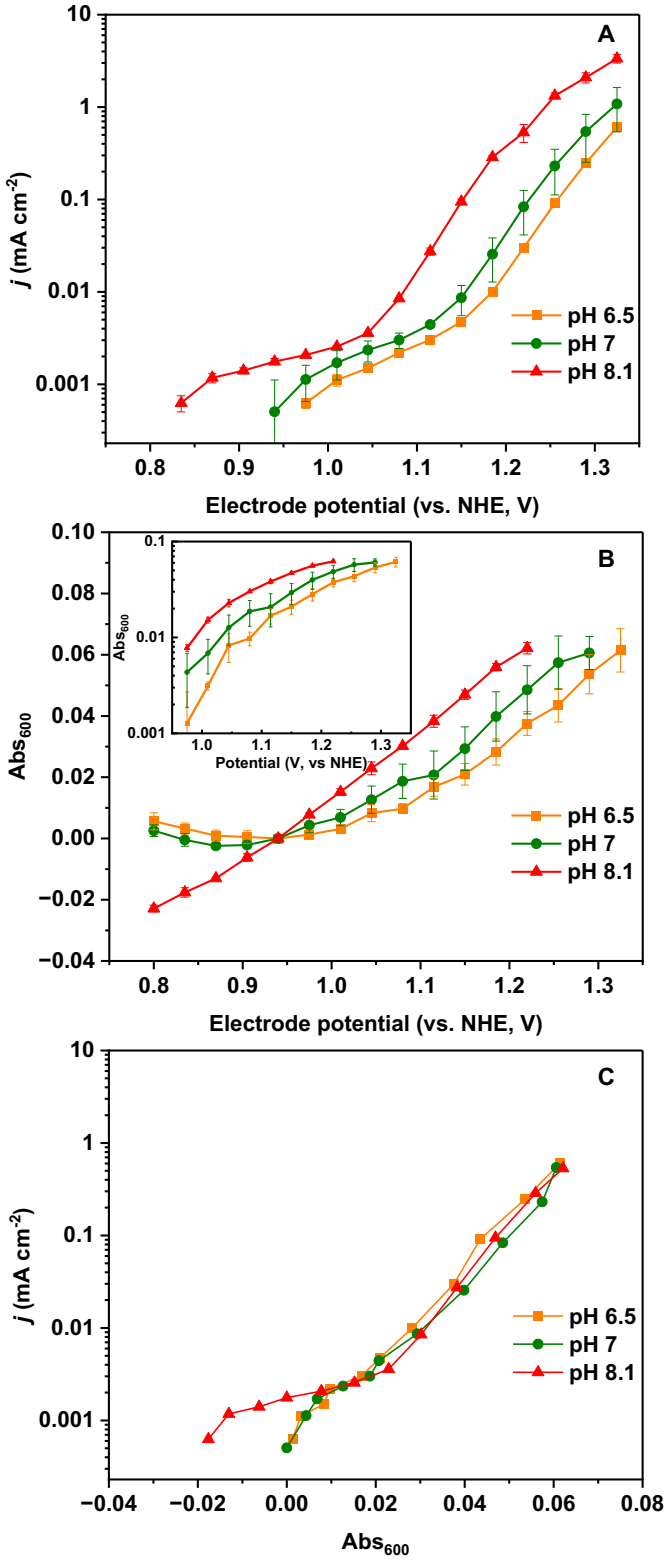

Figure 3-17. Comparison of current density, optical absorption difference (ΔAbs) at 600 nm and electrode potentials for CoCat operated at different pH values of KPi. The results are mean of at least three individual measurements for each condition. Error bar represents one standard deviation (68% confidence interval). The inset highlights the apparent saturation effect of Abs_{600} as a function of potential, where Abs_{600} is displayed on a logarithmic scale.

With taking the change in absorption (ΔAbs) at 600 nm (denoted as Abs_{600}), the correlation between Abs_{600}, applied potentials and current densities is established in Figure 3-17. Panel A is typical Tafel plots at different pH values (0.1 M KPi), where a pH-dependent Nernstian cathodic shift is observed at the same current density (e.g., 10 μA). At high potential, current is saturating, and this saturation current tends to increase with a rise in pH level due to the higher amount of buffer base at higher pH. Interestingly, when the applied potential is higher than 0.94 V, the trend between Abs_{600} and the potential follows the same trend as the *j*-V curve. At the same potential (e.g., 1.2 V), a larger Abs_{600} is associated with a higher pH value of the KPi buffer. Similarly, a cathodic shift of the potential was observed at the same absorption level. Absorption saturation emerges at the onset potential similar to that of *j*-V curve (Figure 3-17 A). However, due to light scattering of accumulated air bubbles attached on the electrode surface, absorption spectra at higher potentials could not be obtained for high pH case, even with the use of a magnetic stirrer (500 rpm). A higher stirring rate may help, but absorption signal will be compromised by signal noise. At pH 6.5, reproducible absorption can be measured at higher potentials. Abs_{600} (ΔAbs, $Abs_V - Abs_{0.94V}$ at 600 nm) are positive or negative depending on the choice of baseline. Here, baseline at 0.94 V was selected for all pH conditions and subtracted separately to calculate ΔAbs at another potentials. At pH 6.5, Abs600 is positive at potential below 0.94 V as its local minimal absorption at 0.94 V. For pH 7 and 8.1, the lowest absorption (Abs) is below 0.94 V. At pH 8, the minimum value of Abs is 0.8 V, thereby ΔAbs ($Abs_{0.8V}$-$Abs_{0.94V}$) is negative when applied potential is belows 0.94 V.

Importantly, the exponential relation between current density and the change in absorption at 600 nm is agreement with that of the first two experiment techniques and is irrespective of pH. Analogously, power law between current density and the optical absorption (Figure 7-3) is also applicable for in situ UV-vis absorption results.

3.3 Summary

A. Experimental finding

Three methods of operando XAS, basic electrochemistry, and in situ UV-vis absorption spectroscopy support the critical role of metal-centered redox chemistry in determining OER catalytic rate:

(1) Operando XAS at the Co K-edge directly monitored the oxidation state over a wide potential range (0.85-1.61 V vs. NHE). The current density in the catalytic region was independent of the electrode potential but was exponentially related to the oxidation state at different pH and KPi concentrations. Meanwhile, the exponential behavior is not affected by pH and KPi concentration.

(2) With simple electrochemical potential jumps, oxidatively stored charge at different potentials has been quantified and the total redox-charge change is coincident with the change of cobalt oxidation states. It confirms that the redox chemistry of the cobalt center rather than the oxidation of bound water species contributes to the charge accumulation. For pH or KPi concentration series, a unified slope between accumulated charge and logarithmic current

density suggests intrinsic behavior that is independent of electrolyte proton activity and mass transport limitation.

(3) In situ UV-vis absorption spectroscopy was used as a complementary technique to record steady-state light absorption at different potentials. The change in absorption intensity at a fixed wavelength (600 nm) is linearly related to the logarithm of the current density, which further solidifies our new concept that the catalytic rate is directly determined by the chemical states of cobalt ions.

B. Generalizing hypothesis

The OER catalytic rate is determined by the redox chemistry of the catalyst material. This conclusion may be of general importance for an extended class of OER catalyst materials that are either thoroughly amorphous, hydrated oxyhydroxides (as here is the case for the CoCat) or form an amorphous, hydrated oxyhydroxide overlayer under operation conditions (as likely is the case for most materials in OER catalysis). The relevance of the here reported finding for these materials is summarized in the following.

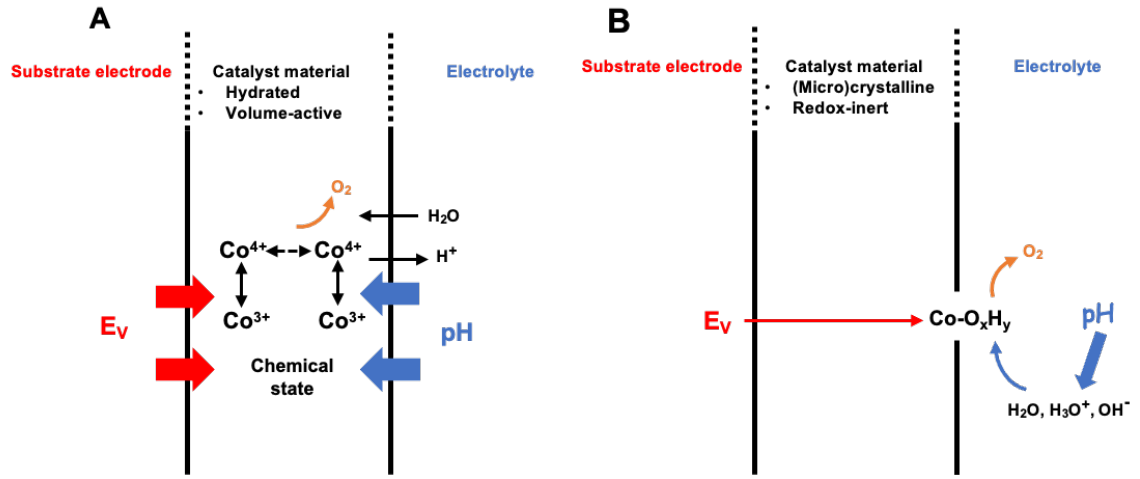

Figure 3-18 Basic concepts explaining OER electrocatalysis for (A) typically amorphous, volume-active material layers (here proposed new concept) and (B) surface-active crystalline materials (conventional concept). (A) In A, the material undergoes redox transitions such that its chemical state follows the electrode potential, E_V, and the electrolyte pH at the outer surface of the catalyst material. The chemical state in turn determines the OER rate. Because of energetic interactions within the catalyst material, the redox-transitions are non-Nernstian and the rate of OER catalysis depends exponentially on the number of high-valent metal ions (Co^{4+} ions). The electrode potential affects the rate of OER catalysis indirectly by controlling the chemical state of the material. Electric fields and ionic double-layer effects are not decisively involved. (B) In b, the electrode potential, E_V, is transmitted by the crystalline catalyst material towards the material surface where it facilitates the reaction chemistry of surface-adsorbed H_yO_x species, typically bound to a metal ion (M–OH_2, M–OH, M=O, M–O–OH). The electrolyte pH determines the relative availability (local concentration) of H_3O^+ or OH^- and thereby affects the OER rates. The ionic double-layer structure, the potential drop at the material-electrocyte interface and related electric fields may decisively affect the rate of OER catalysis.

The results summarized above (in Section 3.3 A) support a fundamental concept for the interpretation of OER electrocatalysis in non-crystalline (amorphous) materials like the

(CoCat), which is illustrated in Figure 3-18A. The electrochemical potential, ϕ_{EC} comprising both the electric potential at the working electrode and the contribution of the electrolyte pH uniquely determines the chemical state of the catalyst material, that is, the metal ion oxidation states, protonation states and related changes in atomic structure. Various combinations of electric and pH contributions to a specific value of ϕ_{EC} result in the same chemical state of the catalyst material. The rate of catalysis then depends on the chemical state of the catalyst material; it does not directly depend on the applied potential or related electric fields. This contrasts the classical view of the electric potential (or related electric fields) that directly facilitates oxidation of water species adsorbed at surface sites, and an electrolyte pH determines the availability of H_3O^+ and OH^- ions at the reactive surface sites (Figure 3-18).

Regarding the OER mechanism, amorphous cobalt oxides may differ from the classical pure surface prototype mechanism involving the adsorption and desorption of reaction intermediates.[311;441] The OER mechanism for CoCat (and likely also Mn, Ni and other oxyhydroxides) can be described in terms of molecular mechanisms applied for molecular metal complexes or PSII active centers (Mn_4CaO_x complex).[213] However, the molecular mechanism does not fully explain this due to the non-classical Nernstian behavior during the redox transition of Co.[126] The exponential relationship between reaction rate and oxidation state appears to be related to the reduction of activation energy, which can be explained by the presence of interaction energy between several high-valent cobalt species. In conclusion, amorphous CoCat-type heterogeneous materials may exhibit molecular mechanisms[138;159] as well as solid-state material properties.

We assumed that the catalytically active phase of all materials, especially the oxides or hydroxides prevalent in OER, generally conforms to the picture of molecular-and-material-properties, inter alis because it is hardly possible to maintain an absolutely crystalline material under OER operation. It has been frequently reported that extended surface modification (amorphization) often occurs under harsh chemical conditions and in the course of prolonged operation.[67;105;107;153;154;178;234;442-445] The Janus character of the OER materials may be summarized as follows:

(1) In the molecular picture, the molecular chemistry depends on the oxidation state, which is consistent with the observation of the structural arrangement of CoCat during the redox process,[126] illustrating the molecular properties of solid-state CoCat material.

(2) On the other hand, a property not covered in the simple molecular picture is the interaction between metal ions regarding material aspect properties. However, this interaction does not reach the extreme case where strong interactions have to be modeled using a band model, which is quite different from the model in ref.[126].

Therefore, we suggest that CoCat and its derivatives have an in-between state, i.e., having redox chemistry in their molecular properties, while also being affected by interactions between metal sites in solid-state materials.

3.4 Experimental details

3.4.1 Oxidation states determination from XAS

For pH or KPi concentration series of XAS experiments, CoCat (20 mC cm^{-2}) was deposited on a graphene sheet or glassy carbon by applying a potential of 1.05 V vs. NHE, and the deposition methods were described elsewhere.[70;126] The pH of KPi buffer is adjusted by adding concentrated KOH or same concentration of phosphate solution (K_2HPO_4 or KH_2PO_4). Electrolyte salt KNO_3 (500 mM) in the pH series was added to enhance ionic conductivity. Different concentrations of the electrolyte salt KNO_3 (0 and 1.6 mM KPi: 500 mM; 25 mM KPi: 450 mM; 100 mM KPi: 300 mM) were added in KPi concentration series while maintaining the total ionic strength at a high level of ca. 500 mM. The pH series is stirred at ca. 300 rpm without ohmic resistance compensation. KPi concentration series measured in steady state conditions with iR correction (85% iR compensation, software mode, BioLogic 200). Three CVs (0.45 V to 1.45 V vs. NHE, 20 mV s^{-1}) were performed followed by a potential staircase protocol. A Pt grid and a double-junction Ag/AgCl (Metrohm, saturated KCl, + 0.197 V converted to NHE) were used as counter electrode or reference electrode, respectively.

XAS experiments at the cobalt K-edges were carried out at the bending-magnet beamline KMC-3 at the BESSY-II synchrotron (Helmholtz Center Berlin, Germany, top-up mode of the storage ring, ca. 300 mA) using a 13-element Si-drift detector (RaySpec) for X-ray fluorescence monitoring. A Si [111] double-crystal monochromator was employed for continuous scanning of the incident energy. All spectra were collected in situ at room temperature in customized electrochemical cells with graphene sheets or glassy carbon serving as substrate. X-ray beam passes through the backside of the substrate covered with Kapton tape. CoCat was exposed to a KPi solution with an area of 1.33 cm^{-2}. In the pH series, spectra at certain potentials were not available or lost due to monochromator or spectral computer crashes. Thus, the spectra were recollected using fresh samples under the same conditions, i.e., at pH 8, spectrum at 0.95 V vs. NHE; at pH 7, spectra at 0.95 V, 1.33 V vs. NHE. Note that spectra in the low potential region (0.85 V–1.28 V vs. NHE) were collected unstirred at 100 mM KPi (pH 7), otherwise the pH series data were collected with stirring. All spectra were obtained after 1 min of equilibration for each potential step.

Current density at each electrode potential is determined by averaging current between 420 and 425 s (pH series) or 300–340 s (KPi concentration series). XAS data analysis initiated with deadtime correction and normalization of incident X-ray intensity (I_0) (See Figure 3-19 operando XAS configuration). Dead time correction is applied by exponentially fitting of the incoming count rate (ICR) value to correct the outcoming count rate (OCR). Afterwards, fluorescence signals of the 13 channels were averaged. Since operando XAS measurement cannot measure transmission, simultaneous energy calibration cannot be performed by calibrating the absorption of Co foil. Typically, the Co foil spectrum is measured several times during sample collection to compare the peak center of the derivative of the absorption spectrum $-\ln(I_2/I_1)$, i.e., after subtracting the background and normalization followed by a Gaussian fit. The peak center positions should keep constant, otherwise an overall calibration

should be performed to ensure the comparability of the results, especially for samples that are not measured in the same batch.

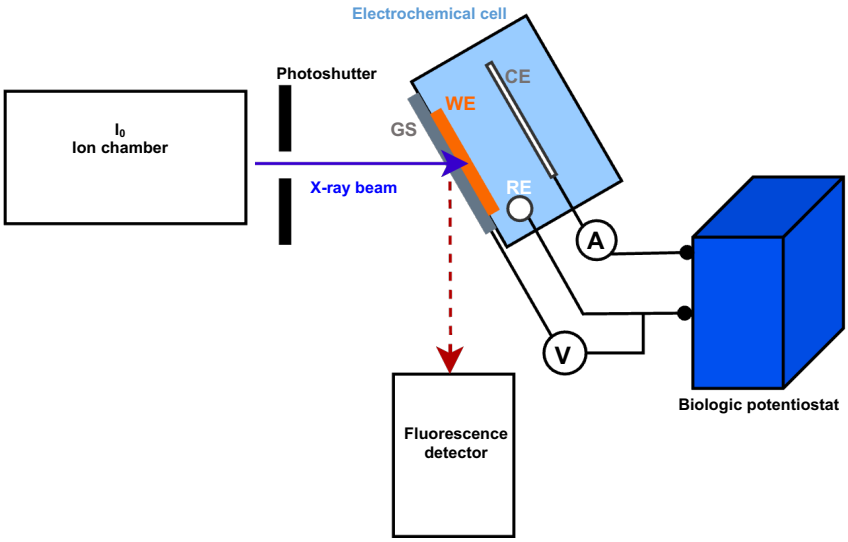

Figure 3-19. Experimental setup for in situ XAS in fluorescence mode (schematic drawing). WE, working electrode; CE, counter electrode (Pt grid, 20 ×20 mm^2); RE, reference electrode (Ag/AgCl); GS, graphene sheet; the orange area symbolizes the thin (nm thickness) CoCat film (not drawn to scale) electro-deposited onto the graphene support. The X-ray fluorescence is monitored by a 13-element Si-drift detector (Ray Spec) operated in an energy-resolving photon-counting mode. A SP-200 BioLogic potentiostat is used.

Besides, based on our earlier work, the peak center of the derivatives of the pre-edge spectrum of CoCat maintains at same excitation energy, irrespective of the applied potential and the change in the cobalt oxidation state.[126] Thereby, a fine energy calibration in the pre-edge region was conducted. Specifically, the incident X-ray energy axis is shifted such that the center position of the first peak of the derivative of the fluorescence signal is aligned with 7707.8±0.1 eV. In addition, comparison of OCP spectra of dried samples for the pH and KPi concentration series can aid in the pre-edge calibration. The spectra were normalized by subtracting a constant (here, pH series fitted between 7675 and 7684 eV; KPi concentration series fitted between 7679 and 7688 eV) and divided by a quadratic function (pH series fitted from 7764 to 8279 eV; KPi concentration series fitted from 7769 to 8270 eV). Subsequently, edge positions were determined by the integral method.[316]

3.4.2 Determining of oxidatively stored charge

Oxidatively stored charge was obtained by the potential jumps protocol using the CA technique. The potential rises from 1.548 V vs. RHE with a potential increment of 35 mV and then constantly jumps to 1.513 V vs. RHE. Each potential applied for 2 min. Current curve was acquired with a resolution of 10 ms, and current density was determined from the average current of the last 5 s (500 pts). The oxidatively stored charge during the oxidation process was determined by integrating over the 2-minute time course of the reduction current trace. The applied potential was corrected for iR drop (85%). Three CVs were collected from 0.45 V to

1.45 V vs. NHE before starting CA jumps. CoCat deposited on ITO (20 mC cm^{-2}) was used to determine the oxidative stored charge at different KPi conditions. The electrolyte system was varied by adding KNO_3 (500 mM) or using a magnetic bar stirring system (400 rpm).

3.4.3 In situ UV-vis absorption spectroscopy

UV-vis absorption spectrum measurements were performed using a commercial UV-vis spectrophotometer (ALS SEC 2020) equipped with a deuterium halogen light source. The spectrometer consists of a detector (2048 element linear silicon CCD array) and two lenses (collimating lens and fiber optic collimator). Taking advantage of the advanced detector of the spectrometer, absorption spectra at all wavelengths can be obtained simultaneously. Here, we have collected absorption spectra from 300 nm to 1000 nm. The reference and dark spectra were measured by averaging 10,000 acquisitions before the sample spectra were taken. After correction of the reference spectrum, the deuterium lamp absorption at ~ 656 nm is still observed. Sample spectra were taken as an average of 100 measurements (~1 s) and a 10 ms integration time. A 3D-printed cuvette holder was used to block external light and placed between the light source and the detector. The configuration of in situ UV-vis experiment is shown in Figure 3-20.

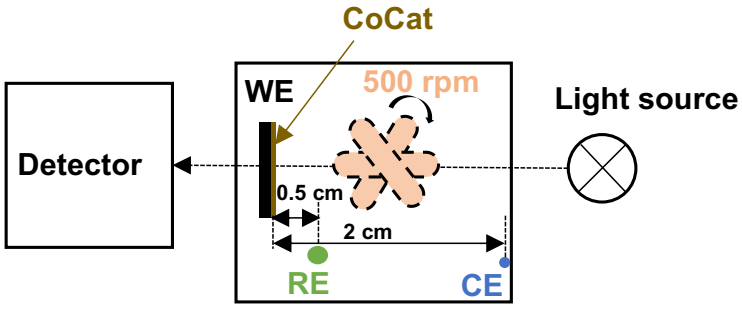

Figure 3-20. Top view of in situ UV-vis photoelectrochemistry experimental setup (ALS spectrometer) with magnetic bar stirring in the electrolyte. WE, CoCat (10 mC cm^{-2}) deposited on ITO (1 cm^2); RE, 3 M Ag/AgCl (+ 0.205 V converting to NHE); CE, Pt wire. The distance between the Pt wire and the ITO working electrode was 2 cm. The distance between RE and WE was 0.5 cm. We note that this scheme is a simplified version. The cuvette holder is flanked by two light guides. The detector system consists of a grating and a linear silicon CCD array detector.

Glass cuvette containing ca. 6 mL of KPi solution (0.1 M, pH 6.5/7/8.1) was placed in a 3D-printed cuvette holder. CoCat catalyst (10 mC cm^{-2}) deposited at 1.05 V was used as the working electrode (WE) with ITO as the substrate (10 mm × 25 mm, Visiontek Systems Ltd.). A single chamber Ag/AgCl (filled with 3 M KCl, Ossila) (RE, $E_{NHE} = E_{Ag/AgCl} + 0.205$ V) and a platinum wire act as reference electrode and counter electrode (CE), respectively. The printed cover fixes the relative positions of the three electrodes to ensure reproducibility of the experiment (WE/RE, 0.5 cm; WE/CE, 2 cm). A stirrer (1.5 cm length) was used during spectra collection to prevent bubble accumulation. The ITO side deposited with CoCat is first exposed to a light beam followed by the transmitted light detected by a short-range detector. ITO substrates were cleaned by sonication with ethanol, acetone and Milli-Q water for 15 min prior to film deposition. Electrolytes were prepared according to previously reported methods.[142]

The spectrometer was connected to the electrochemical potentiostat (BioLogic SP-300) via fiber optic cables. Prior to the acquisition of the CA step, a trigger pulse was applied to synchronize the BioLogic potentiostat with the spectrometer. All potentials (vs. NHE) are reported by iR drops correction (85%). Each electrode potential was applied for 180 s, ranging from 0.8 V to 1.325 V in 35 mV step increments. After 120 s of equilibration, the stirrer was manually turned off and the UV-vis spectra at each potential were recorded to prevent signal interference of stir bar. Three CVs of 0.45 V to 1.3 V vs. NHE were measured before performing the CA step. Note that during potential applied period, stirrer is used all the time except the period of spectrum acquisition (~5 s, including the time of stabilizing system). As shown in Figure 3-15A-C, current density droped due to the absence of stirring. Current density is an average of 120–125 s. For the spectra at different pH values, at least three individual samples were measured. In order to compare ΔAbs at different pH, spectra at 0.94 V were chosen as a baseline, resulting in positive ΔAbs at pH 6.5 for all potentials, and negative absorption in the low potential region at pH 7 or 8.1 (see more in Figure 3-15). ΔAbs were normalized by taking ΔAbs to 1 at 310 nm (average of ΔAbs at 308 nm–312 nm) and 0 for ΔAbs at 900 nm (average of ΔAbs at 880–900 nm). ΔAbs at 600 nm was averaged between 590 nm and 610 nm.

4 Role of potassium in electrocatalytic water oxidation investigated in a volume-active cobalt material at neutral pH

Abstract Catalytic OER materials often undergo potential-induced redox transitions located at metal sites. For volume-active catalyst-materials, these are necessarily coupled to charge-compensating relocation of ions entering or leaving the material, which is insufficiently understood. In this chapter, the binding mode and mechanistic role of redox-inert potassium ions for CoCat when operated at neutral pH in the potassium-phosphate electrolyte are investigated by i) determination of K:Co and P:Co stoichiometries for various KPi-concentrations and electrode potentials, ii) operando X-ray spectroscopy at the potassium and cobalt K-edges, and iii) novel time-resolved X-ray experiments facilitating comparison of K-release and Co-oxidation kinetics. Potassium likely binds non-specifically within water layers interfacing Co-oxyhydoxide fragments involving potassium–phosphate ion pairs. The potassium-release kinetics are potential-independent with a fast-phase time-constant of about 5 s and thus clearly slower than the potential-induced Co oxidation (result from Shima Farhoosh, not shown here) of about 300 ms. It is concluded that the charge-compensating ion flow is realized neither by potassium nor by phosphate ions, but by protons. The results reported here are likely relevant also for a broader class of volume-active OER catalyst materials and for the amorphized near-surface regions of microcrystalline materials.

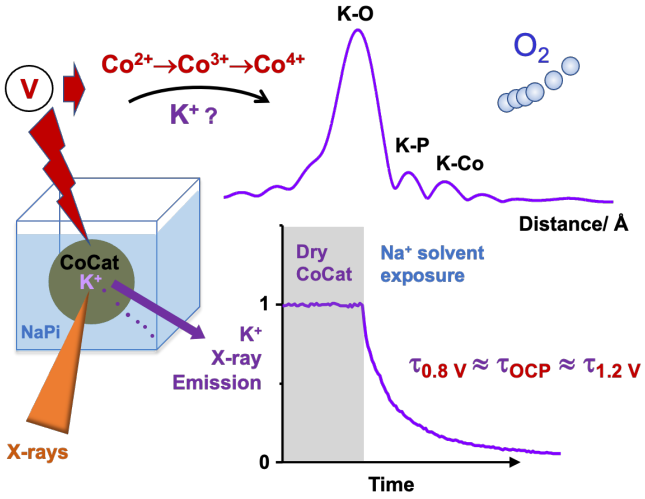

A portion of this chapter reproduced from:

a) S. Liu, S. Farhoosh, P. Beyer, S. Mebs, I. Zaharieva, M. Haumann, H. Dau*. Role of potassium in electrocatalytic water oxidation investigated in a volume-active cobalt material at neutral pH. *Advanced Sustainable Systems* **2023**, 7, 2300008. https://doi.org/10.1002/adsu.202300008

b) S. Liu, S. Farhoosh, P. Beyer, S. Mebs, M. Haumann, H. Dau*. Phosphate coordination in a water-oxidizing cobalt-oxide electrocatalyst revealed by X-ray absorption spectroscopy at the phosphorus K edge. *Catalysts* **2023**, 13, 1151. https://doi.org/10.3390/catal13081151

Author Contributions:

S. Liu performed all the experiments and data evaluation of this chapter unless otherwise noted;

S. Farhoosh provided time-resolved operando XAS data;

S. Mebs supported the illustration of the structural motif of potassium;

M. Haumann and H. Dau assisted in the XAS analysis;

I. Zaharieva, S. Mebs, P. Beyer, M. Haumann supported synchrotron measurements and contributed by valuable discussion;

H. Dau supervised research.

4.1 Introduction and motivation

In recent decades, numerous catalysts or materials have been extensively investigated for improving the electrocatalytic OER performance.[40;53;229;415;446;447] The focus is often on the properties of the transition metals (e.g., Mn, Fe, Co, Ni, Ir, Ru), inter alia because they are often redox-active, meaning that their oxidation state varies reversibly in response to applied electric potentials.[99;126;250-252] Also the role in OER of redox-inert cations present in the electrolyte and/or within the catalyst material has been investigated,[123;201;202;253-259] but their function is still insufficiently understood.

Here, we investigate the binding mode and mechanistic role of redox-inert potassium ions for volume-active CoCat[65;70;99;112;113;116;119;125;135;158] when operated at neutral pH in potassium-phosphate (KPi) electrolyte. For volume-active catalyst materials, electrochemical processes are necessarily coupled to charge-compensating relocation of ions entering or leaving the material, which guides the core of this chapter. Central open questions regarding the role of potassium ions are:

(1) What is the structural role of K^+ ions bound within the CoCat material? In our earlier Co K-edge extended X-ray absorption fine structure (EXAFS) analysis, the presence of Co(μ–O)K motifs with a Co–K distance of ~3.8 Å was proposed.[112] Subsequently, Kanan et al. compared the EXAFS spectra of potassium-phosphate (KPi-) CoCat and sodium-phosphate (NaPi-) CoCat and found no structural difference.[158] Ex-situ X-ray absorption spectroscopy (XAS) at the potassium K-edge suggested that ca. 10 % of K^+ ions may be constituents of (distorted) $KCo_3(\mu\text{–}O)_4$ cubane structures.[123] The question remains whether potassium ions can be part of specific K–Co coordination motifs, i.e., in cubane structures similar to those suggested for calcium (Ca^{2+}) ions in Ca-containing Mn oxides,[153;341;448;449] with analogies to the biological (Mn_4Ca) OER catalyst of oxygenic photosynthesis.[148;149;450]

(2) Do K^+ ions facilitate charge compensation in the redox transitions of the catalyst material? The potential-dependent redox transitions of the CoCat bulk material (Co^{II}<-> Co^{III} <-> Co^{IV}) involve proton-coupled electron transfer and likely charge-compensation by proton release (for Co oxidation) or uptake (for Co reduction).[40;126;134] However, whether K^+ ions or other redox-inactive cations can also participate in the charge compensation process is insufficiently understood. A role of K^+ uptake and release for alkaline OER in KOH electrolyte indeed has been suggested recently. Grimaud et al. reported K^+ insertion into layered iridium oxides during OER, with the insertion process incurring a phase transformation of oxidized α-Li_1IrO_3

coupled with Ir reduction and K^+ ions likely participating in the overall charge balance process.[265] For NiFe and CoFe oxyhydroxides, Strasser and coworkers reported α to γ phase conversions and contraction of lattice spacing in the OER catalytic regime,[269] as induced by Co/Ni oxidation and associated with intercalation of K^+ ions.

Here, in this chapter, we provide insights by addressing experimentally (1) the structural and (2) the charge-compensating role of K^+ ions for the Co-based catalyst material which may serve as a model system for OER at neutral pH in general. Progress comes from monitoring the response of CoCat electrocatalytic films to electrolyte variations and changes in electrical potential by quantitative elemental analysis, experimentally challenging ex situ and operando (in situ) XAS at the potassium K-edge, and novel time-resolved X-ray experiments (results from S. Farhoosh[143]).

4.2 Results and discussion

4.2.1 Elemental analysis after variation of electrolyte and electrode potential

Potassium as well as phosphate have been verified to be internal constituents of CoCat at an approximate Co:P:K ratio of 2-3:1:1, for catalyst films electrodeposited in 100 mM potassium phosphate (at pH 7).[70] The question remained whether and how the potassium content of the catalyst film changes during operation (i) in electrolytes with varying K^+ concentrations and (ii) in response to changes of the electrode potential. Therefore, elemental analysis via total reflection X-ray fluorescence (TXRF) was carried out for CoCat films after operation 15 min at different KPi concentrations (1.6 mM, 25 mM, or 100 mM) or electrode potentials (1.0 V or 1.3 V vs. NHE).

In order to approach a precise determination of the light element K, each digested CoCat sample was divided into six portions with each portion adding well-known concentrations of a K-standard (Table 4-1). The amounts of Co and K in CoCat films can be concomitantly quantified by adding gallium (as a concentration standard for Co) and caesium ($Ga/Cs(NO_3)_3$, 1 g L^{-1}, Fluka Tracecert) standards. A scheme of the TXRF sample preparation procedure is shown in Figure 4-1. Calibration curves of CoCat films operated at three KPi concentrations and two electrode potentials are obtained (Figure 4-2, Table 4-2). Correspondingly, the molar ratio of K and Co within CoCat films are summarized in Figure 4-3. Noteworthy, the CoCat undergoes the same oxidation state and structural changes in response to the electrode potential at all three KPi electrolyte concentrations.[142]

Table 4-1. K standard solutions that were added to the assay mixtures.

Potassium conc.	K1	K2	K3	K4	K5
[mg L^{-1}]	1.97	3.78	5.68	7.58	9.42

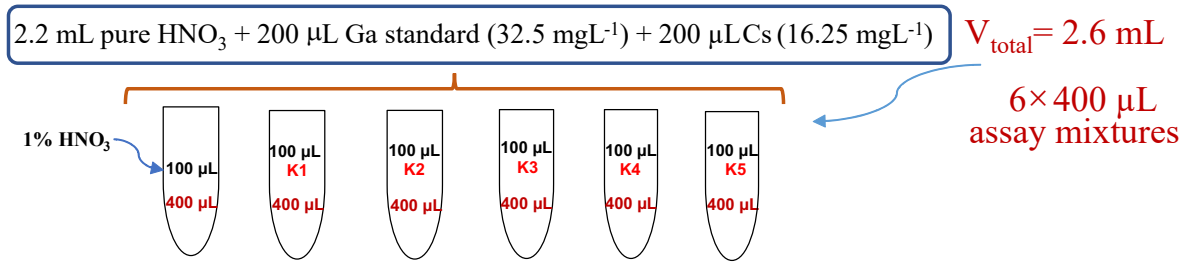

Figure 4-1. Scheme of the CoCat film dissolution procedure. The concentrated Ga and Cs standard was diluted to the indicated concentration with 1% (v/v) HNO_3. K1–K5 stands for the known K standard concentrations added to each assay mixture. The standard K concentrations are listed in Table 4-1.

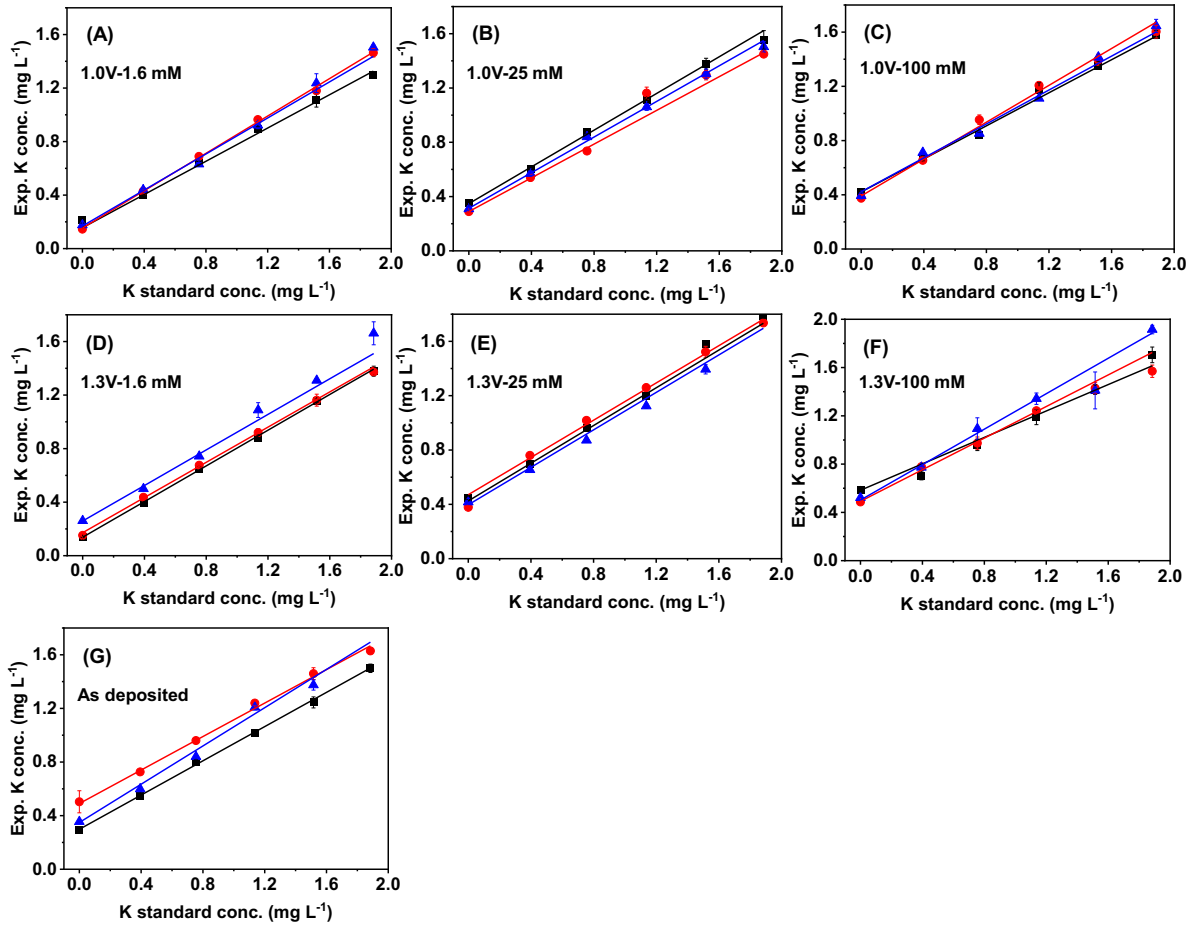

Figure 4-2. Quantification of potassium contents in CoCat films. Calibration curves of CoCat films operated at three KPi concentrations and two electrode potentials (A-F) or of as-deposited CoCat film (G). Symbols show experimental data and solid lines show linear regressions with parameters listed in Table 4-2. The three curves in each figure result from three independently prepared CoCat samples. The experimental K amount was calculated from the intercept of the fit lines divided by the corresponding slope. The indicated potassium standard concentrations are the concentrations of the added amounts of K in each assay mixtures. Data points represent the mean values of at least three TXRF measurement repetitions for each sample, error bars show standard deviations.

Table 4-2. Linear regression parameters in Figure 4-2.

KPi conc. [mM]	1.0 V vs. NHE	R^2	1.3 V vs. NHE	R^2
1.6	Y = 0.62 X + 0.16	0.99512	Y = 0.67 X + 0.14	0.99963
	Y = 0.70 X + 0.15	0.9984	Y = 0.66 X + 0.17	0.99643
	Y = 0.67 X + 0.17	0.9924	Y = 0.66 X + 0.26	0.9969
25	Y = 0.68 X + 0.35	0.99764	Y = 0.69 X + 0.43	0.99452
	Y = 0.62 X + 0.29	0.99741	Y = 0.69 X + 0.47	0.98697
	Y = 0.66 X + 0.31	0.99757	Y = 0.69 X + 0.40	0.96759
100	Y = 0.61 X + 0.42	0.99769	Y = 0.55 X + 0.58	0.98458
	Y = 0.68 X + 0.39	0.9917	Y = 0.65 X + 0.49	0.99322
	Y = 0.63 X + 0.42	0.98167	Y = 0.73 X + 0.50	0.99503
As deposited	/	/	Y = 0.64 X + 0.30	0.99915
			Y = 0.62 X + 0.49	0.99243
			Y = 0.71 X + 0.35	0.98477

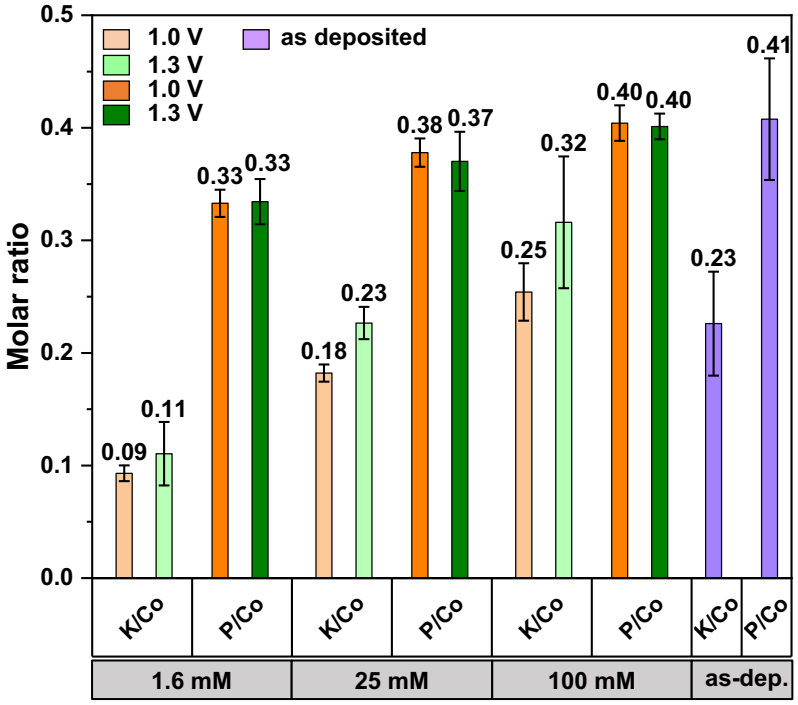

Figure 4-3. Molar ratio of potassium, phosphorus, and cobalt for CoCat films after operation at two electrode potentials (1.0 V or 1.3 V vs. NHE, pH 7) and in various electrolyte concentrations of potassium phosphate (KPi). Each film was operated at the indicated electrode potential for 15 min. The molar ratios for CoCat directly after electrodeposition in 100 mM KPi are labelled "as deposited" (as-dep.). The K/Co ratios resulted from 3 experiments on 3 CoCat films; for each CoCat film, minimally 3 quantifications of the Co and K^+ contents were conducted; error bars show standard deviations (Equation 2-1). For further details, see Figures 4-1 and 4-2 and Tables 4-1 to 4-3. The molar ratios of P and Co were calculated from data reported by us elsewhere.[142] Here the molar K/Co ratios were determined for CoCat films deposited on a platinum sheet whereas the P/Co quantification refers

to films deposited on indium tin oxide (ITO); there are no indications that the substrate electrode material affects the elemental composition of the comparably thick CoCat films (ca. 140 nm[99;105]). Reproduced with permission from ref.[143]. Copyright Wiley-VCH (2023).

Table 4-3. Molar ratio of K and Co amounts within CoCat films operated at different KPi concentrations and electrode potentials. The potassium amounts (mg L^{-1}) were calculated according to the regression lines in Figure 4-2 using the intercept of the y-axis divided by the slope (see Table 4-2). In the two K/Co columns, the underlined values provide the averaged molar ratios shown in Figure 4-3, which were calculated from the corresponding weight ratios, multiplied by 59/39 (ratio of atomic weights of Co and K). The cobalt amount was quantified using a Gallium (Ga) standard added to the samples as a reference. The indicated amounts in mg L^{-1} are the mean values from at least 3 independent CoCat films and 3 measurements each. The statistical error of the K/Co ratio value is calculated as the standard deviation of the molar ratios, for the three independent samples at each KPi concentration and potential (in V vs. NHE) shown in this table.

KPi conc. [mM]	1.0 V ***K/Co*** weight ratio <u>molar ratio</u>	1.3 V ***K/Co*** weight ratio <u>molar ratio</u>	K 1.0 V [*mg* L^{-1}]	K 1.3 V [*mg* L^{-1}]	Co 1.0 V [*mg* L^{-1}]	Co 1.3 V [*mg* L^{-1}]
1.6	0.06±0.01	0.07±0.02	0.25	0.21	3.97±0.06	3.99±0.07
	<u>0.09±0.01</u>	<u>0.11±0.03</u>	0.22	0.26	3.98±0.08	3.72±0.12
			0.25	0.39	3.78±0.04	4.01±0.30
25	0.12±0.01	0.15±0.01	0.51	0.61	4.03±0.12	4.11±0.15
	<u>0.18±0.01</u>	<u>0.23±0.01</u>	0.47	0.69	3.98±0.11	4.24±0.18
			0.48	0.58	4.09±0.06	4.15±0.44
100	0.17±0.02	0.21±0.05	0.69	1.07	3.81±0.07	4.05±0.07
	<u>0.25±0.03</u>	<u>0.32±0.06</u>	0.58	0.75	4.00±0.09	4.01±0.04
			0.68	0.68	3.78±0.16	3.89±0.12
as deposited	/	0.15±0.04	/	0.47	/	3.28±0.12
		<u>0.23±0.05</u>		0.79		4.14±0.11
				0.49		4.20±0.45

In Figure 4-3, we determined molar ratios of ~0.3 for K:Co and ~0.4 for P:Co and thus of ca. 1.3 for P:K for films electrodeposited at 1.05 V_{NHE} and operated at 1.3 V_{NHE} (both in 100 mM KPi, pH 7). These figures are close to previously reported values for CoCat films electrodeposited at 1.29 V_{NHE} in 100 mM KPi, thus verifying the reproducibility of the molar ratios of the main CoCat ingredients as resulting from different electrodeposition and elemental quantification protocols.[70] It furthermore reveals:

(1) The K:Co stoichiometry is not a constant but depends strongly on the K^+ concentration during electrocatalytic operation; a by factor of ~3 smaller K:Co ratio was found for CoCat operation in 1.6 mM vs. 100 mM KPi. In contrast, the P:Co ratio showed much smaller variations (≤20 %) for the same large KPi concentration change. This suggests comparably weak binding of the majority of potassium ions within the CoCat material. This point is further detailed further below. Comparison of potassium K-edge XAS spectra collected before and after CoCat exposure to NaPi electrolyte (Figures 4-13B and 4-16) shows that essentially all K^+ ions leave the CoCat film on a minute time-scale in contrast to the time-scale of hour for phosphate exchange (Figure 4-21).[107;131]

(2) Both the P:Co and the K:Co molar ratios are essentially potential-independent, excluding that these ions contribute significantly to charge compensation in response to the massive potential-induced valence changes of the Co ions, as explicated in the following.

As we already reported in ref. [142], the phosphate content of CoCat films is fully potential-independent ruling out that phosphate uptake facilitates charge compensation upon oxidation of Co ions. For the K:Co molar ratio, we observe a trend towards a slightly increased K^+ content in response to operation at catalytic vs. pre-catalytic potential. However, this trend is not only of debatable statistical significance, but also the observation of *increased* K^+ content for Co oxidation (positive charging of Co ions) rather would suggest a minor K^+ uptake than charge compensation by K^+ release.

The extent of the contradiction between the data in Figure 4-3 and charge balancing by uptake/release of phosphate or K^+ ions is particularly evident when comparing the fraction of Co ions that undergo valence changes. The increase in electrode potential from 1.0 to 1.3 V_{NHE} is associated with an increase in the mean Co oxidation state from about 2.75 to 3.13,[126;142] which corresponds to 0.38 oxidizing equivalents (positive charges) per Co ion. Consequently, for the CoCat operated in 100 mM KPi electrolyte, the potential increase from 1.0 V_{NHE} to 1.3 V_{NHE} would *require the release of all K^+ ions* to compensate for the charging of the material by Co oxidation, whereas *not any release of K^+ ions* was detected. For operation at 1.6 mM KPi, even the release of all K^+ ions could not provide efficient charge compensation because the total amount of K^+ ions is too low. Similarly, also the potential-independent phosphate content excludes charge-compensation by phosphate uptake or release. Furthermore, in the Section 4.2.4, kinetic studies on K^+/Na^+ exchange demonstrate K^+ depletion of CoCat material around 5 s upon film being exposed in K-free solution, which is one order of magnitude slower than the changes in the Co oxidation states as evidenced by time-resolved X-ray experiment,[143] thereby also excluding charge compensation by potassium ions. The exchange of phosphate ions is even by several orders of magnitude slower (Figure 4-21), and also supported by refs.[107;131;139]. Therefore, we can safely conclude that neither K^+ ions nor phosphate ions facilitate charge compensation in the redox transitions of the CoCat material.

4.2.2 Potassium coordination from X-ray absorption spectroscopy

4.2.2.1 Comparison of XANES spectra

The CoCat material belongs to the family of amorphous layered oxyhydroxides of the MO_2 type (M = Mn, Co, Ni, Ru, Ir), but is distinguished by especially small MO_2 fragments possibly

comprising less than 20 Co ions.[110;112;125;126;158;409] The layered-oxide fragments of CoCat are likely not directly stacked, but separated by water molecules and ions, namely potassium and phosphate.[110;112;125;126;158;409] The CoCat thus resembles the well-known birnessite structures of Mn oxides or other layered oxides, for which intercalated cations, typically alkali metals or alkaline earth metals, are widely found.[261;263;265;451-453] The K^+–M distance is typically around 3.0–3.5 Å[123;451;454;455]. Since the CoCat material is highly amorphous and thus does not diffract, X-ray absorption spectroscopy (XAS) is the method of choice for structural investigation of such catalyst films, which are volume-active regarding oxidation-state dynamics and OER catalysis.[99] Whereas PDF (pair distribution function) analysis on CoCat has been used to study domain size and structural features, it does not provide an element-specific focus,[122;133;138] in contrast to our present EXAFS analysis revealing the K^+ binding motifs. XAS at the Co K-edge has been repeatedly applied to CoCat material for assessment of Co oxidation states (electronic structure), via analysis of the X-ray absorption near-edge structure (XANES), and for insight in the atomic structure, via analysis of the extended X-ray absorption fine-structure (EXAFS).[110;112;126;134;142;158] Here, we provide complementary structural information by XANES and EXAFS analyses at the potassium K-edge, which is experimentally challenging and has been applied before only once to the CoCat material (to our knowledge).[123]

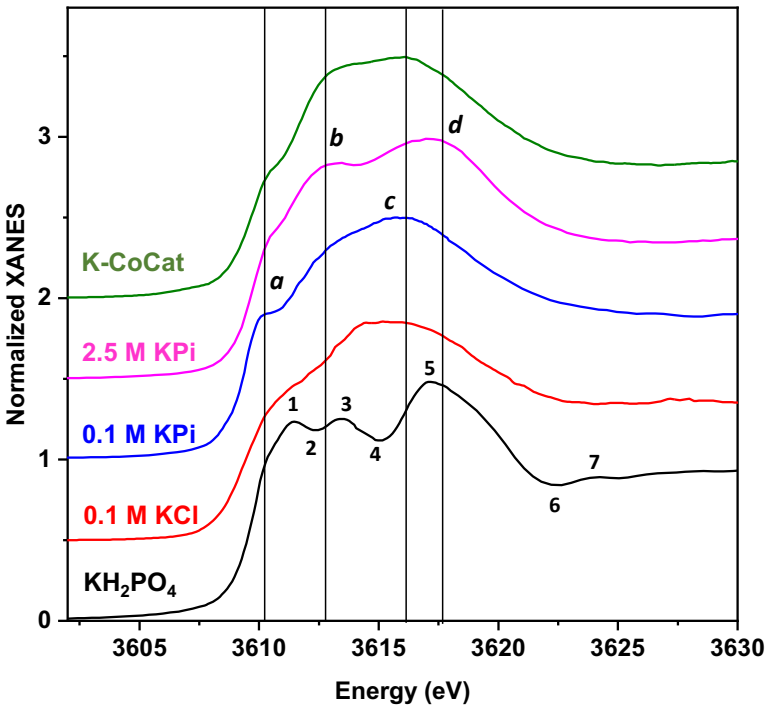

Figure 4-4. Comparison of potassium K-edge XANES spectra for dry CoCat film (K–CoCat) and potassium reference compounds. XANES spectra were collected for CoCat films, microcrystalline KH_2PO_4 powder, aqueous solutions of cobalt phosphate (KPi) at 0.1 M or 2.5 M (pH 7), and an aqueous KCl solution at 0.1 M. The 2.5 M KPi spectrum was corrected for self-absorption (Figures 4-5 and 4-7). For further details of the measurement conditions (temperature, etc.), see the experimental section and Figure 4-5. Spectra are stacked for clarity. Prominent features are marked by lower-case letters and for KH_2PO_4 by numbers. Reproduced with permission from ref.[143]. Copyright Wiley-VCH (2023).

Visual comparison of the K-edge spectra in Figure 4-4 reveals overall similar, but not identical spectra of CoCat and K^+ ions in solution (0.1 M KCl, 0.1 M KPi, 2.5 M KPi), suggesting a K^+ coordination environment in the CoCat that is quite similar to that of hydrated K^+ ions, but differs in specific features. The 2.5 M KPi spectrum is expected to differ from the 0.1 M KPi spectrum due to the presence of an increased number of potassium–phosphate ion pair interactions at high KPi concentrations. We assign features *b* and *d* to ion pair interaction because these features are well resolved in the 2.5 M KPi spectrum and merely absent in the 0.1 M KPi and KCl spectra. Vice versa, the features denoted *a* and *c* are more prominent in 0.1 M vs. 2.5 M KPi. In the CoCat spectrum, the discernible *b*–feature and the *d*–feature shoulder, as well as the relatively diminished features *a* and *c* suggest that potassium-phosphate ion pair formation, with phosphate ions in the first K^+ coordination sphere, to some extent occurs also in the CoCat. In comparison to micro-crystalline solid KH_2PO_4 (or K_2HPO_4, data not shown), we note the absence of pronounced features typical for crystalline materials (1-6 in Figure 4-4) in the CoCat XANES spectrum, suggesting that (nano-) crystalline domains of $K_xH_yPO_4$ are not present within the CoCat material.

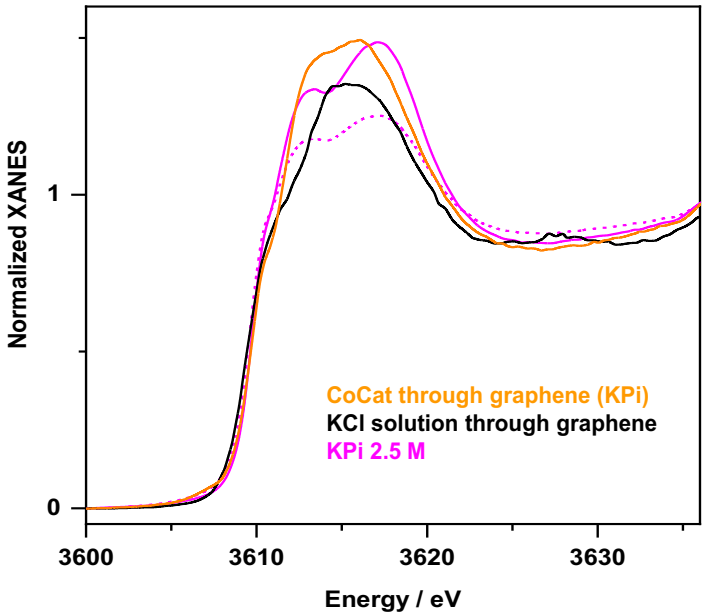

Figure 4-5. Potassium K-edge XANES spectra of CoCat and solution references. The CoCat film and KPi solution samples were measured at 20 K (CoCat, front side in contact with KPi, probed through the graphene support from the back side); the KCl solution (0.1 M) spectrum was collected at RT. The dotted magenta line shows the KPi 2.5 M spectrum before self-absorption correction using the curve in Figure 4-7. For further information on the XAS experiment, see Experimental Section 4.4.2.

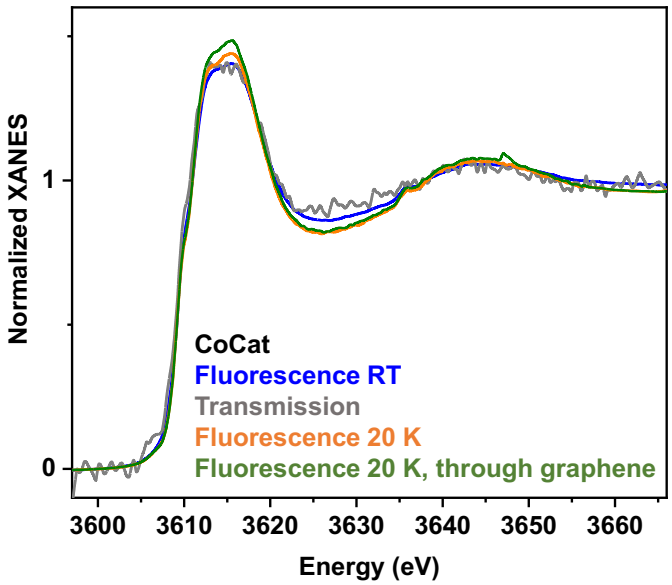

Figure 4-6. XANES spectra of potassium in CoCat at 20 K or room temperature. Dry CoCat films deposited on graphene sheet (300 mC cm^{-2}) in vacuum (RT) or in 0.1 bar He atmosphere (20 K) were measured in fluorescence or transmission mode (transmission at RT). Samples were probed either directly (i.e., from the front side) when facing the incident X-ray beam without any cover or through the graphene sheet support (i.e., from the back side) when the front side was in contact with 20 mM KPi electrolyte.

XAS spectra of potassium were measured on thicker CoCat films. To rule out a putative reabsorption effect for thicker films (300 mC cm^{-2}), the transmission spectrum was collected in vacuum (Figure 4-6). The similar X-ray fluorescence and transmission spectra reveal that spectral flattening due to sample self-absorption was unlikely.

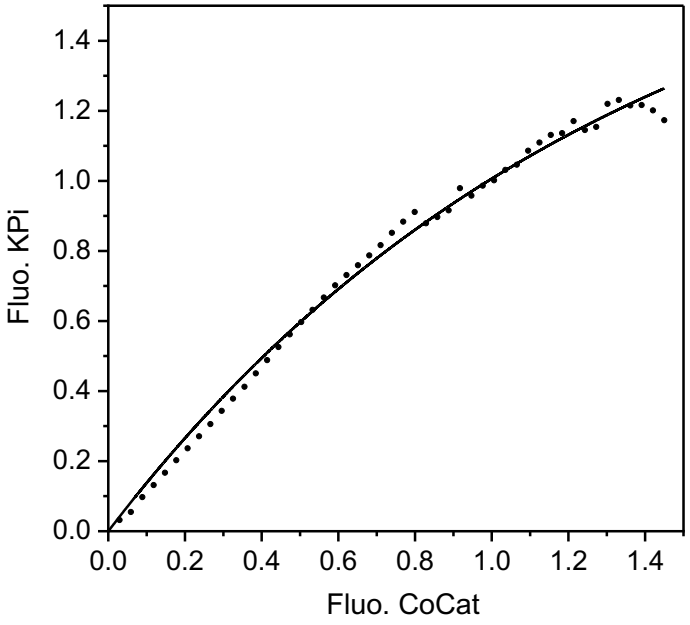

Figure 4-7. X-ray fluorescence (interpolated data from normalized-XANES spectra) of KPi (2.5 M, 20 K) plotted versus the data for CoCat in contact with KPi measured through the graphene support (dots) and exponential-rise fit (line). Data corresponds to spectra in Figure 4-5.

4.2.2.2 Analysis of EXAFS spectra

Selected EXAFS spectra are shown in Figure 4-8; for experimental details, further spectra, and EXAFS simulation parameters see experimental Section 4.4.2 and
Table 4-4.
The EXAFS spectra of CoCat collected at 20 K or room temperature (RT) reveal (within noise limits) the similarity of the main interatomic interactions, e.g., K–O bonds (peak I in the FT-spectrum), which are also detectable in the 2.5 M KPi EXAFS (see
Table 4-4). The EXAFS oscillations in the RT spectrum of CoCat are overall similar to that of the 20 K spectrum, indicating the absence of significant structural changes upon freezing of the material. The clearly more damped EXAFS amplitudes in the RT spectrum are expected due to increased vibrational disorder (increased Debye-Waller factors), which hence are closer to the noise level. This difference motivates our focus on the 20 K spectra. The coordination number (N) of hydrated K^+ is consistent with 6±2 oxygen atoms (from water molecules or O-atoms within CoCat) surrounding the K^+ ion;[456] a coordination number close to 7 seems likely[457;458] (Figure 4-9, motif δ). In our EXAFS simulations, the longer distances relating to peaks II and III in the FT-spectrum are modeled as a K–O–PO_3 motif (peak II, K–P around 3.5 Å, motif γ in Figure 4-9) and a K–O–Co motif (peak III, K–Co around 4.1 Å, motif β in Figure 4-9). For both motifs a low coordination number of about 0.5 is well compatible with the experimental data. EXAFS fit-error contour plots reveal parameter correlations and likely coordination number boundaries (Figures 4-10 and 4-11). A more precise determination of N_K and N_{Co} cannot be reached from the present data, but values significantly exceeding 0.5 P and 0.5 K distances per Co center seem to be unlikely.

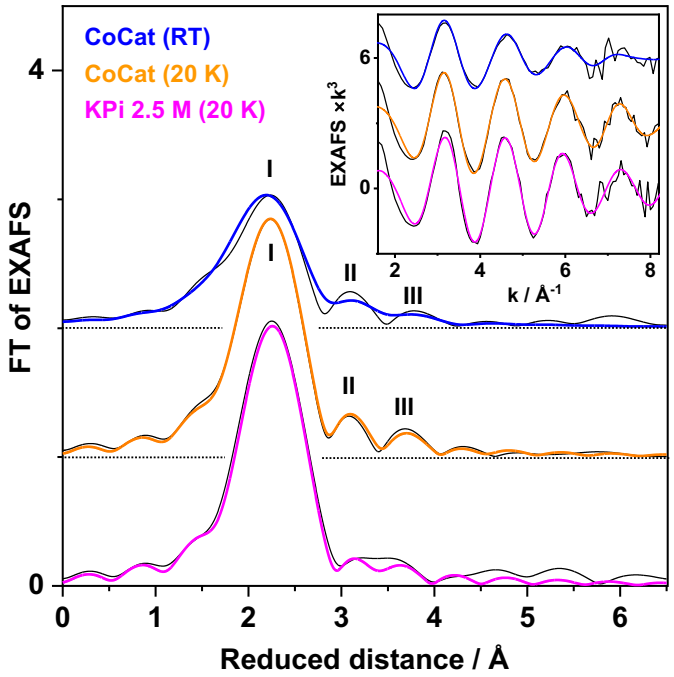

Figure 4-8. EXAFS analysis of CoCat films and KPi solution. Spectra were collected at 20 K or room temperature (RT). The main panel shows Fourier-transforms (FTs, calculated from 1.6-8.2 $Å^{-1}$) of the EXAFS oscillations in the inset (experimental data, black lines; simulations with parameters in

Table 4-4, colored lines). Spectra are vertically stacked for clarity. Reproduced with permission from ref.[143]. Copyright Wiley-VCH (2023).

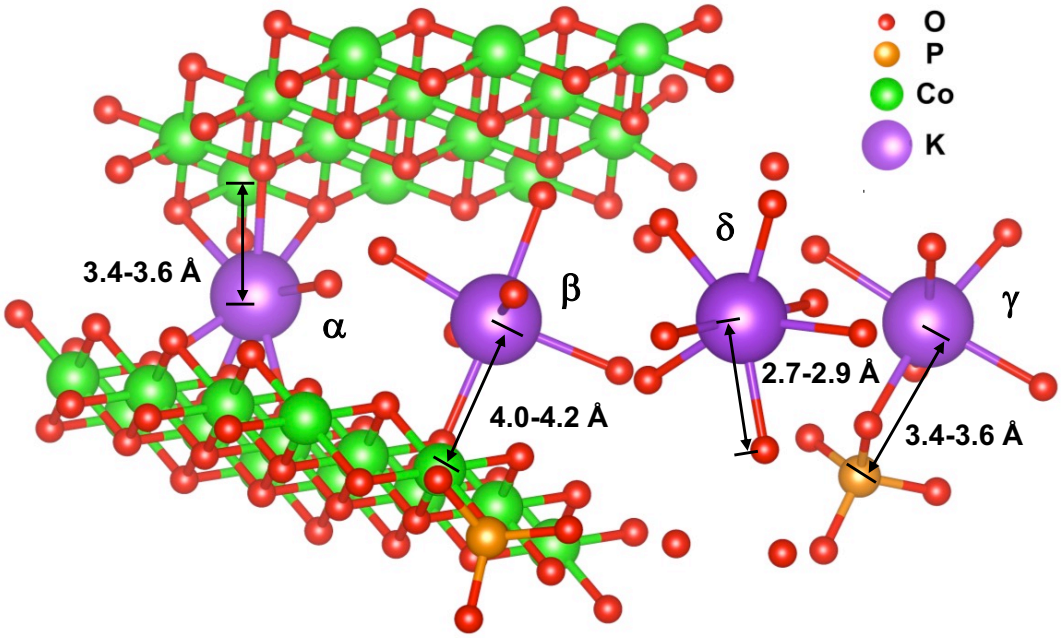

Figure 4-9. Hypothetical structural motifs of potassium binding in the CoCat material. Two-layer fragments interconnected by binding to the same interlayer K^+ ions are shown. (α) K^+ bound to three oxygen atoms of a CoO_2 layer fragment forming a $KCo_3(\mu\text{–}O)_4$ cubane motif. (*β*) K^+ bound via one oxygen atom to a Co ion of the CoO_2 layer fragment; K^+ binding via an O-atom bridging between Co ions or to a terminal oxygen of a CoO_2 layer fragment is conceivable. (γ) Ion-pair of K^+ and phosphate ($H_xPO_4^{-(3-x)}$) formed via one bridging oxygen atom. (δ) Fully hydrated K^+ ion present in the interlayer region of neighbouring CoO_2 layers without O-bridging to Co ions. The indicated distances or distance ranges represent estimates that are compatible with the EXAFS data. Reproduced with permission from ref.[143]. Copyright Wiley-VCH (2023).

The cubane-type binding of K^+ to a central Co ion of a CoO_2 layer fragment (motif α in Figure 4-9) predicts an N_{Co} of 3 for the nearest Co ions at around 3.4–3.6 Å and additionally a similarly high N_{Co} for the next-nearest Co ions of the CoO_2 layer fragment at around 4.6 Å. For interconnection of two layers by a K^+ ion, the corresponding coordination numbers could be as high as 6. These figures are so much larger than the experimental value that we can exclude the binding of a sizeable fraction of K^+ ions in the form of well-ordered $KCo_3(\mu_3\text{–}O)_4$ cubanes. However, highly disordered or loose binding of a sizeable fraction of K^+ ions via a single O atom to CoO_2 layer fragments (motif β) is compatible with the EXAFS data.

The formation of potassium-phosphate ion pairs (motif γ in Figure 4-9) is supported by the XANES spectra (as discussed further above, Figure 4-4) and is in line with the EXAFS analysis. The EXAFS analysis leads to values of N_{Co} and N_P around 0.5 which suggests that for 6-7-fold coordination of K^+ to O atoms, the majority of coordination partners are likely water molecules present in the space between CoO_2 layer fragments.

Table 4-4. EXAFS simulation parameters in Figure 4-8. #Coordination numbers were set to 7. *The Debye-Waller parameter ($2\sigma^2$) resulted from a joint fit to yield the same value for all coordination shells. The fit error parameter, R_f, was calculated for reduced distances of 1–4 Å.[316]

	CoCat RT R_f = 12.9 %			CoCat 20 K R_f = 4.6 %			KPi 20 K R_f = 7.3 %		
shell	N (per K)	R (Å)	$2\sigma^2$ (Å^2)	N (per K)	R (Å)	$2\sigma^2$ (Å^2)	N (per K)	R (Å)	$2\sigma^2$ (Å^2)
K–O	7#	2.74	0.059*	7#	2.76	0.029*	7#	2.76	0.027*
K--P	0.9	3.51	0.059*	0.5	3.45	0.029*	0.4	3.67	0.027*
K--Co	0.8	4.21	0.059*	0.5	4.13	0.029*	/	/	/

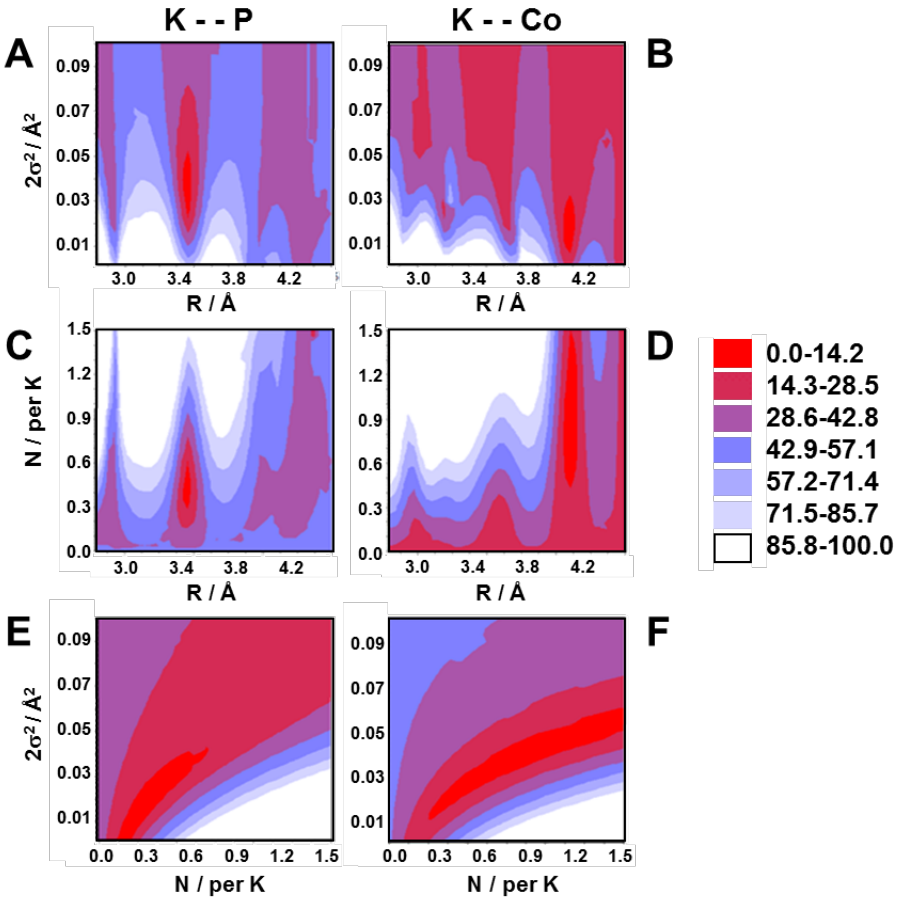

Figure 4-10. K-EXAFS fit error contour plots for CoCat. The spectrum of CoCat at 20 K (Figure 4-8) was simulated in a k-range of 1.6–8.2 Å^{-1} (up to 250 eV above E_0) and the fit error (R_f) was calculated in a 1–4 Å range of reduced distance (panels A–D) or in a 2.8–4.5 Å range of reduced distance (panels E and F). Color variations represent variations of the fit error, R_f, which was normalized between 0 % and 100 %, as given in the color annotations. Absolute R_f values ranged about between 4 % (red areas) to 16 % (white areas) in panels A–D and extended to larger errors in panels E and F (see Figure 4-11

below). Note that, e.g., in the center of the red error areas, R_f is ca. 4 % while at the border to the dark-red areas, it is ca. 6 %, meaning the fit quality is already ca. by 50 % diminished. In each fit, 3 interatomic distances were used (K–O, K···P, K···Co, see

Table 4-4), The coordination number N(K-O) was set to 7 and $2\sigma^2$ (K–O) was set to the unrestraint best-fit value (

Table 4-4) in each fit. If not both fixed (panels A and B), the N-value of the K···P or K···Co distance was variable in the fits and the respective N-value of the other distance was set to 0.5. If not both fixed to the same value as for the K-O distance (panels C and D), the $2\sigma^2$ value of the K···P or K···Co distance was variable in the fits and the respective $2\sigma^2$ value of the other distance was set to the value of the K–O distance. If not both fixed to the best-fit values (panels E and F), the R-value of the K···P or K···Co distance was variable in the fits and the respective R-value of the other distance was set to the best-fit value. Left column, data for the K- -P distance. Right column, data for the K···Co distance. Panels A and B: variation of the Debye-Waller factor ($2\sigma^2$) vs. the interatomic distance I for 0.5 P and 0.5 Co distances per K ion. Panels C and D: variation of the coordination number (N) vs. the interatomic distance (R) for $2\sigma^2 = 0.03$ Å^2 for both shells. Panels E and F: variation of the Debye-Waller factor ($2\sigma^2$) vs. the coordination number (N) for R = 3.45 Å (K···P) and R = 4.13 Å (K···Co) as in the unrestraint best fit.

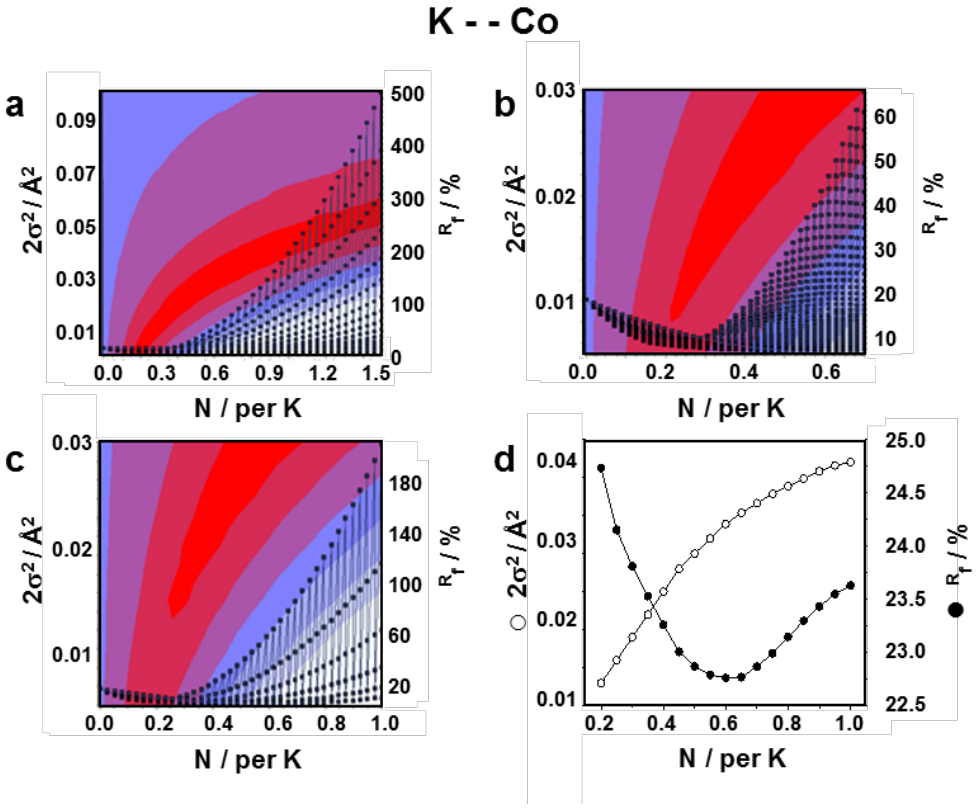

Figure 4-11. Error contour plot for the K···Co distance. The plot corresponds to Figure 4-10F, $2\sigma^2$ was varied in a 0.002–0.1 Å^2 range. In addition, the R_f value calculated in a 2.8–4.5 Å range is shown (black dots, right y-axis). Panels a and b: each symbol series from high to low N-values represent the EXAFS fit errors for decreasing $2\sigma^2$ values (40 series, top to bottom, the lower series corresponds to $2\sigma^2$ = 0.002 Å^2). Panel a, full range plot; panel b, zoom into panel a; panel c: error calculations similar as in panels a and b, but using only 6 different $2\sigma^2$ values over a smaller range to emphasize the fit minima. Panel d: error values for best-fit $2\sigma^2$/N pairs (in the center of the red area in panels a-c).

4.2.3 Operando XAS detecting K^+ exchange kinetics

The CoCat undergoes potential-dependent redox transitions of the amorphous bulk material, with the mean Co oxidation states ranging from about +2.6 at low potentials to +3.25 at catalytic potentials.[126] For basic physical reasons, the Co oxidation (reduction), within the bulk of the CoCat films of significant thickness, essentially needs to be coupled to stoichiometric charge-compensating ion uptake or release, with ions moving between the CoCat bulk and the electrolyte. By comparison of the K^+ content of the CoCat material equilibrated at various electrolyte concentrations and electrode potentials (Figure 4-3), we showed that neither K^+ nor phosphate ions facilitate charge-compensation in the equilibrated catalyst film, supporting XAS investigations that suggested charge compensation in the $Co^{II/III}$ and the $Co^{III/IV}$ transitions by protonation-state changes of bridging or terminal oxygen ligands of Co ions.[126;134] However, merely based on the results obtained for the fully equilibrated CoCat, the following scenario cannot be excluded:

In an initial response to an increased potential, K^+ ions leave the catalyst material, which may be understood as charging of double-layer capacities at CoCat-intrinsic nanoscopic surfaces. Subsequently, structural changes associated with deprotonation and proton release proceed, which are coupled to K^+ uptake from the electrolyte.

To scrutinize the above scenario, we developed a novel operando X-ray experiments employing potassium K-edge XAS for deciphering K^+ exchange kinetics. Briefly, the X-ray fluorescence far above the potassium K-edge, which is proportional to the detectable amount of potassium in the CoCat film, was monitored in situ before and after sudden exposure to a potassium-free electrolyte (NaPi), to follow the release of K^+ from the catalyst, which most likely proceeds in form of a K^+ vs. Na^+ exchange. For the timing protocol and time courses of K^+ release, see Figures 4-12 and 4-13A.

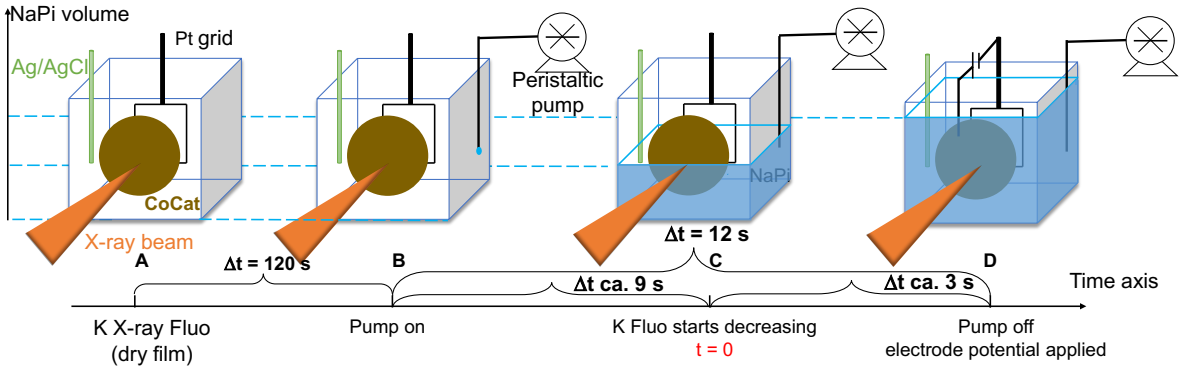

Figure 4-12. Scheme of the timeline of operando XAS experiments for monitoring K^+ exchange kinetics. The total time range from potassium (K) X-ray fluorescence acquisition on the dry film (A) to application of an electrode potential to the film (D) is 132 s. The dry-film K-fluorescence collection at 4 keV lasts for 120 s until switching on the peristaltic pump for injecting NaPi (0.1 M, pH 7) buffer solution (B). After the level of the NaPi solution reaches the area of the film exposed to the X-ray beam, the K-fluorescence starts decreasing and this point was defined as time zero (±1 s estimated inaccuracy) for the K^+ exchange kinetics analysis (C). The process after switching on the pump (C) took ca. 9 s including ca. 5 s pump response time. After less than 3 s, an electrode potential was applied to CoCat and the K fluorescence was recorded for 10 min.

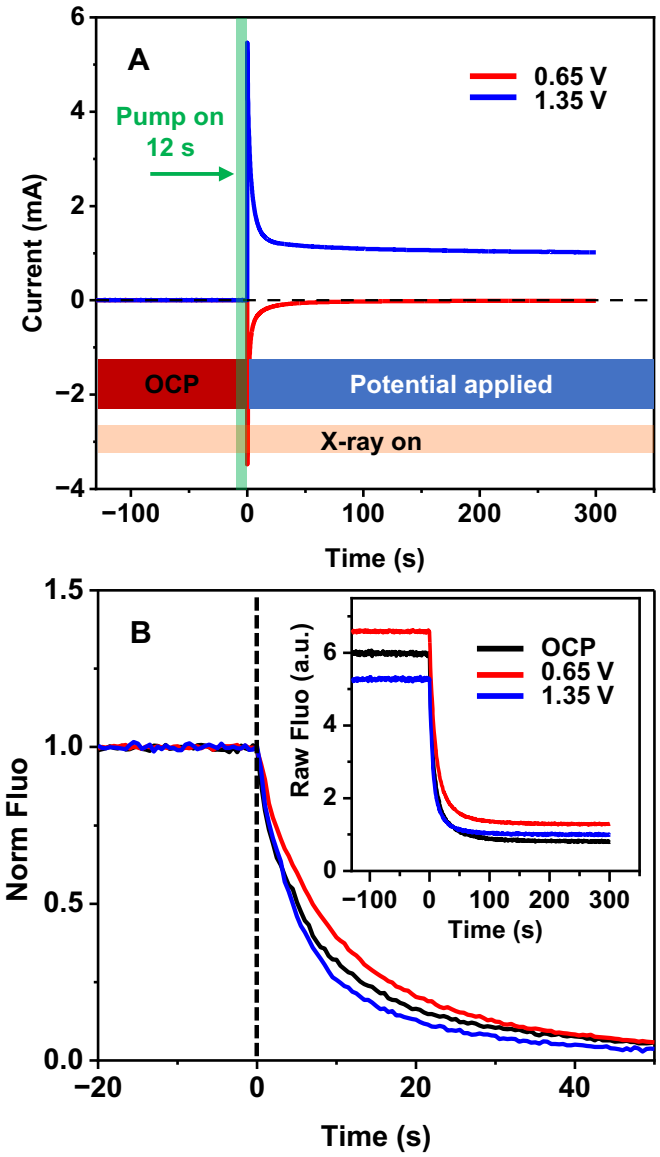

Figure 4-13. Time-resolved X-ray experiment for tracking K^+ release from CoCat films. (A) Experimental protocol and current traces. (B) Time course of the potassium K_α-fluorescence for X-ray excitation at 4 keV, reflecting the detectable amount of K^+ within the CoCat film; the inset shows the same data on an expanded time scale, but without signal normalization. For measuring K^+ release kinetics, dry CoCat films electrodeposited in 100 mM KPi were exposed to 100 mM NaPi electrolyte. The NaPi electrolyte was injected within 12 s by employing a pump system, with more sudden exposure of the X-ray irradiated CoCat areas to the NaPi electrolyte (< 2 s). At this point K^+ ions started to leave the catalyst material (t = 0 in B), resulting in the decrease of the X-ray fluorescence shown in panel B. Roughly at the same time (t = 0 in panel A), either a potential of 0.65 V_{NHE} or of 1.35 V_{NHE} was applied for 10 minutes, or the open-circuit potential (OCP) condition continued; for complete time traces see Figure 4-15. CoCat film thickness corresponding to 100 mC cm^{-2} deposition charge; deposition on graphene sheets; KPi and NaPi at pH 7; rapid stirring of NaPi electrolyte to remove K^+ ions released from the CoCat film. Reproduced with permission from ref.[143]. Copyright Wiley-VCH (2023).

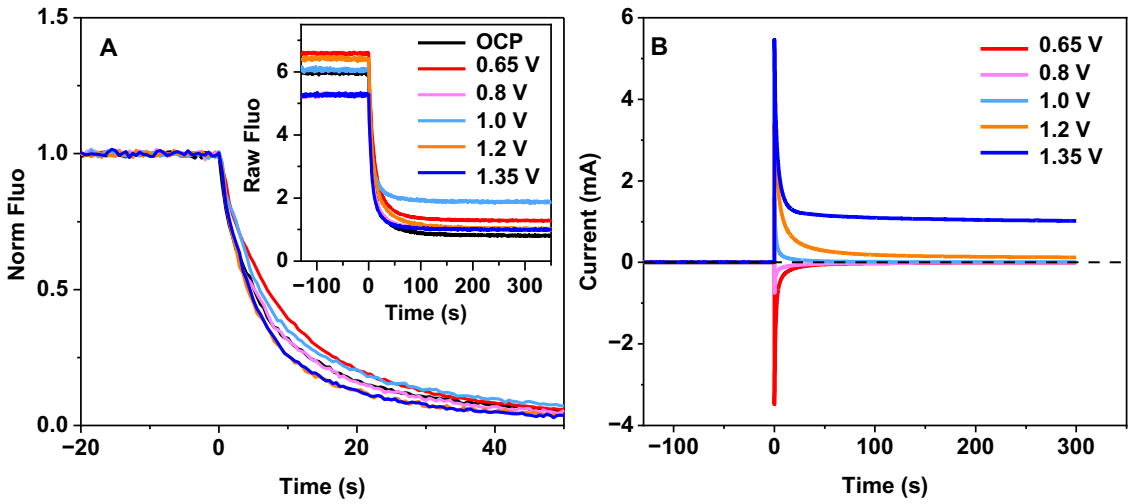

Figure 4-14. Time traces of the potassium K_α-fluorescence for X-ray excitation at 4 keV (A) and corresponding current traces (B) at additional applied electrode potentials (compare Figure 4-13 and its legend).

The concentration of K^+ ions within the CoCat film decreases monotonously after exposure of the K^+-containing CoCat film to NaPi electrolyte (Figure 4-13B), with an estimated half-time around 5 s. Noteworthily, there is no electric potential dependence of K^+ exchange because similarly fast K^+ release was observed without any applied potential (OCP transient in Figure 4-13B) or at pre-catalytic (0.65 V_{NHE}) or catalytic (1.35 V_{NHE}) potentials. Visual inspection of the normalized K^+ fluorescence traces in Figure 4-13B appears to indicate slightly more rapid K^+ release for CoCat films operated at 1.35 V_{NHE} (Co oxidation, positive currents) than at 0.65 V_{NHE} (Co reduction, negative currents), and K^+ release at an intermediate rate without any applied potential (OCP, no Co oxidation-state change). However, potential jumps to further potentials (Figure 4-14) and also simulations of K^+-release traces (Figure 4-15, Table 4-5) do not support a potential-dependence of the K^+ release kinetics; the scatter in the experimental transients may relate merely to limited reproducibility of the NaPi-electrolyte exposure rate.

The K^+ release, which presumably proceeds as a K^+/Na^+ exchange here, represents an essentially complete K^+ depletion, as indicated by the practically negligible amplitude of the final potassium X-ray absorption spectrum (Figure 4-16). This finding indicates that there is no major fraction of K^+ ions that are firmly bound within the CoCat, in line with the above observation of a comparably large change of the K amount upon variation of the KPi concentration (Figure 4-3). Notably, XAS data at the Co K-edge show that the CoCat film was fully stable (Figures 4-18 and 4-19), indicating that within the time course of the kinetic experiment, K^+ release is not related to any film degradation.

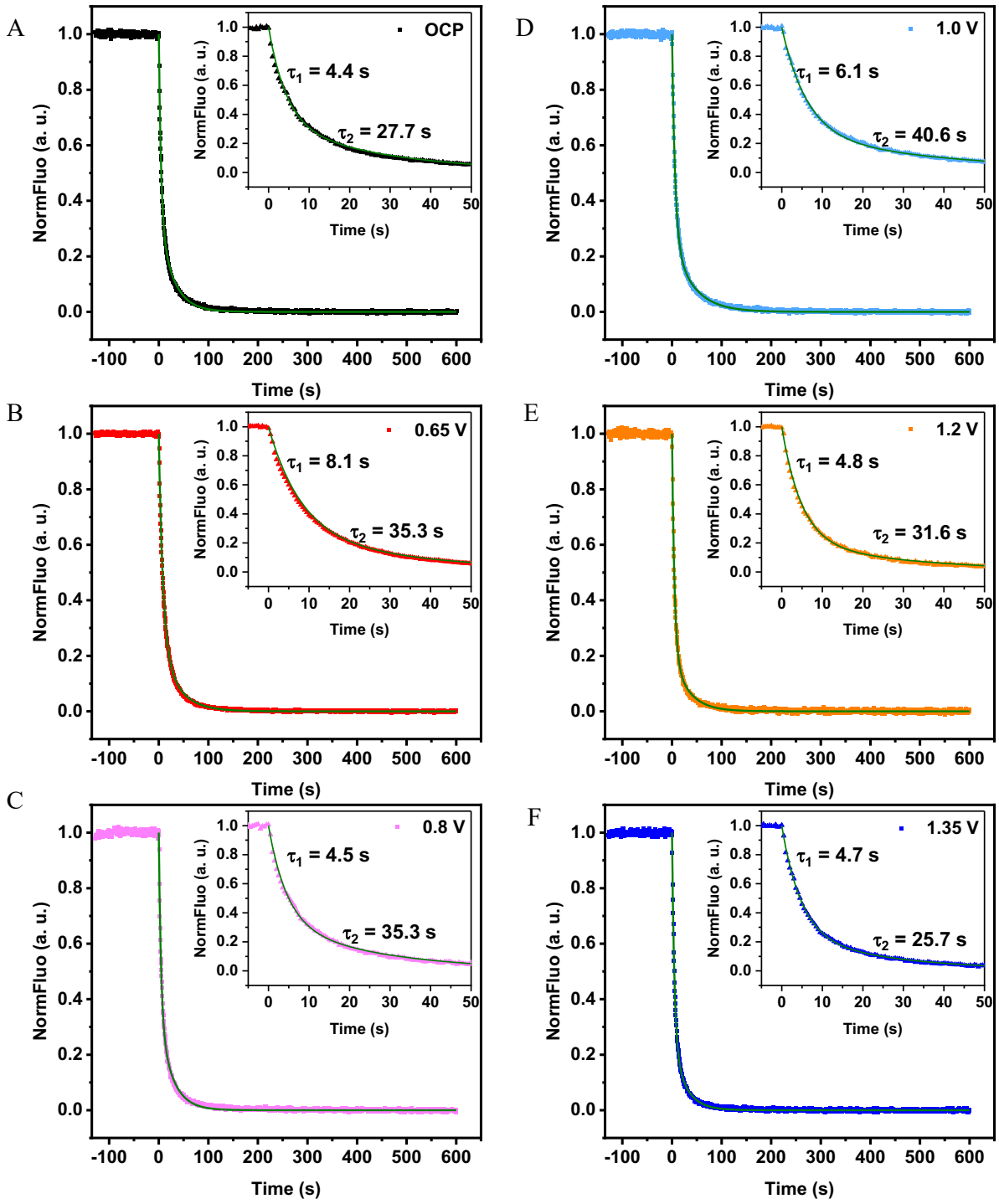

Figure 4-15. Simulation of normalized time traces of potassium X-ray fluorescence at 6 potentials. Insets show the same data on an extended time scale (compare Figure 4-14). Traces were simulated using the sum of two exponential functions with parameters listed in Table 4-5. Green lines show fitted curves.

Table 4-5. Simulation parameters for time courses of the potassium X-ray fluorescence in Figure 4-15 (relative rounded amplitudes, A; time constants, τ).

	OCP	0.65 V	0.8 V	1.0 V	1.2 V	1.35 V
A_1 [%]	65	74	66	73	79	75
τ_1 [s]	4.4	8.1	4.5	6.1	4.8	4.7
A_2 [%]	35	26	34	27	21	25
τ_2 [s]	27.7	35.3	26.0	40.6	31.6	25.7
R^2	0.9954	0.9970	0.9950	0.9980	0.9951	0.9974

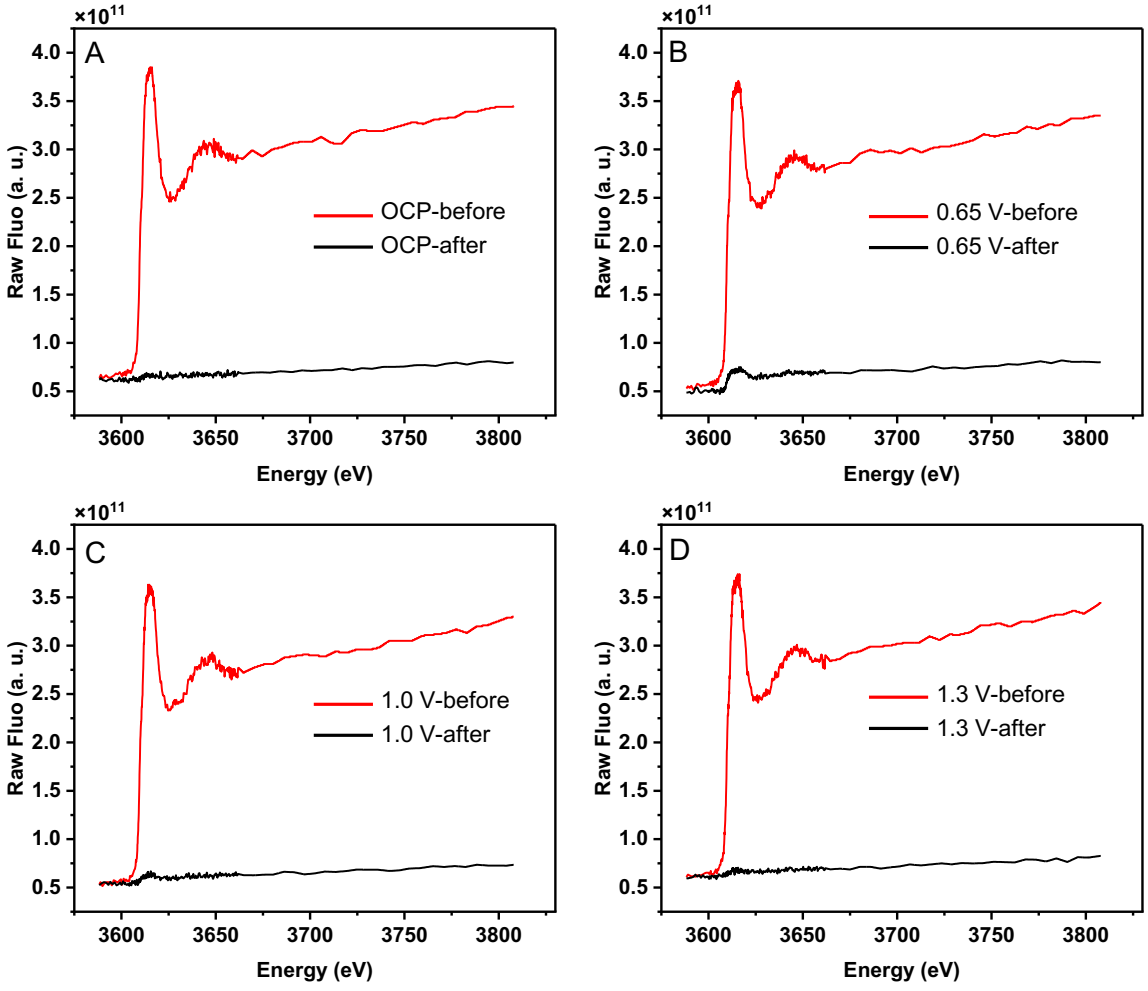

Figure 4-16. Potassium K-edge X-ray absorption spectra (non-normalized I_{fluo}/I_0 data) collected on the dry film (100 mC cm^{-2}) "before" K^+ release and "after" exposure for 15 min to the continuously stirred NaPi electrolyte (0.1 M NaPi buffer, pH 7), illustrating that most or even all K^+ ions leave the CoCat film when exposed to NaPi. The potassium K-edge amplitude is close to zero after the NaPi exposure irrespective of potential and the remaining fluorescence intensity (i.e., at higher energies) reflects the background signal (due to scattered incident light and excitation of lighter elements in the sample). The

background amplitude (ca. 15-20 % at 4 keV) also accounts for the residual fluorescence amplitudes after longer NaPi exposure as visible in Figure 4-13.

In addition, another experimental approach, involving a series of short (1 s) potential-steps during the NaPi-exposure period (Figure 4-17), does not support an electric-potential dependence of the K^+ release rate. In summary, the role of redox-inert cations inside of CoCat was studied via operando-XAS at the potassium K-edge, revealing comparably weak binding of K^+ in the material and, importantly, the absence of any significant charge compensation role for K^+ ions.

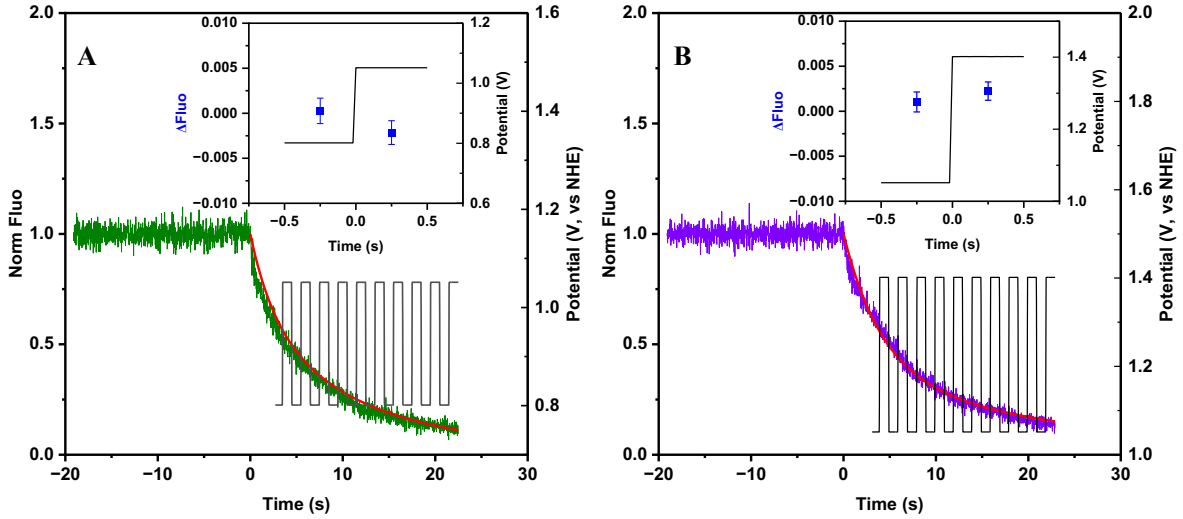

Figure 4-17. K X-ray fluorescence of CoCat recorded after NaPi exposure during application of potential jump sequences. The fluorescence (normalized traces) was recorded at a fixed X-ray excitation energy of 4 keV for 100 mC cm^{-2} CoCat films prior to ($t < 0$) and after ($t > 0$) exposure to stirred NaPi buffer (0.1 M, pH 7). In addition, a sequence of 10 up-down potential jumps between 0.8 V_{NHE} and 1.05 V_{NHE} (panel A) or 1.05 V_{NHE} and 1.40 V_{NHE} (panel B) was applied, with application of the respective potential for 1 s. The insets show that there is no significant variation in the K^+ release rate in response to the potential jumps, i.e., the averaged jump levels reveal a fluorescence change of <<1 %. Insets: averaged fluorescence levels (blue dots) at low and high potentials. The levels were determined after subtraction of a triple-exponential fit curve (red lines) from the normalized experimental fluorescence traces (green or purple lines) and averaging of the 19 potential jumps and of the 25 data points collected within 0.5 s at low or high potentials, respectively (the error bars show standard errors calculated from 475 data points). Further details of the experiment are described in the experimental section. The potassium X-ray fluorescence changes ($t > 0$) seem to correspond to a decrease by ca. 0.2 % (in A) and an increase by ca. 0.1 % (in B) of the initial fluorescence level ($t < 0$), which is below the likely error (1σ confidence interval) of 68%.

Table 4-6. Simulation parameters for K fluorescence traces in Figure 4-17.

Fit parameters	0.8 V → 1.05 V	1.05 V → 1.4 V
A_1 [%]	4±1	17±21
A_2 [%]	60±1	36±1
A_3 [%]	36±1	47± 41
τ_1 [s]	138±3	5±41
τ_2 [s]	11±1	26±1
τ_3 [s]	2.5 ±0.1	4.0 ±14
R^2	0.9420	0.9342

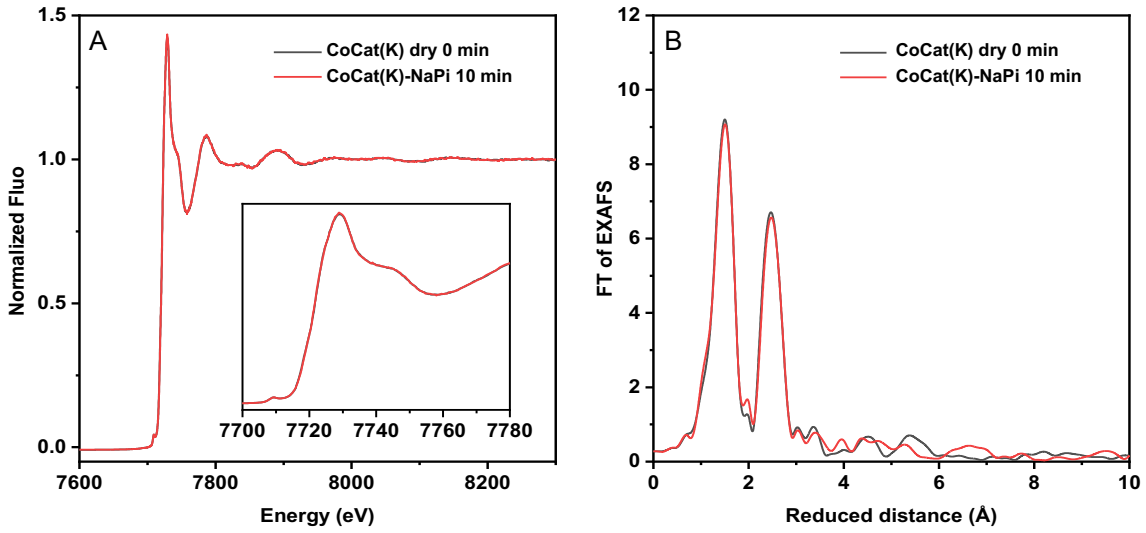

Figure 4-18. Comparison of Co XAS spectra of CoCat. (A) XANES and (B) FT of EXAFS spectra at the Co K-edge for CoCat (100 mC cm^{-2}). Black line: dry CoCat film; red line: spectrum collected at OCP after the film was exposed to stirred 0.1 M NaPi (pH 7) electrolyte for 10 min. Note within noise limits identical spectra prior to and after NaPi exposure. The non-normalized fluorescence spectra are shown in Figure 4-19.

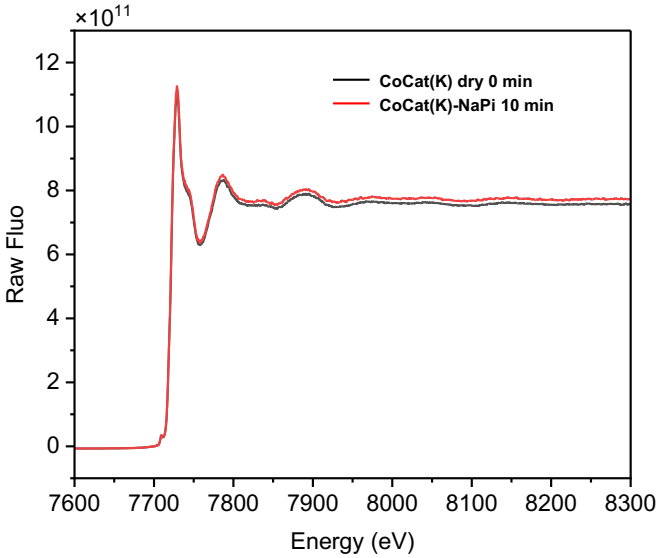

Figure 4-19. Raw (non-normalized) X-ray absorption spectra at the Co K-edge corresponding to Figure 4-18A. Spectral amplitudes represent I_{fluo}/I_0 values after dead-time correction, averaging of the 13 detector channels and pre-edge background subtraction. The change of X-ray fluorescence intensity at high X-ray energy (8100 eV) is less than ca. 2%, indicating negligible film degradation.

The absence of a significant influence of K^+/Na^+ exchange on the Co K-edge XAS spectra of the CoCat indicates similar structures under both conditions (Figures 4-18, 4-19, 4-20B), in agreement with earlier data.[158] Our K–EXAFS data (Figure 4-8,
Table 4-4) suggested a coordination number of K(–O–)Co distances (N_{Co}) around 0.5, which, when taking the Co:K stoichiometry of 3:1 as it is expected for cubane-type binding into account, would correspond to a coordination number of only about 0.17 (= 0.5/3) in the Co–EXAFS. For a coordination number of 0.17 with a likely sizeable Debye-Waller factor (σ), a discernable contribution of a K(–O–)Co distance to the Co K-edge EXAFS spectra is not expected. We conclude that both the K^+ and the Co EXAFS are compatible with only rare occurrences of K(–O–)Co distances.

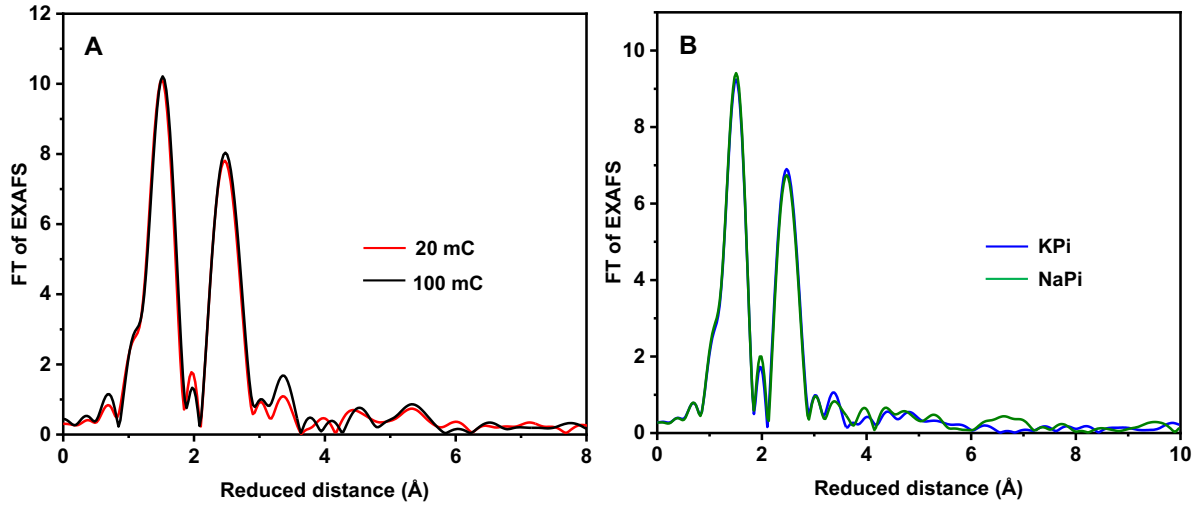

Figure 4-20. Operando EXAFS spectra at the Co K-edge for different types of CoCat film. Fourier-transforms (FT) of experimental spectra correspond (A) to different deposited amounts of CoCat measured at 1.05 V vs. NHE in 0.1 M KPi buffer (pH 7) or (B) to CoCat (100 mC cm^{-2}) that was

equilibrated in KPi or NaPi buffer (0.1 M, pH 7) at OCP for 2 min. Comparison of the two FTs in A suggests that the atomic CoCat structure is the same for the thin 20 mC cm^{-2} and the thick 100 mC cm^{-2} electrode film. Comparison of the two FTs in B shows the absence of clear changes for the K^+/Na^+ exchange. We note that after electrodeposition, CoCat electrodes were stabilized by drying in air for 1-2 days. This drying presumably results in decreased long-range order reflected in decreased peak amplitudes in B at about 4.5 Å and 5.3 Å of reduced distance, corresponding to Co-(Co)-Co distances of about 4.8 Å and 5.6 Å. Upon electrolyte exposure alone, the long-range order is not restored (in B); upon electrolyte exposure and application of an electrode potential, the long-range order is restored (in A).

4.2.4 Slow release of phosphate from CoCa film

Operando XAS detected K^+ exchange kinetics with a fast K^+/Na^+ exchange of ca. 5 s and reveals its independence of applied potential. Here, the dynamic behavior of phosphorus in the CoCat catalyst operated in a KPi-free electrolyte was studied by using the malachite-green assay for P quantification (Figure 4-21).[459-461] For obtaining the release rate of phosphate ions from the CoCat material, the film was exposed to a phosphate-free electrolyte (KNO_3, 500 mM, pH 7.0) at a working electrode potential of 1.0 V_{NHE}. The potential was similar to the deposition potential where the film is long-term stable and cobalt is mainly in the Co (III) oxidation state.[126] The P content within CoCat film was determined for various operation time (0, 2, 4, 10, 20, 30, 40, 60, 80 min).

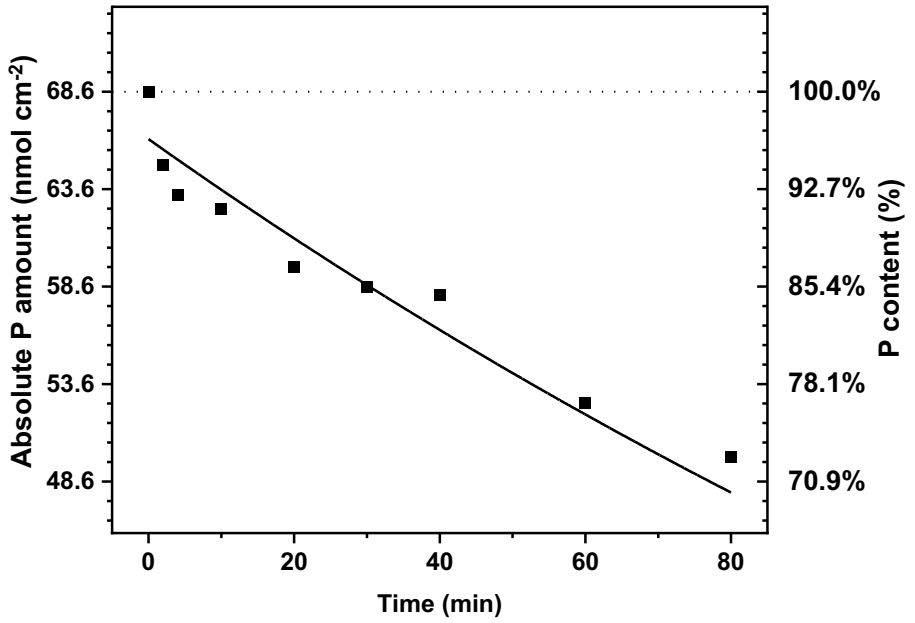

Figure 4-21. Phosphate content in CoCat films (20 mC cm^{-2}) exposed to a phosphate-free electrolyte (KNO_3 500 mM, pH 7.0) at a potential of 1.0 V_{NHE} (pH 7) for the indicated time periods. Left y-axis, P content in the total CoCat film determined by the malachite-green assay (see Experimental Section 4.4.3). Right y-axis, respective relative P contents. Each data point (squares) shows the mean of two individual films with three assays for each film. The fit line is a single-exponential decay with a time constant of 250 min and zero offset. The first data point is assumed to be the intrinsic P content of the electrodeposited CoCat film (before electrolyte exposure) and was used to calculate the relative P content in percent The dotted line denotes 100% P content.

The P content was quantified by UV-vis spectrometry based on the optical absorption at 620 nm. The absorption spectrum (500–750 nm) was measured after 30 min incubation (Figure 4-22) and the absorption at 620 nm was determined. According to the calibration curve [142] in Chapter 2 (Figure 2-22B), the P concentration in each assay solution was determined and the P contents in the respective CoCat samples were calculated accordingly (i.e., considering the dilution process). The rationale and procedure of P quantification via malachite green assay is described in Chapter 2 (see Section 2.4.4).

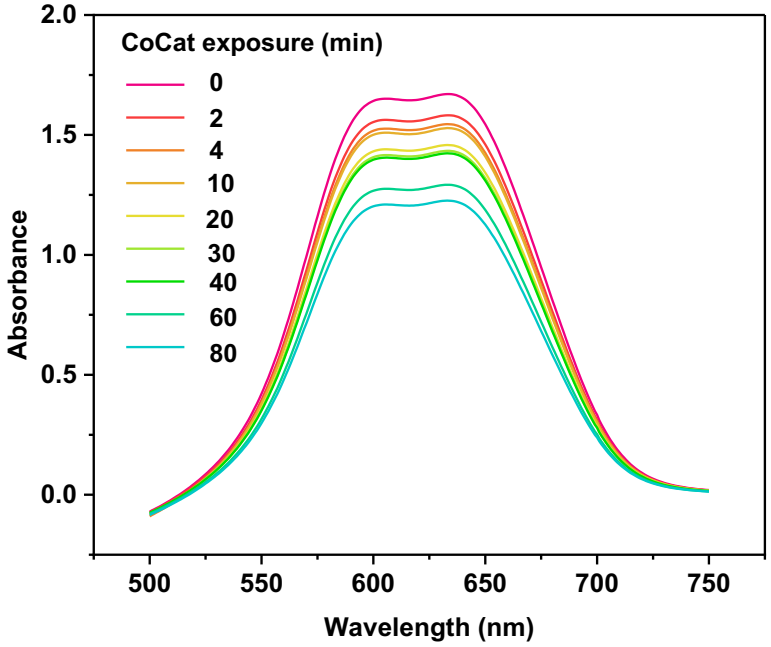

Figure 4-22. UV-vis absorption spectra of malachite-green/CoCat assay solutions. After exposure for the indicated time spans to P-free electrolyte at 1.0 V_{NHE}, CoCat films were dissolved and reacted with the malachite-green assay kit for 30 min (see experimental section) and then the spectra were recorded. Absolute P contents in each assay were determined using our earlier reported calibration curve (Figure 2-22).[142] The total P contents in CoCat film were calculated with considering dilution procedure.

The P amount for various operation time (Figure 4-21) revealed very slow release of phosphate ions within more than four hours, as opposed to rapid release of potassium ions within less than one minute. Within 80 min the P content in the film decreased by only about 30 % and a single-exponential fit revealed a time-constant of ca. 250 min for the P loss. The slow P release is consistent with an earlier report.[131] The initial P content is about 70 nmol cm^{-2}, which matches the reported Co:P stoichiometry of ca. 2-3:1 for a Co content of ca. 200 nmol cm^{-2} for a 20 mC cm^{-2} film.[70] Also the P content after 10 min exposure agrees with an earlier report (Figure 2-21).[142] The slow P release from CoCat suggests that phosphate does not act as a mobile counterion, which compensates surplus positive charges that appear in the film upon oxidation of the cobalt ions. Because also potassium ions cannot effectively balance the cobalt charges (Figures 4-3 and 4-13), compensation of positive charges must occur by the release of protons from the CoCat film. Phosphate ions rather serve as quasi-stationary proton-accepting

buffer molecules that channel the charge-compensating H^+ ions to the bulk electrolyte. In summary, a charge-compensating role of phosphate in CoCat can be excluded, but such ions may be important for maintaining a defined arrangement of redox inert ions in the interlayer spaces, which are required for efficient proton conduction for charge compensation in response to the cobalt redox reactions and for release of the protons produced during water oxidation and O_2 formation.

4.3 Summary

(1) What is the structural role of K^+ ions bound within the CoCat material?

The CoCat-internal K^+ ions are structurally innocent, which is not related to the K^+ coordination that tight binding to three Co ions to form a cubane motif [153;341;448;449], as found for Ca^{2+} in the Mn_4Ca-oxo cluster of the biological catalyst of photosystem II[153;341;448;449] and also in inorganic OER catalyst materials. Instead, a sizeable fraction of otherwise hydrated K^+ ions likely form ion pairs with phosphate species, resulting in a K^+ coordination environment similar to that found in concentrated KPi solution. Meanwhile, the potential dependence of the Co oxidation states and coordination environment is independent of electrolyte concentration, indicating a non-essential role of K^+ ions for the atomic structure and electrochemical functionality. This conclusion is also supported by the similar CoCat structure after K^+/Na^+ exchange. To sum up, the properties of K^+ within the CoCat are in agreement with a dissolved ion in the aqueous quasi-electrolyte[99] that fills the space between Co oxide fragment layers without any direct influence on the structure, redox chemistry, and catalytic performance of the material.

(2) Do K^+ ions facilitate charge compensation in the redox transitions of the catalyst material?

The volume-active CoCat material implies that Co oxidation within the macroscopic catalyst volume needs to be associated with a corresponding quantity of cations (incl. protons) leaving the catalyst volume (or anions entering it) in order to maintain the neutrality of charge accumulation. The structural analysis suggests loose binding of K^+ within the CoCat as part of interlayer quasi-electrolyte. Elemental analysis of the CoCat material equilibrated at reducing and oxidizing potentials reveals that potential-dependent Co oxidation is associated neither with K^+ depletion nor with phosphate enrichment (see Figure 4-2).

The temporal sequence of events associated with the potential-induced Co oxidation may involve K^+ release as a fast initial response to an increased electrode potential, followed by Co oxidation associated with deprotonation of Co ligands paralleled by a reverse K^+ uptake. This per se plausible scenario was excluded herein by time-resolved X-ray experiments revealing clearly faster Co oxidation (around 300 ms)[143] than K^+ release (around 5 s).

In conclusion, the stoichiometric charge compensation in the Co redox transitions of the volume-active CoCat material is not facilitated by any ions aside from protons. Early electrokinetic investigations have provided evidence that OER involves proton-coupled electron transfer reactions in CoCat, pointing towards coupling of the $Co^{II/III}$ oxidation to proton release.[119;134] The coupling to proton release and uptake is in line with the clear pH-dependence[99;113;126] and H/D isotope effect[134] of the midpoint potential of the Co redox transitions.[126;158] At an atomic level, the proton release coupled to Co oxidation likely

proceeds by deprotonation of bound water species (H_2O/OH^-) coordinated to Co ions, as previously suggested based on structural changes detected by XAS,[126] later supported by the H/D exchange influence on electrokinetic data [134] and operando Raman spectra.[139]

(3) Relevance for other catalyst materials

The structural changes associated with the $Co^{II/III}$ and $Co^{III/IV}$ redox transitions of the CoCat material are comparably moderate; non-stoichiometric mixed-valence Co oxidation states ($Co^{II}_{0.4}Co^{III}_{0.6}$ and $Co^{III}_{0.8}Co^{IV}_{0.2}$, respectively) are encountered at lowest and highest potentials.[126] In other OER catalyst materials, potential-induced redox transitions are coupled to clearly more pronounced structural changes and more complete redox transitions, thus corresponding to a full-fledged phase transition. A prime example is layered Ni-based oxyhydroxides, for which the $Ni^{2+/3+}$ transition is associated with the decrease of layer spacing, likely involving K^+ ion insertion.[269] In the latter material the structural and charge-compensating role of K^+ ions may differ from the one in the CoCat and related amorphous materials.

The CoCat is a dynamic material for which redox activity and catalytic activity are not restricted to the bulk-electrolyte exposed surface, but are occurring in the complete bulk volume of the catalyst material (volume activity),[99] even for the ca. 700 nm material thickness of the 100 mC cm^{-2} CoCat as used in the present study.[99] On a first glance, this volume activity appears as a very special property. However, by prolonged OER operation, several initially crystalline, molecular, and metallic catalyst materials were transformed partially or completely into an amorphous material with similar redox properties of the amorphized regions as observed for the bulk-volume of the CoCat.[67;105;107;115;153;154;178;234;343;442-445;462;463] Therefore we believe that the here reported findings on the K^+ binding mode and likely absence of a charge-compensating role of K^+ ions are of relevance for a larger group of OER-active materials, but possibly not for OER materials where the redox transitions exhibit phase-transition character. For optimization of charge-compensating ion flows in volume-active OER materials, rather than catalyst-internal cations, the (de)protonation reactions and proton mobility may be especially promising targets.

4.4 Experimental details

4.4.1 Sample preparation

XAS sample: solid potassium-phosphate (KH_2PO_4, Roth, ≥99%) was finely ground and uniformly dispersed onto Kapton tape to form a thin film. KCl (Sigma-Aldrich, 99.999% purity) was dissolved in MillQ water to prepare a 0.1 M KCl solution. Potassium or sodium phosphate buffer (KPi/NaPi, 0.1 M or 2.5 M, pH 7) was prepared by mixing ~40% $K(Na)H_2PO_4$ and ~60% $K_2(Na)_2HPO_4$ at specific concentration. Graphene sheet (15×15 mm^2, Graphene Supermarket) without Kapton tape covering the backside serves as electrode substrate. CoCat depositing amount in XAS measurement for this chapter is 100 or 300 mC cm^{-2} which was controlled by a well-known electrodeposition protocol.[134]

TXRF samples were prepared as follows: each CoCat film (20 mC cm^{-2}) electrodeposited on Pt foil (0.1 mm, 99.95% purity, Labor-Platina Kft) was exposed to respective KPi concentrations (1.6 mM, 25 mM, or 100 mM) and electrode potentials (1.0 V or 1.3 V vs. NHE) for 15 min followed by Millipore water rinsing. The operated CoCat films on Pt foil were dissolved by immersion in pure nitric acid (HNO_3, 3 mL, 70%, 99.999% purity, Sigma-Aldrich) for 5 min. To 400 µL aliquots of these samples, 100 µL aliquots of K standards were added with various concentrations (Table 4-1) prepared from KH_2PO_4 stock (1 g L^{-1}, Merck Millipore). In addition, gallium and caesium ($Ga/Cs(NO_3)_3$, 1 g L^{-1}, Fluka Tracecert) standards (Figure 4-1) were added for quantifying cobalt and potassium amount, respectively. For TXRF measurement, 10 µL aliquots of the digested sample solution were dried on quartz glass holders and TXRF spectra were recorded for 30 min and analyzed with the software available with the spectrometer. The calibration curves of each assay for films operated at various operation conditions are shown in Figure 4-2. The K amount quantification within each film was described in the caption of Figure 4-2.

4.4.2 XAS measurement

XAS spectra at potassium or cobalt K-edge were collected either with samples held at 20 K in a closed-cycle liquid-helium cryostat (Oxford) or under operando conditions at room temperature in an electrochemical cell (setup scheme see Figure 3-19, samples were probed through the thin graphene sheet support) or in a vacuum chamber (samples were probed through thin Mylar foil or directly exposed to the beam). Further measurement conditions (Figure 4-4): spectra of K-CoCat and KPi (2.5 M solution) were obtained at 20 K, spectra of KH_2PO_4 powder and KPi (0.1 M solution) were collected at RT. The KCl (0.1 M) solution spectrum was measured at RT in vacuum. K–CoCat and KPi (0.1 M) were probed by the incident X-ray beam passing through a thin graphene sheet (25 µm) without a foil window while the other samples were probed through a 3 µm Mylar foil window. At least 4 spectra per sample were averaged to improve the signal statistics. The monochromator was detuned by 50% at the potassium K-edge to suppress harmonics; detuning is not required at the Co K-edge because harmonics are absent due to the intensity cutoff of the beamline at ca. 15 keV. Deadtime-corrected XAS spectra were normalized to yield XANES spectra and EXAFS oscillations were extracted as described earlier[123] using an E_0 of 3608 eV (K) or 7709 eV (Co). Fourier-transforms (FTs) were calculated for a k-range of 1.6–8.2 $Å^{-1}$ (K) or 1.6–12.3 $Å^{-1}$ (Co)

using cos windows extending over 10 % of both K-range ends, S_0^2 was 0.8. EXAFS simulations were carried out using in-house software and phase functions from FEFF9.[67;169] XAS spectra of potassium were measured on thicker CoCat films. In Figure 4-20, XAS spectra at the Co K-edge for different film thickness and/or different electrolyte (NaPi or KPi) are measured, suggesting similar atomic structure of CoCat that is independent of film thickness and electrolyte component.

Operando XAS experiments at the potassium K-edge were conducted to measure the potassium content by monitoring the potassium X-ray fluorescence at a fixed excitation energy of 4 keV. CoCat films (100 mC cm^{-2}) were deposited on graphene sheets with the X-ray beam passing through the graphene sheet (without covering Kapton tape). The CoCat was operated in stirred (~300 rpm) NaPi buffer (0.1 M, pH 7). To study K-exchange kinetics, dry CoCat films were mounted in the electrochemical cell, in which NaPi electrolyte was rapidly filled through a triggered peristaltic pump (flow rate 116 mL min^{-1}). More specific protocol as follows: (a) Switching on fast shutter to make sample irradiated under the X-ray beam, and recording the potassium Kα fluorescence of dry CoCat film at open circuit potential (OCP) for 120 s; (b) switching on pump to fill ~20 mL NaPi within ca. 12 s; (c) after 132 s, different potentials (OCP, 0.65 V, 0.8 V, 1.0 V, 1.2 V or 1.35 V vs. NHE, without iR drop correction) were applied for 10 min and simutaneously recording potassium X-ray fluorescence. Fluorescence was recorded at 0.5 s per point and analyzed using bi-exponential functions (Figure 4-15). Meanwhile, a potential jump protocol was employed by using the same cell configuration and electrolyte condition as described above (Figure 4-13), but here with each potential applying for 1s, see more in Figure 4-15 caption.

4.4.3 P quantification via malachite green assay

Phosphate release dynamics was conducted by using malachite green assay method. The details of this technique were explained in Section 2.4.4 of Chapter 2.

5 Local pH and electrolyte pH profiles in neutral-pH water oxidation quantified by operando Raman spectroscopy

Abstract The electrolyte pH at the catalyst-electrode−electrolyte interface is a major determinant of the electrocatalytic current density (see Chapter 2). Fluxes of proton-transporting molecules, here phosphate ions in different protonation states, are decisive regarding formation of the local pH under electrocatalytic operation conditions. In this chapter, a non-intrusive method is introduced that facilitates the spatially resolved detection of local pH values based on detection of Raman bands of the electrolyte phosphate ions. It is applied for investigation of water electrolysis using a cobalt-based catalyst film (CoCat) at the anode and a platinum cathode. For water oxidation at the anode, pronounced local acidification was detected close to the outer surface of the CoCat material, but only for electric potentials beyond the Tafel slope regime. This result supports the conclusion of Chapter 2 that macroscopic proton transport limitations lead to a decrease in the local pH near the catalyst surface which in turn limits the catalytic current density. Time-resolved investigation revealed that establishment of largely stationary concentrations required minimally 5 min. Unexpectedly, non-linear $H_2PO_4^-$ and HPO_4^{2-} amount profiles were detected between anode and cathode, with steep concentration gradients that level off within about 800 µm from the respective electrode. This can be explained by a circular electrolyte flow that involves the transport of (protonated) buffer molecules from the anode to the cathode at the top of the cell and (deprotonated) buffer molecules from the cathode to the anode at the bottom of the cell. Natural convection caused by buoyancy effect relating to density difference of the hydrated phosphate ions may drive the circular flow. In conclusion, for the here investigated geometry, the direct 'passive' diffusion of proton carrying molecules within a stagnant electrolyte is not the major route of proton transport from the anode to the cathode; other non-diffusive flows dominate the electrolyte proton transport. This conclusion likely is generally valid for technically relevant electrolysis cells.

All experiments and data evaluation presented in this chapter were performed by Si Liu.

A portion of this chapter reproduced from the following open-access article:
S. Liu, I. Zaharieva, L. D'Amario, S. Mebs, P. Kubella, F. Yang, P. Beyer, M. Haumann, H. Dau*. Electrocatalytic Water Oxidation at Neutral pH–Deciphering the Rate Constraints for an Amorphous Cobalt-Phosphate Catalyst System. *Advanced Energy Materials* **2022**, 12, 2202914. https://doi.org/10.1002/aenm.202202914

The experimental scheme of Figure 5-1 has been reproduced from the following article (with the permission from Elsevier):

S. Liu, L. D'Amario, S. Jiang, H. Dau*. Recent operando Raman spectroscopy applications in electrochemistry. *Current Opinion in Electrochem*istry **2022**, 35, 101042. https://doi.org/10.1016/j.coelec.2022.101042

In this review article, S. Liu was the lead author; she predominantly wrote and edited the manuscript. L. D'Amario, S. Jiang, and H. Dau contributed to writing and editing.

5.1 Introduction and motivation

In electrocatalytic water oxidation reactions, electron transfer affects the catalytic reaction rate. Notably, proton release and its transfer or transport can also have a significant impact on reaction kinetics, activity, and selectivity, and thus must be incorporated into the understanding of the intrinsic mechanism of OER and its relation to transport processes in the electrolyte.[464-466] In order to elucidate the structure-activity relationship of OER, it is important to consider also the the mass-transport limitations, in particular the local pH at the conductive substrate-catalyst or catalyst-bulk electrolyte interface. Changes in local pH are expected to arise from redox transitions in the metal centers as well as the release or uptake of protons during water oxidation.

Relevant factors affecting the local pH value (or proton activity) include current density, diffusivity and buffering capacity of the electrolyte system.[467] We have demonstrated experimentally that buffer bases in electrolytes can mitigate proton transport limitations under neutral conditions,[142] and found that the activity of CoCat-catalyzed OER in the intermediate potential region is directly proportional to the availability of unprotonated buffer molecules (see Chapter 2).[142] In ref. [135], a first-order model describing the effect of pH changes at the working electrode on catalytic current densities was reported. In this model, proton transfer is mediated by the macroscopic diffusion of the buffer base molecules between anode and cathode; for parallel arrangement of planar electrode, a linear spatial amount distribution of the buffer-base molecules between the anode electrode and the cathode electrode (Figure 1-7A), but a recent investigation suggests it is the presence of buoyancy effects[207] (Figure 1-7B). Therefore, the following section presents an experimental study of the local pH in the vicinity of the electrodes and explores the validity of the first-order model, which assumes a linear (de-)protonated buffered base amount profile between the electrodes.

Various methods for quantifying local pH have recently been reviewed.[57;142;204;205;207;391;465;468-472] Operando Raman spectroscopy under optimal operating conditions facilitates non-invasive assessment of proton activity at a three-dimensional spatial resolution close to 1–2 μm.[206] To the best of our knowledge, this is the first time that this method has been used to assess the localized alkalization of copper foam electrodes during CO_2RR, based on an analysis of the HCO_3^-/CO_3^{2-} amount ratio.[57] Similar optical experiments had been reported by employing the attenuated total-reflection IR spectroscopy.[466;473] However, the IR technique suffers from strong adsorption of Infrared light by water molecules or electrolytes and requires specific electrodes. Operando Raman experiments do not require additional electrodes[465;471;474-477] or indicator dyes,[470;471;478] which facilitated to study local pH effects quantitively by determining the protonation states of protonatable “buffer” molecules. The pH is quantified by collecting Raman reference spectra of the buffer molecules at various pH followed by constructing

calibration curve. Here the protonatable molecules are phosphate species serving as electrolyte used for neutral-pH OER.

In this chapter, we quantify the local and overall electrolyte pH profiles during neutral OER at low concentrations (25 mM, pH 7) of KPi by operando Raman spectroscopy. Electrochemical techniques are applied including chronoamperometry (CA) or chronopotentiometry (CP) as well as jumping current protocols. As outlined further above, the rationale of pH determination is based on changes in the amplitude of the vibrational band caused by changes in the amount of the phosphate protonation state.[57;142] Two types of electrochemical cells were employed to quantify local and bulk-electrolyte pH (Figures 5-1 and 5-6), respectively. For local pH measurements, we examined the pH at the microscale distance (20 μm) of the electrode/bulk-electrolyte interface. To investigate the overall pH profile between anode and cathode, a simple two-electrode geometry was employed for collecting Raman spectra at different spatial positions of the electrochemical cell and time traces changes of pH or phosphate amounts at different positions are obtained.

5.2 Results and discussion

For determining local (spatially resolved) pH values and their temporal evolution, first Raman spectra were measured, second the amounts of phosphate species were calculated based on calibration equation and third the local pH values were obtained according to pH calibration curve. For a presentation of the results, however, mostly a different sequence was chosen to avoid the reader getting lost in the details of the experimental approach. In the various subsections of this chapter, the central results on the evolution of local pH values are presented first, followed by more detailed presentations on calibration, phosphate species amounts, and exemplary Raman spectra.

5.2.1 Local electrolyte pH at the catalyst electrode

In Chapter 2, we have proposed that the plateau-level current density of the *j*-V curves is determined by the availability of a buffer base (HPO_4^{2-}) in the vicinity of the CoCat electrode.[142] In the Tafel-slope regime, those basic species mitigate local electrolyte acidification by accepting protons produced by the OER. The plateau-level of the current density is reached once diffusion of the buffer ions between CoCat anode and cathode (here a Pt counter electrode) approaches its maximal rate, resulting in pronounced local acidification of the electrolyte close to the electrolyte-catalyst interface. To verify the above scenario, we investigated the local pH close to the outer catalyst-electrolyte interface (20 μm) during electrocatalysis using Raman spectroscopy (Figures 5-1 and 5-2). A laboratory-build three-electrode Teflon cell was used to collect spectra of CoCat films (1 cm diameter) deposited on a Pt-foil substrate in 25 mM KPi solution (pH 7). Spectra were collected from CoCat film (20 mC cm^{-2}) operated at various potential steps from 0.6 V to 1.38 V for 1 min (total step duration 2.5 min) via a chronoamperometric protocol. In Figure 5-2A, the intermediate band at 991 cm^{-1} corresponding to the basic phosphate species (HPO_4^{2-}) sharply decreases with applying increasingly positive potentials, whereas the bands at 877 and 1077 cm^{-1} corresponding to the protonated base (i.e., $H_2PO_4^-$) rise. The quantitative analysis takes into

account broad potential-dependent bands from the CoCat material[139] as shown in Figure 5-2B and the calibration curve prepared from various pH of KPi buffer (25 mM) (Figures 5-3 and 5-4). The results in the potential dependence of the local pH close to the outer CoCat surface are shown in Figure 5-2C.

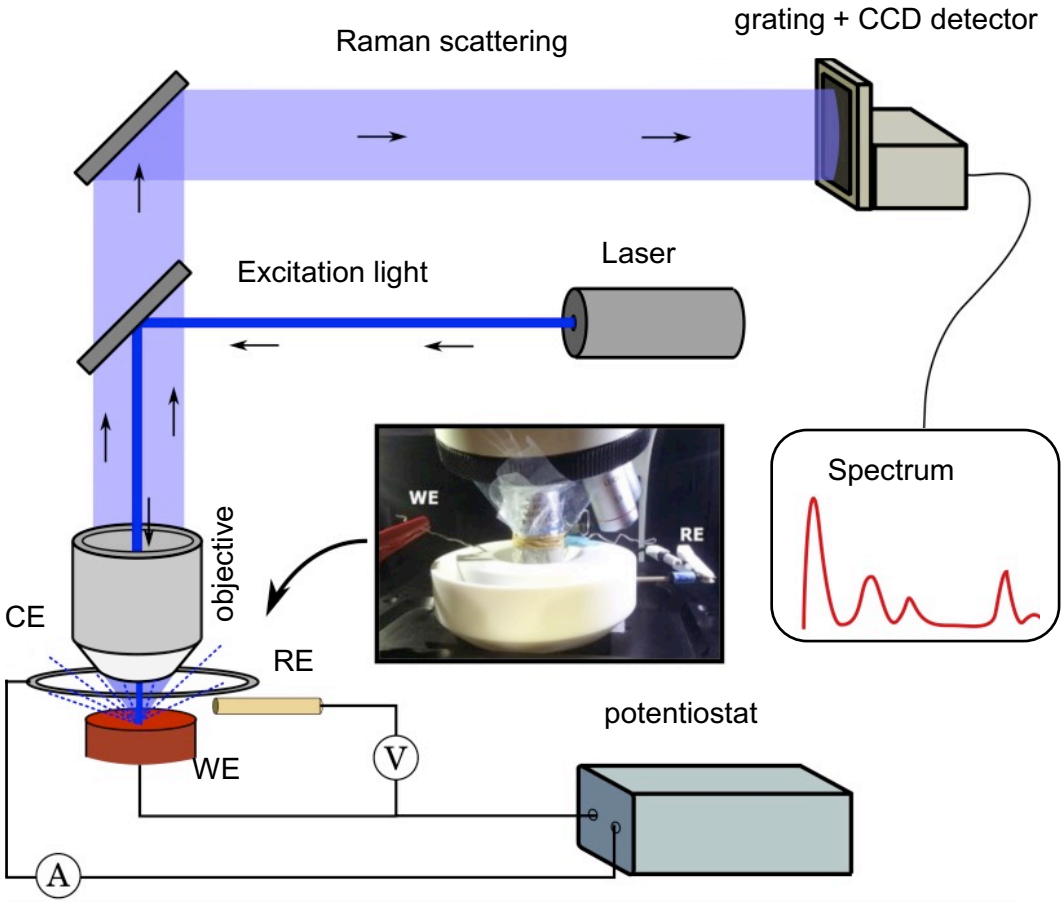

Figure 5-1. Scheme of the operando Raman spectroscopy setup for local pH measurement. WE, working electrode; CE, counter electrode; RE, reference electrode. The indicated voltmeter and amperemeter are not physically part of the set-up but represent the potentiostat functionality. The inserted photo shows a simple electrochemical cell (made from Teflon®PTFE) for operando Raman spectroscopy using an immersion microscope objective. A thin Teflon film (Teflon® FEP, 13 μm, DuPont) is wrapped around the microscope objective for protection of the lens, as it is needed for measurements in corrosive electrolytes. (Here experiments are reported for electrolytes in the near-neutral pH regime; therefore, the lens-protection membrane was not used.) Reproduced with permission from ref.[206]. Copyright Elsevier (2022).

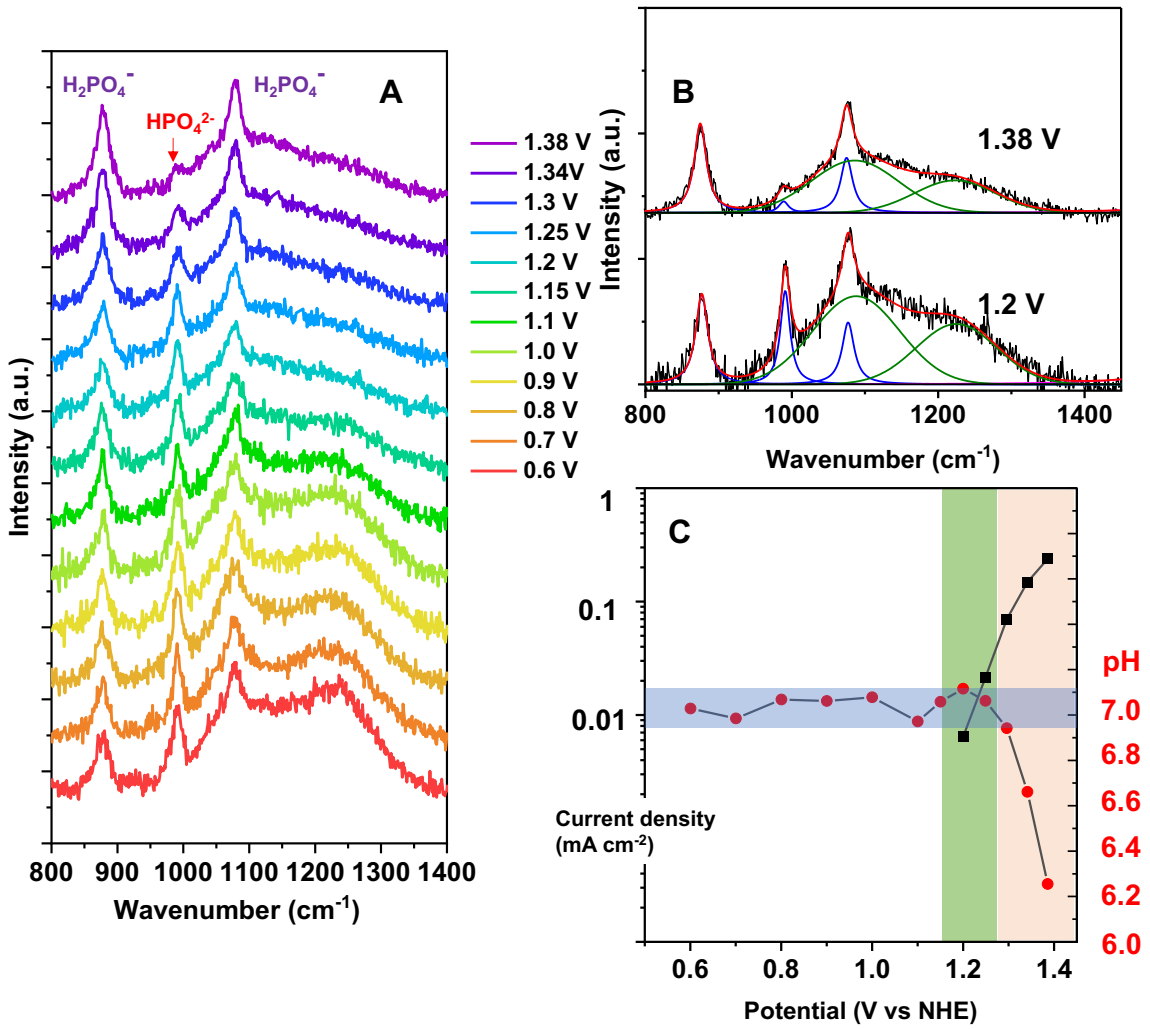

Figure 5-2. Estimation of local acidification by operando Raman experiments for electrocatalytic operation in 25 mM KPi buffer at pH 7 (CoCat deposition amount of 20 mC cm^{-2}, spectra collected at about 20 µm distance from the catalyst surface). (A) Spectra collected for CoCat films operated at the indicated electrode potentials (in V vs. NHE); from bottom to top, the applied potential was increased stepwise. (B) Examples of simulations for Raman spectra collected at 1.2 or 1.38 V versus NHE. The spectra were background subtracted and simulated from 800 to 1400 cm^{-1} as described in the experimental method. Briefly, for each spectrum, three Lorentzian functions (blue lines) and two Gaussian functions (green lines) were fitted with fixed band positions (Lorentzian: 877, 991, and 1077 cm^{-1}; Gaussian: 1088 and 1225 cm^{-1}) and widths (half-width at half-maximum: Lorentzian: 25, 8, and 10 cm^{-1}; Gaussian: 70 and 65 cm^{-1}), but varying band amplitudes. (C) Catalytic current densities (left y-axis, black squares) and local pH (right y-axis, red circles). The squares indicate static current densities after applying the respective potential for 2.5 min (current densities below 7 µA cm^{-2} are not shown). Reproduced with permission from ref.[142]. The olive background indicates the Tafel-slope region with exponentially increasing current density, but without significant pH change. The beige background indicates increasing saturation of the current density, which is found to be associated with increasing acidification at the catalyst-electrolyte interface. Copyright Wiley-VCH (2022).

In Figure 5-2C, we observe pronounced local acidification by almost one pH unit close to the outer CoCat surface for electric potentials beyond the Tafel-slope regime. This finding supports

that, during OER operation, macroscopic proton transport limitations result in a local pH decrease (increased proton activity) in the vicinity of the catalyst surface, which in turn limits the catalytic current density.

5.2.2 Calibration curve

To accurately quantify the local pH, constructing a reliable calibration curve is crucial. A broad pH range from 4.5 to around 9.8 was prepared to collect Raman spectra and its change of phosphate species amplitude at various pH can be used for constructing the calibration curve. In the spectra of a phosphate standard solution (Figure 5-3), two phosphate species prevail, $H_2PO_4^-$ and HPO_4^{2-}.[479;480] $H_2PO_4^-$ shows Raman bands at ~877 cm^{-1} and 1077 cm^{-1}, assigned to the Vs $P(OH)_2$ and Vs PO_2 vibrations. Another band at ~991 cm^{-1} belongs to Vs PO_3 from HPO_4^{2-}. At more alkaline pH, a broad band around 855 cm^{-1} with lower intensity is ascribed to Vs P(OH). In addition to the vibrations associated with phosphorus species, a broad water band at ~1642 cm^{-1} corresponds to the H-O-H bending vibration and was chosen as an internal calibration standard.[139;481] The ratio of the $H_2PO_4^-$ and HPO_4^{2-} amounts according to the Henderson-Hasselbalch equation was used to quantify the local pH. Here, we chose the HPO_4^{2-} vibrational band at 991 cm^{-1} and the $H_2PO_4^-$ band at 1077 cm^{-1} to determine the standard curve. The normalized amplitudes of the two bands at different pH values are shown in Figure 5-4 and Table 5-1. For obtaining the amount of phosphate species, a calibration factor (υ) was introduced, assuming that the sum of the $HPO_4^{2-}$and $H_2PO_4^-$ amounts are constant. According to the data in Figure 5-4A and Table 5-1, we calculated υ (1.558) as the band intensity at 991 cm^{-1} (9.77) divided by the intensity at 1077 cm^{-1} (4.56). The calibrated phosphate amount of HPO_4^{2-} and $H_2PO_4^-$ are given by the following relations:

$$[H_2PO_4^-] = \upsilon * A_{1077}/(\upsilon * A_{1077} + A_{991}) \qquad \text{Equation 5-1}$$

$$[HPO_4^{2-}] = A_{991}/(\upsilon * A_{1077} + A_{991}) \qquad \text{Equation 5-2}$$

A is the normalized peak amplitude with respect to the average water peak amplitude. The resulting calibration curve as a function of the pH is shown in Figure 5-4. It reveals an apparent pK_a of 7.13, which is in good agreement with the reported pK_a of phosphate buffer of 7.21. The calibration curve was used to determine the pH at different potentials close to the CoCat surface or in the bulk at different positions between the electrodes. For the band quantification, each spectrum was analyzed using five apparent vibrational features, with the P band from the KPi electrolyte being simulated similar to the P standards, and the internal phosphate band simulated by a Gaussian function. The simulation parameters are shown in
Table 5-2. In addition, the amplitudes of inner phosphate bands provided access to dynamic changes in the P localization at different potentials (Figure 5-5).

$$s = \sqrt{\frac{1}{n}\sum_{i=1}^{n}(x_i - \bar{x})^2} \qquad \text{Equation 5-3}$$

Here n is the number of samples measured in each condition, x_i is result of a single measurement, $\bar{x}$ is the average result.

Table 5-1. Fitted Raman band amplitudes for standard phosphate solutions at various pH values. Amplitudes (in counts) are for normalized spectra. Respective normalization factors (NF) were derived from mean values of fitted water band amplitudes. Numbers in parentheses represent peak position and half-width-at-half maximum (HWHM) (both in cm^{-1}), a slash means that no band was visible. A calibration factor (υ) of 1.558 was obtained from the normalized band intensities at 991 cm^{-1} (at pH 9.77) and 1077 cm^{-1} (at pH 4.56). The values for the column of "absolute P amount" (a.u.) only show their numerator part since the final ratio of P amount (P_{991}/P_{1077}) only considers the numerator. The absolute phosphate ratio values and the measured pH values were used to construct the calibration curve in Figure 5-4.

pH	HPO_4^{2-} (855, 10) V_s P(OH)	$H_2PO_4^-$ (877, 10) V_s $P(OH)_2$	HPO_4^{2-} (991, 10) V_s PO_2	$H_2PO_4^-$ (1077, 10) V_s PO_2	NF	Absolute P amount (991)	Absolute P amount (1077)	P_{991}/P_{1077}
4.56	/	12082	/	9016	0.98	/	14047	/
4.78	/	11989	/	8622	0.97	/	13433	/
5.38	/	11753	/	8876	0.99	/	13829	/
5.58	/	11226	/	8465	1.00	/	13189	/
5.98	/	10976	581	8168	1.00	581	12727	0.05
6.29	/	10217	1274	7881	1.20	1274	12279	0.10
6.67	/	9344	4053	6169	1.00	4053	9612	0.42
6.88	/	8188	5560	5435	1.05	5560	8469	0.66
7.14	5197	4098	7948	4045	1.03	7948	6302	1.26
7.44	4369	3750	10596	2795	1.12	10596	4355	2.43
7.96	4872	2168	13044	1087	1.05	13044	1694	7.70
8.27	4662	1610	13822	665	1.02	13822	1036	13.34
8.5	5001	1375	14393	381	1.01	14393	594	24.23
9.12	5196	1260	14146	/	1.01	14146	/	/
9.32	6613	/	14203	/	1.00	14203	/	/
9.77	5425	/	14047	/	1.02	14047	/	/

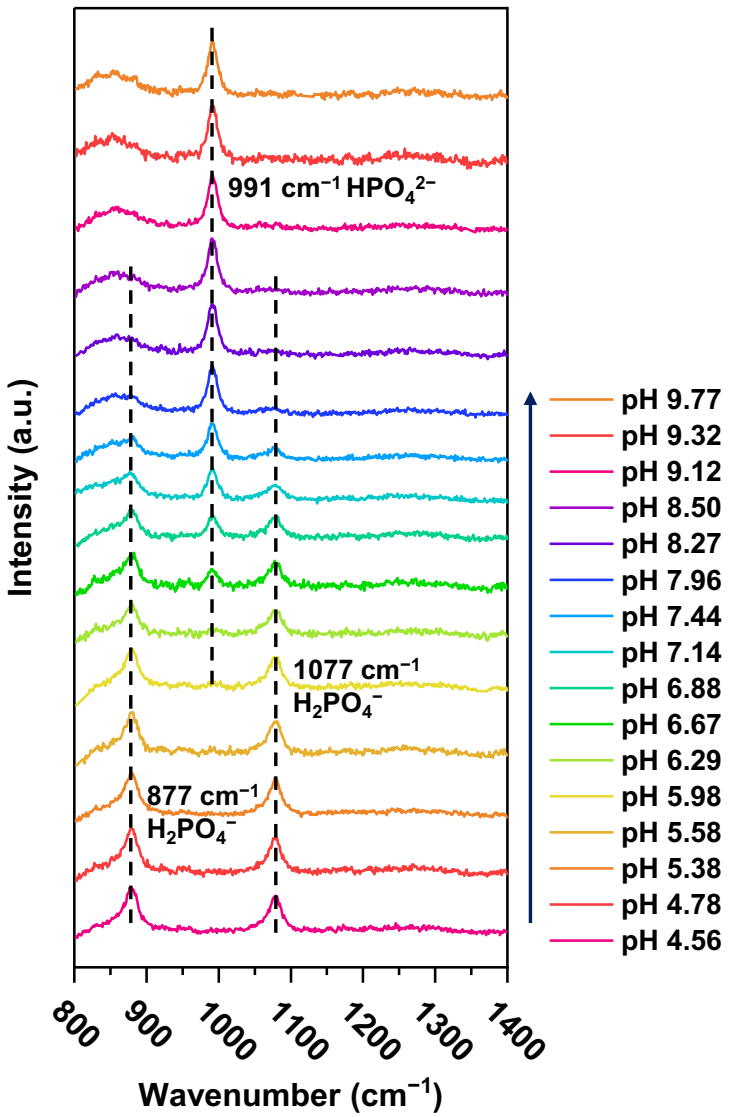

Figure 5-3. Raman spectra of phosphate standard solutions (25 mM) at various pH values. The dotted lines mark the vibrational bands of three main phosphate species prevailing in respective pH ranges; from left to right: $H_2PO_4^-$ (~877 cm^{-1}), HPO_4^{2-} (~991 cm^{-1}), $H_2PO_4^-$ (~1077 cm^{-1}). At high pH, a broad phosphate vibration at 855 cm^{-1} is furthermore observed. The shown spectra were background corrected.

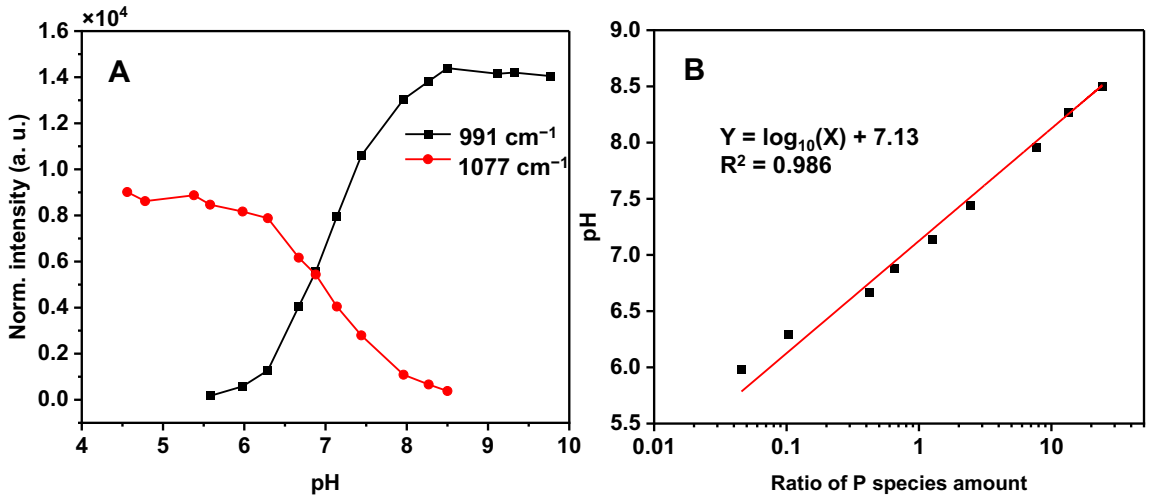

Figure 5-4. Normalized Raman band intensities of phosphate species at 991 cm^{-1} and 1077 cm^{-1} (A) and pH calibration curve determined from the amount (absolute P amount) ratio of phosphate species (B). Band intensities in Panel A were normalized with respect to the water band at ~1642 cm^{-1} (Table 5-1). Panel B shows the calculated ratio of HPO_4^{2-} and $H_2PO_4^-$ amounts (symbols). The line is a linear regression line.

Table 5-2. Normalized Raman band amplitudes from CoCat spectra at various potentials. Normalization factors (NF) were calculated as in Table 5-1. The absolute phosphate amount (a. u.) and their ratio were obtained as described in Table 5-1. The calculated pH was derived by using the calibration curve in Figure 5-4.

Potential (V vs. NHE)	Normalized intensity (counts) at band position in cm^{-1}					NF	Absolute P amount (a.u.)		P_{991}/P_{1077}	Calc. pH
	877	991	1077	1088	1225		991	1077		
0.6	6451	6998	5672	8451	11186	4.13	6998	8837	0.79	7.03
0.7	6060	6951	6235	7142	9260	4.06	6951	9714	0.72	6.98
0.8	5836	8041	5954	7654	8808	4.03	8041	9277	0.87	7.07
0.9	5849	7642	5742	6909	8574	4.03	7642	8946	0.85	7.06
1.0	6349	7144	5171	7757	8810	4.14	7144	8056	0.89	7.08
1.1	7076	6307	5828	6934	6766	4.32	6307	9081	0.69	6.97
1.15	7280	6681	5061	6388	5179	4.52	6681	7884	0.85	7.06
1.20	6728	7018	4652	6611	4526	4.71	7018	7248	0.97	7.12
1.25	7263	7246	5432	6504	4426	4.82	7246	8464	0.86	7.06
1.30	9093	5528	5473	6863	4247	4.87	5528	8527	0.65	6.94
1.34	11940	3836	7249	7063	4411	4.97	3836	11293	0.34	6.66
1.38	12659	1626	7830	7435	4610	4.95	1626	12199	0.13	6.25
OCP	5768	6471	5447	9284	13192	4.36	6471	8487	0.76	7.01

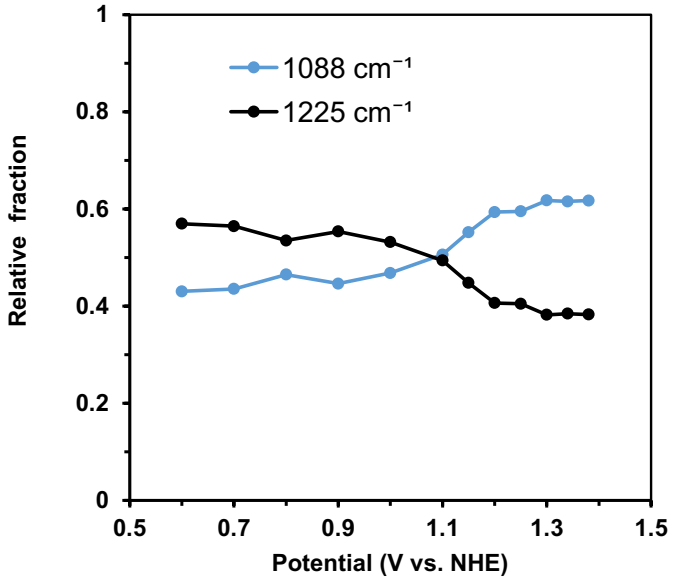

Figure 5-5. Broad Raman bands possibly assignable to catalyst-internal phosphate ions. For the (still hypothetical) assignment to two distinct protonation states of phosphate ions, the relative amount (fraction) of the two phosphate protonation states were calculated. In
Table 5-2, the respective phosphate band amplitudes from Raman spectra at 1088 cm^{-1} and 1225 cm^{-1} are shown. The relative fractions are calculated based on the sum of the two normalized band amplitudes.

5.2.3 Bulk electrolyte pH quantification

After quantifying the local acidification near the CoCat-bulk electrolyte interface, we experimentally investigated buffer base-assisted proton transport in the bulk-phase electrolyte. [135] In ref.[135], we propose that at constant diffusive flux, the change in base amount exhibits a linear curve between WE and CE. Raman cells featuring complicate geometries may result in especially intricate pH profiles (Figure 5-1). Therefore, a simpler two-electrode cell is employed where CoCat deposited on platinum foil acts as the working electrode (WE), and a blank platinum foil acts as the counter electrode (CE). Raman spectroscopy scheme used to measure bulk electrolyte pH is shown in Figure 5-6. A digital photograph of the two-electrode cell is shown in Figure 5-7A. The distance between WE and CE (10 mm) was controlled by a Teflon spacer (2 mm thickness) to ensure that the Pt electrodes fit tightly against the Teflon or aluminium holder. Copper tape is used for the electric circuit connection. The effective geometric area (1 cm^2) of electrodes is controlled by Kapton tape. In principle, facilitated by the microscale resolution of Raman spectroscopy, it is possible to obtain Raman spectra at any location between the two electrodes and thus can quantify the pH or phosphate amount based on changes in the amplitude of the phosphate peaks, as described in the rationale for local pH quantification (Figure 5-4). However, collecting spectra in the vicinity of the electrodes (less than 1 mm) was challenging when the electrode system had reached equilibrium due to bubble accumulation after a long period of operation (Figure 5-7D). Air bubbles positioned on the platinum foil can lead to strong attenuation or scattering of the Raman signal. Therefore, it is crucial to optimize the applied current density and the protocol of spectrum collection. One approach is to collect time-dependent spectra at various positions close to the electrodes upon the electrochemical protocol initiated, for which not only we can acquire time scale of the

electrochemical cell equilibrated but also mitigate the interference of large amount of bubble generation. Thereby, pH profiles can be obtained horizontally and vertically in the entire electrochemical system.

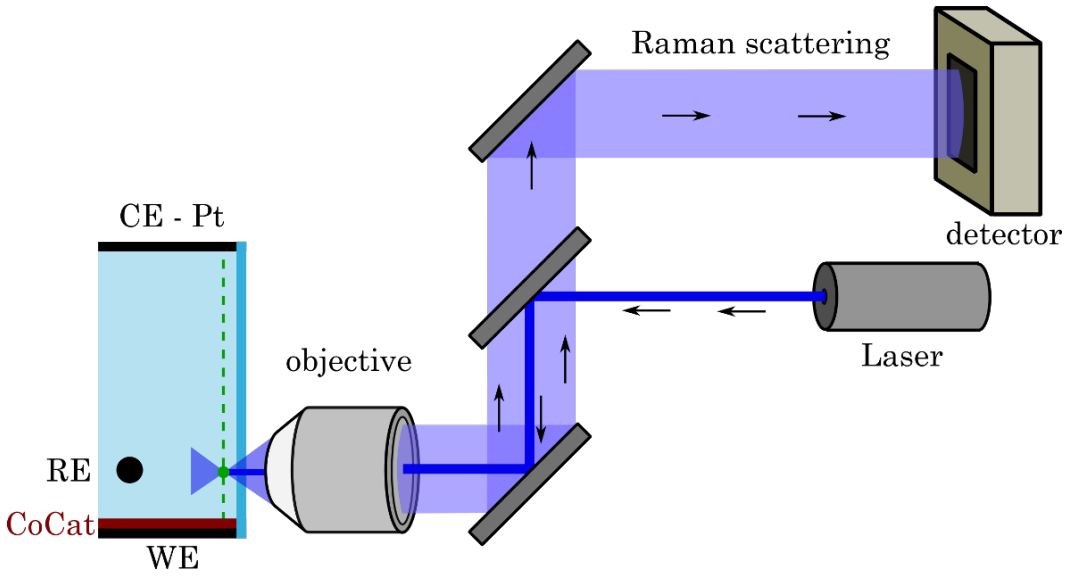

Figure 5-6. Scheme of operando Raman spectroscopy setup for the spatially resolved measurement of the electrolyte (bulk) pH. WE: working electrode (CoCat deposited on a platinum foil); CE: counter electrode (platinum foil); RE: reference electrode (Ag/AgCl, used only to measure the working electrode potential). A drop of water was added in front of the water-immersion microscope objective (×40, numerical aperture NA, 0.8). The dark blue rectangle represents 1 mm thick glass. The laser focusing point (green) is approximately 1 mm from the backside of the glass. The green dashed line represents the one-dimensional pathway for spectra collection. The geometry of the electrochemical cell is shown in Figure 5-7.

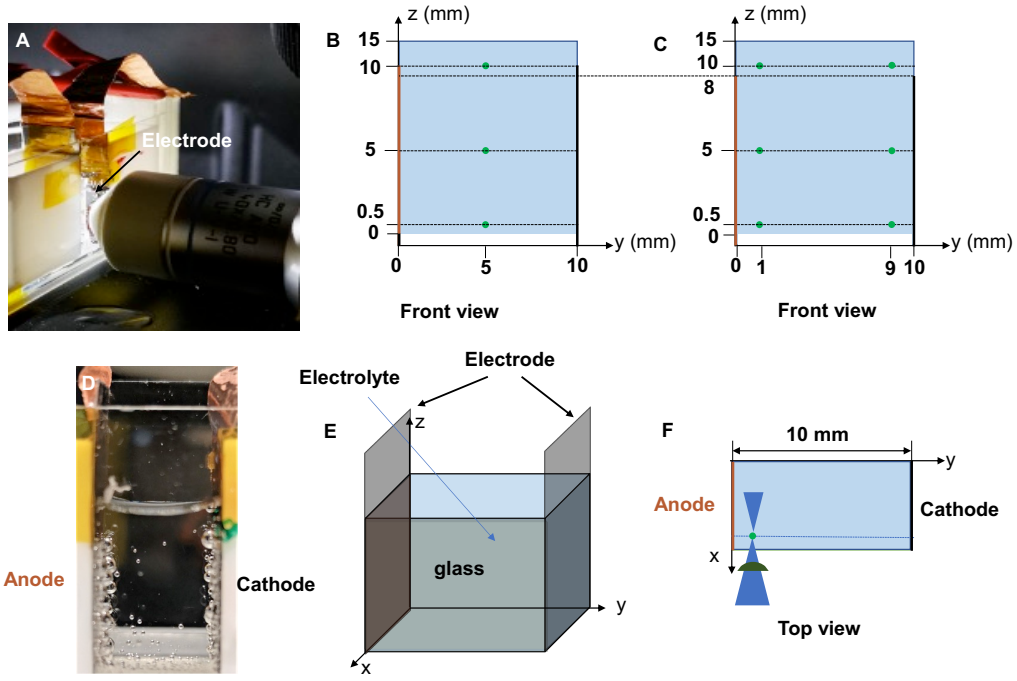

Figure 5-7. The two-electrode electrochemical cell used for spatially resolved detection of local pH in the bulk electrolyte. (A) Digital photograph shows the setup for operando Raman collection. (B and C) Front view of spectrum collection positions. The distance between the electrodes was 10 mm. Pt foils supported by Teflon or aluminium rectangular blocks were exposed in electrolyte with an effective area of 10 ×10 mm^2 (B) or 10 × 8 mm^2 (C); B, C, E, and F illustrates spectrum collecting dimensions and the electrochemical cell geometry. z represents the vertical distance from the bottom line of the cell (z = 0). The white area in B and C is Teflon spacer (2 mm thick) positioned between the electrodes for controlling the electrode distance. Note that the laser focus positions of B and C (z = 5 mm and 10 mm) are different relative to the height of the effectively solvent exposed catalyst. The collection point at the top of B is ca. 2 mm above the film. The blue area represents the electrolyte solution at a height of 15 mm; the thick lines on the far left (orange line) and far right (black line) represent the anode and cathode, respectively; (D) Photograph of bubbles accumulated on electrode surface at 0.5 mA cm^{-2} after ca. 2 h (left: CoCat deposited on Pt foil; right: blank Pt foil).

5.2.3.1 Temporal evolution of pH at various near-electrode positions (z = 5 mm)

Temporal pH or phosphate amount profiles between electrodes were quantified at a constant horizontal layer of 5 mm height (z) with applying current density of 0.3 mA cm^{-2}. However, pH measurement in the vicinity of the electrodes (i.e., within 1 mm of each other) is interfered by the rapid generation of air bubbles upon the electrochemical cell reach equilibrium. Thus, we measured the temporal evolution of pH profile at various positions within 1 mm distance from the electrode (Figure 5-8). Spectrum acquisition immediately starts upon current is applied to electrode, i.e., equilibrium does not reach. The temporal evolution of pH or the corresponding phosphate amount profile is terminated earlier (Figure 5-8) due to the interference of air bubbles. Thereby, collecting spectra with a spatial resolution of 1–2 μm is a challenge. In the following experiments, spectra were measured at an absolute distance of at least 50 μm. An edge-mode green laser (532 nm) was employed. Other experimental parameters are detailed in the experimental section. CoCat (40 mC cm^{-2}) deposited on Pt foil was operated in 25 mM KPi (pH 7) at a current of 0.3 mA cm^{-2}. Prior to the measurement, we adjusted the micrometer-step sample stage until an electrode position blocking the clear laser spot, where the position is defined as zero point (y = 0). Collecting OCP spectra in the vicinity of the electrodes also facilitates to find the zero point, i.e., to check if the measured spectra contain phosphate, water peaks, and Teflon peaks. Subsequently, measuring and comparing spectra measured at different positions between the electrodes ensures reproducible positions defined.

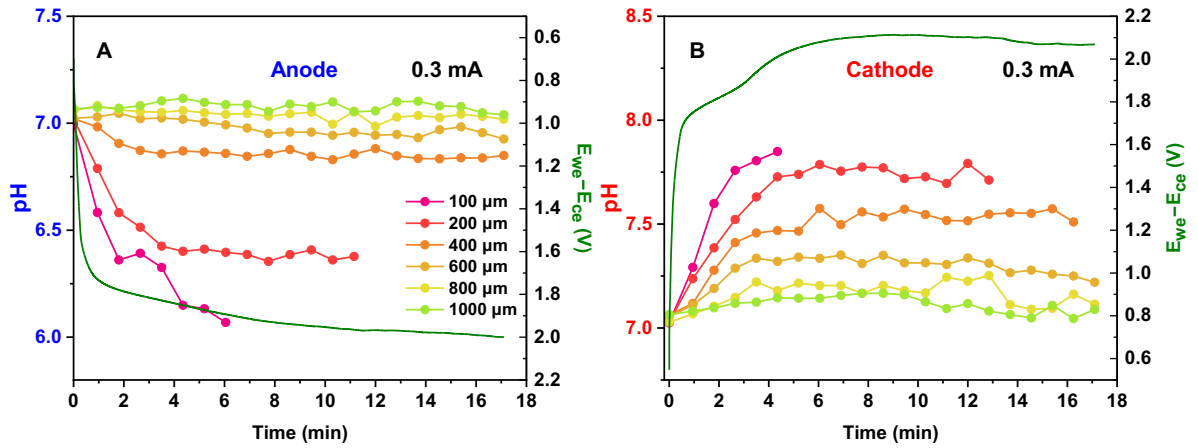

Figure 5-8. Comparison of the temporal evolution pH profiles at the indicated distances (y) from the electrode-bulk electrolyte interface for anode (A) or cathode (B) with applying a constant current of 0.3mA cm^{-2}. The legends are the respective distances towards the electrodes. The solid green line is the overall cell voltage of the two-electrode cell. The data points are mean values of several individual measurements (see more in Figure 5-9). The corresponding error bars are shown in Figure 5-9. pH calculation follows the same rules as Figure 5-4B. Note that panels A and B use the same color code and that the right-side y-axis for anode is reversed.

Notably, pH value at OCP (t = 0) was around 7 (electrolyte initial pH), suggesting that Raman spectroscopy can effectively quantify absolute pH values. At 100 µm and 200 µm, neither close to the anode nor close to the cathode it is possible to collect good-quality spectra after prolonged catalytic operation because of accumulation of large bubbles. After 5 minutes, the available pH values near to anode and cathode were around 6.2 and 7.8, respectively. Interestingly, the absolute pH change (ΔpH) was consistent, implying that at that moment the electrochemical cell reaches equilibrated state. It may indicate the dynamic equilibrium of proton production and depletion in the vicinity of the electrodes, which is co-determined by the diffusion rates of phosphate species, gas production rates, and catalytic reaction rates. Finally, with the temporal evolution pH profile at various positions, we can observe a clear pH gradient in the vicinity of the anode with a range of 600 µm. At the cathode, this gradient extends over about 800 µm. With applying a current of 0.3 mA cm^{-2}, the anodic and cathodic pH values measured by Raman spectroscopy were around 6.2 and 7.8, respectively.

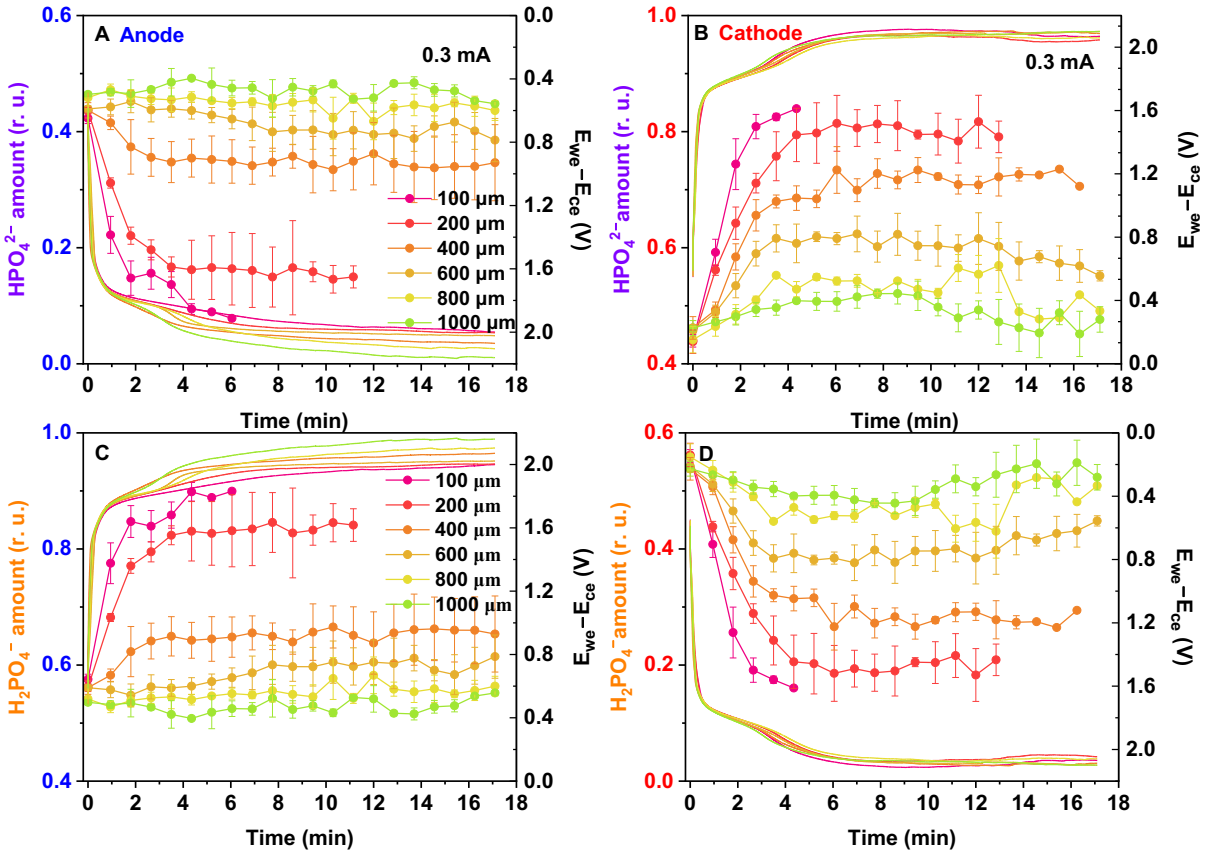

Figure 5-9. Temporal evolution of (de)protonated phosphate amounts at different distances from the anode (left) and the cathode (right) at 0.3 mA cm^{-2}. The legends show that the respective distance towards the electrode. The displayed $H_2PO_4^-$ or HPO_4^{2-} amount is calculated according to Equation 5-1 or Equation 5-2. Phosphate base amount (P_b, HPO_4^{2-}, ~991 cm^{-1}, A and B) and phosphate acid amount (P_a, $H_2PO_4^-$, ~1077 cm^{-1}, C and D) are shown separately on the upper and lower rows. The solid line shows the corresponding voltage at each position. The ratio of P_b and P_a amount is used for calculating pH shown in Figure 5-8. Curves collected between 100 μm to 600 μm are mean of at least three independent measurements, and the error bars are standard deviations (s) calculated according to Equation 5-3. At distances of 800 μm and 1000 μm, mean values and error bars were calculated from two measurements.

The phosphate species amount profiles in Figure 5-9 exhibits opposite trends, i.e., more protonated phosphate species at anode and more deprotonated phosphate species at cathode, and vice versa. More closer to electrode surface, more larger deviation of pH from the bulk pH 7, implying a greater difference on the amount of the two phosphates (HPO_4^{2-}/ $H_2PO_4^-$). Similarly, the variation of phosphate peak intensity within 1 mm from the electrode (Figure 5-10) follows a similar trend to that of the phosphate amount profile (Figure 5-9). The only difference is that the latter method shows a better signal-to-noise ratio due to the "noise-robust" normalization method, for which we assume that the sum of the amounts of the two phosphate ions (HPO_4^{2-}/ $H_2PO_4^-$) is the same everywhere, see the experimental methods for more details.

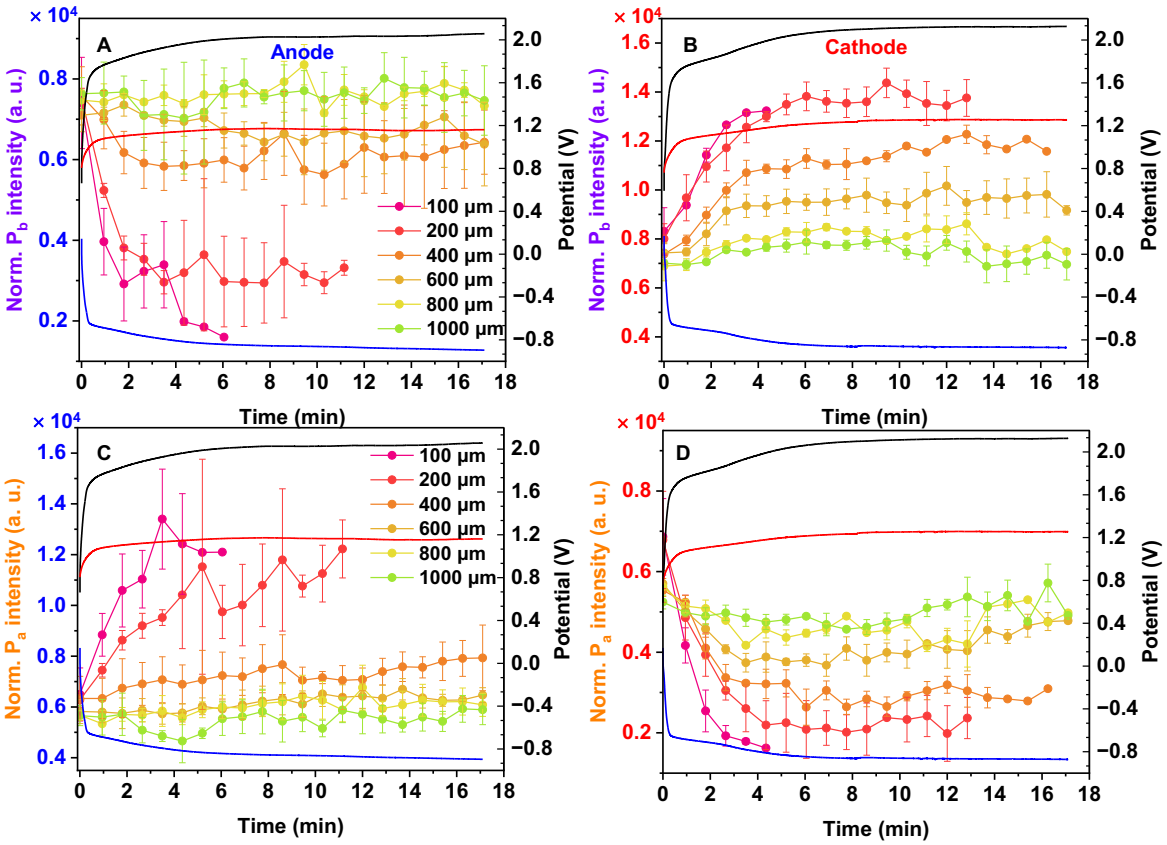

Figure 5-10. Normalized Raman peak intensities for phosphate at the indicated distances from the anode (left) and cathode (right) at 0.3 mA cm^{-2}. The normalization approach is relative to the water peak at1642 cm^{-1}. The phosphate species correspond to phosphate base (P_b, HPO_4^{2-}, ~991 cm^{-1}, A and B) and phosphate acid (P_a, $H_2PO_4^-$, ~1077 cm^{-1}, C and D) with y-axis labeled in purple and orange, respectively. Solid curves (right axis) show the potentials of working electrode (red) , counter electrode (blue), and total cell voltage (black), with a miniature saturated Ag/AgCl (3 M NaCl) electrode as the reference electrode. Phosphate amounts were calculated by using the normalized phosphate intensities, assuming that the sum of phosphate species amounts was equal everywhere in the cell. Error bars is the standard deviation calculated according to Equation 5-3, calculated mainly from three or more individual measurements, but occasionally also from two measurements. See Figure 5-9 for more details.

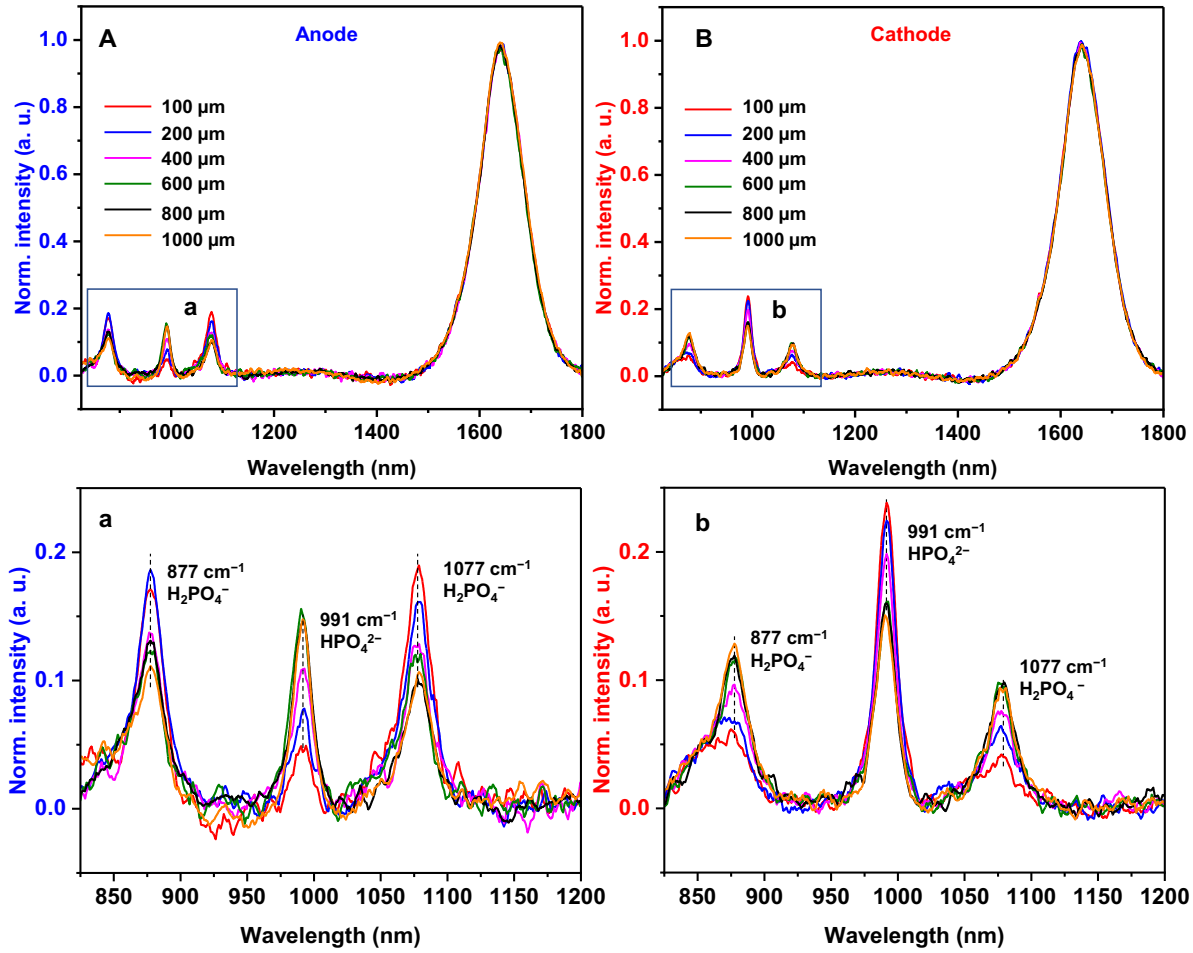

Figure 5-11. The 2nd acquisition of Raman spectra at various positions (along the y-axis) near the anode (A) and cathode (B) upon applying a current of 0.3 mA cm^{-2}. The legends are absolute distances from the electrode-electrolyte interface. (a and b) Zoom in the area of the phosphate zone in panels A and B. The displayed spectra were background corrected and normalized to 1 of water peak. The dashed lines are the major vibrational bands of phosphate species; from left to right: $H_2PO_4^-$ (~877 cm^{-1}), HPO_4^{2-} (~991 cm^{-1}), $H_2PO_4^-$ (~1077 cm^{-1}). Data were smoothed using the Savitzky-Golay method with a span of 5 pts.

Figure 5-11 shows the normalized Raman spectra at the indicated distance that were extracted from the second acquisition after applying the current for 1.8 min (0.3 mA cm^{-2}). It is noteworthy that the amplitudes of the phosphate bands at the indicated locations are different. The amplitude of the intermediate peak (P_b, 991 cm^{-1}) gradually increases with increasing distance from the anode, whereas the acidic phosphates peak (P_a) at 1077 cm^{-1} gradually decreases, suggesting that the ratio of P_b/P_a becomes larger, resulting in an alkaline pH. Similarly, a decrease of P_b/P_a is clearly observed upon measuring positions moving away from the cathode, indicating a gradual reduction of localized alkalization. In addition, at the anode and cathode, beyond 600 µm, the peak amplitudes of the phosphate species almost overlapped, suggesting that there was no significant pH change and that proton transfer was not limited. The spectra shown in Figure 5-11 are from a single sample collection under the corresponding conditions and may slightly deviate from the mean results shown in Figure 5-8 to Figure 5-10.

Importantly, the temporal evolution of pH measurement provides an important approach to quantify the overall pH profile in the bulk electrolyte also at near electrode region.

5.2.3.2 pH profiles between electrodes for various equilibration time (z = 5 mm)

In a stagnant cell, it is challenging to acquire pH values at different locations between electrodes when the electrochemical system has reached equilibrium, especially within 1 mm from the electrodes. By acquiring spectra immediately after energization, pH values in the vicinity of the electrodes can be obtained within a limited time frame. After time-dependent data acquisition is completed at fixed position near the electrode, spectra at other positions along the y-axis away from the electrode can be measured by moving the micro-step sample stage in different steps, i.e., small steps of 50, 100, or 200 µm beyond a range of 2 mm, and moving the sample stage in 1-mm increments. To ensure that the collected spectra spanned the entire range of the cell, the spectra were measured within a distance of 6 mm from the anode or cathode, respectively. It is noteworthy that the completion of the time-dependent measurements takes ~18 min for each distance, thus the following spectrum acquired at other positions is the electrochemical system at equilibrium state corresponding to equilibrium pH (Figure 5-12). Note that equilibrium here refers to the formation of a stable spatial distribution of phosphate species, a stable flow equilibrium, and a steady state of bubbles attached to the electrode.

With jointly observing pH profiles at the anode and cathode, the bulk pH profile along the y-direction corresponding to the middle layer of the cell (z = 5 mm) is not linear at 0.3 mA cm^{-2} (Figure 5-12 A and B), suggesting a more complex diffusion process that involves buffer species to alleviate proton transport limitations. The pH gradient only occurs within 1 mm from the electrode, especially at distances of less than 600 µm from the anode and less than 800 µm from the cathode. The pH gradient at the cathode is slightly prolonged, probably because the cathode involves more hydrogen than oxygen. Bulk pH is reproducibly maintained at 7 over 1 mm. Figure 5-12 a and b adapted from Figure 5-8 shows rapid pH change at closer distances from the electrodes-bulk electrolyte interface not for distance over 1 mm. After around 5 minutes, the detectable pH values at the anode and cathode were ca. 6.2 and 7.8 at a current density of 0.3 mA cm^{-2}. As a complement, the corresponding phosphate amount profiles and normalized phosphate intensities are shown in Figure 5-13 and Figure 5-14.

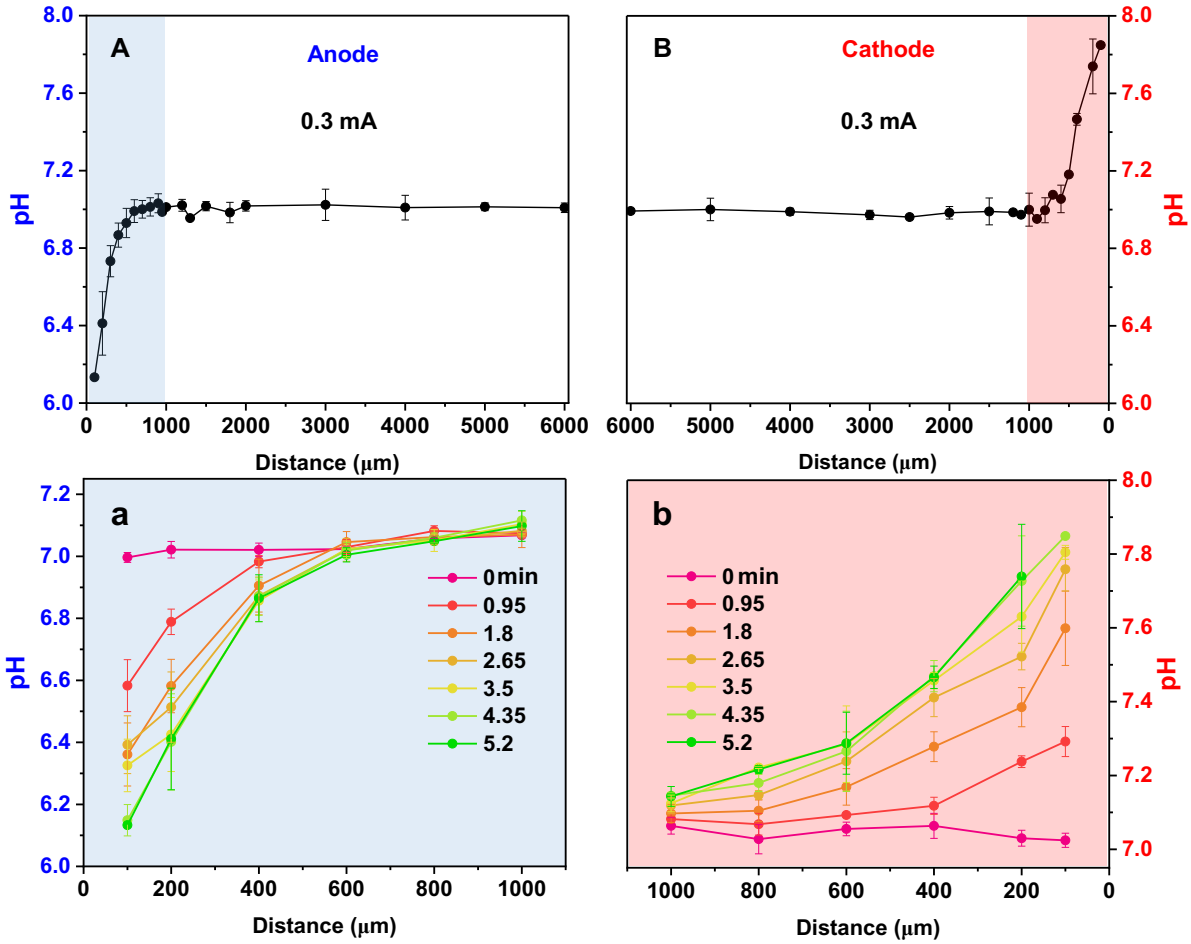

Figure 5-12. pH profile in the range of 0.1 to 6 mm from the anode (A) or cathode (B) and time dependence of pH changes at specified positions near the anode (a) or cathode (b). The overall pH along the y-axis for the entire cell can be jointly visualized from Figure 5-12 A and B. Note that pH values at 100 μm and 200 μm in panel A are data from panel a at 5.2 min. pH values in the vicinity of the cathode (y = 100, 200, 400 μm) is taken from the data at t = 4.35 and 5.2 min (panel b). Unless otherwise noted, pH values at other locations are equilibrated. Areas close to the electrodes (less than 1 mm) are highlighted in blue and pink and further zoomed in panels a and b. We also note that panels a and b are adapted versions of Figure 5-8. Panels A and B show the average results of at least three separate measurements. Error bars indicate the standard deviation according to Equation 5-3. Data point without an error bar indicates a single measurement.

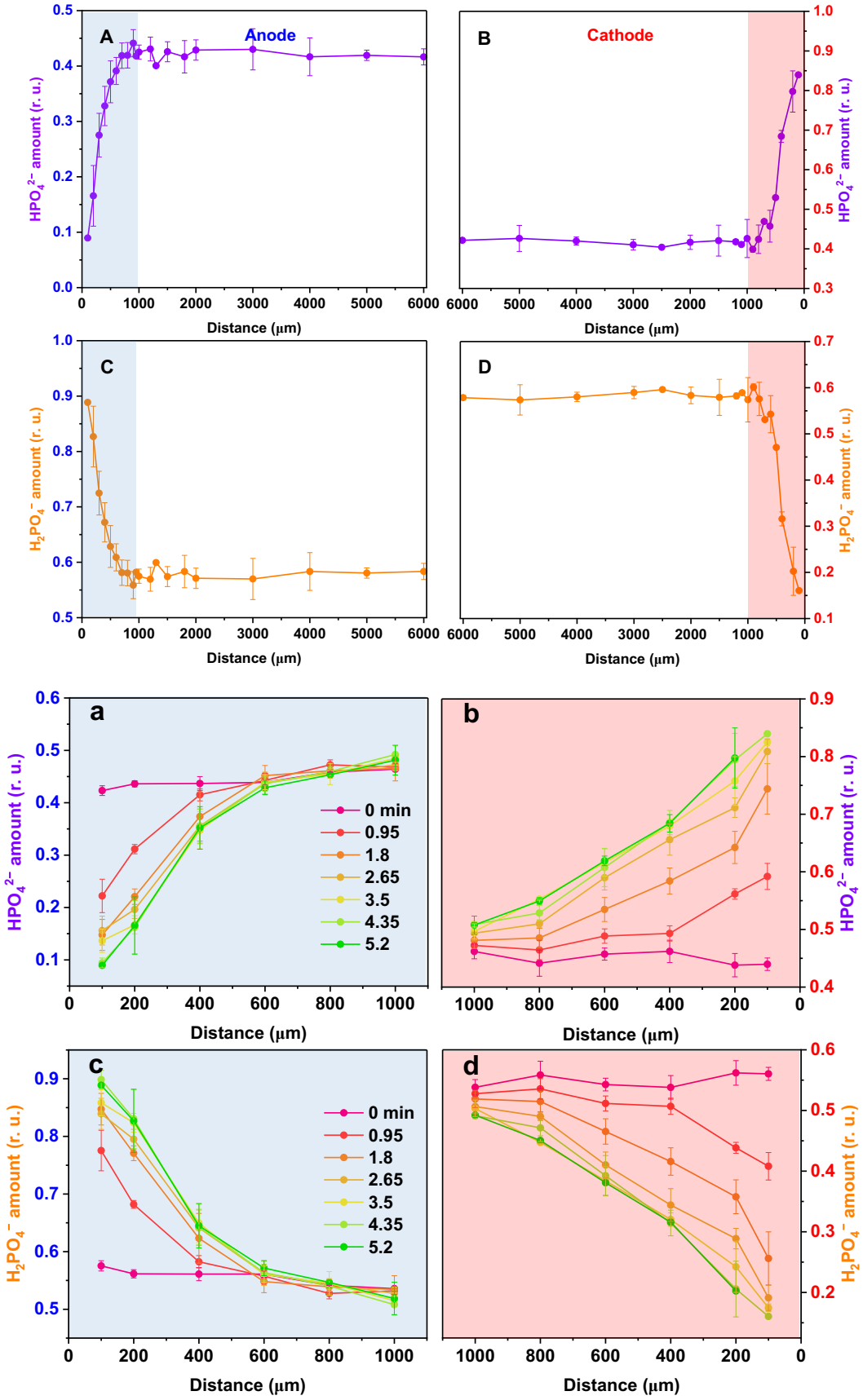

Figure 5-13. Spatial amount of alkaline phosphate (A and B, purple) and acid phosphate (C and D, orange) within 6 mm from anode (left) and cathode (right). Panels a–d show the amount of HPO_4^{2-} and $H_2PO_4^-$ amount as a dependence of time at 0.3 mA cm^{-2} at a range of 1 mm from the electrodes. At t =

0, it represents the amount of phosphate species in the OCP condition. The calculation of the error bars and more details are shown in Figure 5-12.

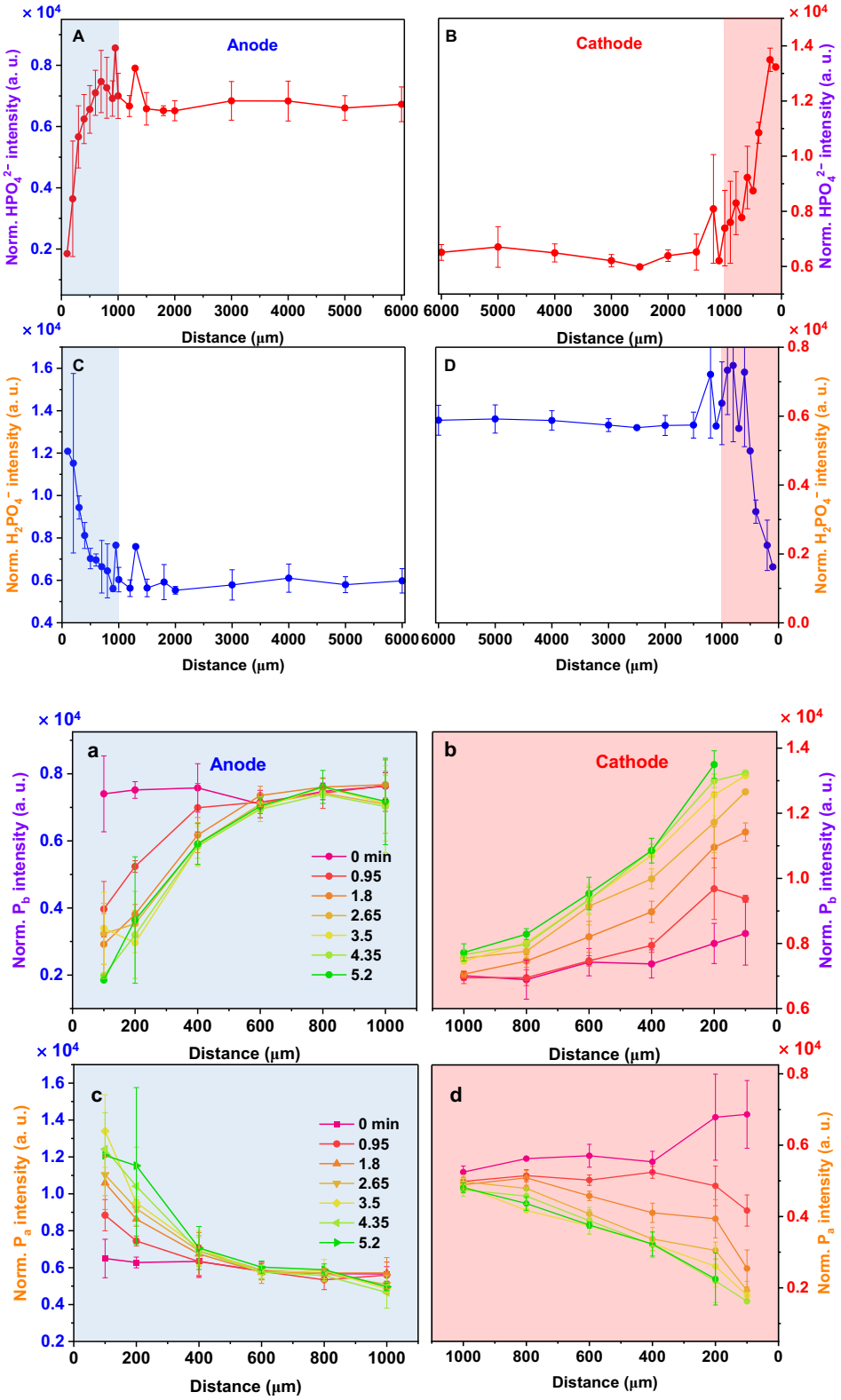

Figure 5-14. Spatial distribution of normalized alkaline phosphate (A and B, red) and acid phosphate (C and D, blue) peak intensities within 6 mm of the anode (left) and cathode (right). The highlighted area near the electrode (1 mm) is zoomed in panels a-d to show the change in intensity of the normalized phosphate peak as a dependence of time over a range of 1 mm from the electrode. The displayed

normalized phosphate intensity is used to calculate the phosphate amount in Figure 5-13 by using the same calibration method described in Section 5.2.2 (see Equation 5-1 and Equation 5-2). Calculation of the error bars and more details are provided in the figure caption of Figure 5-12.

In summary, by operando Raman spectroscopy in a neutral KPi solution (25 mM, pH 7), we could quantify the spatial distribution of phosphate-species amounts and the corresponding pH profiles in a parallel two-electrode system upon applying a current density of 0.3 mA cm^{-2}. The bulk pH was stable at about pH 7, the electrolyte pH before the onset electrocatalytic operation, for a distance from the electrolyte-electrode interface exceeding 1 mm. The phosphate species amounts profile does not fit with the earlier proposal[135] of the presence of linear phosphate concentration profiles between electrodes at constant flux flow (Figure 1-7A). However, it is undeniable that in unstirred electrochemical cells, the diffusion process of phosphate species are much more complex and are likely to be influenced by other factors, such as natural convection that can shape the phosphate concentration profile, as verified in Section 5.2.3.4. A non-linear pH gradient is observed between electrodes, and we observed subtle difference on pH gradient ranges, for which local acidification occurs within 600 µm and local alkalization range is ca. 800 µm. It should be emphasized that in a stagnant cell with prolonged catalytic operation, estimating the actual pH near the electrode surface by RM may be imprecise or even impossible due to the effect of light (of the Raman experiment) scattered by gas bubbles, resulting in the inaccessibility of spectra collection (Figure 5-8).

5.2.3.3 pH profiles near to and between electrodes at 0.12 mA cm^{-2} (z = 5 mm)

In order to study the diffusion of phosphate species without the Raman experiment being negatively affected by bubble production, a lower current density (0.12 mA cm^{-2}) was applied so that spectra at equilibrium could be measured also at small distance to the respective electrode. The Raman spectra were collected for largely completed equilibration of the pH profile (at ca. at least 14 min after current onsets) (Figure 5-15).

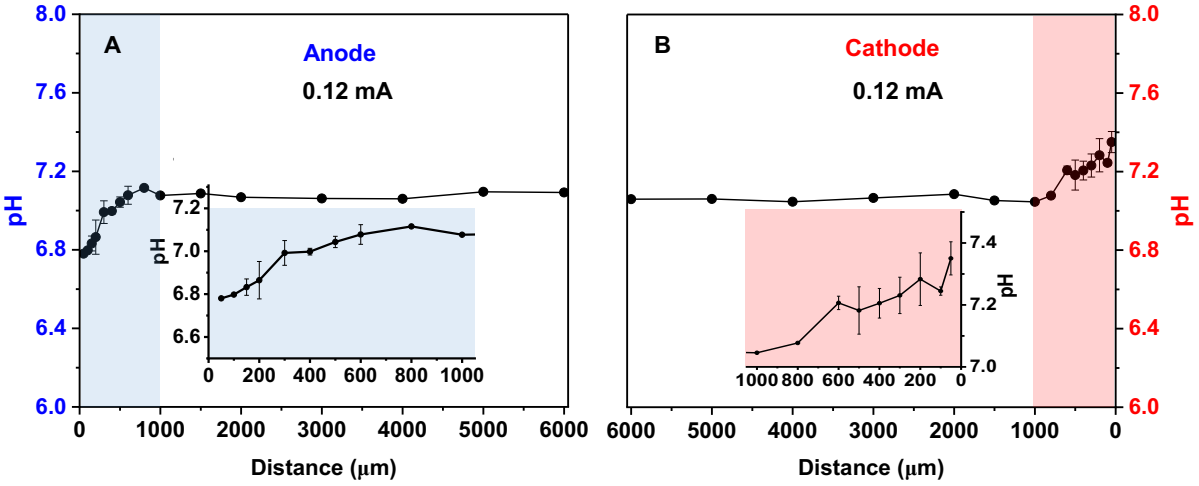

Figure 5-15. Equilibrated pH near the anode (A) or cathode (B). The inset shows the magnified range within 1 mm from the electrodes. Data points with error bars are the mean of at least two independent measurements, otherwise from single measurement. Spectra in the bulk electrolyte are readily measured and assignable to a pH value of about 7, which matches the initial electrolyte pH before current onsets.

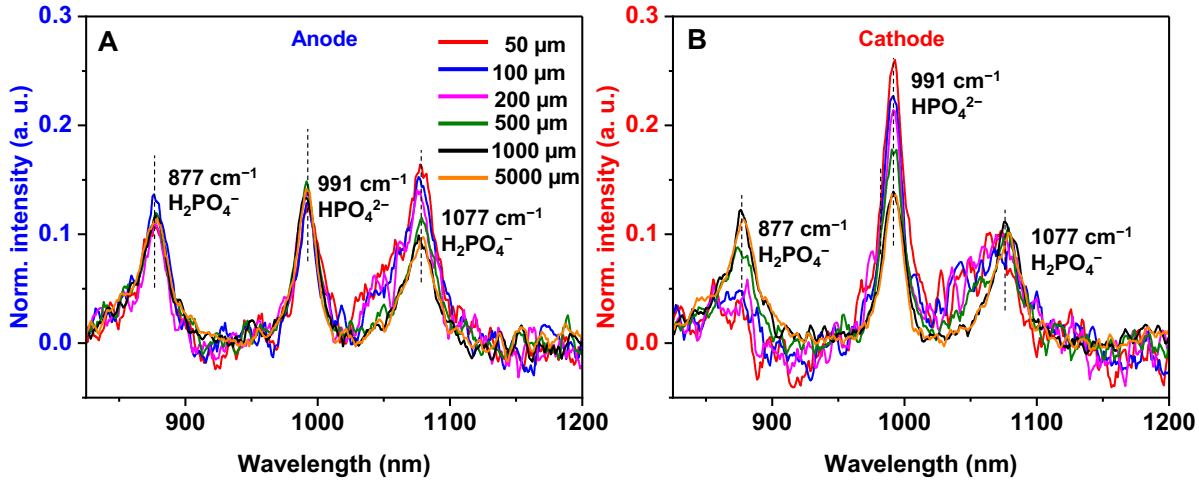

Figure 5-16. Raman spectra taken at selected locations (along the y-axis) near the anode (A) and cathode (B) when the system was equilibrated at 0.12 mA cm^{-1}. Legend numbers indicate the distance from the corresponding electrode-electrolyte interface. Spectra are background corrected and normalized to unity height (1.0) of the water peak located at about ~1642 cm^{-1}. The dashed lines indicate the major vibrational bands of phosphate species; from left to right, $H_2PO_4^-$ (~877 cm^{-1}), HPO_4^{2-} (~991 cm^{-1}), $H_2PO_4^-$ (~1077 cm^{-1}). The data were smoothed using the Savitzky-Golay method with a span of 5 pts.

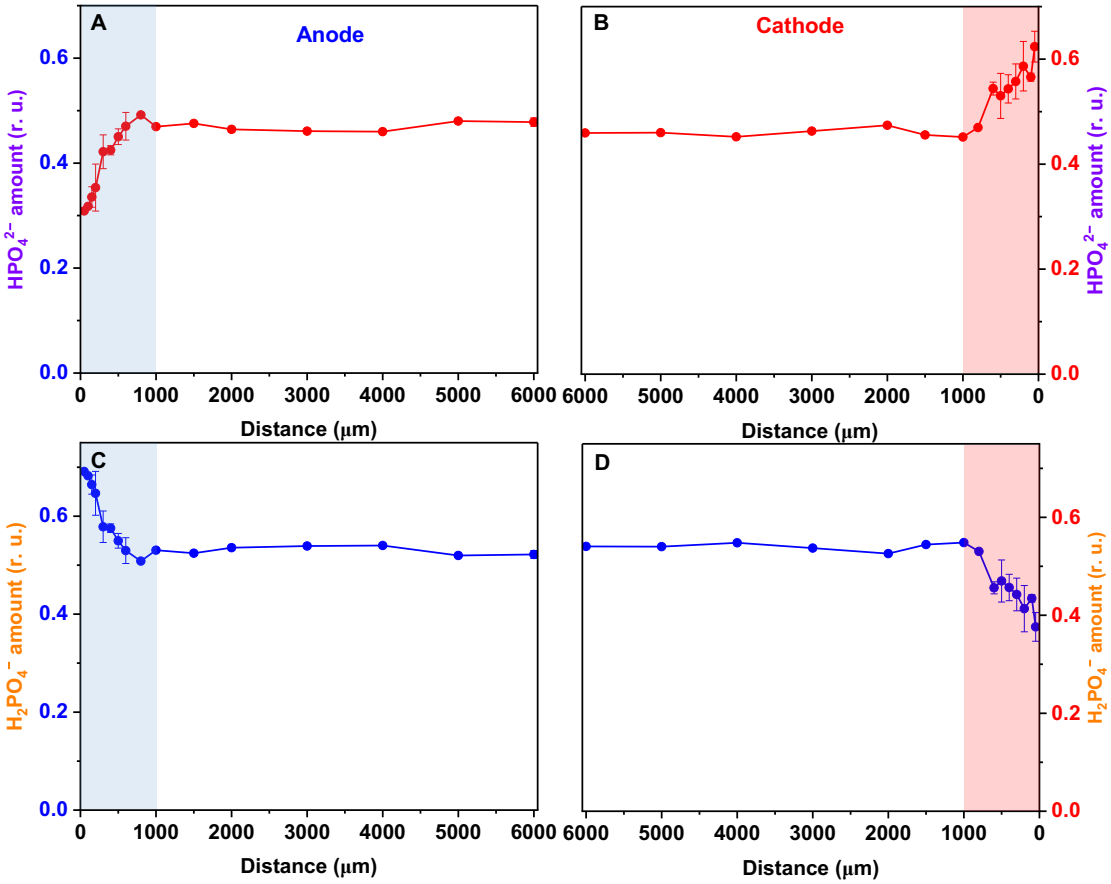

Figure 5-17. Spatial profile of two phosphate species (HPO_4^{2-}, A and B; $H_2PO_4^-$, C and D) near the anode (left) and cathode (right). The calculation of the error bars is consistent with Figure 5-15.

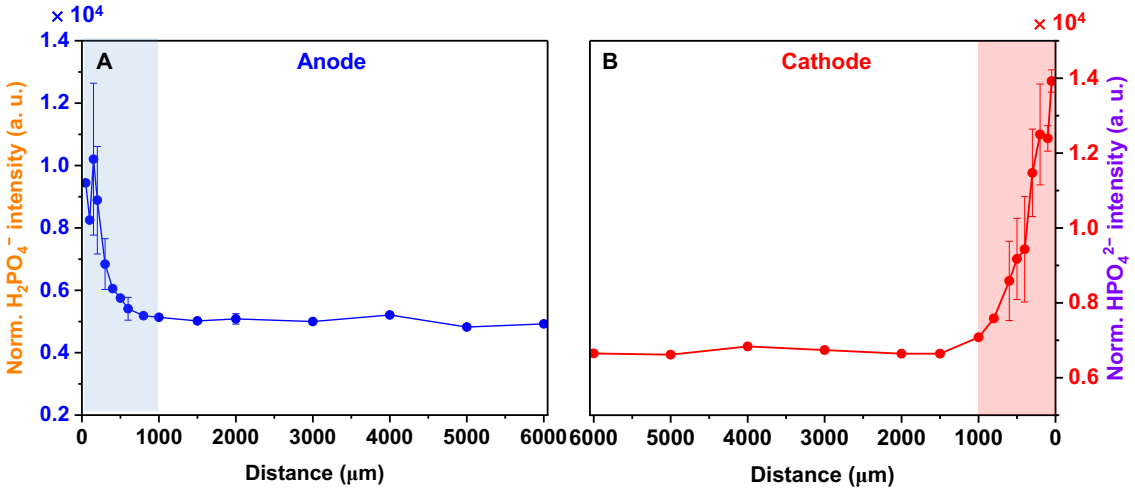

Figure 5-18. Spatial profile of normalized Raman peak intensities for acid phosphate ($H_2PO_4^-$, A, blue) and basic phosphate (HPO_4^{2-}, B, red) within 6 mm range from anode (left) and cathode (right). The calculation of the error bars is consistent with Figure 5-15.

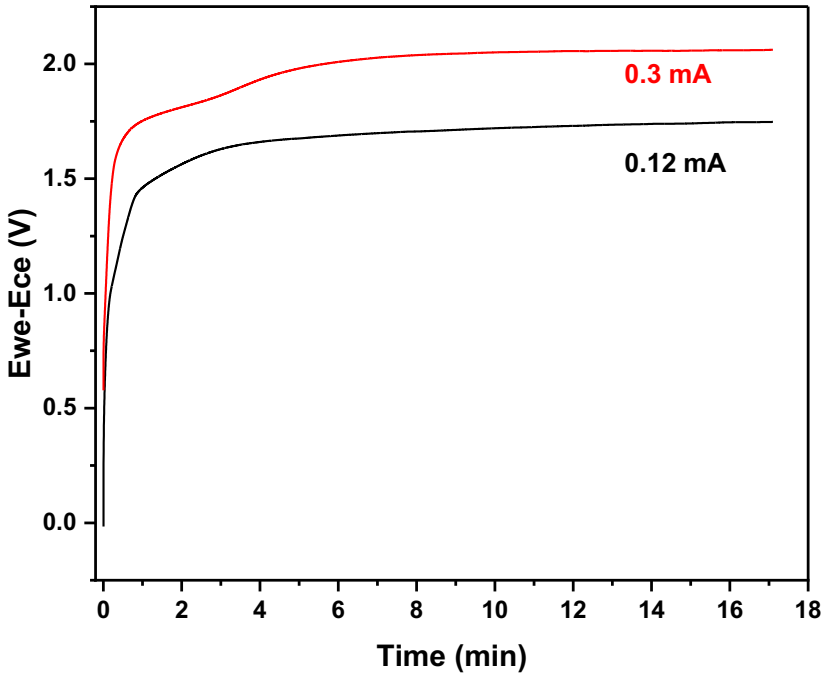

Figure 5-19. Comparison of cell voltage at 0.3 mA cm^{-2} and 0.12 mA cm^{-2}.

As expected, pH gradient near electrodes is weaker at lower current densities (0.12 mA cm^{-2}) than at 0.3 mA cm^{-2}. For example, at 50 μm from the electrode, the pH at anode are about 6.8 and at cathode is about 7.4, whereas at 0.3 mA cm^{-2}, the pH at 100 μm from the anode and cathode are about 6.2 and 7.8, respectively. We note that the calculated pH values are based on Raman spectra collected under non-equilibrated state, thereby the actual pH change upon reaching a static state may have a larger different from the here presented results. At both anode and cathode, pH changes resulting from the respective catalytic reaction seem to level off at distances greater than 800 μm at 0.12 mA cm^{-2}.

In spite of significant noise contributions, visual inspection of the normalized Raman spectra clearly suggests the corresponding changes in the peak magnitude of phosphate peaks at 991 and 1077 cm^{-1} (Figure 5-16). At the anode, the acidic phosphate peak at 1077 cm^{-1} steadily decreases as the focusing position is gradually moved away from anode side, and vice versa for the alkaline peak (991 cm^{-2}) near the cathode. A qualitative comparison of the normalized peak amplitudes in Figure 5-11 and Figure 5-16 shows that the P_b/P_a ratio is smaller at lower currents (0.12 mA cm^{-2} vs. 0.3 mA cm^{-2}). In addition, in Figure 5-17 and Figure 5-18, the profile of phosphate amount and their normalized Raman peak intensities show the same trend as the pH profile, i.e., acidic phosphate intensities ($H_2PO_4^-$) are higher at the anode, while basic phosphates (HPO_4^{2-}) are higher at the cathode, implying local acidification and alkalinization. Cell voltages at low and high current densities (Figure 5-19) do differ in the magnitude for extended operation time, showing a larger overpotential required at 0.3 mA. A fully stable overpotential level is not reached within 17 min, which may be explainable by still incomplete establishment of stationary flow-equilibrium of the phosphate amounts. Alternatively, the onset of catalyst degradation processes could be involved.[140] Based on the here reported data on the temporal evolution of pH profiles (Figure 5-8), we assume that after about 5 min the situation is reasonably stable and the spatial pH profiles then largely correspond to a stationary flow equilibrium, at both current density levels.

Importantly, also at low current densities, at which bubble-induced convective flows likely affect the diffusion of phosphate species only marginally, the proposed linear profile between the anode and cathode was not observed. This implies that other factors (e.g., natural convection due to changes in electrolyte density) shape the process of buffer species-assisted proton transport. For further insight, we took spectra at three representative positions between the electrodes (y = 1, 5, 9 mm, see Figures 5-7 B and C) to study possible convection in the bulk-phase electrolyte, as reported in the following.

5.2.3.4 3D convective flow

The CoCat film was operated in a neutral KPi buffer (pH 7, 25 mM) with a relatively thick film thickness (40 mC cm^{-2}) (unstirred cell, at RT). Thus, for the spectra taken at three different vertical positions (Figure 5-7 B and C, z = 10, 5, 0.5 mm), we observed a completely different behavior of the pH profile under the same electrochemical scheme (Figure 5-20), i.e., at the top of the cell, the solution was becoming acidic, whereas near the bottom of the cell, the solution was becoming alkaline, while the pH of the middle layer between the electrodes is largely unaffected by the onset of catalytic currents and stays constant at the initial pH of 7. Spectral analysis is shown in the Experimental section. The calibration curve in Figure 5-4B was used to calculate pH.

For measurements at the top position (z = 10 mm, Figure 5-7B and 5-20), the pH value changed from about 7 at OCP to 6.7 after 15 min of applying a current of 0.5 mA cm^{-2}. Subsequently, when the current is turned off, the pH value remains almost constant. Upon reapplication of the current a slight change in pH occurs along with a pH-change delay. After switching to the OCP condition in the final stage, the pH value reaches about 6.5. In the intermediate position (z = 5 mm), the pH value almost stabilizes at about 7, with or without catalytic operation. In

contrast, at the bottom position of the cell, after OCP and current-on cycling, the pH increased from approximately 7 to 7.6. It is noteworthy that similar delay of pH changes was observed at the top and bottom positions, reflecting slow diffusional and convective flows. It was also found that the pH response of the second stage during powering-up (of the catalytic current) was less than the initial value, which could be attributed to convection or buoyancy effects produced by the bubbles[207] compensating for the uneven pH changes after a long period of operation. We note that the pH values at different locations are averaged over two independent samples, and that the cell voltage was around 2.3 V for both samples at 0.5 mA cm^{-2}, suggesting that the individual experiment is reproducible.

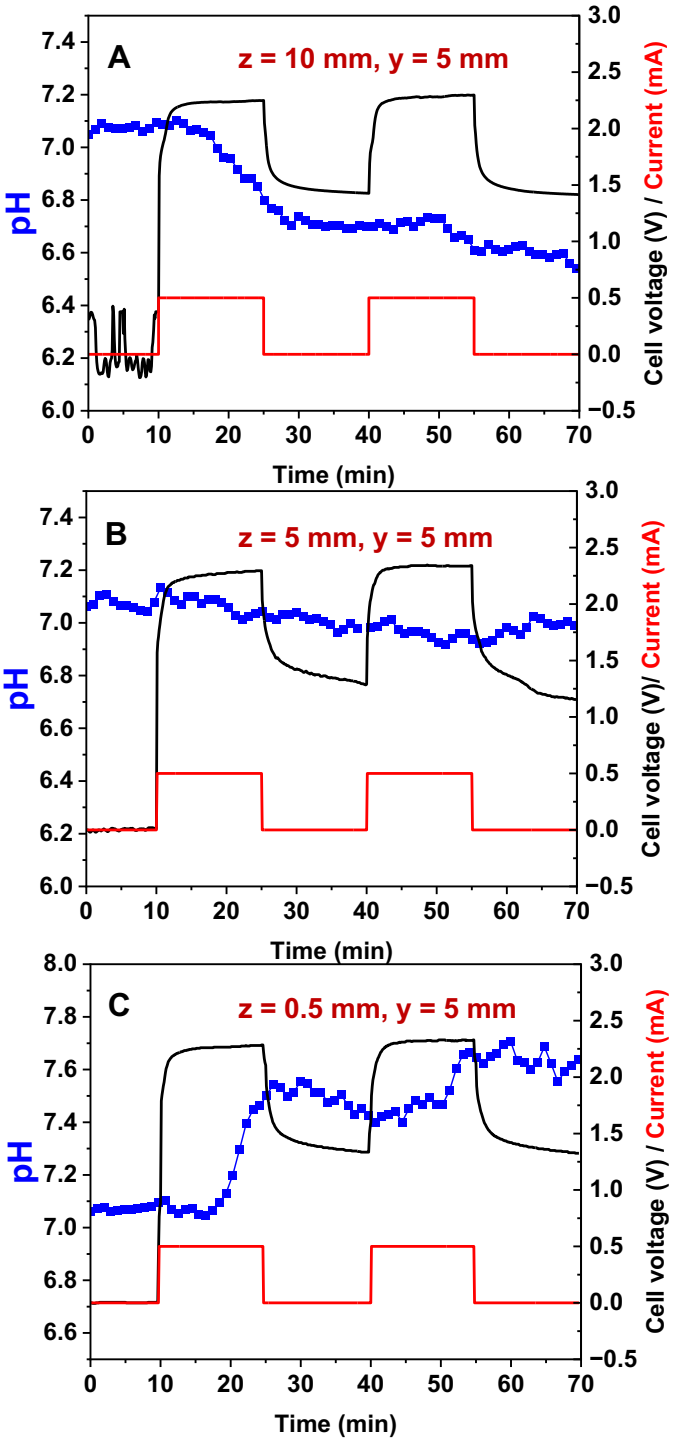

Figure 5-20. pH profile at different vertical distances (z = 10 mm, A; 5 mm, B; 0.5 mm, C) with current jumps from OCP conditions to 0.5 mA cm^{-2} (red). The corresponding cell voltage is shown in black. Spectra were collected with a horizontal position (y) of 5 mm between the electrodes. The CoCat material was deposited on Pt foil (40 mC cm^{-2}) and run in KPi buffer (25 mM, pH 7). The blue dots represent pH values calculated from individual Raman spectra taken consecutively during electrochemistry. Collection of each individual spectrum took 57-58 s. The pH values were quantified using the calibration curve in Figure 5-4B. The corresponding phosphate amounts are shown in Figure 5-23. The blue dots indicate the smoothed average of two nearby data points. The pH at t = 0 is the initial pH (pH = 7) of the KPi solution prepared when the electrochemical reaction has not started. Note

that quantification of pH values may result in a statistical error of ±0.1 pH. Data points shown are average results using at least two independent CoCat films.

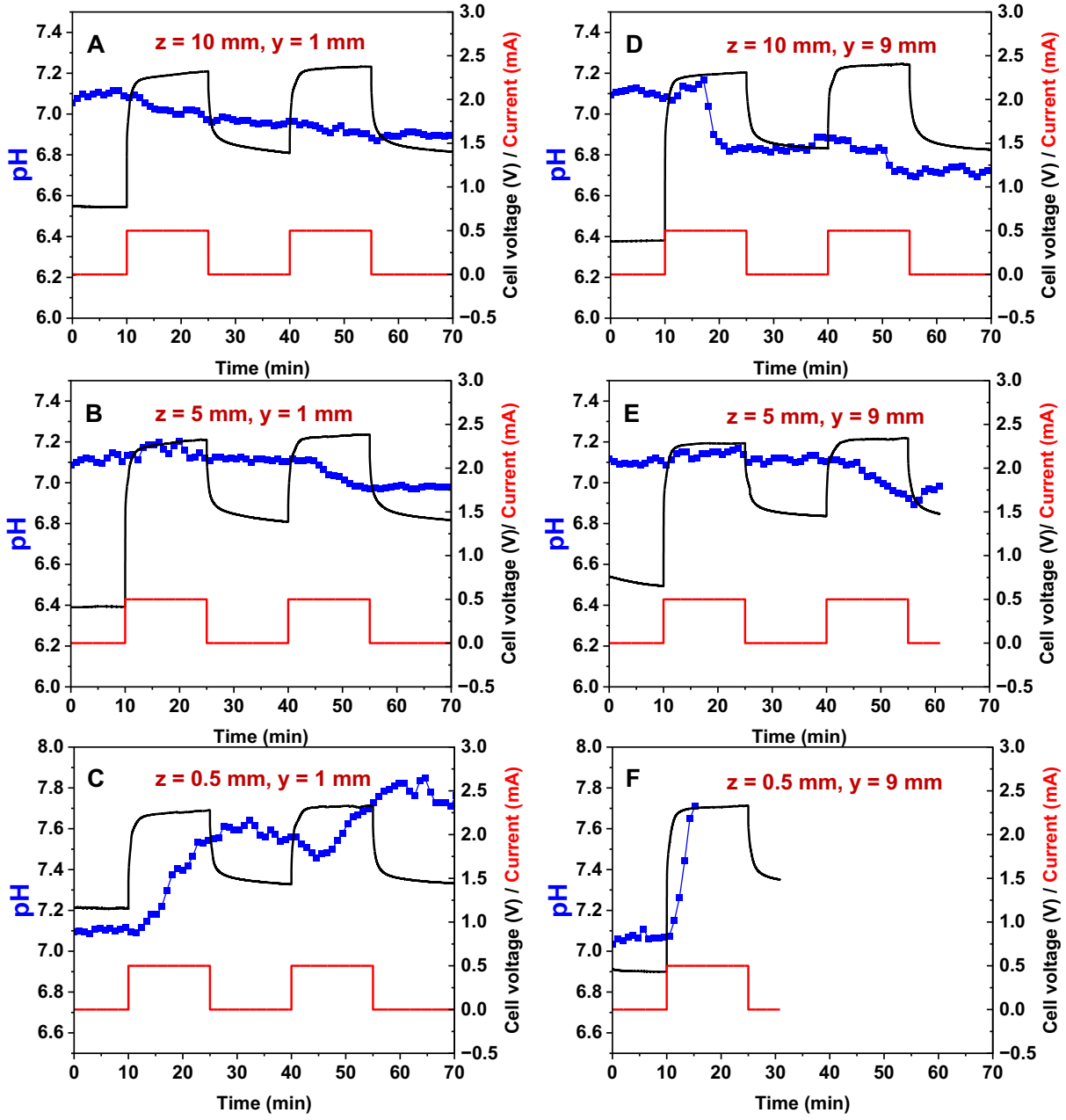

Figure 5-21. pH profile at different vertical distances (z = 10 mm, A; 5 mm, B; 0.5 mm, C) with current jumps from OCP to 0.5 mA cm^{-2} (red). The left or right column shows the pH curve at 1 mm from the anode or cathode. Data points shown are average results using at least two independent CoCat films. In panel E, incomplete curves are caused by manually aborting the experiment. Due to the high local alkalinity, the pH curve in part F shows results for only a short period of time and is therefore outside the quantitative range of the pH calibration curve (Figure 5-4). See Figure 5-20 for details.

The pH profile of the bulk solution was measured at different vertical heights (z = 0.5, 5, 10 mm) starting from a fixed intermediate position between the electrodes (y = 5 mm, Figure 5-7B and 5-20). Subsequently, the series of spectra were further measured at a fixed horizontal distance (y-axis) of 1 mm from the electrodes (y = 1 and 9 mm, see Figure 5-7C and Figure 5-21). The

purpose of obtaining pH profiles in the vicinity of the electrodes is to identify convection loops that may exist in the two-electrode cell. In Figure 5-21A–C, the pH values of the three z-positions (y = 1 mm) close to the anode show different behaviors during the 70 min jumps, i.e., the top layer of the cell is slightly acidified, the pH of the middle layer is around 7.1, and the bottom layer of the cell is alkaline. In the intermediate layer (z = 5 mm) at a distance of 1 mm from the cathode (Figure 5-21, panel D–F), the results were similar to those of the anode, with a slight change in pH over 40 min followed by a slight decrease (panel E). The decrease in pH after a long run may be due to diffusion of protonated phosphate species from the top region. In the top region, there was an overall decrease in pH of about 0.4 pH units with a delayed pH change, which implies that the protonated phosphate species diffused from the anode to the cathode. In addition, strong alkalization was observed in the bottom region near the cathode, and the peaks of acidic phosphate species monitored after energization for about 5 min were almost absent (Figure 5-21F). Thus, it was not possible to quantify pH from the calibration curve. It is also noteworthy that the intensity of the normalized P_b (HPO_4^{2-}) peak at the bottom position (z = 0.5 mm) is significantly greater than that of the peaks at the middle and top positions (z = 5, 10 mm), suggesting the formation of a strong alkalization (Figure 5-24F vs. Figure 5-24 D and E).

In conclusion, we obtained a three-dimensional pH profile of a parallel two-electrode cell and revealed a unique behavior in the vertical space, i.e., acidification at the top of the cell, neutral pH in the middle layer, and strong alkalization at the bottom. In addition, the extent of change in pH varied depending on the horizontal distance of the electrodes (y = 1, 5, 9 mm). The presence of acidity at the top cathode location and the alkalinity at the bottom anode region strongly suggest that (protonated) buffer molecules circulate from the anode toward the top of the cathode (z = 10 mm) and (deprotonated) buffer molecules circulate from the bottom of the cell from the cathode to the anode (z = 0.5 mm). Therefore, we conclude that there is convective flow in the bulk electrolyte.

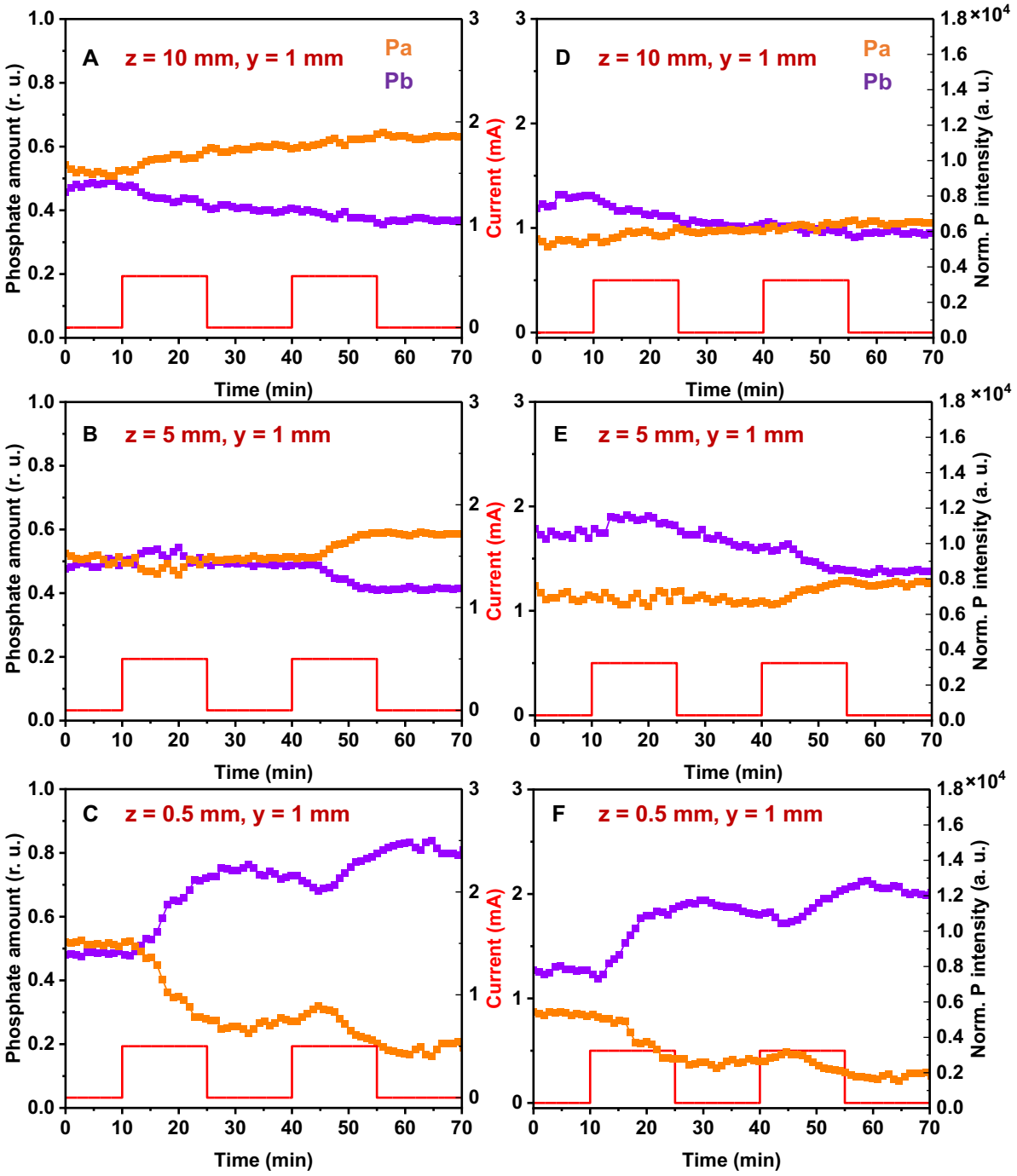

Figure 5-22. Time course of phosphate species amount (left) and normalized phosphate peak intensity (right) profile at the indicated vertical space (z = 10 mm, A, B; 5 mm, C, D; 0.5 mm, E, F) and at a horizontal distance (y) of 1 mm from the anode. A jumping current (red) from OCP to 0.5 mA cm^{-2} was applied. The two phosphate species corresponding to phosphate base (P_b, HPO_4^{2-}, ~991 cm^{-1}) and phosphate acid (Pa, $H_2PO_4^-$, ~1077 cm^{-1}) are shown in purple or orange, respectively. The phosphate amounts are calculated according to Equations 5-1 and 5-2 (see Section 5.2.2). The ratio of phosphate amount was used for pH quantification. Phosphate peak intensities (right) were normalized with respect to the water peak at ~1642 cm^{-1}. The indicated data points are the averages of at least two independent films and are used as supporting information for Figures 5-21 A–C.

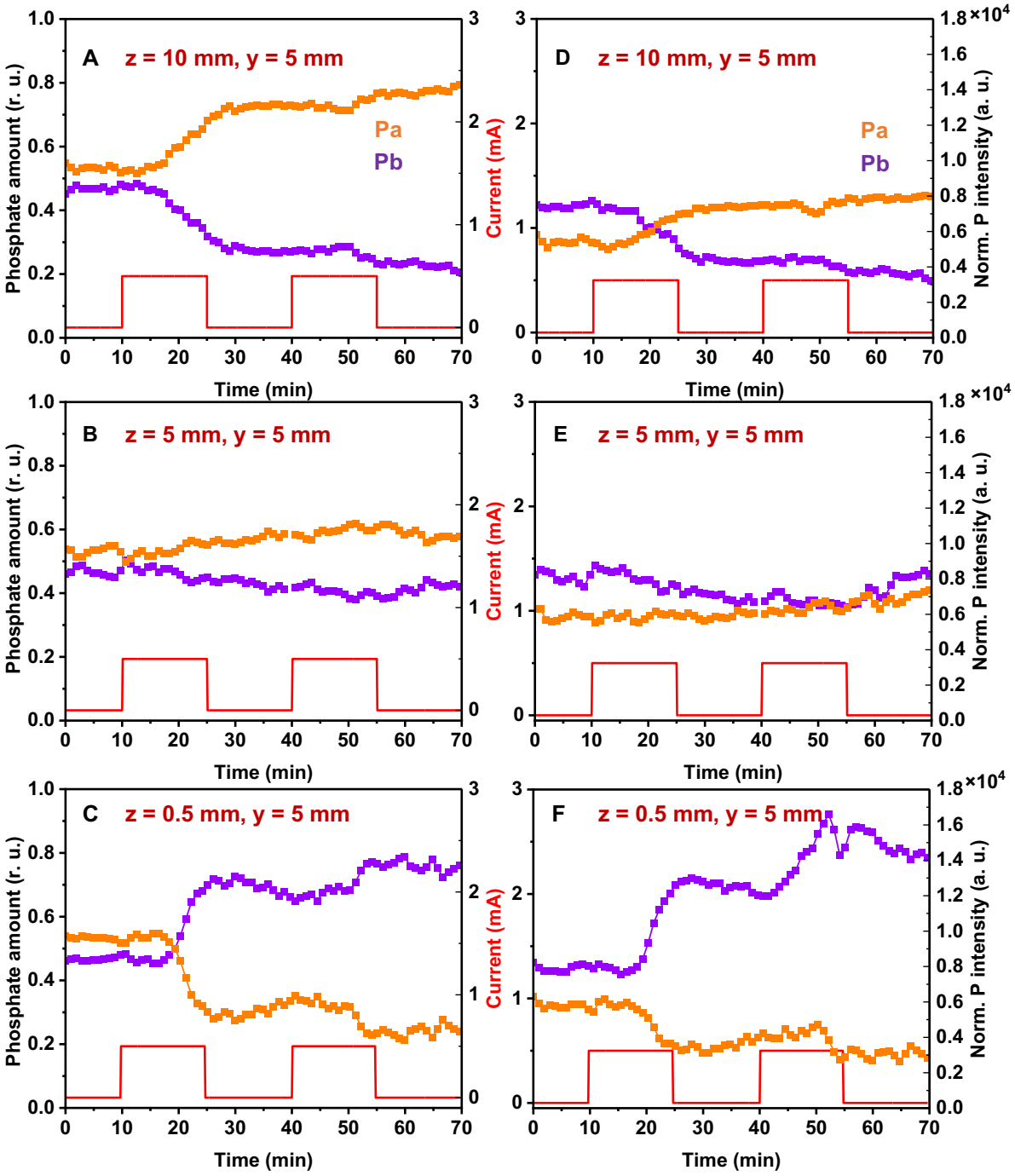

Figure 5-23 Time-course profiles of phosphate species amount (left) and normalized peak phosphate intensity (right) in a specified vertical space (z = 10 mm, A, B; 5 mm, C, D; 0.5 mm, E, F) and at a horizontal distance y of 5 mm from the anode. See Figure 5-22 for more details.

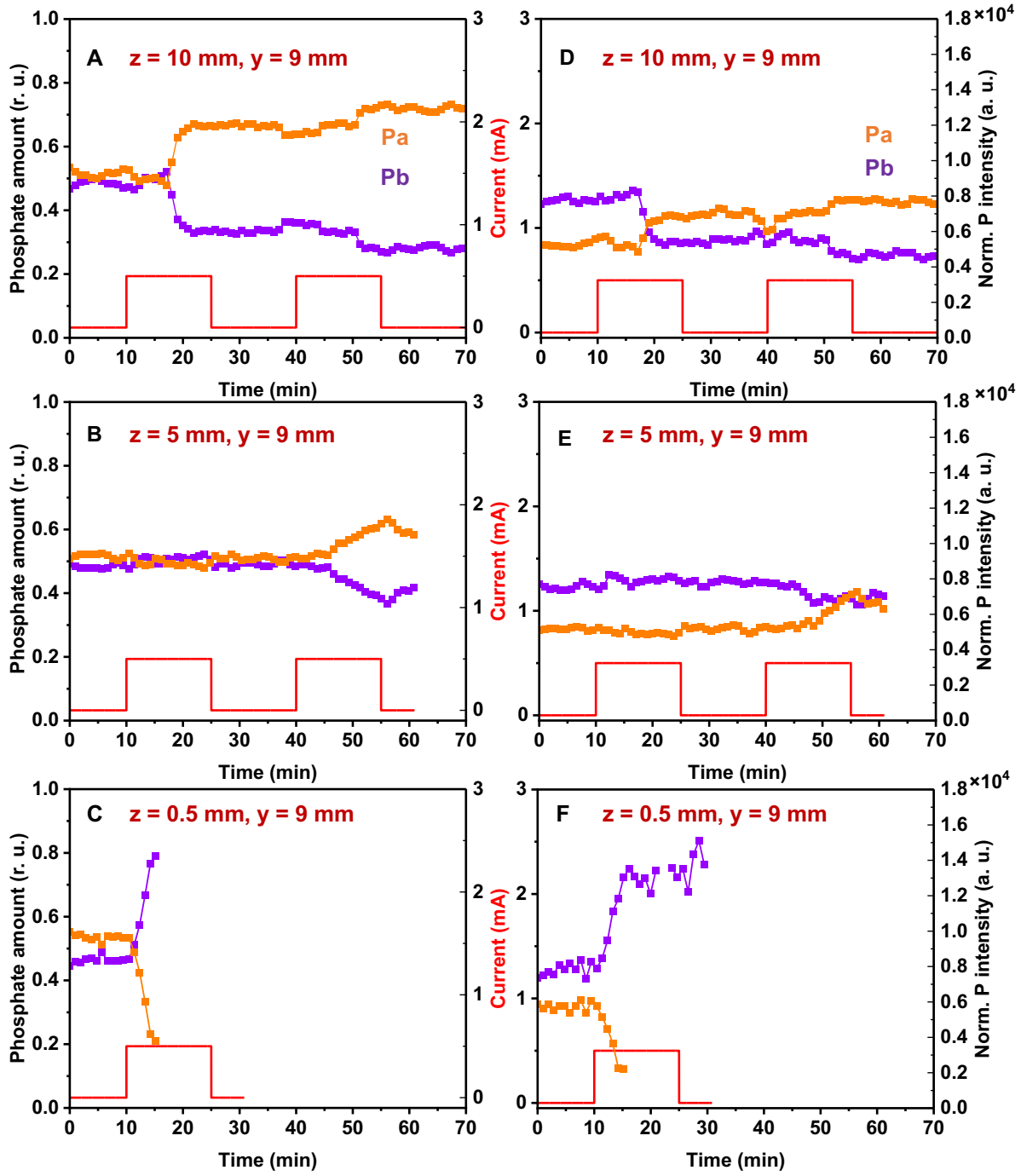

Figure 5-24. Time course of phosphate species amount (left) and normalized phosphate peak intensity (right) in the indicated vertical space (z = 10 mm, A, B; 5 mm, C, D; 0.5 mm, E, F) and at a horizontal distance y of 9 mm (1 mm) from the anode (cathode). The right column is 1 mm relative to the cathode. See Figure 5-22 for more details.

Figures 5-22 to 5-24 is the time course of phosphate amount (left) and normalized phosphate intensity (right) corresponding to Figures 5-20 and 5-21. Comparing the top (z = 10 mm) and bottom (z = 0.5 mm) profiles, the amount profiles for P_b or P_a are reversed if we do not account for the effects of late jumps caused by the diffusion of phosphate species from nearby vertical space, while the profiles at the middle positions (z = 5 mm) are relatively stable. In addition, we observed delayed changes in phosphate species amounts in the horizontal one-dimensional

direction. It is noteworthy that the major phosphate species involving Pa at the top of the anode (Figure 5-22A) or P_b at the bottom of the cathode (Figure 5-24C) did not show any delay in the initial period. However, a significant delay of phosphate species was observed in the middle layer of the cell (Figure 5-23B). This delay can be attributed to the 5 mm macroscopic distance from the electrode-bulk electrolyte interface.

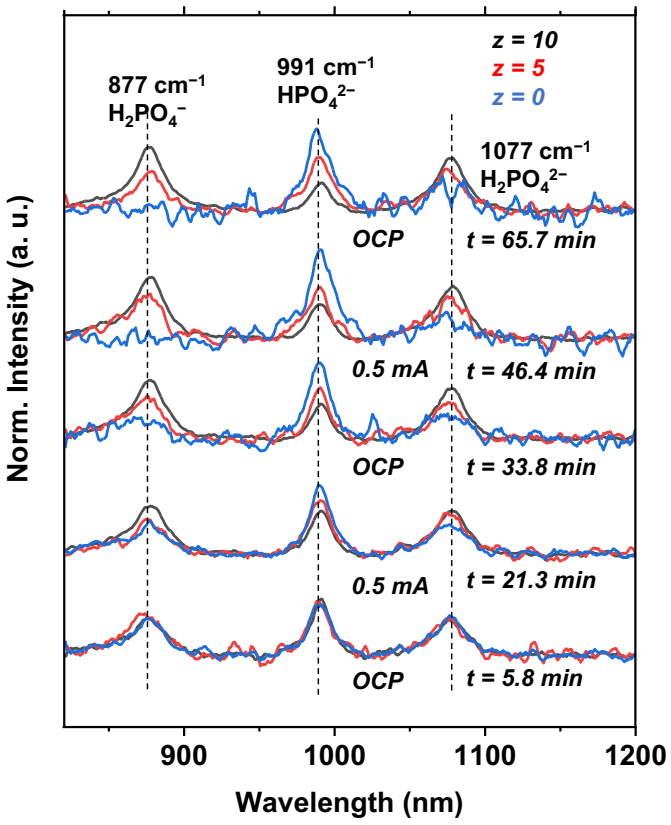

Figure 5-25. Comparison of normalized Raman spectra at specified vertical positions (z = 10, black; 5, red; 0 mm, blue) with jump currents tuned from zero (OCP) to 0.5 mA cm^{-2}. CoCat was operated in 25 mM KPi buffer (pH 7). The overlapping spectra represent simultaneously acquired spectra, normalized for water peaks and corrected for background. The dashed lines indicate the major vibrational bands of the phosphate species; from left to right: $H_2PO_4^-$ (~877 cm^{-1}), HPO_4^{2-} (~991 cm^{-1}), $H_2PO_4^-$ (~1077 cm^{-1}). The results are aligned with Figure 5-20 to Figure 5-24. Data were smoothed by commercially available software (OriginPro 2020b) using the Savitzky-Golay method for 5 points.

Raman spectra were acquired at a fixed distance of 5 mm from the electrode at the specified z position (Figure 5-25). At 5.8 min (OCP), the peaks at 991 cm^{-1} (P_b) and 1077 cm^{-1} (P_a) clearly overlapped, indicating the same pH at different vertical positions. When a current of 0.5 mA cm^{-2} is applied, the amplitude of P_b increases while P_a at the bottom position decreases. In contrast, the spectra taken at the top of the cell had the smallest amplitude at 991 cm^{-1} and therefore a smaller pH. The spectra recorded at z = 5 mm were repetitively localized between the spectra recorded at the top and bottom positions. After turning off the current, the phosphate peaks were no longer similar at all locations (z = 0.5, 5, and 10 mm), suggesting insufficient equilibration of phosphate species over a 15-minute period. Consequently, the amplitude changes of the phosphate peaks (P_b or P_a) do not increase or decrease to the same extent

compared to the first stage, because the previous OCP process did not reach full equilibrium. It is worth noting that after 1 hour, the bottom region has the largest peak of alkaline phosphate species (HPO_4^{2-}) and the smallest peak of acid phosphate, indicating the formation of an alkaline region at the bottom of the cell and vice versa. In the mid-cell layer (z = 5 mm), the peaks at 991 cm^{-1} and 1077 cm^{-1} show little change during the jump (solid red curves), reflecting the presence of a stagnant layer in the mid-cell layer. This provides an explanation for the quantification of the overall pH profile at the mid-cell layer (see Section 5.2.3.1 to 5.2.3.3).

To sum up, Raman spectrum measurement with jump currents in the vertical direction of the cell suggests the presence of convective flow in the bulk electrolyte cell. In a previous study,[207] significant changes in pH (or phosphate amount) in three dimensions were also observed by using pH-sensitive fluorescent foils and attributed to the presence of natural convection.[207] Through numerical modeling, they confirmed that it is the change in electrolyte density that drives natural convection (i.e., the buoyancy effect) and further mitigates the large changes in local pH. In a practical electrolyzer, the evolution of bubbles generated by electrochemical reactions may play an important role in convective mixing, which obviously depends on the current density, the departure diameter and coverage of the bubbles.[291;292;298;309] Bubbles of different sizes affect the mass transfer characteristics. Thermal effects from the overpotential may also lead to macroscopic convection. As for the formation of convection here, it may be related to natural convection caused by changes in electrolyte density due to (de)protonation of phosphates. In addition, the evolution of bubbles is negligible at low current density (0.12 mA cm^{-2}), where the bulk pH profile is similar to that at high current density (0.3 mA cm^{-2}), and thereby we tend to attribute the convection to buoyancy effects.[207]

5.3 Summarizing discussion

A. Pronounced acidification at the CoCat—electrolyte interface

By operando Raman spectroscopy, we observed that pronounced local acidification by almost one pH unit close to the outer surface of CoCat for electric potentials beyond the Tafel-slope regime. This finding suggests that macroscopic proton transport limitations lead to a decrease in the local pH near the catalyst surface, which in turn limits the catalytic current density. This finding strongly supports the conclusions presented in Chapter 2, where also a more detailed discussion can be found.

B. Circular flow enhances proton transport between anode and cathode

For stationary operation, transport of protons by diffusion of $H_2PO_4^-$ ions directly from the anode to the cathode would require $H_2PO_4^-$ amount profile that changes linearly between a maximum at the anode-electrolyte interface to a minimum at the cathode-electrolyte interface (and vice versa for the HPO_4^{2-} amount profile, see also dash lines in Figure 5-26A). This behavior is clearly predicted by the one-dimensional diffusion equation for the stationary situation, but it contrasts with the here reported experimental findings (solid lines in Figure 5-26A). Instead, by collecting Raman spectra of the middle layer of the water electrolyzer (z = 5 mm), remarkable concentration gradients were observed, but only within about 800 μm from the anodic and cathodic electrodes. The otherwise lacking concentration gradients excludes

significant proton transport by diffusion of $H_2PO_4^-$ ions directly from the anode to the cathode (as well as the HPO_4^{2-} diffusion in the reverse direction).

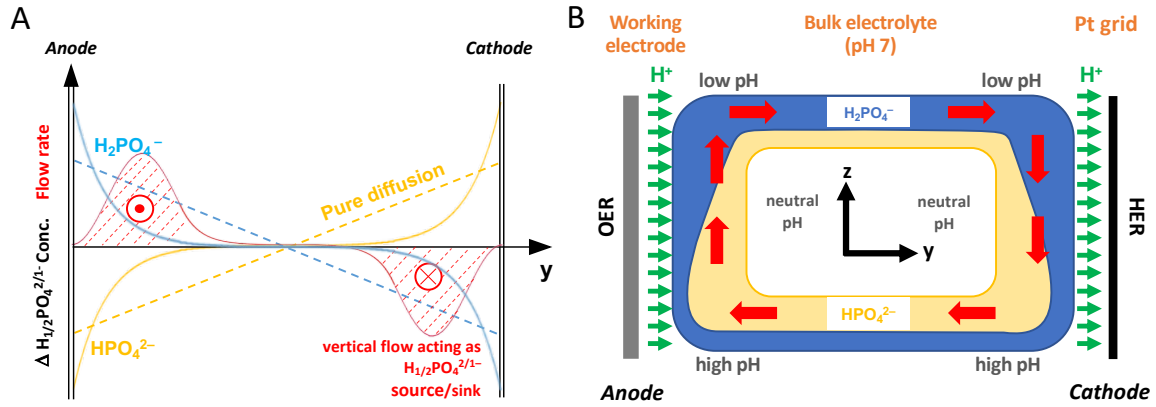

Figure 5-26. Circular flow within the two-electrode cell facilitating accelerated proton transport by the protonated buffer base ($H_2PO_4^-$). (A) One-dimensional concentration profiles of proton transport assisted by electrolyte phosphate ions from theoretical prediction (dashed lines) at constant diffusive flux and experimental results (solid lines) generating steep concentration gradient. (B) Schematic circular flow enhancing proton transport between the anode and cathode. The blue area indicates more protonated HPO_4^{2-} at the top of the cell and salient HPO_4^{2-} (orange) at the bottom of the cell. Arrow (red) marks the direction of convective flow.

The steep non-linear concentration gradients that level off within about 800 µm can be explained by a circular electrolyte flow as schematically shown in Figure 5-26. This explanation is strongly suggested by the experiments of Figures 5-20 to 5-25. The circular flow involves the transport of (protonated) buffer molecules from the anode to the cathode at the top of the cell (z = 10 mm) and (deprotonated) buffer molecules from the cathode to the anode at the bottom of the cell (z = 0.5 mm). It is likely that for the here investigated electrode geometry, the rate of proton transport through the circular flow of phosphate ions clearly exceeds the rate of proton transport by direct diffusion between anode and cathode.

The origin of the circular flow is not fully clear. As discussed in the preceding section, it is conceivable that natural convection caused by buoyancy drives the here described circular flow. The buoyancy would result from a density difference of the hydrated phosphate ions. The doubly charged HPO_4^{2-} is expected to carry a more extended and denser hydration shell than the singly charged $H_2PO_4^-$ so that the latter would experience a relative buoyancy force.

Here its found that the electrolyte pH in the vicinity of the anode and the cathode (here detected at 1 mm distance) can differ pronouncedly between the lower part of the electrodes (more alkaline) and the upper part of the electrodes (more acidic). Such a wide spread of pH values in the vicinity of the same electrode may complicate the interpretation of potential and pH dependencies in mechanistic investigations. For example, a heterogeneity in the local pH at the working electrode may be related to the imperfectly linear relation between oxidation state and the logarithm of the current density in unstirred electrolyte (Panels A3 and B3 of Figures 3-11 and 3-12), contrasting the perfectly linear relation in stirred electrolyte (Panels C3 and D3 of Figures 3-11 and 3-12). Moreover, it will hamper the reproducibility of the results for changes

in the cell geometry. In mechanistic investigations, diffusion acceleration by strong electrolyte stirring may be generally a useful experimental approach for minimization of diffusion limitations and avoidance local-pH heterogeneities at the working electrode.

In conclusion, for the here investigated geometry the direct diffusion of proton carrying molecules within a stagnant electrolyte is not the major route of proton transport from the anode to the cathode. This conclusion likely is generally valid for technically relevant electrolysis cells. (Noteworthily, also in alkaline electrolysis, the proton transport between electrodes typically is facilitated by diffusion and/or flow of molecules, specifically of hydroxide ions.)

5.4 Experimental details

5.4.1 Sample preparation

For local and bulk electrolyte pH quantification, CoCat was deposited on a Pt foil with an active area of 1 cm^2. For local pH measurements, the area of the film exposed to the electrolyte was 0.785 cm^2 (diameter: 1 cm). In bulk pH quantification, the exposed film is 1 cm^2 unless otherwise noted. In vertically oriented acquisitions (Figure 5-7C), the exposed area in the electrolyte was 0.8 cm^2 at a distance of 1 mm from both electrodes. The deposited amounts of CoCat are 20 and 40 mC cm^{-2}, as described everywhere.[70;126] The prepared CoCat was operated in 25 mM neutral KPi buffer solution. Standard phosphate solutions (25 mM) of different pH values were prepared from stock solutions of H_3PO_4, KH_2PO_4 with the pH adjustment by adding concentrated KOH solution (1 M or 5 M).

5.4.2 Raman configuration

Operando Raman spectroscopy was performed using Renishaw inVia confocal Raman spectrometer equipped with a Leica water immersion objective (×40, NA 0.8, laser position and intensity calibrated to standard silicon). Two types of electrochemical cells were used to quantify local and bulk pH, respectively (Figure 5-1, Figure 5-6).

Spectra of CoCat films (1 cm in diameter, exposed to the electrolyte) deposited on a platinum foil substrate were collected for local pH experiments in 25 mM KPi solution using a laboratory-made three-electrode Teflon cell (Teflon® PTFE) (Figure 5-1). Water-immersion objective of the Raman microscope was covered with a Teflon film (Teflon® FEP, 13 μm, DuPont) to avoid exposure to corrosive electrolyte solutions during data collection for pH calibration. Spectra were collected in phosphate solutions of different pH values using green laser (532 nm edge mode) and a circular spot as an excitation source (grating of 2400 lines/mm, laser power of 35 mW, each spectrum collection for 3 min 50 s acquisition). In order to monitor the local pH change of the CoCat film during the electrocatalytic process, a motorized sample stage was used and the laser focus was adjusted to approximately 20 µm above the CoCat surface. Line focusing was performed using a 532 nm laser (beam size of approximately 100 × 10 μm^2, intensity of 17.5 mW, acquisition time of around 1 minute per spectrum) to avoid damage to the sample. The electrochemical system is controlled by a SP-200 BioLogic potentiostat. With the BioLogic potentiostat's ZIR technology, the iR voltage drop is compensated by 85%. During the chronoamperometric steps, the collection of spectra was initiated after applying corresponding potentials in the range of 0.6 V to 1.38 V for 1 minute (total step size of 2.5 min).

To measure bulk pH, a simple two-electrode electrochemical cell was built. The laser focusing point of Raman spectrometer was located around 1 mm from the back side of the transparent glass wall (Figure 5-6) so that measurements could be made along the path of the two parallel electrodes. For using the water immersion objective, a drop of water is placed between the glass wall and the objective. The distance between electrodes is 1 cm and is wedged with a Teflon spacer (2 mm thick). Pt foil (10 × 20 mm) can be used as an anode or cathode but is coated or uncoated with CoCat. The electrodes are fastened with Kapton tape to a PTFE or aluminium holder. Spectra were collected using a green laser (532 nm) in edge mode (100 % power). The exposure time for each spectrum was 10 s, with 5 accumulations. The acquisition time for each spectrum is approximately 58 s. The position where a clear laser spot is blocked by the electrode is defined as the zero point by adjusting the micrometer motorized sample stage. Similarly, the bottom line of the electrochemical cell is defined as the "zero" height of the vertical jump current experiment. To ensure the repeatability of the zero point, the OCP spectra were continuously acquired with the presence of of KPi buffer. The zero point is defined as the position where the Raman peaks of phosphate and water first appear, and the PTFE peak disappears. The protocols applied include jump currents between OCP and 0.5 mA cm^{-2} and fixing currents of 0.3 mA cm^{-2} or 0.12 mA cm^{-2}. A miniature Ag/AgCl electrode (3 M NaCl) was added in the top solution region near the anode in order to obtain the specific potential of the working or counter electrode.

5.4.3 Raman analysis

Raman spectra were analyzed using Fityk software. Calibration curves (Figure 5-4B) are obtained by collecting spectra with well-known phosphate concentrations and used for local and bulk pH quantification. Lorentzian, Gaussian, or Voigt function are used to fit the Raman bands of the phosphate solution species or water. In more detail, the half-width-at-half maximum (HWHM) and peak position values are fixed, and the band amplitudes are normalized to the water band intensity. Note that the water peak intensity is from the average of phosphate standard solutions (~1642 cm^{-1}, 45508 a.u.). See Section 5.2.2 for details on obtaining calibration curves. Here, we focus on spectral modeling for bulk electrolyte pH and thus fit only the phosphate peaks. There are two main types of phosphates, $H_2PO_4^-$ and HPO_4^{2-}. The $H_2PO_4^-$ bands at ~ 877 cm^{-1} and 1077 cm^{-1} were fitted with a fixed HWHM of 10 cm^{-1}. Another band at ~991 cm^{-1} assignable to HPO_4^{2-} was fitted with the HWHM of 8 cm^{-1}. The Voigt function (77.5 cm^{-1}, shape = 0.1) was used to fit the water peak at ~1642 cm^{-1}. Background was corrected by using a sixth-order polynomial. Direct peak amplitudes of phosphate species were obtained by concurrently fitting the peak bands of phosphate species and calibrating background. Subsequently, normalized phosphate peak amplitude is calculated after normalization respect to water peak (~1642 cm^{-1}). Note that a calibration factor (υ) was introduced to obtain the relative phosphate amounts, as described in the calibration curve section 5.2.2.

6 Key results

This thesis focuses on the activity determinants and limiting factors in neutral-pH water oxidation, the oxygen evolution reaction (OER) elucidated for an electrocatalytic cobalt-phosphate (CoCat) system. The main topics include the role of macroscopic proton transport limitation as determinants of electrocatalytic rates (Chapter 2), the role of metal redox chemistry in determining the rate of OER catalysis (Chapter 3), the structural and functional role of redox-inert ions (Chapter 4), and the quantification of local pH and electrolyte pH profiles under electrocatalytic operation conditions (Chapter 5). The involved techniques comprise electrochemical techniques combined with operando X-ray absorption spectroscopy (XAS), operando Raman spectroscopy (RM), UV-vis spectroscopy, and elemental analysis (total reflection X-ray fluorescence, TXRF) as well as numerical simulations. The most important results are summarized below and concern (A) the macroscopic transport phenomena acting back on the catalyst material and (B) the rate-determining factors of the OER at the microscopic (atomistic) level.

A. Macroscopic Proton Transport Limitations in the Bulk Electrolyte Determine Catalyst-Internal OER Rates (Chapters 2 and 5)

Comprehensive analysis of current-potential (*j*-V) curves at different KPi concentrations reveals distinct rate determinants of OER in different potential regimes as summarized in the following. (*Chapter 2*)

a) ***Low overpotential regime.*** At low overpotentials, essentially identical Tafel slopes at different KPi concentrations reflect the fact that the intrinsic OER mechanism is unaffected by the electrolyte (KPi) composition. Both potential-dependent oxidation states and the atomic structures that are relevant to catalytic mechanisms are indeed unaffected by the electrolyte phosphate concentration, as found by XAS analysis. (*Chapter 2*)

b) ***Intermediate overpotential regime.*** Upon further extension to the intermediate overpotential regime, plateau current density and KPi concentration show a first-order relation, implying that current limitation arises from the available amount of nonprotonated buffer ions (HPO_4^{2-}) that can accept protons. Upon accelerating diffusion in the electrolyte, the plateau current density significantly increases, supporting that the proton-carrying buffer ion is macroscopically diffusion-limited. (*Chapter 2*)

   i. Localized acidification was detected close to the outer surface of the CoCat material by operando Raman spectroscopy when the electric potential exceeded the region of the Tafel slope, implying that the macroscopic transport of protons was limiting. (*Chapter 5*)

   ii. By analyzing the first-order derivatives of the X-ray fluorescence signal collected during CVs at fixed XAS excitation energy, it is shown that CV peaks observed in low-KPi electrolyte are not resulting from redox transitions but result from KPi diffusion limitations. This supports that sufficient amounts of electrolyte bases acting as proton acceptors are critical to mitigate decreased catalytic activity resulting from

local acidification at the electrode surface and consequently within the CoCat material (increase proton activity within the volume-active CoCat material). (*Chapter 2*)

iii. Phosphate ions do not facilitate the catalyst-internal proton transport. By quantifying the absolute amount of internal phosphate as a function of (i) electrolyte KPi concentration and (ii) applied electrode potential, limitation from internal proton transport mediated by phosphate ions was essentially ruled out. The negligible influence of changes in KPi electrolyte concentration and electrode potential on the amount of internal phosphate suggests that a low exchange efficiency of phosphate between electrode material and bulk electrolyte. This finding conflicts with the first-order dependence between current density and KPi concentration relating to catalyst-internal proton transport by phosphate ions (see Figure 2-1). The slow release of phosphate from the interior of CoCat when the film is operated in an unbuffered electrolyte with a relatively stable potential also suggests an inefficient exchange of phosphate. (*Chapters 2 and 4*)

iv. Modeling of experimental *j*-V curves confirms the roles of the buffer pathway and an additional water pathway (see also c) in mediating electrolyte proton transfer in neutral-pH water oxidation, as schematically summarized in Figure 2-23. (*Chapter 2*)

c) ***High overpotential regime.*** At higher potentials, the *j*-V curves at low KPi concentrations asymptote to those of the electrolyte without KPi (pure water), indicating that water acts as a proton acceptor once the capacity of the phosphate buffer system for proton transport is exhausted. The increased activity for the stirred pure water system implies that also for the water pathway of proton transport diffusion (of the H_3O^+ ion) is a limiting factor. Experiments and mathematical modeling consistently predicted a doubling of the Tafel slope when run in a non-buffered electrolyte. Therefore, the water pathway is technologically largely irrelevant in neutral OER due to the need for high overpotentials. (*Chapter 2*) The following further effects were observed in the high overpotential (and thus high current) regime:

i. Experiments and simulations show a relevant limitation by the Ohmic resistance of the substrate electrode (mainly from ITO electrodes) and the electrolyte. (*Chapter 2*)

ii. Additional enhancement due to natural convection, such as buoyancy, was detected by numerical modeling of *j*-V curves, in line with results obtained by operando Raman spectroscopy. (*Chapters 2 and 5*)

d) ***Further results on proton-transport limitations and their removal.***

i. *Ionic strength.* The effect of varying the ionic strengths was investigated by adding high concentrations of electrolyte salts (here KNO_3) at different KPi concentrations. It was found that the catalytic activity is largely independent of the increased electrical conductivity or other possible salt effects (when a non-proton-accepting electrolyte salt is added). (*Chapter 2*)

ii. *Current densities exceeding 1 A cm^{-2} in neutral-pH OER.* A proof-of-principle experiment using a three-electrode rapid-flow system achieved OER current densities

well above 1 A cm^{-2} by consequently removing the limitations identified above. (*Chapter 2*)

iii. *Non-diffusive, convective flows dominate electrolyte proton transport.* Spatially-resolved operando Raman spectroscopy investigated electrolyte pH profiles of a water-electrolysis cell, which involved a cobalt-based catalyst film (CoCat) at the anode and a platinum cathode. By analysis of Raman bands of the electrolyte phosphate ions, their concentrations and local pH values were determined at selected locations on the electrochemical cell. Non-linear $H_2PO_4^-$ and HPO_4^{2-} concentration profiles were detected between anode and cathode, with steep concentration gradients close to the electrodes that level off within about 800 µm from the respective electrode. This could be explained by a circular electrolyte flow that involves the transport of (protonated) buffer molecules from the anode to the cathode at the top of the cell and (deprotonated) buffer molecules from the cathode to the anode at the bottom of the cell (see scheme of Figure 5-26). Natural convection caused by buoyancy effect relating to density differences of the hydrated phosphate ions may drive the circular flow. Consequently, the direct diffusion of proton-carrying molecules within a stagnant electrolyte is not the major route of proton transport from the anode to the cathode; other non-diffusive flows dominate the electrolyte proton transport. This conclusion likely is generally valid for technically relevant electrolysis cells. (*Chapter 5*)

B1. Microscopic Determinants of Catalyst-Internal Redox and Reaction Chemistry (Chapter 3)

The redox-active CoCat material is investigated by combining electrochemical experimentation with X-ray absorption and visible-light spectroscopy in operando experiments. It was found that the atomic structure and average metal oxidation state of the catalyst material are in equilibrium with the electrochemical potential, which is determined by the applied potential and the electrolyte proton activity. It is not the electric potential or the strength of the electric field per se that determines the OER catalytic rate, but rather the chemical state of the equilibrated material (see scheme of Figure 3-18). The steepness of the potential dependence of the catalytic current and non-Nernstian redox transition of the catalyst material can be explained in terms of energetically interacting high-valence metal sites. (*Chapter 3*)

a) Finding one: The catalytic current and thus the catalytic rate depends strictly exponentially on the Co^{4+} concentration in the redox-active catalyst material, independent of the electrolyte pH or mass-transfer limitations. (*Chapter 3*)
b) Finding two: The Co^{IV} ions are formed in a redox transition in which the Co^{IV} concentration does not follow the classical Nernstian behavior but depends linearly on the electrochemical potential. This is due to the rather strong interactions between the Co^{IV} metal ions, whose total positive interaction energy is proportional to the Co^{IV} concentration, thus placing the catalyst material between a redox-active molecular

solution with Nernstian behavior and a redox-inactive solid material with a potential-dependent Fermi energy. (*Chapter 3*)

c) Based on these experimental results, we propose that (i) the average oxidation state of cobalt is linearly related to the electrochemical potential due to the fact that the total positive interaction energy increases linearly with increasing Co^{4+} concentration. (ii) The same interaction energy leads to an increase in the oxidizing ability of the OER active site. Accordingly, the free energy difference of the transition state decreases linearly with increasing overpotential, thus explaining the exponential relationship between Co^{IV} concentration and catalytic current. (*Chapter 3*)

B2. Microscopic Determinants: The Role of Catalyst-Internal Redox-Inert Ions (Chapter 4)

The structure of the redox-inert potassium ion within the CoCat material and its role in the charge compensation process of the cobalt redox transition have been investigated by operando XAS at potassium K-edge and elemental analysis. (*Chapter 4*)

a) The K^+ ion binding within CoCat material involves comparably weak binding motifs, most likely hydrated K^+ ions and a minor fraction of K^+ ions forming ions pair with phosphate species as well as a potassium bound via a single O atom to Co ions of CoO_2 layer fragments. These binding motifs were deduced from XANES and EXAFS data collected at the potassium K-edge in technically challenging experiments. (*Chapter 4*)

b) In the CoCat material, the $Co^{II/III}$ and the $Co^{III/IV}$ redox transitions take place throughout the CoCat material involving a major fraction of cobalt ions. These transitions require massive charge-compensating ion flows. Previous electrokinetic data and analysis of H_2O/D_2O exchange[134] effects suggest charge-compensation by protons exiting (upon Co oxidation) or entering (upon Co reduction) the CoCat bulk material. Here it was investigated whether also charge compensation by potassium ion flows is involved. It was found that cobalt redox transitions involving K^+ ions are not supported by elemental quantification and operando XAS detection of K^+ exchange kinetics. Electric-potential independence of the P:Co and K:Co molar ratios rules out any relevant contribution of these inert ions to charge compensation in the CoCat redox processes. The charge-compensating role of potassium ions was also ruled out from the novel potassium K-edge XAS experiment, where the releasing rate of potassium ion was one order of magnitude slower than the rate of oxidation of cobalt ion in the CoCat. Therefore, in combination with the inherent slow-release rate of phosphate, we conclude that neither K^+ ions nor phosphate ions can participate in charge compensation events in the redox transition of CoCat materials. (*Chapter 4)*

7 Appendix

7.1 Additional figures

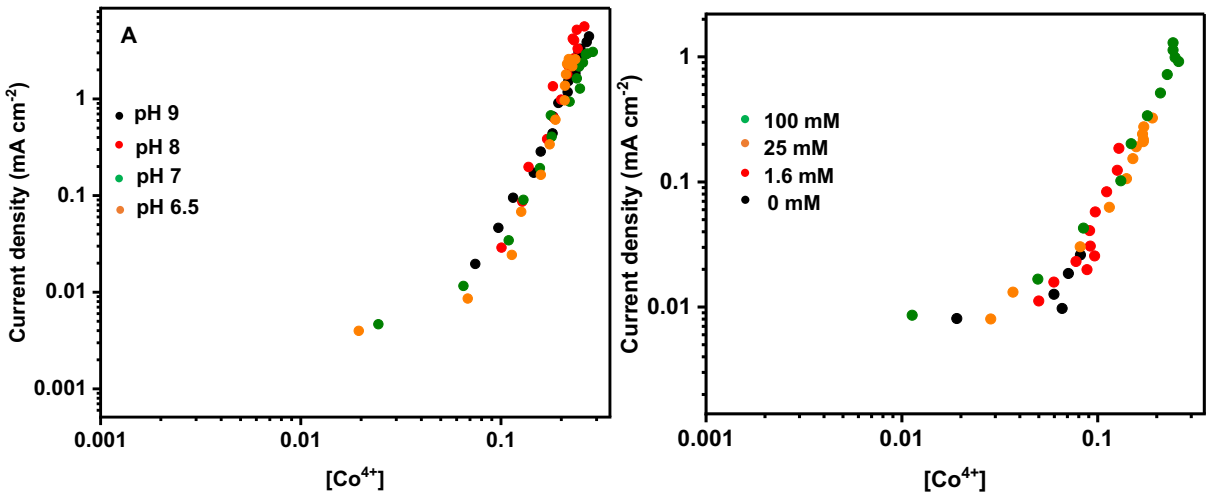

Figure 7-1. Rate law plots between log(current density) and log(Co^{4+} concentration) for CoCat operating at different pH or KPi concentrations. The results shown here are adapted from Figure 3-1D and Figure 3-5A, but the X-axis is shown on a logarithmic scale. The [Co^{4+}] indicates an average oxidation state greater than 3.0. Specifically, the Co^{4+} concentration shown here is obtained by subtracting 3.0±0.05 from the displayed mean oxidation state in Figure 3-1D and Figure 3-5A, respectively. See Figure 3-1 and Figure 3-5 for more details.

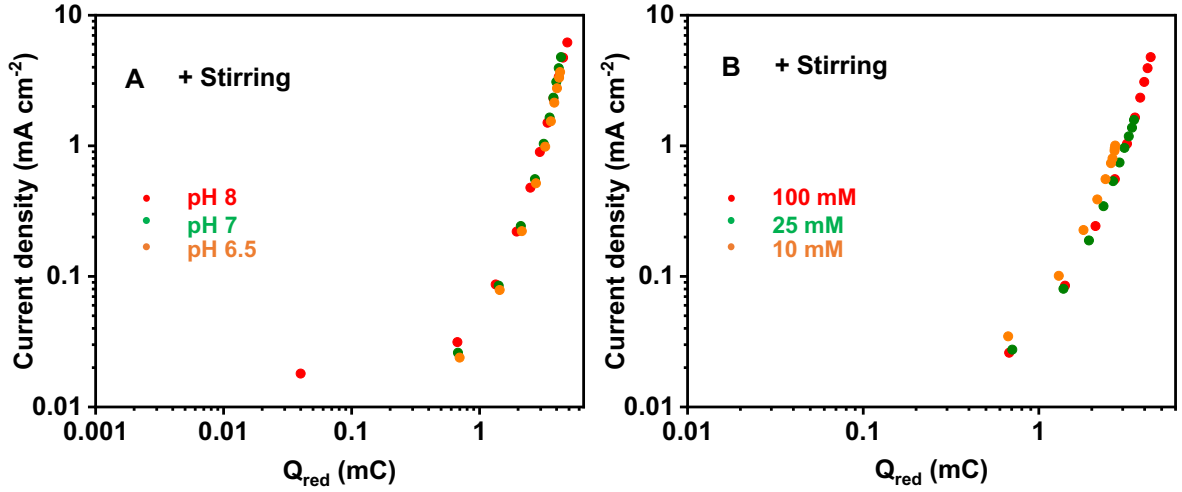

Figure 7-2. Logarithmic plots of current density and oxidatively stored charge for CoCat films operated at different pH or KPi concentrations. Note that the here displayed graphs are adapted from Figure 3-11 C3 and Figure 3-12 C3, with offset values (~0.5) subtracted from each curve because of the deviation from the zero point of Figure 3-11 C3 and Figure 3-12 C3. The presence of offset is likely related to the choice of the jump-back potential. Ideally, the potential at which the mean oxidation state of cobalt is equal to 3.0 is used as the jump-back potential. See Figure 3-11 C3 and Figure 3-12 C3 for more details.

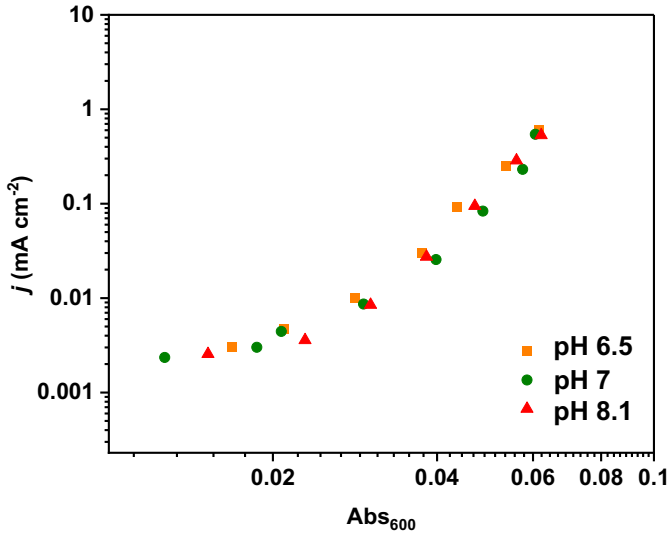

Figure 7-3. Logarithmic plot of optical absorption difference at 600 nm and current density, adapted from Figure 3-17C. Note that absorption values less than 0 cannot be displayed.

7.2 Lists of own publications

1. S. Liu, L. D'Amario*, S. Shit, S. Mebs, H. Dau*. Origin of potential and pH dependence of electrocatalytic rates. *ChemRxiv*. **2024**; https://doi.org/10.26434/chemrxiv-2024-wkgpt (preprint)

2. S. Liu, L. D'Amario, S. Jiang, H. Dau*. Recent operando Raman spectroscopy applications in electrochemistry. *Current Opinion in Electrochem*istry **2022**, 35, 101042. https://doi.org/10.1016/j.coelec.2022.101042

3. S. Liu, I. Zaharieva, L. D'Amario, S. Mebs, K. Paul, F. Yang, P. Beyer, M. Haumann, H. Dau*. Electrocatalytic water oxidation at neutral pH – Deciphering the rate constraints for an amorphous cobalt-phosphate catalyst system. *Advanced Energy Materials* **2022**, 12, 2202914. https://doi.org/10.1002/aenm.202202914

4. S. Liu, S. Farhoosh, P. Beyer, S. Mebs, I. Zaharieva, M. Haumann, H. Dau*. Role of potassium in electrocatalytic water oxidation investigated in a volume-active cobalt material at neutral pH. *Advanced Sustainable Syst*ems **2023**, 7, 2300008. https://onlinelibrary.wiley.com/doi/10.1002/adsu.202300008

5. S. Liu, S. Farhoosh, P. Beyer, S. Mebs, M. Haumann, H. Dau*. Phosphate coordination in a water-oxidizing cobalt-oxide electrocatalyst revealed by X-ray absorption spectroscopy at the phosphorus K edge. *Catalyst*s **2023**, 13, 1151. https://www.mdpi.com/2073-4344/13/8/1151

6. C. Pasquini, S. Liu, P. Chernev, D. Gonzalez-Flores, M. R. Mohammadi, P. Kubella, S. Jiang, S. Loos, K. Klingan, V. Sikolenko, S. Mebs, M. Haumann, P. Beyer, L. D'Amario, R. D. L. Smith, I. Zaharieva, H. Dau*. Operando tracking of oxidation-state changes by coupling electrochemistry with time-resolved X-ray absorption spectroscopy demonstrated for water oxidation by a cobalt-based catalyst film. *Analytical and Bioanalytical Chemistry* **2021**, 413, 5395. https://link.springer.com/article/10.1007/s00216-021-03515-0

7. F. Yang, S. Jiang, S. Liu, P. Beyer, S. Mebs, H. Dau. Dynamics of bulk and surface oxide evolution in copper foams for electrochemical CO_2 reduction. *Communications Chemistry* **2024**, 7, 66. https://www.nature.com/articles/s42004-024-01151-0

7.3 Lists of international conferences attended

1. 4-8. November 2019, nanoGe Fall Meeting 2019, Berlin, *Elucidation of phosphate-buffer function for water Oxidation by Cobalt-based electrode films (CoCat): concentration effect at neutral pH.* (Poster)

2. 26-29. July 2021, International Solar Fuels Conference (online), *Systematic experimental evidence for proton management by phosphate buffer molecules in neutral-pH water Oxidation obtained for a Co-based catalyst material*. (Poster)

3. 27-30. September 2022, Electrochemistry 2022, Berlin, *The role of catalyst-internal ions and electrolyte ions for water oxidation at neutral pH investigated for potassium and phosphate in a Cobalt-based electrocatalyst*. (Poster)

4. 18-25. June 2023, MECART Thematic School, Paris, *Vibrational and electronic spectroscopies applied to the study of reaction mechanisms*.

To my Family

8 Acknowledgment

As time goes by, my PhD journey is coming to an end. If it is said that "scientific research is a circle without circumference", then these years of doctoral training is to pursue the longest radius and the largest circumference possible. The interdisciplinary study from materials science, chemistry to physics is probably the most unforgettable experience in my life, I am full of joy because of the understanding of an experimental method, but also because of countless experiments failed to feel anxiety and frustration, from the first time to step out of the country's timidity to the present to take charge of the situation. I would like to express my sincere gratitude to my family, supervisor, colleagues, and friends who have grown up with me and given me care and guidance. Without your help, I would not have had the courage to start this unforgettable journey.

First of all, I would like to express my gratitude to my supervisor Prof. Dr. Holger Dau for his careful guidance during my Ph.D. Holger is very knowledgeable and rigorous, and his insight and insight into scientific research is a role model for me, and his diligence and enthusiasm for work will always have a deep impact on me. I would also like to thank Holger for providing me with the opportunity to study at UniSysCat for three months before joining the lab, which not only allowed me to gain a wide range of experimental methods and techniques but also allowed me to get to know students from different countries and cultures, which greatly broadened my horizons during the process of mutual communication and improved my language skills.

Then I would like to thank Dr. Luca D'Amario and Dr. Ivelina Zaharieva. Every time I encountered an experimental problem, you were always eager to help me and discuss and analyse the reason with me patiently and in detail, and I am very grateful for your valuable suggestions in the process of publishing my work. Not only in the scientific research, but also in the life, you shared with me the experience and feelings of working as a postdoctoral fellow, thank you for making me understand the bigger world beyond my PhD life. During the late stage of my PhD studying, I am very grateful to Michael for his guidance and analysis of the low energy XAS data. Michael's dedication to scientific research has always touched me with admiration, and he is a role model for me to follow. Moreover, I would like to thank Dr. Stefan Mebs and Dr. Paul Beyer for their patience in teaching me about the various devices and their operation during the time I worked with you in the synchrotron radiation laboratory, and I appreciate their guidance and corrections of my PhD thesis. I am very glad to have a humorous and brotherly colleague in the lab, Stefan, you are always so kind and I get a lot of happiness factor every time I talk to you. Meanwhile, I am very honored to work with Paul Beyer in the same office, you are always so well organized in your work, thank you for doing a lot of organizing work for the lab, I am very impressed by your calm and efficient attitude towards your work, which is also the working attitude I need to learn from now on: be less impatient, be calm, and understand that less is more.

In addition, I would like to thank Dr. Chiara Pasquini, Dr. Mohammad Reza Mohammadi, and Paul Kubella for their patience and guidance at the beginning of my experiment, who helped me to get familiar with the use of the instruments in the lab and allowed me to carry out my

own experiments more quickly, and made me feel the warmth of a big family in the lab. Thank you for the group meetings before Covid-19, which exposed me to the beauty of biology, and I also took a biology-related course, thank you Dr. Dennis Nürnberg for your lively lectures, and thank you for your advice on my project about how to accurately quantify phosphorous. I would also like to thank Leonard Pfister, a master student, for taking the time to show me how to use the instruments he was using so that I could complete an experiment smoothly and efficiently.

Thank you for all the time we spent together during my PhD, for all the learning and growing, for all the conferences we attended, for all the lunches we had, for all the relaxing weekends we had, for all the fun we had, for all the "complaining" about the never-ending experiments we had to do together, and for all the kindness and selflessness you all showed me to get me through all the difficulties I had to deal with, thank you all! Shan, Paul Greife, Sarah, Nicholas, Fan, Shima, and many thanks to Janis and Endrias for their help in purchasing chemicals and helping me with the day-to-day running of the lab.

In addition, I am very grateful to the China Scholarship Council (CSC) for funding my PhD in Germany, which provided a great opportunity for a rural student to come out and open her eyes to the world, and to the teachers and friends who helped me with the application process.

Finally, thanks to my beloved family, thanks to my parents' hard work outside to create a favorable environment for us, thanks to my grandmother to take care of me growing up, your wisdom, doing things boldly, the attitude of good at accepting new things has always been very much in my admiration. Thank you all in this journey for standing with me side by side, your tolerance, understanding and support are my infinite power to move forward, I am proud of living in this happy family. Here, I wish you all good health and a happy mood. Last but not least, I also want to thank my boyfriend, although we have not seen for four years, you are always in support of me, giving me great care and encouragement, thank you!

9 Selbstständigkeitserklärung

Name: Liu

Vorname: Si

Ich erkläre gegenüber der Freien Universität Berlin, dass ich die vorliegende Dissertation selbstständig und ohne Benutzung anderer als der angegebenen Quellen und Hilfsmittel angefertigt habe. Die vorliegende Arbeit ist frei von Plagiaten. Alle Ausführungen, die wörtlich oder inhaltlich aus anderen Schriften entnommen sind, habe ich als solche kenntlich gemacht. Diese Dissertation wurde in gleicher oder ähnlicher Form noch in keinem früheren Promotionsverfahren eingereicht.

Mit einer Prüfung meiner Arbeit durch ein Plagiatsprüfungsprogramm erkläre ich mich einverstanden.

Datum: den 02. May 2024 Unterschrift:

10 Bibliography

1 D. Gust, T. A. Moore, & A. L. Moore. (2009). Solar fuels via artificial photosynthesis. *Acc. Chem. Res.*, *42*(12), 1890-1898. https://doi.org/10.1021/ar900209b

2 BP. (2022). *Primary energy consumption worldwide from 2000 to 2021 (in exajoules)*. Statista inc. Retrieved May 17 from https://www.statista.com/statistics/265598/consumption-of-primary-energy-worldwide/

3 N. S. Lewis, & D. G. Nocera. (2006). Powering the planet: chemical challenges in solar energy utilization. *Proc. Natl. Acad. Sci. U.S.A.*, *103*(43), 15729-15735. https://doi.org/10.1073/pnas.0603395103

4 J. Barber, & P. D. Tran. (2013). From natural to artificial photosynthesis. *J R Soc Interface*, *10*(81), 20120984. https://doi.org/10.1098/rsif.2012.0984

5 BP. (2021). *BP Statistical Review of World Energy* Retrieved May 17 from https://www.bp.com/en/global/corporate/energy-economics/statistical-review-of-world-energy.html

6 J. Barber. (2009). Photosynthetic energy conversion: natural and artificial. *Chem. Soc. Rev.*, *38*(1), 185-196. https://doi.org/10.1039/b802262n

7 T. Faunce, S. Styring, M. R. Wasielewski, G. W. Brudvig, A. W. Rutherford, J. Messinger, A. F. Lee, C. L. Hill, H. deGroot, M. Fontecave, D. R. MacFarlane, B. Hankamer, D. G. Nocera, D. M. Tiede, H. Dau, W. Hillier, L. Z. Wang, & R. Amal. (2013). Artificial photosynthesis as a frontier technology for energy sustainability. *Energy Environ. Sci.*, *6*(4), 1074-1076. https://doi.org/10.1039/C3ee40534f

8 P. Friedlingstein, M. O'Sullivan, M. W. Jones, R. M. Andrew, L. Gregor, J. Hauck, C. Le Quéré, I. T. Luijkx, A. Olsen, G. P. Peters, et al.B. Zheng. (2022). Global Carbon Budget 2022. *Earth Syst. Sci. Data*, *14*(11), 4811-4900. https://doi.org/10.5194/essd-14-4811-2022

9 COP21. (2015). Paris Agreement to the United Nations Framework Convention on Climate Change. *T.I.A.S.*, 16-1104. https://unfccc.int/files/essential_background/convention/application/pdf/english_paris_agreement.pdf

10 D. Zhang, J. Wang, Y. Lin, Y. Si, C. Huang, J. Yang, B. Huang, & W. Li. (2017). Present situation and future prospect of renewable energy in China. *Renew. Sustain. Energy Rev.*, *76*, 865-871. https://doi.org/10.1016/j.rser.2017.03.023

11 P. De Luna, C. Hahn, D. Higgins, S. A. Jaffer, T. F. Jaramillo, & E. H. Sargent. (2019). What would it take for renewably powered electrosynthesis to displace petrochemical processes? *Science*, *364*(6438). https://doi.org/10.1126/science.aav3506

12 IEA. (2019). *The Future of Hydrogen*. IEA. https://www.iea.org/reports/the-future-of-hydrogen

13 S. Song, H. Lin, P. Sherman, X. Yang, C. P. Nielsen, X. Chen, & M. B. McElroy. (2021). Production of hydrogen from offshore wind in China and cost-competitive supply to Japan. *Nat. Commun.*, *12*(1), 6953. https://doi.org/10.1038/s41467-021-27214-7

14 G. Kakoulaki, I. Kougias, N. Taylor, F. Dolci, J. Moya, & A. Jäger-Waldau. (2021). Green hydrogen in Europe – A regional assessment: Substituting existing production

with electrolysis powered by renewables. *Energy Conversion and Management*, *228*, 113649. https://doi.org/10.1016/j.enconman.2020.113649

15 Y. Xia, H. Cheng, H. He, & W. Wei. (2023). Efficiency and consistency enhancement for alkaline electrolyzers driven by renewable energy sources. *Communications Engineering*, *2*(1), 22. https://doi.org/10.1038/s44172-023-00070-7

16 A. Fujishima, & K. Honda. (1972). Electrochemical Photolysis of Water at a Semiconductor Electrode. *Nature*, *238*, 37-38. https://doi.org/10.1038/238037a0

17 G. Glenk, & S. Reichelstein. (2019). Economics of converting renewable power to hydrogen. *Nat. Energy*, *4*(3), 216-222. https://doi.org/10.1038/s41560-019-0326-1

18 C. Acar, & I. Dincer. (2014). Comparative assessment of hydrogen production methods from renewable and non-renewable sources. *Int. J. Hydrog. Energy*, *39*(1), 1-12. https://doi.org/10.1016/j.ijhydene.2013.10.060

19 D. Dissanayake, M. P. Rosynek, K. C. C. Kharas, & J. H. Lunsford. (1991). Partial oxidation of methane to carbon monoxide and hydrogen over a Ni/Al_2O_3 catalyst. *Journal of Catalysis*, *132*(1), 117-127. https://doi.org/10.1016/0021-9517(91)90252-Y

20 T. Hisatomi, & K. Domen. (2023). Overall water splitting: What's next? *Next Energy*, *1*(1), 100006. https://doi.org/10.1016/j.nxener.2023.100006

21 T. G. Deutsch. (2023). Concentrating on solar for hydrogen. *Nat. Energy*. https://doi.org/10.1038/s41560-023-01256-1

22 I. Holmes-Gentle, S. Tembhurne, C. Suter, & S. Haussener. (2023). Kilowatt-scale solar hydrogen production system using a concentrated integrated photoelectrochemical device. *Nat. Energy*. https://doi.org/10.1038/s41560-023-01247-2

23 D. W. Keith, G. Holmes, D. St. Angelo, & K. Heidel. (2018). A Process for Capturing CO_2 from the Atmosphere. *Joule*, *2*(8), 1573-1594. https://doi.org/10.1016/j.joule.2018.05.006

24 W. Lubitz, & H. Ogata. (2013). Hydrogenases, Structure and Function. In W. J. Lennarz & M. D. Lane (Eds.), *Encyclopedia of Biological Chemistry (Second Edition)* (pp. 562-567). Academic Press. https://doi.org/10.1016/B978-0-12-378630-2.00205-X

25 V. Engelbrecht, & T. Happe. (2018). Chapter Eight - [FeFe]-hydrogenases from green algae. In F. Armstrong (Ed.), *Methods in Enzymology* (Vol. 613, pp. 203-230). Academic Press. https://doi.org/10.1016/bs.mie.2018.10.004

26 G. D. Farquhar, S. von Caemmerer, & J. A. Berry. (1980). A biochemical model of photosynthetic CO_2 assimilation in leaves of C_3 species. *Planta*, *149*(1), 78-90. https://doi.org/10.1007/BF00386231

27 G. D. Farquhar, S. von Caemmerer, & J. A. Berry. (2001). Models of Photosynthesis. *Plant Physiology*, *125*(1), 42-45. https://doi.org/10.1104/pp.125.1.42

28 B. B. Buchanan. (2016). The carbon (formerly dark) reactions of photosynthesis. *Photosynthesis Research*, *128*(2), 215-217. https://doi.org/10.1007/s11120-015-0212-z

29 R. Emerson, & W. Arnold. (1932). The Photochemical Reaction In Photosynthesis. *Journal of General Physiology*, *16*(2), 191-205. https://doi.org/10.1085/jgp.16.2.191

30 H. Dau, E. Fujita, & L. Sun. (2017). Artificial Photosynthesis: Beyond Mimicking Nature. *ChemSusChem*, *10*(22), 4228-4235. https://doi.org/10.1002/cssc.201702106

31 C. X. Zhang, C. H. Chen, H. X. Dong, J. R. Shen, H. Dau, & J. Q. Zhao. (2015). A synthetic Mn_4Ca-cluster mimicking the oxygen-evolving center of photosynthesis. *Science*, *348*(6235), 690-693. https://doi.org/10.1126/science.aaa6550

32 D. G. Nocera. (2012). The artificial leaf. *Acc. Chem. Res.*, *45*(5), 767-776. https://doi.org/10.1021/ar2003013

33 I. McConnell, G. Li, & G. W. Brudvig. (2010). Energy conversion in natural and artificial photosynthesis. *Chemistry & Biology*, *17*(5), 434-447. https://doi.org/10.1016/j.chembiol.2010.05.005

34 D. Gust, & T. A. Moore. (1989). Mimicking photosynthesis. *Science*, *244*(4900), 35-41. http://www.sciencemag.org/cgi/content/abstract/244/4900/35

35 J. Lv, J. Xie, A. G. A. Mohamed, X. Zhang, Y. Feng, L. Jiao, E. Zhou, D. Yuan, & Y. Wang. (2023). Solar utilization beyond photosynthesis. *Nat. Rev. Chem*, *7*(2), 91-105. https://doi.org/10.1038/s41570-022-00448-9

36 C. S. Silva, W. D. Seider, & N. Lior. (2015). Exergy efficiency of plant photosynthesis. *Chem. Eng. Sci.*, *130*, 151-171. https://doi.org/10.1016/j.ces.2015.02.011

37 A. J. Bard. (1979). Photoelectrochemistry and heterogeneous photo-catalysis at semiconductors. *Journal of Photochemistry*, *10*(1), 59-75. https://doi.org/10.1016/0047-2670(79)80037-4

38 G. Segev, J. Kibsgaard, C. Hahn, Z. J. Xu, W.-H. Cheng, T. G. Deutsch, C. Xiang, J. Z. Zhang, L. Hammarström, D. G. Nocera, et al.F. Houle. (2022). The 2022 solar fuels roadmap. *J. Phys. D: Appl. Phys.*, *55*(32), 323003. https://doi.org/10.1088/1361-6463/ac6f97

39 G. F. Moore, & G. W. Brudvig. (2011). Energy conversion in photosynthesis: A paradigm for solar fuel production. *Annual Review of Condensed Matter Physics*, *2*(1), 303-327. https://doi.org/10.1146/annurev-conmatphys-062910-140503

40 H. Dau, C. Limberg, T. Reier, M. Risch, S. Roggan, & P. Strasser. (2010). The mechanism of water oxidation: from electrolysis via homogeneous to biological catalysis. *ChemCatChem*, *2*(7), 724-761. https://doi.org/10.1002/cctc.201000126

41 P. Yang, & J.-M. Tarascon. (2012). Towards systems materials engineering. *Nature Mater.*, *11*(7), 560-563. https://doi.org/10.1038/nmat3367

42 T. Guo, L. Li, & Z. Wang. (2022). Recent Development and Future Perspectives of Amorphous Transition Metal-Based Electrocatalysts for Oxygen Evolution Reaction. *Adv. Energy Mater.*, *12*(24), 2200827. https://doi.org/10.1002/aenm.202200827

43 Z.-Y. Yu, Y. Duan, X.-Y. Feng, X. Yu, M.-R. Gao, & S.-H. Yu. (2021). Clean and Affordable Hydrogen Fuel from Alkaline Water Splitting: Past, Recent Progress, and Future Prospects. *Adv. Mater.*, *33*(31), 2007100. https://doi.org/10.1002/adma.202007100

44 A. Ursua, L. M. Gandia, & P. Sanchis. (2012). Hydrogen Production From Water Electrolysis: Current Status and Future Trends. *Proceedings of the IEEE*, *100*(2), 410-426. https://doi.org/10.1109/JPROC.2011.2156750

45 J. C. Ehlers, A. A. Feidenhans'l, K. T. Therkildsen, & G. O. Larrazábal. (2023). Affordable Green Hydrogen from Alkaline Water Electrolysis: Key Research Needs from an Industrial Perspective. *ACS Energy Lett.*, *8*(3), 1502-1509. https://doi.org/10.1021/acsenergylett.2c02897

46 J. Kibsgaard, & I. Chorkendorff. (2019). Considerations for the scaling-up of water splitting catalysts. *Nat. Energy*, *4*(6), 430-433. https://doi.org/10.1038/s41560-019-0407-1

47 F. P. Lohmann-Richters, S. Renz, W. Lehnert, M. Müller, & M. Carmo. (2021). Review—Challenges and Opportunities for Increased Current Density in Alkaline Electrolysis by Increasing the Operating Temperature. *J. Electrochem. Soc.*, *168*(11). https://doi.org/10.1149/1945-7111/ac34cc

48 M. Carmo, D. L. Fritz, J. Mergel, & D. Stolten. (2013). A comprehensive review on PEM water electrolysis. *Int. J. Hydrog. Energy*, *38*(12), 4901-4934. https://doi.org/10.1016/j.ijhydene.2013.01.151

49 M. Chatenet, B. G. Pollet, D. R. Dekel, F. Dionigi, J. Deseure, P. Millet, R. D. Braatz, M. Z. Bazant, M. Eikerling, I. Staffell, P. Balcombe, Y. Shao-Horn, & H. Schäfer. (2022). Water electrolysis: from textbook knowledge to the latest scientific strategies and industrial developments. *Chem. Soc. Rev.*, *51*(11), 4583-4762. https://doi.org/10.1039/D0CS01079K

50 Y. Zhang, C. Wang, N. Wan, Z. Liu, & Z. Mao. (2007). Study on a novel manufacturing process of membrane electrode assemblies for solid polymer electrolyte water electrolysis. *Electrochem. commun.*, *9*(4), 667-670. https://doi.org/10.1016/j.elecom.2006.10.048

51 A. Buttler, & H. Spliethoff. (2018). Current status of water electrolysis for energy storage, grid balancing and sector coupling via power-to-gas and power-to-liquids: A review. *Renew. Sustain. Energy Rev.*, *82*, 2440-2454. https://doi.org/10.1016/j.rser.2017.09.003

52 R. Wu, B. Xiao, Q. Gao, Y.-R. Zheng, X.-S. Zheng, J.-F. Zhu, M.-R. Gao, & S.-H. Yu. (2018). A Janus Nickel Cobalt Phosphide Catalyst for High-Efficiency Neutral-pH Water Splitting. *Angew. Chem. Int. Ed.*, *57*(47), 15445-15449. https://doi.org/10.1002/anie.201808929

53 M. Plevová, J. Hnát, & K. Bouzek. (2021). Electrocatalysts for the oxygen evolution reaction in alkaline and neutral media. A comparative review. *J. Power Sources*, *507*, 230072. https://doi.org/10.1016/j.jpowsour.2021.230072

54 T. Shinagawa, M. T.-K. Ng, & K. Takanabe. (2017). Electrolyte Engineering towards Efficient Water Splitting at Mild pH. *ChemSusChem*, *10*(21), 4155-4162. https://doi.org/10.1002/cssc.201701266

55 J. M. Yu, J. Song, Y. K. Kim, J. Oh, K. Y. Kim, W. Y. Noh, W. J. Byun, J. U. Lee, C. Yang, J.-W. Jang, J. S. Lee, & S. Cho. (2023). High-Performance Electrochemical and Photoelectrochemical Water Splitting at Neutral pH by Ir Nanocluster-Anchored CoFe-Layered Double Hydroxide Nanosheets. *Nano Lett.* https://doi.org/10.1021/acs.nanolett.3c01024

56 A. S. Varela, M. Kroschel, T. Reier, & P. Strasser. (2016). Controlling the selectivity of CO_2 electroreduction on copper: The effect of the electrolyte concentration and the importance of the local pH. *Catalysis Today*, *260*, 8-13. https://doi.org/10.1016/j.cattod.2015.06.009

57 K. Klingan, T. Kottakkat, Z. P. Jovanov, S. Jiang, C. Pasquini, F. Scholten, P. Kubella, A. Bergmann, B. Cuenya, C. Roth, & H. Dau. (2018). Reactivity Determinants in Electrodeposited Cu Foams for Electrochemical CO_2 Reduction. *ChemSusChem*, *11*(19), 3449-3459. https://doi.org/10.1002/cssc.201801582

58 S. Jiang, L. D'Amario, & H. Dau. (2022). Copper Carbonate Hydroxide as Precursor of Interfacial CO in CO_2 Electroreduction. *ChemSusChem*, *15*(8), e202102506. https://doi.org/10.1002/cssc.202102506

59 H.-Y. Qu, X. He, Y. Wang, & S. Hou. (2021). Electrocatalysis for the Oxygen Evolution Reaction in Acidic Media: Progress and Challenges. *Appl. Sci.*, *11*(10). https://doi.org/10.3390/app11104320

60 E. Fabbri, & T. J. Schmidt. (2018). Oxygen Evolution Reaction—The Enigma in Water Electrolysis. *ACS Catal.*, *8*(10), 9765-9774. https://doi.org/10.1021/acscatal.8b02712

61 Z. Shi, X. Wang, J. Ge, C. Liu, & W. Xing. (2020). Fundamental understanding of the acidic oxygen evolution reaction: mechanism study and state-of-the-art catalysts. *Nanoscale*, *12*(25), 13249-13275. https://doi.org/10.1039/D0NR02410D

62 Q. Liang, G. Brocks, & A. Bieberle-Hütter. (2021). Oxygen evolution reaction (OER) mechanism under alkaline and acidic conditions. *J. Phys. Energy*, *3*(2), 026001. https://doi.org/10.1088/2515-7655/abdc85

63 T. Reier, H. N. Nong, D. Teschner, R. Schlögl, & P. Strasser. (2017). Electrocatalytic Oxygen Evolution Reaction in Acidic Environments – Reaction Mechanisms and Catalysts. *Adv. Energy Mater.*, *7*(1), 1601275. https://doi.org/10.1002/aenm.201601275

64 S. Y. Reece, J. A. Hamel, K. Sung, T. D. Jarvi, A. J. Esswein, J. J. H. Pijpers, & D. G. Nocera. (2011). Wireless solar water splitting using silicon-based semiconductors and earth-abundant catalysts. *Science*, *334*, 645-648 https://doi.org/10.1126/science.1209816

65 A. J. Esswein, Y. Surendranath, S. Y. Reece, & D. G. Nocera. (2011). Highly active cobalt phosphate and borate based oxygen evolving catalysts operating in neutral and natural waters. *Energy Environ. Sci.*, *4*(2), 499-504. http://dx.doi.org/10.1039/C0EE00518E

66 D. G. Nocera. (2009). Chemistry of personalized solar energy. *Inorg. Chem*, *48*(21), 10001-10017. https://doi.org/10.1021/ic901328v

67 J. Villalobos, D. González-Flores, R. Urcuyo, M. L. Montero, G. Schuck, P. Beyer, & M. Risch. (2021). Requirements for Beneficial Electrochemical Restructuring: A Model Study on a Cobalt Oxide in Selected Electrolytes. *Adv. Energy Mater.*, *11*(36), 2101737. https://doi.org/10.1002/aenm.202101737

68 L. Q. Zhou, C. Ling, H. Zhou, X. Wang, J. Liao, G. K. Reddy, L. Deng, T. C. Peck, R. Zhang, M. S. Whittingham, C. Wang, C.-W. Chu, Y. Yao, & H. Jia. (2019). A high-performance oxygen evolution catalyst in neutral-pH for sunlight-driven CO_2 reduction. *Nat. Commun.*, *10*(1), 4081. https://doi.org/10.1038/s41467-019-12009-8

69 J. Qi, W. Zhang, & R. Cao. (2018). Solar-to-Hydrogen Energy Conversion Based on Water Splitting. *Adv. Energy Mater.*, *8*(5), 1701620. https://doi.org/10.1002/aenm.201701620

70 M. W. Kanan, & D. G. Nocera. (2008). In situ formation of an oxygen-evolving catalyst in neutral water containing phosphate and Co^{2+}. *Science*, *321*(5892), 1072-1075. https://doi.org/10.1126/science.1162018

71 D. A. Lutterman, Y. Surendranath, & D. G. Nocera. (2009). A self-healing oxygen-evolving catalyst. *J. Am. Chem. Soc.*, *131*(11), 3838-3839. https://doi.org/10.1021/ja900023k

72 M. Tahir, L. Pan, F. Idrees, X. Zhang, L. Wang, J.-J. Zou, & Z. L. Wang. (2017). Electrocatalytic oxygen evolution reaction for energy conversion and storage: A comprehensive review. *Nano Energy*, *37*, 136-157. https://doi.org/10.1016/j.nanoen.2017.05.022

73 R.-Y. Fan, J.-Y. Xie, N. Yu, Y.-M. Chai, & B. Dong. (2022). Interface design and composition regulation of cobalt-based electrocatalysts for oxygen evolution reaction. *Int. J. Hydrog. Energy*, *47*(19), 10547-10572. https://doi.org/10.1016/j.ijhydene.2021.12.239

74 J. Li. (2022). Oxygen Evolution Reaction in Energy Conversion and Storage: Design Strategies Under and Beyond the Energy Scaling Relationship. *Nano-Micro Letters*, *14*(1), 112. https://doi.org/10.1007/s40820-022-00857-x

75 J. Park, S. Lee, & S. Kim. (2022). Recent advances in amorphous electrocatalysts for oxygen evolution reaction. *Front. Chem.*, *10*. https://doi.org/10.3389/fchem.2022.1030803

76 M. Yu, E. Budiyanto, & H. Tüysüz. (2022). Principles of Water Electrolysis and Recent Progress in Cobalt-, Nickel-, and Iron-Based Oxides for the Oxygen Evolution Reaction. *Angew. Chem. Int. Ed.*, *61*(1), e202103824. https://doi.org/10.1002/anie.202103824

77 C. Wei, R. R. Rao, J. Peng, B. Huang, I. E. L. Stephens, M. Risch, Z. J. Xu, & Y. Shao-Horn. (2019). Recommended Practices and Benchmark Activity for Hydrogen and Oxygen Electrocatalysis in Water Splitting and Fuel Cells. *Adv. Mater.*, *31*(31), 1806296. https://doi.org/10.1002/adma.201806296

78 C. Wei, & Z. J. Xu. (2018). The Comprehensive Understanding of as an Evaluation Parameter for Electrochemical Water Splitting. *Small Methods*, *2*(11), 1800168. https://doi.org/10.1002/smtd.201800168

79 M. C. Lefebvre. (2002). Establishing the link between multistep electrochemical reaction mechanisms and experimental Tafel slopes. In B. E. Conway, J. O. Bockris, & R. E. White (Eds.), *Modern Aspects of Electrochemistry* (Vol. 32). Springer. https://doi.org/10.1007/0-306-46916-2_3

80 Y.-H. Fang, & Z.-P. Liu. (2010). Mechanism and Tafel Lines of Electro-Oxidation of Water to Oxygen on RuO_2(110). *J. Am. Chem. Soc.*, *132*(51), 18214-18222. https://doi.org/10.1021/ja1069272

81 D. Antipin, & M. Risch. (2022). Calculation of the Tafel slope and reaction order of the oxygen evolution reaction between pH 12 and pH 14 for the adsorbate mechanism. *Electrochemical Science Advances*, *00*, e2100213. https://doi.org/10.1002/elsa.202100213

82 H. Prats, & K. Chan. (2021). The determination of the HOR/HER reaction mechanism from experimental kinetic data. *Phys. Chem. Chem. Phys.*, *23*(48), 27150-27158. https://doi.org/10.1039/D1CP04134G

83 L. Han, S. Dong, & E. Wang. (2016). Transition-Metal (Co, Ni, and Fe)-Based Electrocatalysts for the Water Oxidation Reaction. *Adv. Mater.*, *28*(42), 9266-9291. https://doi.org/10.1002/adma.201602270

84 H. Feizi, R. Bagheri, Z. Song, J.-R. Shen, S. I. Allakhverdiev, & M. M. Najafpour. (2019). Cobalt/Cobalt Oxide Surface for Water Oxidation. *ACS Sustainable Chemistry & Engineering*, *7*(6), 6093-6105. https://doi.org/10.1021/acssuschemeng.8b06269

85 M. Corva, N. Blanc, C. J. Bondue, & K. Tschulik. (2022). Differential Tafel Analysis: A Quick and Robust Tool to Inspect and Benchmark Charge Transfer in Electrocatalysis. *ACS Catal.*, *12*(21), 13805-13812. https://doi.org/10.1021/acscatal.2c03581

86 N. Blanc, C. Rurainsky, & K. Tschulik. (2020). Implications of resistance and mass transport limitations on the common Tafel approach at composite catalyst thin-film electrodes. *J. Electroanal. Chem.*, *872*, 114345. https://doi.org/10.1016/j.jelechem.2020.114345

87 P. Khadke, T. Tichter, T. Boettcher, F. Muench, W. Ensinger, & C. Roth. (2021). A simple and effective method for the accurate extraction of kinetic parameters using differential Tafel plots. *Sci. Rep.*, *11*(1), 8974. https://doi.org/10.1038/s41598-021-87951-z

88 C. Batchelor-McAuley, D. Li, & R. G. Compton. (2020). Mass-Transport-Corrected Transfer Coefficients: A Fully General Approach. *ChemElectroChem*, *7*(18), 3844-3851. https://doi.org/10.1002/celc.202001107

89 A. J. Bard, L. R. Faulkner, & H. S. White. (2022). *Electrochemical methods: fundamentals and applications*. John Wiley & Sons.

90 W. Schmickler, & E. Santos. (2010). *Interfacial Electrochemistry*. Springer. https://books.google.de/books?id=EM72sgEACAAJ

91 R. Guidelli, R. G. Compton, J. M. Feliu, E. Gileadi, J. Lipkowski, W. Schmickler, & S. Trasatti. (2014). Defining the transfer coefficient in electrochemistry: An assessment (IUPAC Technical Report). *86*(2), 245-258. https://doi.org/doi:10.1515/pac-2014-5026 (Pure and Applied Chemistry)

92 A. Holewinski, & S. Linic. (2012). Elementary Mechanisms in Electrocatalysis: Revisiting the ORR Tafel Slope. *J. Electrochem. Soc.*, *159*(11), H864. https://doi.org/10.1149/2.022211jes

93 S. Palchoudhury, M. Baalousha, & J. R. Lead. (2015). Chapter 5 - Methods for Measuring Concentration (Mass, Surface Area and Number) of Nanomaterials. In M. Baalousha & J. R. Lead (Eds.), *Frontiers of Nanoscience* (Vol. 8, pp. 153-181). Elsevier. https://doi.org/10.1016/B978-0-08-099948-7.00005-1

94 R. D. Holbrook, A. A. Galyean, J. M. Gorham, A. Herzing, & J. Pettibone. (2015). Chapter 2 - Overview of Nanomaterial Characterization and Metrology. In M. Baalousha & J. R. Lead (Eds.), *Frontiers of Nanoscience* (Vol. 8, pp. 47-87). Elsevier. https://doi.org/10.1016/B978-0-08-099948-7.00002-6

95 C. C. L. McCrory, S. Jung, J. C. Peters, & T. F. Jaramillo. (2013). Benchmarking heterogeneous electrocatalysts for the oxygen evolution reaction. *J. Am. Chem. Soc.*, *135*(45), 16977-16987. https://doi.org/10.1021/ja407115p

96 V. D. Jović, B. M. Jović, U. Č. Lačnjevac, N. V. Krstajić, P. Zabinski, & N. R. Elezović. (2018). Accelerated service life test of electrodeposited NiSn alloys as bifunctional catalysts for alkaline water electrolysis under industrial operating conditions. *J. Electroanal. Chem.*, *819*, 16-25. https://doi.org/10.1016/j.jelechem.2017.06.011

97 S. Anantharaj, P. E. Karthik, & S. Noda. (2021). The Significance of Properly Reporting Turnover Frequency in Electrocatalysis Research. *Angew. Chem. Int. Ed.*, *60*(43), 23051-23067. https://doi.org/10.1002/anie.202110352

98 S. Kozuch, & J. M. L. Martin. (2012). “Turning Over” Definitions in Catalytic Cycles. *ACS Catal.*, *2*(12), 2787-2794. https://doi.org/10.1021/cs3005264

99 K. Klingan, F. Ringleb, I. Zaharieva, J. Heidkamp, P. Chernev, D. Gonzalez-Flores, M. Risch, A. Fischer, & H. Dau. (2014). Water oxidation by amorphous cobalt-based oxides: Volume activity and proton transfer to electrolyte bases. *ChemSusChem*, *7*(5), 1301–1310. https://doi.org/10.1002/cssc.201301019

100 S. Anantharaj, S. R. Ede, K. Sakthikumar, K. Karthick, S. Mishra, & S. Kundu. (2016). Recent Trends and Perspectives in Electrochemical Water Splitting with an Emphasis on Sulfide, Selenide, and Phosphide Catalysts of Fe, Co, and Ni: A Review. *ACS Catal.*, *6*(12), 8069-8097. https://doi.org/10.1021/acscatal.6b02479

101 I. S. Filimonenkov, S. Y. Istomin, E. V. Antipov, G. A. Tsirlina, & E. R. Savinova. (2018). Rotating ring-disk electrode as a quantitative tool for the investigation of the oxygen evolution reaction. *Electrochim. Acta*, *286*, 304-312. https://doi.org/10.1016/j.electacta.2018.08.056

102 M. Rana, S. Mondal, L. Sahoo, K. Chatterjee, P. E. Karthik, & U. K. Gautam. (2018). Emerging Materials in Heterogeneous Electrocatalysis Involving Oxygen for Energy Harvesting. *ACS Appl. Mater. Interfaces*, *10*(40), 33737-33767. https://doi.org/10.1021/acsami.8b09024

103 K. Zhang, & R. Zou. (2021). Advanced Transition Metal-Based OER Electrocatalysts: Current Status, Opportunities, and Challenges. *Small*, *17*(37), 2100129. https://doi.org/10.1002/smll.202100129

104 A. Indra, P. W. Menezes, N. R. Sahraie, A. Bergmann, C. Das, M. Tallarida, D. Schmeißer, P. Strasser, & M. Driess. (2014). Unification of Catalytic Water Oxidation and Oxygen Reduction Reactions: Amorphous Beat Crystalline Cobalt Iron Oxides. *J. Am. Chem. Soc.*, *136*(50), 17530-17536. https://doi.org/10.1021/ja509348t

105 D. Gonzalez-Flores, I. Sanchez, I. Zaharieva, K. Klingan, J. Heidkamp, P. Chernev, P. W. Menezes, M. Driess, H. Dau, & M. L. Montero. (2015). Heterogeneous water oxidation: surface activity versus amorphization activation in cobalt phosphate catalysts. *Angew. Chem. Int. Ed.*, *54*(8), 2472-2476. https://doi.org/10.1002/anie.201409333

106 W. Cai, R. Chen, H. Yang, H. B. Tao, H.-Y. Wang, J. Gao, W. Liu, S. Liu, S.-F. Hung, & B. Liu. (2020). Amorphous versus Crystalline in Water Oxidation Catalysis: A Case Study of NiFe Alloy. *Nano Lett.*, *20*(6), 4278-4285. https://doi.org/10.1021/acs.nanolett.0c00840

107 J. N. Hausmann, S. Mebs, H. Dau, M. Driess, & P. W. Menezes. (2022). Oxygen Evolution Activity of Amorphous Cobalt Oxyhydroxides: Interconnecting Precatalyst Reconstruction, Long-Range Order, Buffer-Binding, Morphology, Mass Transport, and Operation Temperature. *Adv. Mater.*, *34*(50), 2207494. https://doi.org/10.1002/adma.202207494

108 J. Liu, & L. Guo. (2021). In situ self-reconstruction inducing amorphous species: A key to electrocatalysis. *Matter*, *4*(9), 2850-2873. https://doi.org/10.1016/j.matt.2021.05.025

109 S. Anantharaj, & S. Noda. (2020). Amorphous Catalysts and Electrochemical Water Splitting: An Untold Story of Harmony. *Small*, *16*(2), e1905779. https://doi.org/10.1002/smll.201905779

110 M. Risch, F. Ringleb, V. Khare, P. Chernev, I. Zaharieva, & H. Dau. (2009). Characterisation of a water-oxidizing Co-film by XAFS. *J. Physics: Conf. Series*, *190*, 012167. https://doi.org/10.1088/1742-6596/190/1/012167

111 Y. Surendranath, M. Dinca, & D. G. Nocera. (2009). Electrolyte-dependent electrosynthesis and activity of cobalt-based water oxidation catalysts. *J. Am. Chem. Soc.*, *131*(7), 2615-2620. https://doi.org/10.1021/ja807769r

112 M. Risch, V. Khare, I. Zaharieva, L. Gerencser, P. Chernev, & H. Dau. (2009). Cobalt-oxo core of a water-oxidizing catalyst film. *J. Am. Chem. Soc.*, *131*(20), 6936-6937. https://doi.org/10.1021/Ja902121f

113 Y. Surendranath, M. W. Kanan, & D. G. Nocera. (2010). Mechanistic studies of the oxygen evolution reaction by a cobalt-phosphate catalyst at neutral pH. *J. Am. Chem. Soc.*, *132*(46), 16501-16509. https://doi.org/10.1021/ja106102b

114 J. B. Gerken, E. C. Landis, R. J. Hamers, & S. S. Stahl. (2010). Fluoride-modulated cobalt catalysts for electrochemical oxidation of water under non-alkaline conditions. *ChemSusChem*, *3*(10), 1176-1179. https://doi.org/10.1002/cssc.201000161

115 E. R. Young, D. G. Nocera, & V. Bulovic. (2010). Direct formation of a water oxidation catalyst from thin-film cobalt. *Energy Environ. Sci.*, *3*(11), 1726-1728. https://doi.org/10.1039/c0ee00177e

116 J. G. McAlpin, Y. Surendranath, M. Dincă, T. A. Stich, S. A. Stoian, W. H. Casey, D. G. Nocera, & R. D. Britt. (2010). EPR evidence for Co(IV) species produced during water oxidation at neutral pH [doi: 10.1021/ja1013344]. *J. Am. Chem. Soc.*, *132*(20), 6882-6883. https://doi.org/10.1021/ja1013344

117 M. W. Kanan, J. Yano, Y. Surendranath, M. Dincă, V. K. Yachandra, & D. G. Nocera. (2010). Structure and Valency of a Cobalt−Phosphate Water Oxidation Catalyst Determined by in Situ X-ray Spectroscopy. *J. Am. Chem. Soc.*, *132*(39), 13692-13701. https://doi.org/10.1021/ja1023767

118 J. B. Gerken, J. G. McAlpin, J. Y. C. Chen, M. L. Rigsby, W. H. Casey, R. D. Britt, & S. S. Stahl. (2011). Electrochemical water oxidation with cobalt-based electrocatalysts from pH 0–14: The thermodynamic basis for catalyst structure, stability, and activity. *J. Am. Chem. Soc.*, *133*(36), 14431-14442. https://doi.org/10.1021/ja205647m

119 M. D. Symes, Y. Surendranath, D. A. Lutterman, & D. G. Nocera. (2011). Bidirectional and unidirectional PCET in a molecular model of a cobalt-based oxygen-evolving catalyst. *J. Am. Chem. Soc.*, *133*(14), 5174–5177. https://doi.org/10.1021/ja110908v

120 G. Mattioli, M. Risch, M. A. Bonapasta, H. Dau, & L. Guidoni. (2011). Protonation states in a cobalt-oxide catalyst for water oxidation: Fine comparison of ab initio molecular dynamics and X-ray absorption spectroscopy results. *Phys. Chem. Chem. Phys.*, *13*, 15437-15441. https://doi.org/10.1039/c1cp21776c

121 Y. Surendranath, D. A. Lutterman, Y. Liu, & D. G. Nocera. (2012). Nucleation, growth, and repair of a cobalt-based oxygen evolving catalyst. *J. Am. Chem. Soc.*, *134*(14), 6326-6336. https://doi.org/10.1021/ja3000084

122 P. W. Du, O. Kokhan, K. W. Chapman, P. J. Chupas, & D. M. Tiede. (2012). Elucidating the domain structure of the cobalt oxide water splitting catalyst by X-ray pair distribution function analysis. *J. Am. Chem. Soc.*, *134*(27), 11096-11099. https://doi.org/10.1021/ja303826a

123 M. Risch, K. Klingan, F. Ringleb, P. Chernev, I. Zaharieva, A. Fischer, & H. Dau. (2012). Water oxidation by electrodeposited cobalt oxides - role of anions and redox-inert cations in structure and function of the amorphous catalyst. *ChemSusChem*, *5*(3), 542-549. https://doi.org/10.1002/cssc.201100574

124 D. K. Bediako, C. Costentin, E. C. Jones, D. G. Nocera, & J.-M. Savéant. (2013). Proton–Electron Transport and Transfer in Electrocatalytic Films. Application to a Cobalt-Based O_2-Evolution Catalyst. *J. Am. Chem. Soc.*, *135*(28), 10492-10502. https://doi.org/10.1021/ja403656w

125 M. Risch, K. Klingan, I. Zaharieva, & H. Dau. (2014). Water Oxidation by Co-Based Oxides with Molecular Properties. In A. Llobet (Ed.), *Molecular Water Oxidation Catalysis* (pp. 163-185). Wiley. https://doi.org/10.1002/9781118698648.ch9

126 M. Risch, F. Ringleb, M. Kohlhoff, P. Bogdanoff, P. Chernev, I. Zaharieva, & H. Dau. (2015). Water oxidation by amorphous cobalt-based oxides: in situ tracking of redox transitions and mode of catalysis. *Energy Environ. Sci.*, *8*(2), 661-674. https://doi.org/10.1039/C4ee03004d

127 H. S. Ahn, & A. J. Bard. (2015). Surface Interrogation of CoPi Water Oxidation Catalyst by Scanning Electrochemical Microscopy. *J. Am. Chem. Soc.*, *137*(2), 612-615. https://doi.org/10.1021/ja511740h

128 C. Costentin, T. R. Porter, & J.-M. Saveant. (2016). Conduction and Reactivity in Heterogeneous-Molecular Catalysis: New Insights in Water Oxidation Catalysis by Phosphate Cobalt Oxide Films. *J. Am. Chem. Soc.*, *138*(17), 5615-5622. https://doi.org/10.1021/jacs.6b00737

129 S. A. Bonke, A. M. Bond, L. Spiccia, & A. N. Simonov. (2016). Parameterization of Water Electrooxidation Catalyzed by Metal Oxides Using Fourier Transformed Alternating Current Voltammetry. *J. Am. Chem. Soc.*, *138*(49), 16095-16104. https://doi.org/10.1021/jacs.6b10304

130 M. Yoshida, T. Mineo, Y. Mitsutomi, F. Yamamoto, H. Kurosu, S. Takakusagi, K. Asakura, & H. Kondoh. (2015). Structural Relationship between CoO_6 Cluster and Phosphate Species in a Cobalt–Phosphate Water Oxidation Catalyst Investigated by Co and P K-edge XAFS. *Chem. Lett.*, *45*(3), 277-279. https://doi.org/10.1246/cl.151073

131 A. M. Ullman, C. N. Brodsky, N. Li, S.-l. Zheng, & D. G. Nocera. (2016). Probing Edge Site Reactivity of Oxidic Cobalt Water Oxidation Catalysts. *J. Am. Chem. Soc.*, *138*, 4229−4236. https://doi.org/10.1021/jacs.6b00762

132 C. Costentin, & D. G. Nocera. (2017). Self-healing catalysis in water. *Proc. Natl. Acad. Sci. U.S.A.*, *114*(51), 13380-13384. https://doi.org/10.1073/pnas.1711836114

133 G. Kwon, H. Jang, J.-S. Lee, A. Mane, D. J. Mandia, S. R. Soltau, L. M. Utschig, A. B. F. Martinson, D. M. Tiede, H. Kim, & J. Kim. (2018). Resolution of Electronic and Structural Factors Underlying Oxygen-Evolving Performance in Amorphous Cobalt Oxide Catalysts. *J. Am. Chem. Soc.*, *140*(34), 10710-10720. https://doi.org/10.1021/jacs.8b02719

134 C. Pasquini, I. Zaharieva, D. Gonzalez-Flores, P. Chernev, M. R. Mohammadi, L. Guidoni, R. D. L. Smith, & H. Dau. (2019). H/D Isotope effects reveal factors controlling catalytic activity in Co-based oxides for water oxidation. *J. Am. Chem. Soc.*, *141*(7), 2938-2948. https://doi.org/10.1021/jacs.8b10002

135 H. Dau, & C. Pasquini. (2019). Modelling the (essential) role of proton transport by electrolyte bases for electrochemical water oxidation at near-neutral pH. *Inorganics*, *7*(2), 20. https://doi.org/10.3390/inorganics7020020

136 Y. Kutin, N. Cox, W. Lubitz, A. Schnegg, & O. Rüdiger. (2019). In Situ EPR Characterization of a Cobalt Oxide Water Oxidation Catalyst at Neutral pH. *Catalysts*, *9*(11), 926. https://doi.org/10.3390/catal9110926

137 C. J. Eom, & J. Suntivich. (2019). In Situ Stimulated Raman Spectroscopy Reveals the Phosphate Network in the Amorphous Cobalt Oxide Catalyst and Its Role in the Catalyst Formation. *J. Phys. Chem. C*, *123*(48), 29284-29290. https://doi.org/10.1021/acs.jpcc.9b10308

138 C. N. Brodsky, D. K. Bediako, C. Shi, T. P. Keane, C. Costentin, S. J. L. Billinge, & D. G. Nocera. (2019). Proton–Electron Conductivity in Thin Films of a Cobalt–Oxygen Evolving Catalyst. *ACS Appl. Mater. Interfaces*, *2*(1), 3-12. https://doi.org/10.1021/acsaem.8b00785

139 C. Pasquini, L. D'Amario, I. Zaharieva, & H. Dau. (2020). Operando Raman spectroscopy tracks oxidation-state changes in an amorphous Co oxide material for electrocatalysis of the oxygen evolution reaction. *J. Chem. Phys.*, *152*(19), 194202. https://doi.org/10.1063/5.0006306

140 M. R. Mohammadi, S. Loos, P. Chernev, C. Pasquini, I. Zaharieva, D. Gonzalez-Flores, P. Kubella, K. Klingan, R. D. L. Smith, & H. Dau. (2020). Exploring the Limits of Self-Repair in Cobalt Oxide Films for Electrocatalytic Water Oxidation. *ACS Catal.*, *10*(14), 7990-7999. https://doi.org/10.1021/acscatal.0c01944

141 C. Lang, J. Li, K. R. Yang, Y. Wang, D. He, J. E. Thorne, S. Croslow, Q. Dong, Y. Zhao, G. Prostko, G. W. Brudvig, V. S. Batista, M. M. Waegele, & D. Wang. (2021). Observation of a potential-dependent switch of water-oxidation mechanism on Co-oxide-based catalysts. *Chem*, *7*(8), 2101-2117. https://doi.org/10.1016/j.chempr.2021.03.015

142 S. Liu, I. Zaharieva, L. D'Amario, S. Mebs, P. Kubella, F. Yang, P. Beyer, M. Haumann, & H. Dau. (2022). Electrocatalytic Water Oxidation at Neutral pH–Deciphering the Rate Constraints for an Amorphous Cobalt-Phosphate Catalyst System. *Adv. Energy Mater.*, *12*(46), 2202914. https://doi.org/10.1002/aenm.202202914

143 S. Liu, S. Farhoosh, P. Beyer, S. Mebs, I. Zaharieva, M. Haumann, & H. Dau. (2023). Role of Potassium in Electrocatalytic Water Oxidation Investigated in a Volume-Active Cobalt Material at Neutral pH. *Advanced Sustainable Systems*, *7*, 2300008. https://doi.org/10.1002/adsu.202300008

144 T. R. Cook, D. K. Dogutan, S. Y. Reece, Y. Surendranath, T. S. Teets, & D. G. Nocera. (2010). Solar energy supply and storage for the legacy and nonlegacy worlds. *Chem. Rev.*, *110*(11), 6474-6502. https://doi.org/10.1021/cr100246c

145 M. W. Kanan, Y. Surendranath, & D. G. Nocera. (2009). Cobalt–phosphate oxygen-evolving compound. *Chem. Soc. Rev.*, *38*(1), 109-114. https://doi.org/10.1039/B802885K

146 J. J. H. Pijpers, M. T. Winkler, Y. Surendranath, T. Buonassisi, & D. G. Nocera. (2011). Light-induced water oxidation at silicon electrodes functionalized with a cobalt oxygen-evolving catalyst. *Proc. Natl. Acad. Sci. U.S.A.*, *108*(25), 10056-10061. https://doi.org/10.1073/pnas.1106545108

147 J. P. McEvoy, & G. W. Brudvig. (2006). Water-splitting chemistry of photosystem II. *Chem. Rev.*, *106*(11), 4455-4483. https://doi.org/10.1021/cr0204294

148 Y. Umena, K. Kawakami, J.-R. Shen, & N. Kamiya. (2011). Crystal structure of oxygen-evolving photosystem II at a resolution of 1.9 Å. *Nature*, *473*, 55-60. https://doi.org/10.1038/nature09913

149 K. N. Ferreira, T. M. Iverson, K. Maghlaoui, J. Barber, & S. Iwata. (2004). Architecture of the photosynthetic oxygen-evolving center. *Science*, *303*, 1831-1838. https://doi.org/10.1126/science.1093087

150 M. Dincă, Y. Surendranath, & D. G. Nocera. (2010). Nickel-borate oxygen-evolving catalyst that functions under benign conditions. *Proceedings of the National Academy of Sciences, USA*, *107*(23), 10337-10341. https://doi.org/10.1073/pnas.1001859107

151 D. K. Bediako, B. Lassalle-Kaiser, Y. Surendranath, J. Yano, V. K. Yachandra, & D. G. Nocera. (2012). Structure–Activity Correlations in a Nickel–Borate Oxygen Evolution Catalyst. *J. Am. Chem. Soc.*, *134*(15), 6801-6809. https://doi.org/10.1021/ja301018q

152 I. Zaharieva, P. Chernev, M. Risch, K. Klingan, M. Kohlhoff, A. Fischer, & H. Dau. (2012). Electrosynthesis, functional, and structural characterization of a water-oxidizing manganese oxide. *Energy Environ. Sci.*, *5*(5), 7081-7089. https://doi.org/10.1039/C2EE21191B

153 I. Zaharieva, M. M. Najafpour, M. Wiechen, M. Haumann, P. Kurz, & H. Dau. (2011). Synthetic manganese–calcium oxides mimic the water-oxidizing complex of photosynthesis functionally and structurally. *Energy Environ. Sci.*, *4*(7), 2400-2408. https://doi.org/10.1039/C0EE00815J

154 M. Risch, K. Klingan, J. Heidkamp, D. Ehrenberg, P. Chernev, I. Zaharieva, & H. Dau. (2011). Nickel-oxido structure of a water-oxidizing catalyst film. *Chem. Commun.*, *47*(43), 11912-11914. https://doi.org/10.1039/C1CC15072C

155 R. S. Khnayzer, M. W. Mara, J. Huang, M. L. Shelby, L. X. Chen, & F. N. Castellano. (2012). Structure and activity of photochemically deposited "CoPi" oxygen evolving catalyst on titania. *ACS Catal.*, *2*(10), 2150-2160. https://doi.org/10.1021/cs3005192

156 D. K. Zhong, & D. R. Gamelin. (2010). Photoelectrochemical water oxidation by cobalt catalyst ("Co−P_i")/α-Fe_2O_3 composite photoanodes: Oxygen evolution and resolution of a kinetic bottleneck. *J. Am. Chem. Soc.*, *132*(12), 4202-4207. https://doi.org/10.1021/ja908730h

157 E. A. Sprague-Klein, X. He, M. W. Mara, B. J. Reinhart, S. Lee, L. M. Utschig, K. L. Mulfort, L. X. Chen, & D. M. Tiede. (2022). Photo-electrochemical Effect in the Amorphous Cobalt Oxide Water Oxidation Catalyst Cobalt–Phosphate (CoPi). *ACS Energy Lett.*, *7*(9), 3129-3138. https://doi.org/10.1021/acsenergylett.2c01560

158 M. W. Kanan, J. Yano, Y. Surendranath, M. Dinca, V. K. Yachandra, & D. G. Nocera. (2010). Structure and valency of a cobalt-phosphate water oxidation catalyst determined by in situ X-ray spectroscopy. *J. Am. Chem. Soc.*, *132*(39), 13692-13701. https://doi.org/10.1021/Ja1023767

159 C. L. Farrow, D. K. Bediako, Y. Surendranath, D. G. Nocera, & S. J. L. Billinge. (2013). Intermediate-Range Structure of Self-Assembled Cobalt-Based Oxygen-Evolving Catalyst. *J. Am. Chem. Soc.*, *135*(17), 6403-6406. https://doi.org/10.1021/ja401276f

160 M. Zhang, M. de Respinis, & H. Frei. (2014). Time-resolved observations of water oxidation intermediates on a cobalt oxide nanoparticle catalyst. *Nature Chem.*, *6*(4), 362-367. https://doi.org/10.1038/Nchem.1874

161 X. Li, & P. E. M. Siegbahn. (2013). Water Oxidation Mechanism for Synthetic Co–Oxides with Small Nuclearity. *J. Am. Chem. Soc.*, *135*(37), 13804-13813. https://doi.org/10.1021/ja4053448

162 S. Koroidov, M. F. Anderlund, S. Styring, A. Thapper, & J. Messinger. (2015). First turnover analysis of water-oxidation catalyzed by Co-oxide nanoparticles. *Energy Environ. Sci.*, *8*, 2492--2503. https://doi.org/10.1039/C5EE00700C

163 A. I. Nguyen, M. S. Ziegler, P. Oña-Burgos, M. Sturzbecher-Hohne, W. Kim, D. E. Bellone, & T. D. Tilley. (2015). Mechanistic Investigations of Water Oxidation by a Molecular Cobalt Oxide Analogue: Evidence for a Highly Oxidized Intermediate and Exclusive Terminal Oxo Participation. *J. Am. Chem. Soc.*, *137*(40), 12865-12872. https://doi.org/10.1021/jacs.5b08396

164 G. Mattioli, P. Giannozzi, A. Amore Bonapasta, & L. Guidoni. (2013). Reaction pathways for oxygen evolution promoted by cobalt catalyst. *J. Am. Chem. Soc.*, *135*(41), 15353-15363. https://doi.org/10.1021/ja401797v

165 L.-P. Wang, & T. Van Voorhis. (2011). Direct-coupling O_2 bond forming a pathway in cobalt oxide water oxidation catalysts. *J. Phys. Chem. Lett.*, *2*(17), 2200-2204. https://doi.org/10.1021/jz201021n

166 X. L. Hu, S. Piccinin, A. Laio, & S. Fabris. (2012). Atomistic Structure of Cobalt-Phosphate Nanoparticles for Catalytic Water Oxidation. *ACS Nano*, *6*(12), 10497-10504. https://doi.org/10.1021/nn3044325

167 D. K. Bediako, Y. Surendranath, & D. G. Nocera. (2013). Mechanistic studies of the oxygen evolution reaction mediated by a nickel–borate thin film electrocatalyst. *J. Am. Chem. Soc.* https://doi.org/10.1021/ja3126432

168 S. J. Harley, H. E. Mason, J. G. McAlpin, R. D. Britt, & W. H. Casey. (2012). A ^{31}P NMR investigation of the CoP_i water-oxidation catalyst. *Chem. Eur. J.*, *18*(34), 10476-10479. https://doi.org/10.1002/chem.201201292

169 J. Villalobos, D. Gonzalez-Flores, K. Klingan, P. Chernev, P. Kubella, R. Urcuyo, C. Pasquini, M. R. Mohammadi, R. D. L. Smith, M. L. Montero, & H. Dau. (2019). Structural and functional role of anions in electrochemical water oxidation probed by arsenate incorporation into cobalt-oxide materials. *Phys. Chem. Chem. Phys.*, *21*(23), 12485-12493. https://doi.org/10.1039/c9cp01754b

170 Y. Liu, & D. G. Nocera. (2014). Spectroscopic Studies of Nanoparticulate Thin Films of a Cobalt-Based Oxygen Evolution Catalyst. *J. Phys. Chem. C*, *118*(30), 17060-17066. https://doi.org/10.1021/jp5008347

171 Z. W. Seh, J. Kibsgaard, C. F. Dickens, I. Chorkendorff, J. K. Nørskov, & T. F. Jaramillo. (2017). Combining theory and experiment in electrocatalysis: Insights into materials design. *Science*, *355*(6321), 4998–5009. https://doi.org/10.1126/science.aad4998

172 J. K. Norskov, T. Bligaard, J. Rossmeisl, & C. H. Christensen. (2009). Towards the computational design of solid catalysts. *Nature Chem.*, *1*(1), 37-46. https://doi.org/10.1038/Nchem.121

173 R. Ramesh, S. Lee, S. Kim, J. Park, S. Lee, M. S. Kim, M. Baek, K. Yong, Y. Ye, & J. Lee. (2018). Oxygen Evolution Reaction on Ni-based Two-dimensional (2D) Titanate Nanosheets: Investigation on Effect of Fe Co-doping and Fe Incorporation from Electrolyte on the Activity. *ChemistrySelect*, *3*(18), 5130-5137. https://doi.org/10.1002/slct.201800594

174 S. Youk, J. Hwang, S. Lee, M. S. Kim, & J. Lee. (2019). Controlled Leaching Derived Synthesis of Atomically Dispersed/Clustered Gold on Mesoporous Cobalt Oxide for Enhanced Oxygen Evolution Reaction Activity. *Small Methods*, *3*(9), 1800293. https://doi.org/10.1002/smtd.201800293

175 P. W. Menezes, A. Indra, A. Bergmann, P. Chernev, C. Walter, H. Dau, P. Strasser, & M. Driess. (2016). Uncovering the prominent role of metal ions in octahedral versus tetrahedral sites of cobalt–zinc oxide catalysts for efficient oxidation of water. *J. Mater. Chem. A*, *4*(25), 10014-10022. https://doi.org/10.1039/C6TA03644A

176 H. Kim, J. Park, I. Park, K. Jin, S. E. Jerng, S. H. Kim, K. T. Nam, & K. Kang. (2015). Coordination tuning of cobalt phosphates towards efficient water oxidation catalyst. *Nat. Commun.*, *6*(1), 8253. https://doi.org/10.1038/ncomms9253

177 Y. Chen, J. K. Seo, Y. Sun, T. A. Wynn, M. Olguin, M. Zhang, J. Wang, S. Xi, Y. Du, K. Yuan, et al.Z. J. Xu. (2022). Enhanced oxygen evolution over dual corner-shared cobalt tetrahedra. *Nat. Commun.*, *13*(1), 5510. https://doi.org/10.1038/s41467-022-33000-w

178 P. W. Menezes, C. Panda, C. Walter, M. Schwarze, & M. Driess. (2019). A Cobalt-Based Amorphous Bifunctional Electrocatalysts for Water-Splitting Evolved from a Single-Source Lazulite Cobalt Phosphate. *Adv. Func. Mater.*, *29*(32), 1808632. https://doi.org/10.1002/adfm.201808632

179 J. Suntivich, K. J. May, H. A. Gasteiger, J. B. Goodenough, & Y. Shao-Horn. (2011). A perovskite oxide optimized for oxygen evolution catalysis from molecular orbital principles. *Science*, *334*, 1383-1385. https://doi.org/10.1126/science.1212858

180 J. Hwang, R. R. Rao, L. Giordano, Y. Katayama, Y. Yu, & Y. Shao-Horn. (2017). Perovskites in catalysis and electrocatalysis. *Science*, *358*(6364), 751-756. https://doi.org/10.1126/science.aam7092

181 S. Chen, Z. Kang, X. Hu, X. Zhang, H. Wang, J. Xie, X. Zheng, W. Yan, B. Pan, & Y. Xie. (2017). Delocalized Spin States in 2D Atomic Layers Realizing Enhanced Electrocatalytic Oxygen Evolution. *Adv. Mater.*, *29*(30), 1701687. https://doi.org/10.1002/adma.201701687

182 M. S. Burke, M. G. Kast, L. Trotochaud, A. M. Smith, & S. W. Boettcher. (2015). Cobalt–Iron (Oxy)hydroxide Oxygen Evolution Electrocatalysts: The Role of Structure and Composition on Activity, Stability, and Mechanism. *J. Am. Chem. Soc.*, *137*(10), 3638-3648. https://doi.org/10.1021/jacs.5b00281

183 Z.-P. Wu, H. Zhang, S. Zuo, Y. Wang, S. L. Zhang, J. Zhang, S.-Q. Zang, & X. W. Lou. (2021). Manipulating the Local Coordination and Electronic Structures for Efficient Electrocatalytic Oxygen Evolution. *Adv. Mater.*, *33*(40), 2103004. https://doi.org/10.1002/adma.202103004

184 Y. Meng, W. Song, H. Huang, Z. Ren, S.-Y. Chen, & S. L. Suib. (2014). Structure–Property Relationship of Bifunctional MnO_2 Nanostructures: Highly Efficient, Ultra-Stable Electrochemical Water Oxidation and Oxygen Reduction Reaction Catalysts

Identified in Alkaline Media. *J. Am. Chem. Soc.*, *136*(32), 11452-11464. https://doi.org/10.1021/ja505186m

185 J. Saha, S. Verma, R. Ball, C. Subramaniam, & R. Murugavel. (2020). Compositional Control as the Key for Achieving Highly Efficient OER Electrocatalysis with Cobalt Phosphates Decorated Nanocarbon Florets. *Small*, *16*(12), 1903334. https://doi.org/10.1002/smll.201903334

186 D. Yan, Y. Li, J. Huo, R. Chen, L. Dai, & S. Wang. (2017). Defect Chemistry of Nonprecious-Metal Electrocatalysts for Oxygen Reactions. *Adv. Mater.*, *29*(48), 1606459. https://doi.org/10.1002/adma.201606459

187 Z. Y. Yu, Y. Duan, J. D. Liu, Y. Chen, X. K. Liu, W. Liu, T. Ma, Y. Li, X. S. Zheng, T. Yao, M. R. Gao, J. F. Zhu, B. J. Ye, & S.-H. Yu. (2019). Unconventional CN vacancies suppress iron-leaching in Prussian blue analogue pre-catalyst for boosted oxygen evolution catalysis. *Nat. Commun.*, *10*(1), 2799. https://doi.org/10.1038/s41467-019-10698-9

188 R. Zhang, Y. C. Zhang, L. Pan, G. Q. Shen, N. Mahmood, Y. H. Ma, Y. Shi, W. Jia, L. Wang, X. Zhang, W. Xu, & J. J. Zou. (2018). Engineering Cobalt Defects in Cobalt Oxide for Highly Efficient Electrocatalytic Oxygen Evolution. *ACS Catal.*, *8*(5), 3803-3811. https://doi.org/10.1021/acscatal.8b01046

189 R. Zhang, L. Pan, B. Guo, Z.-F. Huang, Z. Chen, L. Wang, X. Zhang, Z. Guo, W. Xu, K. P. Loh, & J.-J. Zou. (2023). Tracking the Role of Defect Types in Co_3O_4 Structural Evolution and Active Motifs during Oxygen Evolution Reaction. *J. Am. Chem. Soc.*, *145*(4), 2271-2281. https://doi.org/10.1021/jacs.2c10515

190 Z. Xiao, Y.-C. Huang, C.-L. Dong, C. Xie, Z. Liu, S. Du, W. Chen, D. Yan, L. Tao, Z. Shu, G. Zhang, H. Duan, Y. Wang, Y. Zou, R. Chen, & S. Wang. (2020). Operando Identification of the Dynamic Behavior of Oxygen Vacancy-Rich Co_3O_4 for Oxygen Evolution Reaction. *J. Am. Chem. Soc.*, *142*(28), 12087-12095. https://doi.org/10.1021/jacs.0c00257

191 H. Wu, T. Yang, Y. Du, L. Shen, & G. W. Ho. (2018). Identification of Facet-Governing Reactivity in Hematite for Oxygen Evolution. *Adv. Mater.*, *30*(52), 1804341. https://doi.org/10.1002/adma.201804341

192 T. Liu, A. Li, C. Wang, W. Zhou, S. Liu, & L. Guo. (2018). Interfacial Electron Transfer of Ni_2P–NiP_2 Polymorphs Inducing Enhanced Electrochemical Properties. *Adv. Mater.*, *30*(46), 1803590. https://doi.org/10.1002/adma.201803590

193 Y. Yang, K. Zhang, H. Lin, X. Li, H. C. Chan, L. Yang, & Q. Gao. (2017). MoS_2–Ni_3S_2 Heteronanorods as Efficient and Stable Bifunctional Electrocatalysts for Overall Water Splitting. *ACS Catal.*, *7*(4), 2357-2366. https://doi.org/10.1021/acscatal.6b03192

194 B. Chen, Z. Zhang, S. Kim, S. Lee, J. Lee, W. Kim, & K. Yong. (2018). Ostwald Ripening Driven Exfoliation to Ultrathin Layered Double Hydroxides Nanosheets for Enhanced Oxygen Evolution Reaction. *ACS Appl. Mater. Interfaces*, *10*(51), 44518-44526. https://doi.org/10.1021/acsami.8b16962

195 T. Y. Ma, S. Dai, M. Jaroniec, & S. Z. Qiao. (2014). Metal–Organic Framework Derived Hybrid Co_3O_4-Carbon Porous Nanowire Arrays as Reversible Oxygen Evolution Electrodes. *J. Am. Chem. Soc.*, *136*(39), 13925-13931. https://doi.org/10.1021/ja5082553

196 R. Subbaraman, D. Tripkovic, K.-C. Chang, D. Strmcnik, A. P. Paulikas, P. Hirunsit, M. Chan, J. Greeley, V. Stamenkovic, & N. M. Markovic. (2012). Trends in activity for the

water electrolyser reactions on 3d M(Ni,Co,Fe,Mn) hydr(oxy)oxide catalysts. *Nature Mater.*, *11*(6), 550-557. https://doi.org/10.1038/nmat3313

197 M. Gao, W. Sheng, Z. Zhuang, Q. Fang, S. Gu, J. Jiang, & Y. Yan. (2014). Efficient Water Oxidation Using Nanostructured α-Nickel-Hydroxide as an Electrocatalyst. *J. Am. Chem. Soc.*, *136*(19), 7077-7084. https://doi.org/10.1021/ja502128j

198 T. Shinagawa, & K. Takanabe. (2017). Towards Versatile and Sustainable Hydrogen Production through Electrocatalytic Water Splitting: Electrolyte Engineering. *ChemSusChem*, *10*(7), 1318-1336. https://doi.org/10.1002/cssc.201601583

199 L. Giordano, B. Han, M. Risch, W. T. Hong, R. R. Rao, K. A. Stoerzinger, & Y. Shao-Horn. (2016). pH dependence of OER activity of oxides: Current and future perspectives. *Catalysis Today*, *262*, 2-10. https://doi.org/10.1016/j.cattod.2015.10.006

200 J. C. Fornaciari, L.-C. Weng, S. M. Alia, C. Zhan, T. A. Pham, A. T. Bell, T. Ogitsu, N. Danilovic, & A. Z. Weber. (2022). Mechanistic understanding of pH effects on the oxygen evolution reaction. *Electrochim. Acta*, *405*, 139810. https://doi.org/10.1016/j.electacta.2021.139810

201 Y. Duan, N. Dubouis, J. Huang, D. A. Dalla Corte, V. Pimenta, Z. J. Xu, & A. Grimaud. (2020). Revealing the Impact of Electrolyte Composition for Co-Based Water Oxidation Catalysts by the Study of Reaction Kinetics Parameters. *ACS Catal.*, *10*(7), 4160-4170. https://doi.org/10.1021/acscatal.0c00490

202 G.-F. Li, M. Divinagracia, M. F. Labata, J. D. Ocon, & P.-Y. Abel Chuang. (2019). Electrolyte-Dependent Oxygen Evolution Reactions in Alkaline Media: Electrical Double Layer and Interfacial Interactions. *ACS Appl. Mater. Interfaces*, *11*(37), 33748-33758. https://doi.org/10.1021/acsami.9b06889

203 M. Görlin, J. Ferreira de Araújo, H. Schmies, D. Bernsmeier, S. Dresp, M. Gliech, Z. Jusys, P. Chernev, R. Kraehnert, H. Dau, & P. Strasser. (2017). Tracking Catalyst Redox States and Reaction Dynamics in Ni–Fe Oxyhydroxide Oxygen Evolution Reaction Electrocatalysts: The Role of Catalyst Support and Electrolyte pH. *J. Am. Chem. Soc.*, *139*(5), 2070-2082. https://doi.org/10.1021/jacs.6b12250

204 M. C. O. Monteiro, & M. T. M. Koper. (2021). Measuring local pH in electrochemistry. *Curr. Opin. Electrochem.*, *25*, 100649-100649. https://doi.org/10.1016/j.coelec.2020.100649

205 Y. Yokoyama, K. Miyazaki, Y. Miyahara, T. Fukutsuka, & T. Abe. (2019). In situ measurement of local pH at working electrodes in neutral pH solutions by the rotating ring-disk electrode technique. *ChemElectroChem*, *6*(18), 4750-4756. https://doi.org/10.1002/celc.201900759

206 S. Liu, L. D'Amario, S. Jiang, & H. Dau. (2022). Selected applications of operando Raman spectroscopy in electrocatalysis research. *Curr. Opin. Electrochem.*, *35*, 101042. https://doi.org/10.1016/j.coelec.2022.101042

207 K. Obata, R. van de Krol, M. Schwarze, R. Schomäcker, & F. F. Abdi. (2020). In situ observation of pH change during water splitting in neutral pH conditions: impact of natural convection driven by buoyancy effects. *Energy Environ. Sci.*, *13*(12), 5104-5116. https://doi.org/10.1039/D0EE01760D

208 J. Wang, & H. C. Zeng. (2018). CoHPi Nanoflakes for Enhanced Oxygen Evolution Reaction. *ACS Appl. Mater. Interfaces*, *10*(7), 6288-6298. https://doi.org/10.1021/acsami.7b17257

209 K. Jiang, M. Luo, M. Peng, Y. Yu, Y. R. Lu, T. S. Chan, P. Liu, F. M. F. de Groot, & Y. Tan. (2020). Dynamic active-site generation of atomic iridium stabilized on nanoporous metal phosphides for water oxidation. *Nat. Commun.*, *11*(1), 2701. https://doi.org/10.1038/s41467-020-16558-1

210 W. Liu, D. Zheng, T. Deng, Q. Chen, C. Zhu, C. Pei, H. Li, F. Wu, W. Shi, S.-W. Yang, Y. Zhu, & X. Cao. (2021). Boosting Electrocatalytic Activity of 3d-Block Metal (Hydro)oxides by Ligand-Induced Conversion. *Angew. Chem. Int. Ed.*, *60*(19), 10614-10619. https://doi.org/10.1002/anie.202100371

211 R. Sen, S. Das, A. Nath, P. Maharana, P. Kar, F. Verpoort, P. Liang, & S. Roy. (2022). Electrocatalytic Water Oxidation: An Overview With an Example of Translation From Lab to Market. *Front. Chem.*, *10*. https://www.frontiersin.org/articles/10.3389/fchem.2022.861604

212 C. Costentin. (2020). Proton-Coupled Electron Transfer Catalyst: Heterogeneous Catalysis. Application to an Oxygen Evolution Catalyst. *ACS Catal.*, *10*(14), 7958-7967. https://doi.org/10.1021/acscatal.0c02532

213 I. Zaharieva, D. González-Flores, B. Asfari, C. Pasquini, M. R. Mohammadi, K. Klingan, I. Zizak, S. Loos, P. Chernev, & H. Dau. (2016). Water oxidation catalysis – role of redox and structural dynamics in biological photosynthesis and inorganic manganese oxides. *Energy Environ. Sci.*, *9*(7), 2433-2443. https://doi.org/10.1039/C6EE01222A

214 D. González-Flores, K. Klingan, P. Chernev, S. Loos, M. R. Mohammadi, C. Pasquini, P. Kubella, I. Zaharieva, R. D. L. Smith, & H. Dau. (2018). Nickel-iron catalysts for electrochemical water oxidation-redox synergism investigated by: In situ X-ray spectroscopy with millisecond time resolution. *Sustain. Energy Fuels*, *2*(9), 1986-1994. https://doi.org/10.1039/c8se00114f

215 L. C. Seitz, T. J. P. Hersbach, D. Nordlund, & T. F. Jaramillo. (2015). Enhancement effect of noble metals on manganese oxide for the oxygen evolution reaction. *J. Phys. Chem. Lett.*, *6*(20), 4178-4183. https://doi.org/10.1021/acs.jpclett.5b01928

216 L. Francàs, S. Corby, S. Selim, D. Lee, C. A. Mesa, R. Godin, E. Pastor, I. E. L. Stephens, K.-S. Choi, & J. R. Durrant. (2019). Spectroelectrochemical study of water oxidation on nickel and iron oxyhydroxide electrocatalysts. *Nat. Commun.*, *10*(1), 5208. https://doi.org/10.1038/s41467-019-13061-0

217 H. N. Nong, L. J. Falling, A. Bergmann, M. Klingenhof, H. P. Tran, C. Spori, R. Mom, J. Timoshenko, G. Zichittella, A. Knop-Gericke, S. Piccinin, J. Perez-Ramirez, B. R. Cuenya, R. Schlogl, P. Strasser, D. Teschner, & T. E. Jones. (2020). Key role of chemistry versus bias in electrocatalytic oxygen evolution. *Nature*, *587*(7834), 408-413. https://doi.org/10.1038/s41586-020-2908-2

218 Z.-Z. Wu, F.-Y. Gao, & M.-R. Gao. (2021). Regulating the oxidation state of nanomaterials for electrocatalytic CO_2 reduction. *Energy Environ. Sci.*, *14*(3), 1121-1139. https://doi.org/10.1039/D0EE02747B

219 N. Li, R. G. Hadt, D. Hayes, L. X. Chen, & D. G. Nocera. (2021). Detection of high-valent iron species in alloyed oxidic cobaltates for catalysing the oxygen evolution reaction. *Nat. Commun.*, *12*(1), 4218. https://doi.org/10.1038/s41467-021-24453-6

220 C. Bozal-Ginesta, R. R. Rao, C. A. Mesa, X. Liu, S. A. J. Hillman, I. E. L. Stephens, & J. R. Durrant. (2021). Redox-State Kinetics in Water-Oxidation IrOx Electrocatalysts

Measured by Operando Spectroelectrochemistry. *ACS Catal.*, *11*(24), 15013-15025. https://doi.org/10.1021/acscatal.1c03290

221 R. R. Rao, S. Corby, A. Bucci, M. García-Tecedor, C. A. Mesa, J. Rossmeisl, S. Giménez, J. Lloret-Fillol, I. E. L. Stephens, & J. R. Durrant. (2022). Spectroelectrochemical Analysis of the Water Oxidation Mechanism on Doped Nickel Oxides. *J. Am. Chem. Soc.*, *144*(17), 7622-7633. https://doi.org/10.1021/jacs.1c08152

222 R. R. Rao, I. E. L. Stephens, & J. R. Durrant. (2021). Understanding What Controls the Rate of Electrochemical Oxygen Evolution. *Joule*, *5*(1), 16-18. https://doi.org/10.1016/j.joule.2020.12.017

223 S. W. Boettcher, & Y. Surendranath. (2021). Heterogeneous electrocatalysis goes chemical. *Nat. Catal.*, *4*(1), 4-5. https://doi.org/10.1038/s41929-020-00570-1

224 R. R. Rao, C. A. Mesa, & J. R. Durrant. (2022). Better together. *Nat. Catal.*, *5*(10), 844-845. https://doi.org/10.1038/s41929-022-00861-9

225 J. Jiang, Y. Li, J. Liu, X. Huang, C. Yuan, & X. W. Lou. (2012). Recent Advances in Metal Oxide-based Electrode Architecture Design for Electrochemical Energy Storage. *Adv. Mater.*, *24*(38), 5166-5180. https://doi.org/10.1002/adma.201202146

226 W. Liu, P. Oh, X. Liu, M.-J. Lee, W. Cho, S. Chae, Y. Kim, & J. Cho. (2015). Nickel-Rich Layered Lithium Transition-Metal Oxide for High-Energy Lithium-Ion Batteries. *Angew. Chem. Int. Ed.*, *54*(15), 4440-4457. https://doi.org/10.1002/anie.201409262

227 B. Banov, J. Bourilkov, & M. Mladenov. (1995). Cobalt stabilized layered lithium-nickel oxides, cathodes in lithium rechargeable cells. *J. Power Sources*, *54*(2), 268-270. https://doi.org/10.1016/0378-7753(94)02082-E

228 M. M. Thackeray. (1997). Manganese oxides for lithium batteries. *Progress in Solid State Chemistry*, *25*(1), 1-71. https://doi.org/10.1016/S0079-6786(97)81003-5

229 R. Matheu, P. Garrido-Barros, M. Gil-Sepulcre, M. Z. Ertem, X. Sala, C. Gimbert-Suriñach, & A. Llobet. (2019). The development of molecular water oxidation catalysts. *Nat. Rev. Chem*, *3*(5), 331-341. https://doi.org/10.1038/s41570-019-0096-0

230 N. Cox, D. A. Pantazis, & W. Lubitz. (2020). Current Understanding of the Mechanism of Water Oxidation in Photosystem II and Its Relation to XFEL Data. *Annu. Rev. Biochem.*, *89*, 795-820. https://doi.org/10.1146/annurev-biochem-011520-104801

231 D. A. Pantazis. (2018). Missing pieces in the puzzle of biological water oxidation. *ACS Catal.*, *8*(10), 9477-9507. https://doi.org/10.1021/acscatal.8b01928

232 C. A. Mesa, L. Francàs, K. R. Yang, P. Garrido-Barros, E. Pastor, Y. Ma, A. Kafizas, T. E. Rosser, M. T. Mayer, E. Reisner, M. Grätzel, V. S. Batista, & J. R. Durrant. (2020). Multihole water oxidation catalysis on haematite photoanodes revealed by operando spectroelectrochemistry and DFT. *Nature Chem.*, *12*(1), 82-89. https://doi.org/10.1038/s41557-019-0347-1

233 B. E. Conway, & P. L. Bourgault. (1959). The Electrochemical behavior of the nickel-nickel oxide electrode: part 1. kinetics of self-discharge *Can. J. Chem.*, *37*(1), 292-307. https://doi.org/10.1139/v59-038

234 A. Bergmann, E. Martinez-Moreno, D. Teschner, P. Chernev, M. Gliech, J. F. de Araujo, T. Reier, H. Dau, & P. Strasser. (2015). Reversible amorphization and the catalytically active state of crystalline Co_3O_4 during oxygen evolution. *Nat. Commun.*, *6*, 8625. https://doi.org/10.1038/ncomms9625

235 A. Indra, P. W. Menezes, I. Zaharieva, E. Baktash, J. Pfrommer, M. Schwarze, H. Dau, & M. Driess. (2013). Active mixed-valent MnO_x water oxidation catalysts through partial oxidation (corrosion) of nanostructured MnO particles. *Angew. Chem. Int. Ed.*, *52*(50), 13206–13210. https://doi.org/10.1002/anie.201307543

236 C. W. Tung, Y. Y. Hsu, Y. P. Shen, Y. X. Zheng, T. S. Chan, H. S. Sheu, Y. C. Cheng, & H. M. Chen. (2015). Reversible adapting layer produces robust single-crystal electrocatalyst for oxygen evolution. *Nat. Commun.*, *6*, 8106. https://doi.org/10.1038/Ncomms9106

237 F. Le Formal, E. Pastor, S. D. Tilley, C. A. Mesa, S. R. Pendlebury, M. Grätzel, & J. R. Durrant. (2015). Rate law analysis of water oxidation on a hematite surface. *J. Am. Chem. Soc.*, *137*(20), 6629-6637. https://doi.org/10.1021/jacs.5b02576

238 F. M. Pesci, A. J. Cowan, B. D. Alexander, J. R. Durrant, & D. R. Klug. (2011). Charge Carrier Dynamics on Mesoporous WO_3 during Water Splitting. *J. Phys. Chem. Lett.*, *2*(15), 1900-1903. https://doi.org/10.1021/jz200839n

239 Y. Ma, C. A. Mesa, E. Pastor, A. Kafizas, L. Francas, F. Le Formal, S. R. Pendlebury, & J. R. Durrant. (2016). Rate law analysis of water oxidation and hole scavenging on a $BiVO_4$ photoanode. *ACS Energy Lett.*, *1*(3), 618-623. https://doi.org/10.1021/acsenergylett.6b00263

240 A. Kafizas, Y. Ma, E. Pastor, S. R. Pendlebury, C. Mesa, L. Francàs, F. Le Formal, N. Noor, M. Ling, & C. Sotelo-Vazquez. (2017). Water oxidation kinetics of accumulated holes on the surface of a TiO_2 photoanode: a rate law analysis. *ACS Catal.*, *7*(7), 4896-4903. https://doi.org/10.1021/acscatal.7b01150

241 C. Bozal-Ginesta, R. R. Rao, C. A. Mesa, Y. Wang, Y. Zhao, G. Hu, D. Antón-García, I. E. L. Stephens, E. Reisner, G. W. Brudvig, D. Wang, & J. R. Durrant. (2022). Spectroelectrochemistry of Water Oxidation Kinetics in Molecular versus Heterogeneous Oxide Iridium Electrocatalysts. *J. Am. Chem. Soc.*, *144*(19), 8454-8459. https://doi.org/10.1021/jacs.2c02006

242 J. Desilvestro, D. A. Corrigan, & M. J. Weaver. (1988). Characterization of Redox States of Nickel Hydroxide Film Electrodes by In Situ Surface Raman Spectroscopy. *J. Electrochem. Soc.*, *135*(4), 885. https://doi.org/10.1149/1.2095818

243 D. E. Starr, Z. Liu, M. Hävecker, A. Knop-Gericke, & H. Bluhm. (2013). Investigation of solid/vapor interfaces using ambient pressure X-ray photoelectron spectroscopy. *Chem. Soc. Rev.*, *42*(13), 5833-5857. https://doi.org/10.1039/C3CS60057B

244 K. A. Stoerzinger, W. T. Hong, E. J. Crumlin, H. Bluhm, & Y. Shao-Horn. (2015). Insights into Electrochemical Reactions from Ambient Pressure Photoelectron Spectroscopy. *Acc. Chem. Res.*, *48*(11), 2976-2983. https://doi.org/10.1021/acs.accounts.5b00275

245 M. E. Kreider, & M. Burke Stevens. (2023). Material Changes in Electrocatalysis: An In Situ/Operando Focus on the Dynamics of Cobalt-Based Oxygen Reduction and Evolution Catalysts. *ChemElectroChem*, *10*(3), e202200958. https://doi.org/10.1002/celc.202200958

246 J. Rossmeisl, Z. W. Qu, H. Zhu, G. J. Kroes, & J. K. Norskov. (2007). Electrolysis of water on oxide surfaces. *J. Electroanal. Chem.*, *607*(1-2), 83-89. https://doi.org/10.1016/j.jelechem.2006.11.008

247 I. C. Man, H.-Y. Su, F. Calle-Vallejo, H. A. Hansen, J. I. Martínez, N. G. Inoglu, J. Kitchin, T. F. Jaramillo, J. K. Nørskov, & J. Rossmeisl. (2011). Universality in oxygen evolution electrocatalysis on oxide surfaces. *ChemCatChem*, *3*(7), 1159-1165. https://doi.org/10.1002/cctc.201000397

248 J. B. Goodenough, R. Manoharan, & M. Paranthaman. (1990). Surface protonation and electrochemical activity of oxides in aqueous solution. *J. Am. Chem. Soc.*, *112*(6), 2076-2082. https://doi.org/10.1021/ja00162a006

249 M. G. Mavros, T. Tsuchimochi, T. Kowalczyk, A. McIsaac, L.-P. Wang, & T. V. Voorhis. (2014). What Can Density Functional Theory Tell Us about Artificial Catalytic Water Splitting? *Inorg. Chem*, *53*(13), 6386-6397. https://doi.org/10.1021/ic5002557

250 X. Bo, R. K. Hocking, S. Zhou, Y. Li, X. Chen, J. Zhuang, Y. Du, & C. Zhao. (2020). Capturing the active sites of multimetallic (oxy)hydroxides for the oxygen evolution reaction. *Energy Environ. Sci.*, *13*(11), 4225-4237. https://doi.org/10.1039/D0EE01609H

251 B. Wang, K. Zhao, Z. Yu, C. Sun, Z. Wang, N. Feng, L. Mai, Y. Wang, & Y. Xia. (2020). In situ structural evolution of the multi-site alloy electrocatalyst to manipulate the intermediate for enhanced water oxidation reaction. *Energy Environ. Sci.*, *13*(7), 2200-2208. https://doi.org/10.1039/D0EE00755B

252 R. D. L. Smith, C. Pasquini, S. Loos, P. Chernev, K. Klingan, P. Kubella, M. R. Mohammadi, D. Gonzalez-Flores, & H. Dau. (2017). Spectroscopic identification of active sites for the oxygen evolution reaction on iron-cobalt oxides. *Nat. Commun.*, *8*(1), 2022. https://doi.org/10.1038/s41467-017-01949-8

253 A. C. Garcia, T. Touzalin, C. Nieuwland, N. Perini, & M. T. M. Koper. (2019). Enhancement of Oxygen Evolution Activity of Nickel Oxyhydroxide by Electrolyte Alkali Cations. *Angew. Chem. Int. Ed.*, *58*(37), 12999-13003. https://doi.org/10.1002/anie.201905501

254 V. B. R. Boppana, S. Yusuf, G. S. Hutchings, & F. Jiao. (2013). Nanostructured Alkaline-Cation-Containing δ-MnO_2 for Photocatalytic Water Oxidation. *Adv. Func. Mater.*, *23*(7), 878-884. https://doi.org/10.1002/adfm.201202141

255 S. Lee, L. Bai, & X. Hu. (2020). Deciphering Iron-Dependent Activity in Oxygen Evolution Catalyzed by Nickel–Iron Layered Double Hydroxide. *Angew. Chem. Int. Ed.*, *59*(21), 8072-8077. https://doi.org/10.1002/anie.201915803

256 J. Huang, M. Li, M. J. Eslamibidgoli, M. Eikerling, & A. Groß. (2021). Cation Overcrowding Effect on the Oxygen Evolution Reaction. *JACS Au*, *1*(10), 1752-1765. https://doi.org/10.1021/jacsau.1c00315

257 M. Fu, G. Ning, J. Liu, Q. Zhang, Y. Sun, X. Fan, H. Wang, H. Lu, Y. Zhang, & H. Wang. (2021). Core-shell structure Co–Ni@Fe–Cu doped MOF–GR composites for water splitting. *Int. J. Hydrog. Energy*, *46*(29), 15124-15134. https://doi.org/10.1016/j.ijhydene.2021.02.026

258 V. Kotha, I. Karajagi, P. C. Ghosh, & L. S. Panchakarla. (2022). Potassium-Substituted $LaMnO_3$ as a Highly Active and Exceptionally Stable Electrocatalyst toward Bifunctional Oxygen Reduction and Oxygen Evolution Reactions. *ACS Appl. Mater. Interfaces*, *5*(6), 7297-7307. https://doi.org/10.1021/acsaem.2c00823

259 Y. Zhang, M. Xu, X. Xu, X. Li, G. Zhu, G. Jia, B. Yang, R. Yin, P. Gao, & W. Ye. (2023). Efficient interlayer confined nitrate reduction reaction and oxygen generation enabled by interlayer expansion. *Nanoscale*, *15*(1), 204-214. https://doi.org/10.1039/D2NR05001C

260 A. Kozawa. (1964). Effects of anions and cations on oxygen reduction and oxygen evolution reactions on platinum electrodes. *Journal of Electroanalytical Chemistry 8*(1), 20-39. https://doi.org/10.1016/0022-0728(64)80035-8

261 M. Wiechen, I. Zaharieva, H. Dau, & P. Kurz. (2012). Layered manganese oxides for water-oxidation: alkaline earth cations influence catalytic activity in a photosystem II-like fashion. *Chem. Sci.*, *3*(7), 2330-2339. http://dx.doi.org/10.1039/C2SC20226C

262 E. Y. Tsui, R. Tran, J. Yano, & T. Agapie. (2013). Redox-inactive metals modulate the reduction potential in heterometallic manganese-oxido clusters. *Nature Chem.*, *5*(4), 293-299. https://doi.org/10.1038/Nchem.1578

263 B. M. Hunter, W. Hieringer, J. R. Winkler, H. B. Gray, & A. M. Müller. (2016). Effect of interlayer anions on [NiFe]-LDH nanosheet water oxidation activity. *Energy Environ. Sci.*, *9*, 1734-1743. https://doi.org/10.1039/C6EE00377J

264 D. Zhou, Z. Cai, Y. Bi, W. Tian, M. Luo, Q. Zhang, Q. Zhang, Q. Xie, J. Wang, Y. Li, Y. Kuang, X. Duan, M. Bajdich, S. Siahrostami, & X. Sun. (2018). Effects of redox-active interlayer anions on the oxygen evolution reactivity of NiFe-layered double hydroxide nanosheets. *Nano Res.*, *11*(3), 1358-1368. https://doi.org/10.1007/s12274-017-1750-9

265 C. Yang, G. Rousse, K. Louise Svane, P. E. Pearce, A. M. Abakumov, M. Deschamps, G. Cibin, A. V. Chadwick, D. A. Dalla Corte, H. Anton Hansen, T. Vegge, J.-M. Tarascon, & A. Grimaud. (2020). Cation insertion to break the activity/stability relationship for highly active oxygen evolution reaction catalyst. *Nat. Commun.*, *11*(1), 1378. https://doi.org/10.1038/s41467-020-15231-x

266 M. Görlin, J. Halldin Stenlid, S. Koroidov, H.-Y. Wang, M. Börner, M. Shipilin, A. Kalinko, V. Murzin, O. V. Safonova, M. Nachtegaal, A. Uheida, J. Dutta, M. Bauer, A. Nilsson, & O. Diaz-Morales. (2020). Key activity descriptors of nickel-iron oxygen evolution electrocatalysts in the presence of alkali metal cations. *Nat. Commun.*, *11*(1), 6181. https://doi.org/10.1038/s41467-020-19729-2

267 E. Ronge, J. Ohms, V. Roddatis, T. Jones, F. Sulzmann, A. Knop-Gericke, R. Schlögl, P. Kurz, C. Jooss, & K. Skorupska. (2021). Operation of calcium-birnessite water-oxidation anodes: Interactions of the catalyst with phosphate buffer anions. *Sustain. Energy Fuels*, *5*(21), 5535-5547. https://doi.org/10.1039/d1se01076j

268 G. Kwon, O. Kokhan, A. Han, K. W. Chapman, P. J. Chupas, P. Du, & D. M. Tiede. (2015). Oxyanion induced variations in domain structure for amorphous cobalt oxide oxygen evolving catalysts, resolved by X-ray pair distribution function analysis. *Acta Crystallographica Section B*, *71*(6), 713-721. https://doi.org/10.1107/S2052520615022180

269 F. Dionigi, Z. Zeng, I. Sinev, T. Merzdorf, S. Deshpande, M. B. Lopez, S. Kunze, I. Zegkinoglou, H. Sarodnik, D. Fan, et al.P. Strasser. (2020). In-situ structure and catalytic mechanism of NiFe and CoFe layered double hydroxides during oxygen evolution. *Nat. Commun.*, *11*(1), 2522. https://doi.org/10.1038/s41467-020-16237-1

270 V. K. Yachandra, & J. Yano. (2011). Calcium in the oxygen-evolving complex: Structural and mechanistic role determined by X-ray spectroscopy. *Journal of*

Photochemistry and Photobiology B: Biology, *104*(1), 51-59. https://doi.org/10.1016/j.jphotobiol.2011.02.019

271 C. F. Yocum. (2008). The calcium and chloride requirements of the O_2 evolving complex. *Coord. Chem. Rev.*, *252*(3), 296-305. https://doi.org/10.1016/j.ccr.2007.08.010

272 Y. H. Wang, S. Zheng, W. M. Yang, R. Y. Zhou, Q. F. He, P. Radjenovic, J. C. Dong, S. Li, J. Zheng, Z. L. Yang, G. Attard, F. Pan, Z. Q. Tian, & J. F. Li. (2021). In situ Raman spectroscopy reveals the structure and dissociation of interfacial water. *Nature*, *600*(7887), 81-85. https://doi.org/10.1038/s41586-021-04068-z

273 Y.-C. Hao, Y. Guo, L.-W. Chen, M. Shu, X.-Y. Wang, T.-A. Bu, W.-Y. Gao, N. Zhang, X. Su, X. Feng, J.-W. Zhou, B. Wang, C.-W. Hu, A.-X. Yin, R. Si, Y.-W. Zhang, & C.-H. Yan. (2019). Promoting nitrogen electroreduction to ammonia with bismuth nanocrystals and potassium cations in water. *Nat. Catal.*, *2*(5), 448-456. https://doi.org/10.1038/s41929-019-0241-7

274 L. Zhang, L. Wang, Y. Wen, F. Ni, B. Zhang, & H. Peng. (2020). Boosting Neutral Water Oxidation through Surface Oxygen Modulation. *Adv. Mater.*, *32*(31), 2002297. https://doi.org/10.1002/adma.202002297

275 N. Wang, Z. Cao, X. Zheng, B. Zhang, S. M. Kozlov, P. Chen, C. Zou, X. Kong, Y. Wen, M. Liu, Y. Zhou, C. T. Dinh, L. Zheng, H. Peng, Y. Zhao, L. Cavallo, X. Zhang, & E. H. Sargent. (2020). Hydration-Effect-Promoting Ni–Fe Oxyhydroxide Catalysts for Neutral Water Oxidation. *Adv. Mater.*, *32*(8), 1906806. https://doi.org/10.1002/adma.201906806

276 P. Hosseini-Benhangi, M. A. Garcia-Contreras, A. Alfantazi, & E. L. Gyenge. (2015). Method for Enhancing the Bifunctional Activity and Durability of Oxygen Electrodes with Mixed Oxide Electrocatalysts: Potential Driven Intercalation of Potassium. *J. Electrochem. Soc.*, *162*(12), F1356. https://doi.org/10.1149/2.0561512jes

277 P. Bernard, C. Gabrielli, M. Keddam, H. Takenouti, J. Leonardi, & P. Blanchard. (1991). Ac quartz crystal microbalance applied to the studies of the nickel hydroxide behaviour in alkaline solutions. *Electrochim. Acta*, *36*(3), 743-746. https://doi.org/10.1016/0013-4686(91)85166-5

278 G. T. Cheek, & W. E. O'Grady. (1997). Redox behavior of the nickel oxide electrode system: quartz crystal microbalance studies. *J. Electroanal. Chem.*, *421*(1), 173-177. https://doi.org/10.1016/S0022-0728(96)04821-8

279 I. C. Faria, R. Torresi, & A. Gorenstein. (1993). Electrochemical intercalation in NiOx thin films. *Electrochim. Acta*, *38*(18), 2765-2771. https://doi.org/10.1016/0013-4686(93)85096-H

280 M. Wehrens-Dijksma, & P. H. L. Notten. (2006). Electrochemical Quartz Microbalance characterization of $Ni(OH)_2$-based thin film electrodes. *Electrochim. Acta*, *51*(18), 3609-3621. https://doi.org/10.1016/j.electacta.2005.10.022

281 J. Zaffran, M. B. Stevens, C. D. M. Trang, M. Nagli, M. Shehadeh, S. W. Boettcher, & M. Caspary Toroker. (2017). Influence of Electrolyte Cations on Ni(Fe)OOH Catalyzed Oxygen Evolution Reaction. *Chem. Mater.*, *29*(11), 4761-4767. https://doi.org/10.1021/acs.chemmater.7b00517

282 J. D. Michael, E. L. Demeter, S. M. Illes, Q. Fan, J. R. Boes, & J. R. Kitchin. (2015). Alkaline Electrolyte and Fe Impurity Effects on the Performance and Active-Phase Structure of NiOOH Thin Films for OER Catalysis Applications. *J. Phys. Chem. C*, *119*(21), 11475-11481. https://doi.org/10.1021/acs.jpcc.5b02458

283 C. Yang, O. Fontaine, J.-M. Tarascon, & A. Grimaud. (2017). Chemical Recognition of Active Oxygen Species on the Surface of Oxygen Evolution Reaction Electrocatalysts. *Angew. Chem. Int. Ed.*, *56*(30), 8652-8656. https://doi.org/10.1002/anie.201701984

284 R. R. Rao, B. Huang, Y. Katayama, J. Hwang, T. Kawaguchi, J. R. Lunger, J. Peng, Y. Zhang, A. Morinaga, H. Zhou, H. You, & Y. Shao-Horn. (2021). pH- and Cation-Dependent Water Oxidation on Rutile RuO_2(110). *J. Phys. Chem. C*, *125*(15), 8195-8207. https://doi.org/10.1021/acs.jpcc.1c00413

285 D. Shevchenko, M. F. Anderlund, S. Styring, H. Dau, I. Zaharieva, & A. Thapper. (2014). Water oxidation by manganese oxides formed from tetranuclear precursor complexes: the influence of phosphate on structure and activity. *Phys. Chem. Chem. Phys.*, *16*(24), 11965-11975. https://doi.org/10.1039/C3cp55125c

286 S. Dey, B. Mondal, & A. Dey. (2014). An acetate bound cobalt oxide catalyst for water oxidation: role of monovalent anions and cations in lowering overpotential. *Phys. Chem. Chem. Phys.*, *16*(24), 12221-12227. https://doi.org/10.1039/C4CP01205D

287 I. Y. Ahmet, Y. Ma, J.-W. Jang, T. Henschel, B. Stannowski, T. Lopes, A. Vilanova, A. Mendes, F. F. Abdi, & R. van de Krol. (2019). Demonstration of a 50 cm^2 $BiVO_4$ tandem photoelectrochemical-photovoltaic water splitting device. *Sustain. Energy Fuels*, *3*(9), 2366-2379. https://doi.org/10.1039/c9se00246d

288 F. F. Abdi, R. R. Gutierrez Perez, & S. Haussener. (2020). Mitigating voltage losses in photoelectrochemical cell scale-up. *Sustain. Energy Fuels*, *4*(6), 2734-2740. https://doi.org/10.1039/D0SE00246A

289 M. R. Singh, K. Papadantonakis, C. Xiang, & N. S. Lewis. (2015). An electrochemical engineering assessment of the operational conditions and constraints for solar-driven water-splitting systems at near-neutral pH. *Energy Environ. Sci.*, *8*(9), 2760-2767. https://doi.org/10.1039/C5EE01721A

290 M. R. Singh, C. Xiang, & N. S. Lewis. (2017). Evaluation of flow schemes for near-neutral pH electrolytes in solar-fuel generators. *Sustain. Energy Fuels*, *1*(3), 458-466. https://doi.org/10.1039/C7SE00062F

291 H. Vogt, & K. Stephan. (2015). Local microprocesses at gas-evolving electrodes and their influence on mass transfer. *Electrochim. Acta*, *155*, 348-356. https://doi.org/10.1016/j.electacta.2015.01.008

292 A. Angulo, P. van der Linde, H. Gardeniers, M. Modestino, & D. Fernández Rivas. (2020). Influence of Bubbles on the Energy Conversion Efficiency of Electrochemical Reactors. *Joule*, *4*(3), 555-579. https://doi.org/10.1016/j.joule.2020.01.005

293 A. Hankin, F. E. Bedoya-Lora, C. K. Ong, J. C. Alexander, F. Petter, & G. H. Kelsall. (2017). From millimetres to metres: the critical role of current density distributions in photo-electrochemical reactor design [ ]. *Energy Environ. Sci.*, *10*(1), 346-360. https://doi.org/10.1039/C6EE03036J

294 V. Čolić, J. Tymoczko, A. Maljusch, A. Ganassin, W. Schuhmann, & A. S. Bandarenka. (2015). Experimental Aspects in Benchmarking of the Electrocatalytic Activity. *ChemElectroChem*, *2*(1), 143-149. https://doi.org/10.1002/celc.201402295

295 F. Zhang, & A. C. Co. (2020). Direct Evidence of Local pH Change and the Role of Alkali Cation during CO_2 Electroreduction in Aqueous Media. *Angew. Chem. Int. Ed.*, *59*(4), 1674-1681. https://doi.org/10.1002/anie.201912637

296 A. Li, S. Kong, C. Guo, H. Ooka, K. Adachi, D. Hashizume, Q. Jiang, H. Han, J. Xiao, & R. Nakamura. (2022). Enhancing the stability of cobalt spinel oxide towards sustainable oxygen evolution in acid. *Nat. Catal.*, *5*(2), 109-118. https://doi.org/10.1038/s41929-021-00732-9

297 Z. Long, Y. Zhao, C. Zhang, Y. Zhang, C. Yu, Y. Wu, J. Ma, M. Cao, & L. Jiang. (2020). A Multi-Bioinspired Dual-Gradient Electrode for Microbubble Manipulation toward Controllable Water Splitting. *Adv. Mater.*, *32*(17), 1908099. https://doi.org/10.1002/adma.201908099

298 E. D. Gadea, Y. A. Perez Sirkin, V. Molinero, & D. A. Scherlis. (2020). Electrochemically Generated Nanobubbles: Invariance of the Current with Respect to Electrode Size and Potential. *J. Phys. Chem. Lett.*, *11*(16), 6573-6579. https://doi.org/10.1021/acs.jpclett.0c01404

299 F. Rocha, R. Delmelle, C. Georgiadis, & J. Proost. (2023). Electrochemical Performance Enhancement of 3D Printed Electrodes Tailored for Enhanced Gas Evacuation during Alkaline Water Electrolysis. *Adv. Energy Mater.*, *13*(1), 2203087. https://doi.org/10.1002/aenm.202203087

300 Y. J. Kim, A. Lim, J. M. Kim, D. Lim, K. H. Chae, E. N. Cho, H. J. Han, K. U. Jeon, M. Kim, G. H. Lee, G. R. Lee, H. S. Ahn, H. S. Park, H. Kim, J. Y. Kim, & Y. S. Jung. (2020). Highly efficient oxygen evolution reaction via facile bubble transport realized by three-dimensionally stack-printed catalysts. *Nat. Commun.*, *11*(1), 4921. https://doi.org/10.1038/s41467-020-18686-0

301 G. B. Darband, M. Aliofkhazraei, & S. Shanmugam. (2019). Recent advances in methods and technologies for enhancing bubble detachment during electrochemical water splitting. *Renew. Sustain. Energy Rev.*, *114*, 109300. https://doi.org/10.1016/j.rser.2019.109300

302 R. Andaveh, G. Barati Darband, M. Maleki, & A. Sabour Rouhaghdam. (2022). Superaerophobic/superhydrophilic surfaces as advanced electrocatalysts for the hydrogen evolution reaction: a comprehensive review. *J. Mater. Chem. A*, *10*(10), 5147-5173. https://doi.org/10.1039/D1TA10519A

303 K. M. Cho, P. R. Deshmukh, & W. G. Shin. (2021). Hydrodynamic behavior of bubbles at gas-evolving electrode in ultrasonic field during water electrolysis. *Ultrason. Sonochem.*, *80*, 105796. https://doi.org/10.1016/j.ultsonch.2021.105796

304 F. Foroughi, J. J. Lamb, O. S. Burheim, & B. G. Pollet. (2021). Sonochemical and Sonoelectrochemical Production of Energy Materials. *Catalysts*, *11*(2). https://doi.org/10.3390/catal11020284

305 D. J. Walton, L. D. Burke, & M. M. Murphy. (1996). Sonoelectrochemistry: Chlorine, hydrogen and oxygen evolution at platinised platinum. *Electrochim. Acta*, *41*(17), 2747-2751. https://doi.org/10.1016/0013-4686(96)00133-8

306 G. F. Swiegers, R. N. L. Terrett, G. Tsekouras, T. Tsuzuki, R. J. Pace, & R. Stranger. (2021). The prospects of developing a highly energy-efficient water electrolyser by eliminating or mitigating bubble effects. *Sustain. Energy Fuels*, *5*(5), 1280-1310. https://doi.org/10.1039/D0SE01886D

307 Y.-H. Li, & Y.-J. Chen. (2021). The effect of magnetic field on the dynamics of gas bubbles in water electrolysis. *Sci. Rep.*, *11*(1), 9346. https://doi.org/10.1038/s41598-021-87947-9

308 X. Zhang, S. Pan, H. Song, W. Guo, F. Gu, C. Yan, H. Jin, L. Zhang, Y. Chen, & S. Wang. (2021). Photothermal effect enables markedly enhanced oxygen reduction and evolution activities for high-performance Zn–air batteries. *J. Mater. Chem. A*, *9*(35), 19734-19740. https://doi.org/10.1039/D1TA03652A

309 Y. He, Y. Cui, Z. Zhao, Y. Chen, W. Shang, & P. Tan. (2023). Strategies for bubble removal in electrochemical systems. *Energy Reviews*, *2*(1), 100015. https://doi.org/10.1016/j.enrev.2023.100015

310 A. Hodges, A. L. Hoang, G. Tsekouras, K. Wagner, C.-Y. Lee, G. F. Swiegers, & G. G. Wallace. (2022). A high-performance capillary-fed electrolysis cell promises more cost-competitive renewable hydrogen. *Nat. Commun.*, *13*(1), 1304. https://doi.org/10.1038/s41467-022-28953-x

311 J. Song, C. Wei, Z.-F. Huang, C. Liu, L. Zeng, X. Wang, & Z. J. Xu. (2020). A review on fundamentals for designing oxygen evolution electrocatalysts. *Chem. Soc. Rev.*, *49*(7), 2196-2214. https://doi.org/10.1039/C9CS00607A

312 L. An, C. Wei, M. Lu, H. Liu, Y. Chen, G. G. Scherer, A. C. Fisher, P. Xi, Z. J. Xu, & C.-H. Yan. (2021). Recent Development of Oxygen Evolution Electrocatalysts in Acidic Environment. *Adv. Mater.*, *33*(20), 2006328. https://doi.org/10.1002/adma.202006328

313 D. Drevon, M. Gorlin, P. Chernev, L. F. Xi, H. Dau, & K. M. Lange. (2019). Uncovering The Role of Oxygen in Ni-Fe(OxHy) Electrocatalysts using In situ Soft X-ray Absorption Spectroscopy during the Oxygen Evolution Reaction. *Sci. Rep.*, *9*. https://doi.org/10.1038/s41598-018-37307-x

314 G. Mattioli, I. Zaharieva, H. Dau, & L. Guidoni. (2015). Atomistic texture of amorphous manganese oxides for electrochemical water splitting revealed by *ab initio* calculations combined with X-ray spectroscopy. *J. Am. Chem. Soc.*, *137*(32), 10254-10267. https://doi.org/10.1021/jacs.5b05174

315 C. Pasquini, S. Liu, P. Chernev, D. Gonzalez-Flores, M. R. Mohammadi, P. Kubella, S. Jiang, S. Loos, K. Klingan, V. Sikolenko, S. Mebs, M. Haumann, P. Beyer, L. D'Amario, R. D. L. Smith, I. Zaharieva, & H. Dau. (2021). Operando tracking of oxidation-state changes by coupling electrochemistry with time-resolved X-ray absorption spectroscopy demonstrated for water oxidation by a cobalt-based catalyst film. *Anal. Bioanal. Chem.*, *413*(21), 5395-5408. https://doi.org/10.1007/s00216-021-03515-0

316 H. Dau, P. Liebisch, & M. Haumann. (2003). X-ray absorption spectroscopy to analyze nuclear geometry and electronic structure of biological metal centers - potential and questions examined with special focus on the tetra-nuclear manganese complex of oxygenic photosynthesis. *Anal. Bioanal. Chem.*, *376*(5), 562-583. https://doi.org/10.1007/s00216-003-1982-2

317 L. Gao, X. Cui, C. D. Sewell, J. Li, & Z. Lin. (2021). Recent advances in activating surface reconstruction for the high-efficiency oxygen evolution reaction. *Chem. Soc. Rev.*, *50*(15), 8428-8469. https://doi.org/10.1039/D0CS00962H

318 M. Risch, D. M. Morales, J. Villalobos, & D. Antipin. (2022). What X-Ray Absorption Spectroscopy Can Tell Us About the Active State of Earth-Abundant Electrocatalysts for the Oxygen Evolution Reaction. *Angew. Chem. Int. Ed.*, *61*(50), e202211949. https://doi.org/10.1002/anie.202211949

319 A. D. Handoko, F. Wei, Jenndy, B. S. Yeo, & Z. W. Seh. (2018). Understanding heterogeneous electrocatalytic carbon dioxide reduction through operando techniques. *Nat. Catal.*, *1*(12), 922-934. https://doi.org/10.1038/s41929-018-0182-6

320 M. Newville. (2014). Fundamentals of XAFS. *Reviews in Mineralogy and Geochemistry*, *78*(1), 33-74. https://doi.org/10.2138/rmg.2014.78.2

321 P. Busse, Z. Yin, D. Mierwaldt, J. Scholz, B. Kressdorf, L. Glaser, P. S. Miedema, A. Rothkirch, J. Viefhaus, C. Jooss, S. Techert, & M. Risch. (2020). Probing the Surface of $La_{0.6}Sr_{0.4}MnO_3$ in Water Vapor by In Situ Photon-In/Photon-Out Spectroscopy. *J. Phys. Chem. C*, *124*(14), 7893-7902. https://doi.org/10.1021/acs.jpcc.0c00840

322 J. Timoshenko, & B. Roldan Cuenya. (2021). In Situ/Operando Electrocatalyst Characterization by X-ray Absorption Spectroscopy. *Chem Rev*, *121*(2), 882-961. https://doi.org/10.1021/acs.chemrev.0c00396

323 M. Wang, L. Árnadóttir, Z. J. Xu, & Z. Feng. (2019). In Situ X-ray Absorption Spectroscopy Studies of Nanoscale Electrocatalysts. *Nano-Micro Letters*, *11*(1), 47. https://doi.org/10.1007/s40820-019-0277-x

324 S. Mobilio, F. Boscherini, & C. Meneghini. (2015). *Synchrotron radiation. Basics, methods and applications* (Vol. 46). Springer. https://doi.org/10.1007/978-3-642-55315-8

325 J. J. Rehr, & R. C. Albers. (2000). Theoretical approaches to X-ray absorption fine structure. *Rev. Mod. Phys.*, *72*(3), 621-654. https://doi.org/10.1103/RevModPhys.72.621

326 T. Yamamoto. (2008). Assignment of pre-edge peaks in K-edge X-ray absorption spectra of 3d transition metal compounds: electric dipole or quadrupole? *X-Ray Spectrometry*, *37*(6), 572-584. https://doi.org/10.1002/xrs.1103

327 A. A. Guda, S. A. Guda, A. Martini, A. N. Kravtsova, A. Algasov, A. Bugaev, S. P. Kubrin, L. V. Guda, P. Šot, J. A. van Bokhoven, C. Copéret, & A. V. Soldatov. (2021). Understanding X-ray absorption spectra by means of descriptors and machine learning algorithms. *npj Computational Materials*, *7*(1), 203. https://doi.org/10.1038/s41524-021-00664-9

328 J. Penner-Hahn. (2003). Comprehensive Coordination Chemistry II; McCleverty, JA, Meyer, TJ, Eds. In: Elsevier: Amsterdam.

329 W. Krone, G. Wortmann, K. Frank, G. Kaindl, K. Menke, & S. Roth. (1984). EXAFS Near Edge Structure. In (Vol. 2). Berlin: Springer.

330 C. R. Natoli. (1984). Distance dependence of continuum and bound state of excitonic resonances in X-ray absorption near edge structure (XANES).

331 J. E. Penner-Hahn. (1999). X-ray absorption spectroscopy in coordination chemistry. *Coord. Chem. Rev.*, *190-192*, 1101-1123. https://doi.org/10.1016/S0010-8545(99)00160-5

332 G. G. Li, F. Bridges, & C. H. Booth. (1995). X-ray-absorption fine-structure standards: A comparison of experiment and theory. *Phys. Rev. B*, *52*(9), 6332-6348. https://doi.org/10.1103/PhysRevB.52.6332

333 M. F. Tesch, & A. N. Simonov. (2022). Tracking the transient: Real-time exploration of electromaterials by dynamic single energy X-ray spectroelectrochemistry. *Curr. Opin. Electrochem.*, *35*, 101038. https://doi.org/10.1016/j.coelec.2022.101038

334 A. H. Clark, P. Steiger, B. Bornmann, S. Hitz, R. Frahm, D. Ferri, & M. Nachtegaal. (2020). Fluorescence-detected quick-scanning X-ray absorption spectroscopy. *J. Synchrotron Radiat.*, *27*(3), 681-688. https://doi.org/10.1107/S1600577520002350

335 R. Frahm. (1988). Quick scanning exafs: First experiments. *Nuclear Instruments and Methods in Physics Research Section A: Accelerators, Spectrometers, Detectors and Associated Equipment*, *270*(2), 578-581. https://doi.org/10.1016/0168-9002(88)90732-2

336 O. Muller, M. Nachtegaal, J. Just, D. Lutzenkirchen-Hecht, & R. Frahm. (2016). Quick-EXAFS setup at the SuperXAS beamline for in situ X-ray absorption spectroscopy with 10 ms time resolution. *J. Synchrotron Radiat.*, *23*(1), 260-266. https://doi.org/10.1107/S1600577515018007

337 S. Pascarelli, T. Neisius, & S. De Panfilis. (1999). Turbo-XAS: dispersive XAS using sequential acquisition. *J. Synchrotron Radiat.*, *6*(5), 1044-1050. https://doi.org/10.1107/S0909049599004513

338 J. McBreen, W. E. O'Grady, G. Tourillon, E. Dartyge, A. Fontaine, & K. I. Pandya. (1989). In situ time-resolved x-ray absorption near edge structure study of the nickel oxide electrode. *J. Phys. Chem. C*, *93*(17), 6308-6311. https://doi.org/10.1021/j100354a010

339 A. Filipponi, M. Borowski, P. W. Loeffen, S. D. Panfilis, A. D. Cicco, F. Sperandini, M. Minicucci, & M. Giorgetti. (1998). Single-energy X-ray absorption detection: a combined electronic and structural local probe for phase transitions in condensed matter. *J. Phys. Condens. Matter*, *10*(1), 235-253. https://doi.org/10.1088/0953-8984/10/1/026

340 A. Minguzzi, O. Lugaresi, C. Locatelli, S. Rondinini, F. D'Acapito, E. Achilli, & P. Ghigna. (2013). Fixed Energy X-ray Absorption Voltammetry. *Anal. Chem.*, *85*(15), 7009-7013. https://doi.org/10.1021/ac401414v

341 D. González-Flores, I. Zaharieva, J. Heidkamp, P. Chernev, E. Martinez-Moreno, C. Pasquini, M. R. Mohammadi, K. Klingan, U. Gernet, A. Fischer, & H. Dau. (2016). Electrosynthesis of biomimetic manganese–calcium oxides for water oxidation catalysis–atomic structure and functionality. *ChemSusChem*, *9*(4), 379-387. https://doi.org/10.1002/cssc.201501399

342 M. Gorlin, P. Chernev, P. Paciok, C. W. Tai, J. Ferreira de Araujo, T. Reier, M. Heggen, R. Dunin-Borkowski, P. Strasser, & H. Dau. (2019). Formation of unexpectedly active Ni-Fe oxygen evolution electrocatalysts by physically mixing Ni and Fe oxyhydroxides. *Chem. Commun.*, *55*(6), 818-821. https://doi.org/10.1039/c8cc06410e

343 S. Loos, I. Zaharieva, P. Chernev, A. Lißner, & H. Dau. (2019). Electromodified NiFe Alloys as Electrocatalysts for Water Oxidation: Mechanistic Implications of Time-Resolved UV/Vis Tracking of Oxidation State Changes. *ChemSusChem*, *12*(9), 1966-1976. https://doi.org/10.1002/cssc.201802737

344 N. Kornienko. (2021). Operando spectroscopy of nanoscopic metal/covalent organic framework electrocatalysts. *Nanoscale*, *13*(3), 1507-1514. https://doi.org/10.1039/d0nr07508f

345 C. Long, J. Han, J. Guo, C. Yang, S. Liu, & Z. Tang. (2021). Operando toolbox for heterogeneous interface in electrocatalysis. *Chem Catalysis*, *1*(3), 509-522. https://doi.org/10.1016/j.checat.2021.07.012

346 S. Wahl, S. M. El-Refaei, P. Amsalem, A. G. Buzanich, N. Koch, & N. Pinna. (2020). Operando diffuse reflectance UV-vis spectroelectrochemistry for investigating oxygen

evolution electrocatalysts. *Catal. Sci. Technol.*, *10*(2), 517-528. https://doi.org/10.1039/C9CY02329A

347 G. Ertl, H. Knözinger, F. Schüth, & J. Weitkamp. (2008). *Handbook of heterogeneous catalysis*. Wiley-VCH.

348 C. A. Mesa, E. Pastor, & L. Francàs. (2022). UV–Vis operando spectroelectrochemistry for (photo)electrocatalysis: Principles and guidelines. *Curr. Opin. Electrochem.*, *35*, 101098. https://doi.org/10.1016/j.coelec.2022.101098

349 G. Gauglitz, & D. S. Moore. (2014). *Handbook of spectroscopy* (Vol. 1). Wiley-Vch Weinheim, Germany.

350 J. Huheey, E. Keiter, & R. Keiter. (2014). *Anorganische Chemie*. De Gruyter. https://doi.org/10.1515/9783110307955

351 S. D. a. H. Jackson, J. S. J. (2009). *Metal Oxide Catalysis*. Wiley.

352 T. Kuwana, R. K. Darlington, & D. W. Leedy. (1964). Electrochemical Studies Using Conducting Glass Indicator Electrodes. *Anal. Chem.*, *36*(10), 2023-2025. https://doi.org/10.1021/ac60216a003

353 C. V. Raman, & K. S. Krishnan. (1928). The Optical Analogue of the Compton Effect. *Nature*, *121*(3053), 711-711. https://doi.org/10.1038/121711a0

354 R. R. Jones, D. C. Hooper, L. Zhang, D. Wolverson, & V. K. Valev. (2019). Raman Techniques: Fundamentals and Frontiers. *Nanoscale Res. Lett.*, *14*(1), 231. https://doi.org/10.1186/s11671-019-3039-2

355 Y. AlSalka, S. Schwabe, J. Geweke, G. Ctistis, & H. Wackerbarth. (2023). Electrochemical and Photoelectrochemical Water Splitting: Operando Raman and Fourier Transform Infrared Spectroscopy as Useful Probing Techniques. *Energy Technol.*, *11*(3), 2200788. https://doi.org/10.1002/ente.202200788

356 C. Hess. (2021). New advances in using Raman spectroscopy for the characterization of catalysts and catalytic reactions. *Chem. Soc. Rev.*, *50*(5), 3519-3564. https://doi.org/10.1039/d0cs01059f

357 N. Heidary, K. H. Ly, & N. Kornienko. (2019). Probing CO_2 Conversion Chemistry on Nanostructured Surfaces with Operando Vibrational Spectroscopy. *Nano Lett.*, *19*(8), 4817-4826. https://doi.org/10.1021/acs.nanolett.9b01582

358 H. Li, P. Wei, D. Gao, & G. Wang. (2022). In situ Raman spectroscopy studies for electrochemical CO_2 reduction over Cu catalysts. *Curr. Opin. Green Sustain. Chem.*, *34*, 100589. https://doi.org/10.1016/j.cogsc.2022.100589

359 Z. Xu, Z. Liang, W. Guo, & R. Zou. (2021). In situ/operando vibrational spectroscopy for the investigation of advanced nanostructured electrocatalysts. *Coord. Chem. Rev.*, *436*, 213824-213824. https://doi.org/10.1016/j.ccr.2021.213824

360 H.-S. Su, H.-S. Feng, X. Wu, J.-J. Sun, & B. Ren. (2021). Recent advances in plasmon-enhanced Raman spectroscopy for catalytic reactions on bifunctional metallic nanostructures. *Nanoscale*, *13*(33), 13962-13975. https://doi.org/10.1039/D1NR04009J

361 K. S. Joya, & X. Sala. (2015). In situ Raman and surface-enhanced Raman spectroscopy on working electrodes: spectroelectrochemical characterization of water oxidation electrocatalysts. *Phys. Chem. Chem. Phys.*, *17*(33), 21094-21103. https://doi.org/10.1039/c4cp05053c

362 Y. Deng, & B. S. Yeo. (2017). Characterization of electrocatalytic water splitting and CO_2 reduction reactions using In situ/operando Raman spectroscopy. *ACS Catal.*, *7*(11), 7873-7889. https://doi.org/10.1021/acscatal.7b02561

363 F. Korinth, T. A. Shaik, J. Popp, & C. Krafft. (2021). Assessment of shifted excitation Raman difference spectroscopy in highly fluorescent biological samples. *Analyst*, *146*(22), 6760-6767. https://doi.org/10.1039/D1AN01376A

364 B. S. Yeo, & A. T. Bell. (2011). Enhanced activity of gold-supported cobalt oxide for the electrochemical evolution of oxygen. *J. Am. Chem. Soc.*, *133*(14), 5587-5593. https://doi.org/10.1021/ja200559j

365 J. Huang, H. Sheng, R. D. Ross, J. Han, X. Wang, B. Song, & S. Jin. (2021). Modifying redox properties and local bonding of Co_3O_4 by CeO_2 enhances oxygen evolution catalysis in acid. *Nat. Commun.*, *12*(1), 3036. https://doi.org/10.1038/s41467-021-23390-8

366 S. Guo, Y. Li, S. Tang, Y. Zhang, X. Li, A. J. Sobrido, M. M. Titirici, & B. Wei. (2020). Monitoring hydrogen evolution reaction intermediates of transition metal dichalcogenides via operando Raman spectroscopy. *Adv. Func. Mater.*, *30*(35), 2003035. https://doi.org/10.1002/adfm.202003035

367 K. H. Cho, S. Park, H. Seo, S. Choi, M. Y. Lee, C. Ko, & K. T. Nam. (2021). Capturing manganese oxide intermediates in electrochemical water oxidation at neutral pH by in situ Raman spectroscopy. *Angew. Chem. Int. Ed.*, *60*(9), 4673-4681. https://doi.org/10.1002/anie.202014551

368 A. Moysiadou, S. Lee, C. S. Hsu, H. M. Chen, & X. Hu. (2020). Mechanism of oxygen evolution catalyzed by cobalt oxyhydroxide: cobalt superoxide species as a key intermediate and dioxygen release as a rate-determining step. *J. Am. Chem. Soc.*, *142*(27), 11901-11914. https://doi.org/10.1021/jacs.0c04867

369 H.-Y. Wang, S.-F. Hung, Y.-Y. Hsu, L. Zhang, J. Miao, T.-S. Chan, Q. Xiong, & B. Liu. (2016). In Situ Spectroscopic Identification of μ-OO Bridging on Spinel Co_3O_4 Water Oxidation Electrocatalyst. *J. Phys. Chem. Lett.*, *7*(23), 4847-4853. https://doi.org/10.1021/acs.jpclett.6b02147

370 X. X. Han, R. S. Rodriguez, C. L. Haynes, Y. Ozaki, & B. Zhao. (2021). Surface-enhanced Raman spectroscopy. *Nat. Rev. Methods Primers*, *1*(1), 1-17. https://doi.org/10.1038/s43586-021-00083-6

371 B. Y. Wen, Q. Q. Chen, P. M. Radjenovic, J. C. Dong, Z. Q. Tian, & J. F. Li. (2021). In situ surface-enhanced Raman spectroscopy characterization of electrocatalysis with different nanostructures. *Annu. Rev. Phys. Chem.*, *72*(1), 331-351. https://doi.org/10.1146/annurev-physchem-090519-034645

372 J. A. Dieringer, A. D. McFarland, N. C. Shah, D. A. Stuart, A. V. Whitney, C. R. Yonzon, M. A. Young, X. Zhang, & R. P. Van Duyne. (2006). Surface enhanced Raman spectroscopy: New materials, concepts, characterization tools, and applications. *Faraday Discuss.*, *132*, 9-26. https://doi.org/10.1039/b513431p

373 W. Wei, S. Li, J. E. Millstone, M. J. Banholzer, X. Chen, X. Xu, G. C. Schatz, & C. A. Mirkin. (2009). Surprisingly long-range surface-enhanced raman scattering (SERS) on Au-Ni multisegmented nanowires. *Angew. Chem. Int. Ed.*, *48*(23), 4210-4212. https://doi.org/10.1002/anie.200806116

374 T. Touzalin, S. Joiret, E. Maisonhaute, & I. T. Lucas. (2017). Capturing electrochemical transformations by tip-enhanced Raman spectroscopy. *Curr. Opin. Electrochem.*, *6*(1), 46-52. https://doi.org/10.1016/j.coelec.2017.10.016

375 A. B. Zrimsek, N. Chiang, M. Mattei, S. Zaleski, M. O. McAnally, C. T. Chapman, A.-I. Henry, G. C. Schatz, & R. P. Van Duyne. (2017). Single-molecule chemistry with surface- and tip-enhanced Raman spectroscopy. *Chem. Rev.*, *117*(11), 7583-7613. https://doi.org/10.1021/acs.chemrev.6b00552

376 A. B. Britz-Grell, M. Saumer, & A. Tarasov. (2021). Challenges and opportunities of tip-enhanced Raman spectroscopy in liquids. *J. Phys. Chem. C*, *125*(39), 21321-21340. https://doi.org/10.1021/acs.jpcc.1c05353

377 S. Zaleski, A. J. Wilson, M. Mattei, X. Chen, G. Goubert, M. F. Cardinal, K. A. Willets, & R. P. Van Duyne. (2016). Investigating nanoscale electrochemistry with surface-and tip-enhanced Raman spectroscopy. *Acc. Chem. Res.*, *49*(9), 2023-2030. https://doi.org/10.1021/acs.accounts.6b00327

378 J. F. Li, Y. F. Huang, Y. Ding, Z. L. Yang, S. B. Li, X. S. Zhou, F. R. Fan, W. Zhang, Z. Y. Zhou, D. Y. Wu, B. Ren, Z. L. Wang, & Z. Q. Tian. (2010). Shell-isolated nanoparticle-enhanced Raman spectroscopy. *Nature*, *464*(7287), 392-395. https://doi.org/10.1038/nature08907

379 A. Haryanto, & C. W. Lee. (2022). Shell isolated nanoparticle enhanced Raman spectroscopy for mechanistic investigation of electrochemical reactions. *Nano Converg.*, *9*(1), 9. https://doi.org/10.1186/s40580-022-00301-1

380 K. Kuruvinashetti, Y. Zhang, J. Li, & N. Kornienko. (2020). Shell isolated nanoparticle enhanced Raman spectroscopy for renewable energy electrocatalysis. *New J. Chem.*, *44*(46), 19953-19960. https://doi.org/10.1039/D0NJ03526B

381 M. Fleischmann, P. J. Hendra, & A. J. McQuillan. (1974). Raman spectra of pyridine adsorbed at a silver electrode. *Chem. Phys. Lett.*, *26*(2), 163-166. https://doi.org/10.1016/0009-2614(74)85388-1

382 D. L. Jeanmaire, & R. P. Van Duyne. (1977). Surface raman spectroelectrochemistry: Part I. Heterocyclic, aromatic, and aliphatic amines adsorbed on the anodized silver electrode. *J. electroanal. chem. interfacial electrochem.*, *84*(1), 1-20. https://doi.org/10.1016/S0022-0728(77)80224-6

383 S. S. Masango, R. A. Hackler, N. Large, A. I. Henry, M. O. McAnally, G. C. Schatz, P. C. Stair, & R. P. Van Duyne. (2016). High-resolution distance dependence study of surface-enhanced Raman scattering enabled by atomic layer deposition. *Nano Lett.*, *16*(7), 4251-4259. https://doi.org/10.1021/acs.nanolett.6b01276

384 P. L. Stiles, J. A. Dieringer, N. C. Shah, & R. P. Van Duyne. (2008). Surface-Enhanced Raman Spectroscopy. *Annual Review of Analytical Chemistry*, *1*(1), 601-626. https://doi.org/10.1146/annurev.anchem.1.031207.112814

385 M. D. Sonntag, J. M. Klingsporn, A. B. Zrimsek, B. Sharma, L. K. Ruvuna, & R. P. Van Duyne. (2014). Molecular plasmonics for nanoscale spectroscopy. *Chem. Soc. Rev.*, *43*(4), 1230-1247. https://doi.org/10.1039/C3CS60187K

386 S. Heeg, N. S. Mueller, S. Wasserroth, P. Kusch, & S. Reich. (2021). Experimental tests of surface-enhanced Raman scattering: Moving beyond the electromagnetic enhancement theory. *J. Raman Spectrosc.*, *52*(2), 310-322. https://doi.org/https://doi.org/10.1002/jrs.6014

387 S. M. Morton, & L. Jensen. (2009). Understanding the Molecule−Surface Chemical Coupling in SERS. *J. Am. Chem. Soc.*, *131*(11), 4090-4098. https://doi.org/10.1021/ja809143c

388 L. Jensen, C. M. Aikens, & G. C. Schatz. (2008). Electronic structure methods for studying surface-enhanced Raman scattering. *Chem. Soc. Rev.*, *37*(5), 1061-1073. https://doi.org/10.1039/B706023H

389 R. S. Das, & Y. K. Agrawal. (2011). Raman spectroscopy: Recent advancements, techniques and applications. *Vib. Spectrosc.*, *57*(2), 163-176. https://doi.org/10.1016/j.vibspec.2011.08.003

390 A. Campion, & P. Kambhampati. (1998). Surface-enhanced Raman scattering. *Chem. Soc. Rev.*, *27*(4), 241-250. https://doi.org/10.1039/A827241Z

391 S. Jiang, K. Klingan, C. Pasquini, & H. Dau. (2018). New aspects of operando Raman spectroscopy applied to electrochemical CO_2 reduction on Cu foams. *J. Chem. Phys.*, *150*(4), 041718. https://doi.org/10.1063/1.5054109

392 S. Mahajan, R. M. Cole, J. D. Speed, S. H. Pelfrey, A. E. Russell, P. N. Bartlett, S. M. Barnett, & J. J. Baumberg. (2010). Understanding the surface-enhanced Raman spectroscopy "background". *J. Phys. Chem. C*, *114*(16), 7242-7250. https://doi.org/10.1021/jp907197b

393 K. Q. Lin, J. Yi, J. H. Zhong, S. Hu, B. J. Liu, J. Y. Liu, C. Zong, Z. C. Lei, X. Wang, J. Aizpurua, R. Esteban, & B. Ren. (2017). Plasmonic photoluminescence for recovering native chemical information from surface-enhanced Raman scattering. *Nat. Commun.*, *8*(1), 14891. https://doi.org/10.1038/ncomms14891

394 B. Rivas-Murias, & V. Salgueiriño. (2017). Thermodynamic $CoO–Co_3O_4$ crossover using Raman spectroscopy in magnetic octahedron-shaped nanocrystals. *J. Raman Spectrosc.*, *48*(6), 837-841. https://doi.org/10.1002/jrs.5129

395 F. Korinth, A. S. Mondol, C. Stiebing, I. W. Schie, C. Krafft, & J. Popp. (2020). New methodology to process shifted excitation Raman difference spectroscopy data: a case study of pollen classification. *Sci. Rep.*, *10*(1), 11215. https://doi.org/10.1038/s41598-020-67897-4

396 M. T. Gebrekidan, C. Knipfer, F. Stelzle, J. Popp, S. Will, & A. Braeuer. (2016). A shifted-excitation Raman difference spectroscopy (SERDS) evaluation strategy for the efficient isolation of Raman spectra from extreme fluorescence interference. *J. Raman Spectrosc.*, *47*(2), 198-209. https://doi.org/10.1002/jrs.4775

397 T. Naito, T. Shinagawa, T. Nishimoto, & K. Takanabe. (2020). Water Electrolysis in Saturated Phosphate Buffer at Neutral pH. *ChemSusChem*, *13*(22), 5921-5933. https://doi.org/10.1002/cssc.202001886

398 Y. Dong, & S. Komarneni. (2021). Strategies to Develop Earth-Abundant Heterogeneous Oxygen Evolution Reaction Catalysts for pH-Neutral or pH-Near-Neutral Electrolytes. *Small Methods*, *5*(1), 2000719. https://doi.org/10.1002/smtd.202000719

399 T. Nishimoto, T. Shinagawa, T. Naito, & K. Takanabe. (2021). Delivering the Full Potential of Oxygen Evolving Electrocatalyst by Conditioning Electrolytes at Near-Neutral pH. *ChemSusChem*, *14*(6), 1554-1564. https://doi.org/10.1002/cssc.202002813

400 C. Costentin, & D. G. Nocera. (2019). Dual-Phase Molecular-like Charge Transport in Nanoporous Transition Metal Oxides. *J. Phys. Chem. C*, *123*(3), 1966-1973. https://doi.org/10.1021/acs.jpcc.8b10948

401 A. A. Baykov, O. A. Evtushenko, & S. M. Avaeva. (1988). A malachite green procedure for orthophosphate determination and its use in alkaline phosphatase-based enzyme immunoassay. *Anal. Biochem.*, *171*(2), 266-270. https://doi.org/10.1016/0003-2697(88)90484-8

402 R. Starkey, J. Norman, & M. Hintze. (1986). Who knows the Ka values of water and the hydronium ion? *Journal of Chemical Education*, *63*(6), 473. https://doi.org/10.1021/ed063p473

403 M. L. Campbell, & B. A. Waite. (1990). The Ka values of water and the hydronium ion for comparison with other acids. *Journal of Chemical Education*, *67*(5), 386. https://doi.org/10.1021/ed067p386

404 S. Fletcher. (2009). Tafel slopes from first principles. *J. Solid State Electrochem.*, *13*(4), 537-549. https://doi.org/10.1007/s10008-008-0670-8

405 T. Shinagawa, A. T. Garcia-Esparza, & K. Takanabe. (2015). Insight on Tafel slopes from a microkinetic analysis of aqueous electrocatalysis for energy conversion. *Sci. Rep.*, *5*, 13801-13801. https://doi.org/10.1038/srep13801

406 J. J. Kas, F. D. Vila, C. D. Pemmaraju, T. S. Tan, & J. J. Rehr. (2021). Advanced calculations of X-ray spectroscopies with FEFF10 and Corvus. *J. Synchrotron Radiat.*, *28*(6), 1801-1810. https://doi.org/10.1107/S1600577521008614

407 J. J. Rehr, J. J. Kas, F. D. Vila, M. P. Prange, & K. Jorissen. (2010). Parameter-free calculations of X-ray spectra with FEFF9. *Phys. Chem. Chem. Phys.*, *12*(21), 5503-5513. https://doi.org/10.1039/b926434e

408 M. Huynh, D. K. Bediako, & D. G. Nocera. (2014). A Functionally Stable Manganese Oxide Oxygen Evolution Catalyst in Acid. *J. Am. Chem. Soc.*, *136*(16), 6002-6010. https://doi.org/10.1021/ja413147e

409 A. E. Thorarinsdottir, & D. G. Nocera. (2021). Energy catalysis needs ligands with high oxidative stability. *Chem Catalysis*, *1*(1), 32-43. https://doi.org/10.1016/j.checat.2021.05.012

410 R. Ezhov, A. K. Ravari, G. Bury, P. F. Smith, & Y. Pushkar. (2021). Do multinuclear 3d metal catalysts achieve O–O bond formation via radical coupling or via water nucleophilic attack? WNA leads the way in $[Co_4O_4]^{n+}$. *Chem Catalysis*, *1*(2), 407-422. https://doi.org/10.1016/j.checat.2021.03.013

411 D. M. Tiede, G. Kwon, X. He, K. L. Mulfort, & A. B. F. Martinson. (2020). Characterizing electronic and atomic structures for amorphous and molecular metal oxide catalysts at functional interfaces by combining soft X-ray spectroscopy and high-energy X-ray scattering. *Nanoscale*, *12*(25), 13276-13296. https://doi.org/10.1039/D0NR02350G

412 D. K. Bediako, A. M. Ullman, & D. G. Nocera. (2016). Catalytic Oxygen Evolution by Cobalt Oxido Thin Films. In H. Tüysüz & C. K. Chan (Eds.), *Solar Energy for Fuels. Topics in Current Chemistry* (Vol. 371, pp. 173-213). Springer. https://doi.org/10.1007/128_2015_649

413 J. T. Mefford, A. R. Akbashev, M. K. Kang, C. L. Bentley, W. E. Gent, H. T. D. Deng, D. H. Alsem, Y. S. Yu, N. J. Salmon, D. A. Shapiro, P. R. Unwin, & W. C. Chueh. (2021). Correlative operando microscopy of oxygen evolution electrocatalysts. *Nature*, *593*(7857), 67-73. https://doi.org/10.1038/s41586-021-03454-x

414 Q. Abbas, M. Mirzaeian, M. R. C. Hunt, P. Hall, & R. Raza. (2020). Current state and future prospects for electrochemical energy storage and conversion systems. *Energies*, *13*(21), 5847-5847. https://doi.org/10.3390/en13215847

415 J. Li, C. A. Triana, W. Wan, D. P. Adiyeri Saseendran, Y. Zhao, S. E. Balaghi, S. Heidari, & G. R. Patzke. (2021). Molecular and heterogeneous water oxidation catalysts: recent progress and joint perspectives. *Chem. Soc. Rev.*, *50*(4), 2444-2485. https://doi.org/10.1039/D0CS00978D

416 G. Righi, J. Plescher, F.-P. Schmidt, R. K. Campen, S. Fabris, A. Knop-Gericke, R. Schlögl, T. E. Jones, D. Teschner, & S. Piccinin. (2022). On the origin of multihole oxygen evolution in haematite photoanodes. *Nat. Catal.*, *5*(10), 888-899. https://doi.org/10.1038/s41929-022-00845-9

417 J. Rossmeisl, A. Logadottir, & J. K. Nørskov. (2005). Electrolysis of water on (oxidized) metal surfaces. *Chemical Physics*, *319*(1-3), 178-184.

418 A. Bergmann, T. E. Jones, E. Martinez Moreno, D. Teschner, P. Chernev, M. Gliech, T. Reier, H. Dau, & P. Strasser. (2018). Unified structural motifs of the catalytically active state of Co(oxyhydr)oxides during the electrochemical oxygen evolution reaction. *Nat. Catal.*, *1*(9), 711-719. https://doi.org/10.1038/s41929-018-0141-2

419 C. Ding, J. Shi, Z. Wang, & C. Li. (2017). Photoelectrocatalytic Water Splitting: Significance of Cocatalysts, Electrolyte, and Interfaces. *ACS Catal.*, *7*(1), 675-688. https://doi.org/10.1021/acscatal.6b03107

420 M. Gorlin, P. Chernev, J. Ferreira de Araujo, T. Reier, S. Dresp, B. Paul, R. Krahnert, H. Dau, & P. Strasser. (2016). Oxygen Evolution Reaction Dynamics, Faradaic Charge Efficiency, and the Active Metal Redox States of Ni-Fe Oxide Water Splitting Electrocatalysts. *J. Am. Chem. Soc.*, *138*(17), 5603-5614. https://doi.org/10.1021/jacs.6b00332

421 S. Lee, A. Moysiadou, Y.-C. Chu, H. M. Chen, & X. Hu. (2022). Tracking high-valent surface iron species in the oxygen evolution reaction on cobalt iron (oxy)hydroxides. *Energy Environ. Sci.*, *15*(1), 206-214. https://doi.org/10.1039/D1EE02999A

422 C. N. Brodsky, R. G. Hadt, D. Hayes, B. J. Reinhart, N. Li, L. X. Chen, & D. G. Nocera. (2017). In situ characterization of cofacial Co(IV) centers in Co_4O_4 cubane: Modeling the high-valent active site in oxygen-evolving catalysts. *Proc. Natl. Acad. Sci. U.S.A.*, *114*(15), 3855-3860. https://doi.org/10.1073/pnas.1701816114

423 M. M. Najafpour, D. J. Sedigh, S. M. Hosseini, & I. Zaharieva. (2016). Treated Nanolayered Mn Oxide by Oxidizable Compounds: A Strategy To Improve the Catalytic Activity toward Water Oxidation. *Inorg. Chem*, *55*(17), 8827-8832. https://doi.org/10.1021/acs.inorgchem.6b01334

424 T. Yan, C. Cheng, & L. Zhang. (2021). Exploration of materials electrochemistry in rechargeable batteries using advanced in situ/operando X-ray absorption spectroscopy. *Electron. Struct.*, *3*(1), 013001. https://doi.org/10.1088/2516-1075/abea09

425 K. J. Laidler, & M. C. King. (1983). Development of transition-state theory. *J. Phys. Chem. C*, *87*(15), 2657-2664. https://doi.org/10.1021/j100238a002

426 J. Shan, Y. Zheng, B. Shi, K. Davey, & S.-Z. Qiao. (2019). Regulating Electrocatalysts via Surface and Interface Engineering for Acidic Water Electrooxidation. *ACS Energy Lett.*, *4*(11), 2719-2730. https://doi.org/10.1021/acsenergylett.9b01758

427 M. F. Toney, J. N. Howard, J. Richer, G. L. Borges, J. G. Gordon, O. R. Melroy, D. G. Wiesler, D. Yee, & L. B. Sorensen. (1994). Voltage-dependent ordering of water molecules at an electrode–electrolyte interface. *Nature*, *368*(6470), 444-446. https://doi.org/10.1038/368444a0

428 I. Ledezma-Yanez, W. D. Z. Wallace, P. Sebastián-Pascual, V. Climent, J. M. Feliu, & M. T. M. Koper. (2017). Interfacial water reorganization as a pH-dependent descriptor of the hydrogen evolution rate on platinum electrodes. *Nat. Energy*, *2*(4), 17031. https://doi.org/10.1038/nenergy.2017.31

429 Z. D. Schultz, S. K. Shaw, & A. A. Gewirth. (2005). Potential Dependent Organization of Water at the Electrified Metal−Liquid Interface. *J. Am. Chem. Soc.*, *127*(45), 15916-15922. https://doi.org/10.1021/ja0543393

430 D.-Y. Kuo, J. K. Kawasaki, J. N. Nelson, J. Kloppenburg, G. Hautier, K. M. Shen, D. G. Schlom, & J. Suntivich. (2017). Influence of Surface Adsorption on the Oxygen Evolution Reaction on IrO_2(110). *J. Am. Chem. Soc.*, *139*(9), 3473-3479. https://doi.org/10.1021/jacs.6b11932

431 M. Gorlin, J. F. de Araujo, H. Schmies, D. Bernsmeier, S. Dresp, M. Gliech, Z. Jusys, P. Chernev, R. Kraehnert, H. Dau, & P. Strasser. (2017). Tracking Catalyst Redox States and Reaction Dynamics in Ni-Fe Oxyhydroxide Oxygen Evolution Reaction Electrocatalysts: The Role of Catalyst Support and Electrolyte pH. *J. Am. Chem. Soc.*, *139*(5), 2070-2082. https://doi.org/10.1021/jacs.6b12250

432 T. Takashima, K. Ishikawa, & H. Irie. (2016). Detection of Intermediate Species in Oxygen Evolution on Hematite Electrodes Using Spectroelectrochemical Measurements. *J. Phys. Chem. C*, *120*(43), 24827-24834. https://doi.org/10.1021/acs.jpcc.6b07978

433 Z. K. Goldsmith, A. K. Harshan, J. B. Gerken, M. Vörös, G. Galli, S. S. Stahl, & S. Hammes-Schiffer. (2017). Characterization of NiFe oxyhydroxide electrocatalysts by integrated electronic structure calculations and spectroelectrochemistry. *Proc. Natl. Acad. Sci. U.S.A.*, *114*(12), 3050-3055. https://doi.org/10.1073/pnas.1702081114

434 C. N. P. da Fonseca, M.-A. De Paoli, & A. Gorenstein. (1991). The electrochromic effect in cobalt oxide thin films. *Adv. Mater.*, *3*(11), 553-555. https://doi.org/10.1002/adma.19910031107

435 C. N. Polo da Fonseca, M.-A. De Paoli, & A. Gorenstein. (1994). Electrochromism in cobalt oxide thin films grown by anodic electroprecipitation. *Sol. Energy Mater. Sol. Cells*, *33*(1), 73-81. https://doi.org/10.1016/0927-0248(94)90291-7

436 J. M. Rosolen, F. Decker, M. Fracastoro-Decker, A. Gorenstein, R. M. Torresi, & S. I. C. de Torresi. (1993). A mirage effect analysis of the electrochemical processes in nickel hydroxide electrodes. *J. Electroanal. Chem.*, *354*(1), 273-279. https://doi.org/10.1016/0022-0728(93)80339-J

437 W. Estrada, A. M. Andersson, C. G. Granqvist, A. Gorenstein, & F. Decker. (1991). Infrared reflectance spectroscopy of electrochromic NiOxHy films made by reactive dc sputtering. *J. Mater. Res.*, *6*(8), 1715-1719. https://doi.org/10.1557/JMR.1991.1715

438 R. J. Mortimer. (2011). Electrochromic Materials. *Annu. Rev. Mater. Res.*, *41*(1), 241-268. https://doi.org/10.1146/annurev-matsci-062910-100344

439 R. D. L. Smith, C. Pasquini, S. Loos, P. Chernev, K. Klingan, P. Kubella, M. R. Mohammadi, D. González-Flores, & H. Dau. (2018). Geometric distortions in nickel (oxy)hydroxide electrocatalysts by redox inactive iron ions. *Energy Environ. Sci.*, *11*(9), 2476-2485. https://doi.org/10.1039/C8EE01063C

440 S. Jacquemoud, & S. L. Ustin. (2003, Jan. 01). *Application of radiative transfer models to moisture content estimation and burned land mapping* 4th International Workshop on Remote Sensing and GIS applications to Forest Fire Management,

441 X. Wang, S. Xi, P. Huang, Y. Du, H. Zhong, Q. Wang, A. Borgna, Y.-W. Zhang, Z. Wang, H. Wang, Z. G. Yu, W. S. V. Lee, & J. Xue. (2022). Pivotal role of reversible NiO_6 geometric conversion in oxygen evolution. *Nature*, *611*(7937), 702-708. https://doi.org/10.1038/s41586-022-05296-7

442 K. J. May, C. E. Carlton, K. A. Stoerzinger, M. Risch, J. Suntivich, Y.-L. Lee, A. Grimaud, & Y. Shao-Horn. (2012). Influence of Oxygen Evolution during Water Oxidation on the Surface of Perovskite Oxide Catalysts. *J. Phys. Chem. Lett.*, *3*(22), 3264-3270. https://doi.org/10.1021/jz301414z

443 M. Risch, A. Grimaud, K. J. May, K. A. Stoerzinger, T. J. Chen, A. N. Mansour, & Y. Shao-Horn. (2013). Structural changes of cobalt-based perovskites upon water oxidation investigated by EXAFS. *J. Phys. Chem. C*, *117*(17), 8628-8635. https://doi.org/10.1021/jp3126768

444 S. W. Lee, C. Carlton, M. Risch, Y. Surendranath, S. Chen, S. Furutsuki, A. Yamada, D. G. Nocera, & Y. Shao-Horn. (2012). The Nature of Lithium Battery Materials under Oxygen Evolution Reaction Conditions. *J. Am. Chem. Soc.*, *134*(41), 16959-16962. https://doi.org/10.1021/ja307814j

445 J. D. Blakemore, M. W. Mara, M. N. Kushner-Lenhoff, N. D. Schley, S. J. Konezny, I. Rivalta, C. F. A. Negre, R. C. Snoeberger, O. Kokhan, J. Huang, A. Stickrath, L. A. Tran, M. L. Parr, L. X. Chen, D. M. Tiede, V. S. Batista, R. H. Crabtree, & G. W. Brudvig. (2013). Characterization of an Amorphous Iridium Water-Oxidation Catalyst Electrodeposited from Organometallic Precursors. *Inorg. Chem*, *52*(4), 1860-1871. https://doi.org/10.1021/ic301968j

446 W. J. Jiang, T. Tang, Y. Zhang, & J. S. Hu. (2020). Synergistic Modulation of Non-Precious-Metal Electrocatalysts for Advanced Water Splitting. *Acc. Chem. Res.*, *53*(6), 1111-1123. https://doi.org/10.1021/acs.accounts.0c00127

447 B. M. Hunter, H. B. Gray, & A. M. Müller. (2016). Earth-Abundant Heterogeneous Water Oxidation Catalysts. *Chem. Rev.*, *116*, 14120−14136. https://doi.org/10.1021/acs.chemrev.6b00398

448 E. Baktash, I. Zaharieva, M. Schröder, C. Goebel, H. Dau, & A. Thomas. (2013). Cyanamide route to calcium–manganese oxide foams for water oxidation. *Dalton Trans.*, *42*(48), 16920-16929. https://doi.org/10.1039/C3DT51693H

449 Y. Mousazade, M. R. Mohammadi, R. Bagheri, R. Bikas, P. Chernev, Z. Song, T. Lis, M. Siczek, N. Noshiranzadeh, S. Mebs, H. Dau, I. Zaharieva, & M. M. Najafpour. (2020). A synthetic manganese–calcium cluster similar to the catalyst of Photosystem II: challenges for biomimetic water oxidation. *Dalton Trans.*, *49*(17), 5597-5605. https://doi.org/10.1039/D0DT00536C

450 H. Dau, A. Grundmeier, P. Loja, & M. Haumann. (2008). On the structure of the manganese complex of photosystem II: extended-range EXAFS data and specific atomic-

resolution models for four S-states. *Philos. Trans. R. Soc. B: Biol. Sci.*, *363*(1494), 1237-1244. https://doi.org/10.1098/rstb.2007.2220

451 S. Boyd, K. Ganeshan, W. Y. Tsai, T. Wu, S. Saeed, D. e. Jiang, N. Balke, A. C. T. van Duin, & V. Augustyn. (2021). Effects of interlayer confinement and hydration on capacitive charge storage in birnessite. *Nature Mater.*, *20*(12), 1689-1694. https://doi.org/10.1038/s41563-021-01066-4

452 P. H. Benhangi, A. Alfantazi, & E. Gyenge. (2014). Manganese Dioxide-based Bifunctional Oxygen Reduction/Evolution Electrocatalysts: Effect of Perovskite Doping and Potassium Ion Insertion. *Electrochim. Acta*, *123*, 42-50. https://doi.org/10.1016/j.electacta.2013.12.102

453 S. Dresp, F. Dionigi, M. Klingenhof, T. Merzdorf, H. Schmies, J. Drnec, A. Poulain, & P. Strasser. (2021). Molecular Understanding of the Impact of Saline Contaminants and Alkaline pH on NiFe Layered Double Hydroxide Oxygen Evolution Catalysts. *ACS Catal.*, *11*(12), 6800-6809. https://doi.org/10.1021/acscatal.1c00773

454 A.-C. Gaillot, D. Flot, V. A. Drits, A. Manceau, M. Burghammer, & B. Lanson. (2003). Structure of synthetic K-rich birnessite obtained by high-temperature decomposition of $KMnO_4$. I. Two-layer polytype from 800 °C experiment. *Chem. Mater.*, *15*, 4666-4678. https://doi.org/10.1021/cm021733g

455 V. Vao-soongnern, C. Pipatpanukul, & S. Horpibulsuk. (2015). A combined X-ray absorption spectroscopy and molecular dynamic simulation to study the local structure potassium ion in hydrated montmorillonite. *J. Mater. Sci.*, *50*(21), 7126-7136. https://doi.org/10.1007/s10853-015-9269-5

456 V. A. Glezakou, Y. S. Chen, J. L. Fulton, G. K. Schenter, & L. X. Dang. (2006). Electronic structure, statistical mechanical simulations, and EXAFS spectroscopy of aqueous potassium. *Theor. Chem. Acc.*, *115*(2-3), 86-99. https://doi.org/10.1007/s00214-005-0054-4

457 C. N. Rowley, & B. t. Roux. (2012). The Solvation Structure of Na^+ and K^+ in Liquid Water Determined from High Level ab Initio Molecular Dynamics Simulations. *J. Chem. Theory Comput.*, *8*(10), 3526-3535. https://doi.org/10.1021/ct300091w

458 D. Zhuang, M. Riera, R. Zhou, A. Deary, & F. Paesani. (2022). Hydration Structure of Na^+ and K^+ Ions in Solution Predicted by Data-Driven Many-Body Potentials. *J. Phys. Chem. B*, *126*(45), 9349-9360. https://doi.org/10.1021/acs.jpcb.2c05674

459 A. S. Rao, K. S. Reddy, & P. N. Takkar. (1997). Malachite green method compared to ascorbic acid for estimating small amounts of phosphorus in water, 0.01 M calcium chloride, and olsen soil extracts. *Commun. Soil Sci. Plant Anal.*, *28*(6-8), 589-601. https://doi.org/10.1080/00103629709369813

460 J. Feng, Y. Chen, J. Pu, X. Yang, C. Zhang, S. Zhu, Y. Zhao, Y. Yuan, H. Yuan, & F. Liao. (2011). An improved malachite green assay of phosphate: Mechanism and application. *Anal. Biochem.*, *409*(1), 144-149. https://doi.org/10.1016/j.ab.2010.10.025

461 S. Rahutomo, J. L. Kovar, & M. L. Thompson. (2019). Malachite Green Method for Determining Phosphorus Concentration in Diverse Matrices. *Commun. Soil Sci. Plant Anal.*, *50*(14), 1743-1752. https://doi.org/10.1080/00103624.2019.1635140

462 S. Yan, K. P. Abhilash, L. Tang, M. Yang, Y. Ma, Q. Xia, Q. Guo, & H. Xia. (2019). Research Advances of Amorphous Metal Oxides in Electrochemical Energy Storage and Conversion. *Small*, *15*(4), 1804371. https://doi.org/10.1002/smll.201804371

463 Y. Zhou, & H. J. Fan. (2021). Progress and Challenge of Amorphous Catalysts for Electrochemical Water Splitting. *ACS Mater. Lett.*, *3*(1), 136-147. https://doi.org/10.1021/acsmaterialslett.0c00502

464 K. Yang, R. Kas, & W. A. Smith. (2019). In Situ Infrared Spectroscopy Reveals Persistent Alkalinity near Electrode Surfaces during CO_2 Electroreduction. *J. Am. Chem. Soc.*, *141*(40), 15891-15900. https://doi.org/10.1021/jacs.9b07000

465 M. C. O. Monteiro, L. Jacobse, T. Touzalin, & M. T. M. Koper. (2020). Mediator-Free SECM for Probing the Diffusion Layer pH with Functionalized Gold Ultramicroelectrodes. *Anal. Chem.*, *92*(2), 2237-2243. https://doi.org/10.1021/acs.analchem.9b04952

466 M. Dunwell, X. Yang, B. P. Setzler, J. Anibal, Y. Yan, & B. Xu. (2018). Examination of near-electrode concentration gradients and Kinetic impacts on the electrochemical reduction of CO_2 using surface-enhanced infrared spectroscopy. *ACS Catal.*, *8*(5), 3999-4008. https://doi.org/10.1021/acscatal.8b01032

467 P. Bollella, A. Melman, & E. Katz. (2020). Electrochemically Generated Interfacial pH Change: Application to Signal-Triggered Molecule Release. *ChemElectroChem*, *7*(16), 3386-3403. https://doi.org/10.1002/celc.202000615

468 E. B. Carneiro-Neto, M. C. Lopes, & E. C. Pereira. (2016). Simulation of interfacial pH changes during hydrogen evolution reaction. *J. Electroanal. Chem.*, *765*, 92-99. https://doi.org/10.1016/j.jelechem.2015.09.029

469 A. T. Kuhn, & C. Y. Chan. (1983). pH changes at near-electrode surfaces. *J. Appl. Electrochem.*, *13*(2), 189-207. https://doi.org/10.1007/BF00612481

470 N. C. Rudd, S. Cannan, E. Bitziou, I. Ciani, A. L. Whitworth, & P. R. Unwin. (2005). Fluorescence Confocal Laser Scanning Microscopy as a Probe of pH Gradients in Electrode Reactions and Surface Activity. *Anal. Chem.*, *77*(19), 6205-6217. https://doi.org/10.1021/ac050800y

471 S. Cannan, I. Douglas Macklam, & P. R. Unwin. (2002). Three-dimensional imaging of proton gradients at microelectrode surfaces using confocal laser scanning microscopy. *Electrochem. commun.*, *4*(11), 886-892. https://doi.org/10.1016/S1388-2481(02)00482-4

472 B. Fuladpanjeh-Hojaghan, M. M. Elsutohy, V. Kabanov, B. Heyne, M. Trifkovic, & E. P. L. Roberts. (2019). In-Operando Mapping of pH Distribution in Electrochemical Processes. *Angew. Chem. Int. Ed.*, *58*(47), 16815-16819. https://doi.org/10.1002/anie.201909238

473 O. Ayemoba, & A. Cuesta. (2017). Spectroscopic Evidence of Size-Dependent Buffering of Interfacial pH by Cation Hydrolysis during CO_2 Electroreduction. *ACS Appl. Mater. Interfaces*, *9*(33), 27377-27382. https://doi.org/10.1021/acsami.7b07351

474 R. Song, Q. Xiong, T. Wu, X. Ning, F. Zhang, Q. Wang, & P. He. (2020). Real-time monitoring of extracellular pH using a pH-potentiometric sensing SECM dual-microelectrode. *Anal. Bioanal. Chem.*, *412*(15), 3737-3743. https://doi.org/10.1007/s00216-020-02625-5

475 Z. Zhu, Z. Ye, Q. Zhang, J. Zhang, & F. Cao. (2018). Novel dual Pt-Pt/IrOx ultramicroelectrode for pH imaging using SECM in both potentiometric and amperometric modes. *Electrochem. commun.*, *88*, 47-51. https://doi.org/10.1016/j.elecom.2018.01.018

476 D. Filotás, B. M. Fernández-Pérez, L. Nagy, G. Nagy, & R. M. Souto. (2019). Multi-barrel electrodes containing an internal micro-reference for the improved visualization of galvanic corrosion processes in magnesium-based materials using potentiometric scanning electrochemical microscopy. *Sens. Actuators B Chem.*, *296*, 126625. https://doi.org/10.1016/j.snb.2019.126625

477 Z. Zhu, X. Liu, Z. Ye, J. Zhang, F. Cao, & J. Zhang. (2018). A fabrication of iridium oxide film pH micro-sensor on Pt ultramicroelectrode and its application on in-situ pH distribution of 316L stainless steel corrosion at open circuit potential. *Sens. Actuators B Chem.*, *255*, 1974-1982. https://doi.org/10.1016/j.snb.2017.08.219

478 N. Pande, S. K. Chandrasekar, D. Lohse, G. Mul, J. A. Wood, B. T. Mei, & D. Krug. (2020). Electrochemically Induced pH Change: Time-Resolved Confocal Fluorescence Microscopy Measurements and Comparison with Numerical Model. *J. Phys. Chem. Lett.*, *11*(17), 7042-7048. https://doi.org/10.1021/acs.jpclett.0c01575

479 G. Niaura, A. K. Gaigalas, & V. L. Vilker. (1997). Surface-Enhanced Raman Spectroscopy of Phosphate Anions: Adsorption on Silver, Gold, and Copper Electrodes. *J. Phys. Chem. B*, *101*(45), 9250-9262. https://doi.org/10.1021/jp970097k

480 W. W. Rudolph. (2010). Raman- and infrared-spectroscopic investigations of dilute aqueous phosphoric acid solutions. *Dalton Trans.*, *39*(40), 9642-9653. https://doi.org/10.1039/C0DT00417K

481 G. E. Walrafen. (1964). Raman Spectral Studies of Water Structure. *J. Chem. Phys.*, *40*(11), 3249-3256. https://doi.org/10.1063/1.1724992